The University of Southern Mississippi

The Aquila Digital Community

Spring 3-11-2022

THERMOMECHANICS OF SEMICONDUCTING POLYMERS AND THEIR MORPHOLOGICAL PHENOMENA

Luke Galuska

Follow this and additional works at: https://aquila.usm.edu/dissertations

 Part of the Polymer and Organic Materials Commons, and the Semiconductor and Optical Materials Commons

THERMOMECHANICS OF SEMICONDUCTING POLYMERS AND THEIR

MORPHOLOGICAL PHENOMENA

by

Luke A. Galuska

A Dissertation
Submitted to the Graduate School,
the College of Arts and Sciences
and the School of Polymer Science and Engineering
at The University of Southern Mississippi
in Partial Fulfillment of the Requirements
for the Degree of Doctor of Philosophy

Approved by:

Dr. Xiaodan Gu, Committee Chair
Dr. Jason D. Azoulay
Dr. Sarah E. Morgan
Dr. Sergei Nazarenko
Dr. Song Guo

May 2022

THE UNIVERSITY OF
SOUTHERN
MISSISSIPPI®

ABSTRACT

In contrast to conventional silicon-based electronics, semiconducting polymers show great promise for emerging applications in soft, flexible, and ductile electronic technologies. This is due to their polymeric nature, tailorable structure, and sub-100 nm device thickness. Despite this mechanical novelty, there remains a poor understanding of their structure-property-processing relationships, which has hindered growth within the field. This dissertation elucidates these relationships through investigation of their thermomechanics, and morphological phenomena. This was accomplished through the following projects:

1) To demonstrate the impact of backbone rigidity on semiconducting polymer thermomechanics, we varied the backbone rigidity of an NDI-based polymer by inserting flexible methylene units of varying lengths along the backbone of the monomer unit. Incorporation of the spacer resulted in a vast reduction of the glass transition temperature (T_g) and profound improvements in ductility.

2) We developed a free-standing tensile technique that enabled the characterization of polystyrene and poly(3-hexylthiophene) films down to 19 nm and 80 nm, respectively. Confinement was demonstrated to impact yield stress and strain at failure of polystyrene films, while modulus was relatively unaffected, despite literature suggestion of a sub-room temperature T_g. We then compared water-supported and free-standing films to elucidate their interfacial influence on the observed mechanical performance.

3) Amide and urea moieties were incorporated into a DPP-based polymer to demonstrate the role of hydrogen bonding strength on thermomechanical performance.

Amide and urea were discovered to minimize and promote crystallinity, respectively, which led to a 400% increase in strain at failure for the amide-containing polymer. This finding demonstrated that hydrogen bonding may dictate mechanical performance through control of the crystalline morphology, rather than energy dissipation.

4) Due to the semicrystalline nature of semiconducting polymers, it has been postulated that they may possess a rigid amorphous fraction (RAF) which may dictate their optoelectronic performance. To illuminate the existence and impact of the RAF on semiconducting polymer performance we established a spectroscopic ellipsometry method to fully characterize their temperature-dependent thickness, optical profile, and degree of anisotropy. All semicrystalline semiconducting polymers were observed to possess a RAF which strongly dictated their optoelectronic performance.

ACKNOWLEDGMENTS

Firstly, I would like to thank my advisor Xiaodan Gu for guiding me throughout the Ph.D. process, providing ample opportunities for personal and technical growth, and simply being a fantastic mentor. He has given me the freedom to explore my scientific interests while also guiding me to develop a practical and broad knowledge base within polymer science. This strong foundation has jump-started my scientific career, which I am deeply grateful for.

I want to thank my entire committee, Prof. Sarah E. Morgan, Prof. Jason D. Azoulay, Prof. Sergei Nazarenko, and Prof. Song Guo, for their part in my scientific development. From my first year in the Polymer Science and Engineering program, they have guided my professional development through classroom instruction, collaborations, access to instruments, guidance on lab safety, and scientific communication. I particularly want to thank Prof. Morgan for her assistance in joining the Gu research group the summer before I started the Ph.D. program, as well as for the soft skills I learned during the NRT Bootcamp.

I am incredibly grateful to all the members of the Gu research group whom I have worked alongside and developed strong friendships with these past five years. They have played a pivotal role in my professional growth, scientific projects, and enjoyment of graduate school. I want to thank Song Zhang and Daniel Weller for their friendship and guidance.

The completion of my graduate career was only possible through the strong support of all my collaborators. I specifically want to thank Prof. Simon Rondeau-Gagné's group from the University of Windsor, Prof Jianguo Mei's group from Purdue

University, Dr. John Ankner's group from the Spallation Neutron Source at Oakridge National Laboratory, and Dr. Ilia Ivanov's group from the Center for Nanophase Materials Sciences at Oakridge National Laboratory. Additionally, I want to acknowledge the Stanford Synchrotron Radiation Lightsource at the Stanford Linear Accelerator Center and the Advanced Light Source at Lawrence Berkeley National Lab, where some of this work took place.

I am deeply indebted to my loving family for their support and guidance throughout my time in graduate school. My wife Shianne Galuska, my son Theodore Galuska, my parents Alan and Cyndi Galuska, my brothers Kris and Nick Galuska, and my sister Mckenna Turnbow, your love and encouragement has been the bedrock of my life.

DEDICATION

       I would like to dedicate this dissertation to my one-year-old son, Teddy, who is an utter delight but has yet to sleep through the night. I would also like to dedicate this work to my wife, Shianne, and coffee, without either of which I would not have survived graduate school.

TABLE OF CONTENTS

LIST OF TABLES

LIST OF ILLUSTRATIONS

substrate stiffness.[101,106,108,112] b) Normalized moduli obtained from buckling metrology, film-on-water, and free-standing tensile tests, demonstrating a reduction in modulus occurring at ~25 nm for film-on-water, FS, and 10:1 PDMS while increasing base to crosslinker to 20:1 shifts the reduction to higher thickness dependent on polymer bulk T_g. [76,80,86,116,117] c) Hypothetical moduli of 25 nm PS based on the normalized modulus from DMA in respect to the difference in measurement temperature (25°C) and thin-film Tg.. 6

LIST OF ABBREVIATIONS

AFM	*Atomic Force Microscopy*
ARES-LS	*Advanced Rheometric Expansion System*
CBS	*Conjugation Break Spacer*
COS	*Crack-Onset Strain*
CPs	*Conjugated Polymers*
Đ	*Dispersity*
D-A	*Donor-Acceptor*
DMA	*Dynamic Mechanical Analysis*
DPP	*Diketopyrrolopyrrole*
DSC	*Differential Scanning Calorimetry*
E	*Elastic Modulus*
FOW	*Film-on-Water*
FS	*Free-Standing*
FWHM	*Full Width Half Max*
Gen-Osc	*Gaussian Oscillators*
GIWAXS	*Grazing Incidence Wide Angle X-ray Scattering*
G_N	*Entanglement Plateau Modulus*
HT	*High Temp*
LIQREF	*Liquids Reflectometer*
L_k	*Kuhn Length*
LS	*Light Scattering*

MAF	*Mobile Amorphous Fraction*
M_e	*Entanglement Molecular Weight*
M_n	*Number Average Molecular Weight*
M_w	*Weight Average Molecular Weight*
NDI	*Naphthalene Diimide*
NR	*Neutron Reflectometry*
OFET	*Organic Field-Effect Transistor*
ORNL	*Oak Ridge National Laboratory*
PBTTT	*Poly(2,5-bis(3-tetradecylthiophen-2-yl)thieno[3,2-b] thiophene)*
PDCA	*Pyridine Dicarboxamide*
PDI	*Poly Dispersity Index*
PDMS	*Poly(dimethylsiloxane)*
PF	*Polyfluorene*
PLLA	*Poly(L-lactic acid)*
PPV	*Poly(p-phenylene vinylene)*
PS	*Polystyrene*
PSS	*Poly(4-styrenesulfonic acid)*
PTB7	*Poly(thieno[3,4-b]-thiophene-co-benzodithiophene)*
P3ATs	*Poly(3-alkylthiophenes)*
P3HT	*Poly(3-hexylthiophene)*
QCM	*Quartz Crystal Microbalance*

RAF	*Rigid Amorphous Fraction*
rDoC	*Relative Degree of Crystallinity*
R_{ee}	*End-To-End Distance*
RI	*Refractive Index*
SAF	*Strain at Failure*
SANS	*Small Angle Neutron Scattering*
SAXS	*Small Angle X-ray Scattering*
SE	*Spectroscopic Ellipsometry*
SLD	*Scattering Length Density*
SMART	*Shear Motion Assisted Robust Transfer*
SNS	*Spallation Neutron Source*
STDEV	*Standard Deviation*
TCB	*1,2,4-trichlorobenzene*
TCE-d2	*Deuterated 1,1,2,2-tetrachlotoethane*
T_m	*Melting Temperature*
TUFF	*Tensile Tester for Ultrathin Freestanding Films*
T_g	*Glass Transition Temperature*
vGP-plot	*Van Gurp-Palmen-Plots*
VS	*Viscometer*
WAXS	*Wide Angle X-ray Scattering*
YS	*Yield Stress*
Δf/n	*Normalized Frequency Shift*

ΔD/n   *Normalized Energy Dissipation*

Δn   *Anisotropy of refractive index*

CHAPTER I – BACKGROUND

1.1 Overview of semiconducting polymers

Plastic electronics, such a term in today's age, seems counterintuitive. Current

electronics are highly efficient, precisely engineered pieces of technology. At the same

time, plastics suggest applications like the case of a smartphone, offering mechanical

protection but providing no electronic function to the phone itself. This is no longer the

case. Semiconducting polymers, consisting of an electronically active conjugated

backbone and solubilizing flexible side chains, are exceeding expectations. Today, it is

not uncommon to see charge mobilities upwards of ~10 $cm^2V^{-1}s^{-1}$ in literature, surpassing

that of amorphous silicon, given the use of specialized chemical structures and alignment

techniques.[1–8] In addition to their electrical performance, and owing to their polymeric

nature, semiconducting polymers offer the potential benefit of solution processability,

tunable chemical structures, and an array of mechanical attributes (ex. Softness and

ductility) which are unbeknownst to traditional silicon-based electronics. Thus,

semiconducting polymers are an adept material which may be used for a wide variety of

applications from organic photovoltaics and field-effect transistors to even soft wearable

technologies.[9–18]

Unfortunately, the structure-property-processing relationships **(Figure 1.1(a))**

which dictate mechanical performance have yet to be unraveled and thus this factor of

their operation has largely been neglected. Multiple factors contribute to this lack of

understanding, including their heterogenous structure **(Figure 1.1(b))**, strong

confinement effect due to sub-100 nm thickness **(Figure 1.1(c))**, and complex

semicrystalline morphology **(Figure 1.1(d))**. Thus, this dissertation will focus on
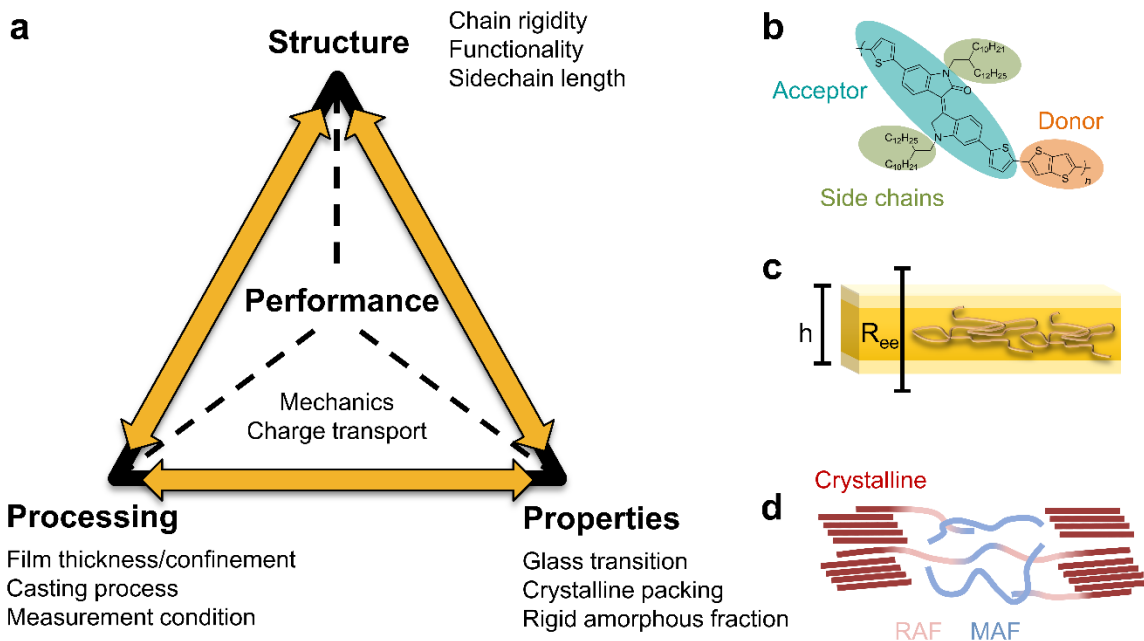
Figure 1.1 *a) Polymer pyramid with representative parameters governing material performance. b) Representative chemical structure of a semiconducting polymer. c) Illustration of geometric confinement associated with thin films. d) Illustration of the three phases found in semiconducting polymers. RAF and MAF are the rigid and mobile amorphous fractions respectively.*

unraveling these relationships to gain insight into the thermomechanics of semiconducting polymers and their morphological phenomenon which dictate performance. The discussion will be divided into four additional chapters outlined below.

Chapter II: We investigated the role of backbone rigidity on the thermomechanical properties and morphology of a series of naphthalene diimide based polymers. This work provided the first quantitative influence of chain rigidity on semiconducting polymer mechanical performance utilizing a holistic suite of characterization techniques.

Chapter III: We developed a method to obtain free-standing films, as thin as 19 nm, and characterize their inherent structural–mechanical properties. The role of

confinement and interfacial influence on mechanics were investigated in relation to glass transition phenomena prevalent throughout literature.

Chapter IV: We explored the role of hydrogen bonding strength on the thermomechanics of a diketopyrrolopyrrole based polymer through the incorporation of amide and urea moieties into the alkyl side chain. Crystalline packing was discovered to be the primary mechanism by which hydrogen bonding governed mechanical performance, rather than energy dissipation.

Chapter V: We established an *in-situ* spectroscopic ellipsometry technique to assess the thermal transitions of semiconducting polymers at device relevant thickness and with high fidelity. Using this method, and an array of thermal characterizations, we demonstrated the existence and impact of the rigid amorphous fraction on the optoelectronic performance of semiconducting polymers.

1.2 Thermal analysis of semiconducting polymers

1.2.1 Background

Despite the importance of T_g in governing many attributes of mechanical performance there remains a lack of information on this phenomenon for D-A polymer systems. This is primarily due to the small batch size in their synthesis (limiting practical application of bulk techniques such as DMA) and the inherent structure of these polymers. Many D-A polymers, such as diketopyrrolopyrrole-based polymers (DPP), possess a minor change in specific heat capacity across T_g, thus hindering the study of this phenomena with conventional DSC.[3,4,19–21] There are primarily three structural factors which contribute to this low transition signal including: high side chain content, semicrystalline nature, and backbone rigidity **(Figure 1.2)**.[21] The sidechain content (often

40-70%) and crystalline domains do not contribute to the signal of the backbone T_g and thus dilute the response.[22] The high backbone rigidity in turn limits the conformation change across the T_g and further results in high crystallization rates which inhibit the quenching of such polymers into the fully amorphous state.
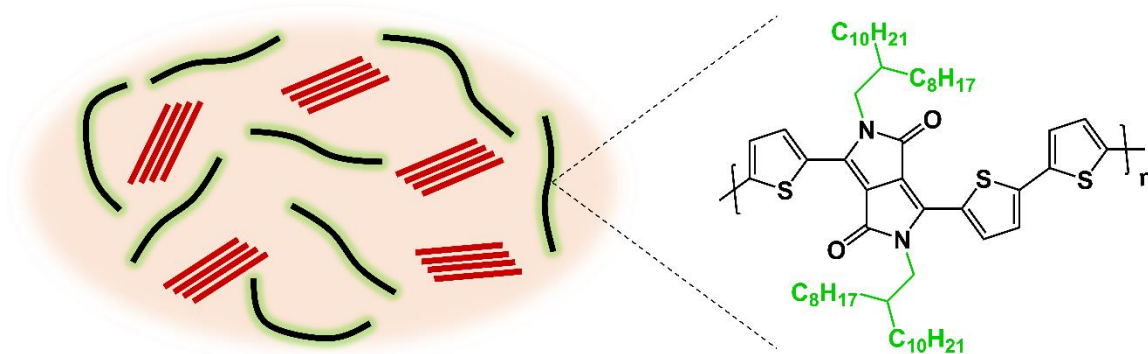
Figure 1.2 *Illustration of the contributing factors to D-A polymers' low glass transition signal. Black lines represent the rigid polymer backbone providing the T_g response. Red and green domains represent the crystalline and side-chain fraction, respectively, which do not contribute to the T_g response of the backbone. The chemical structure is a representative DPP-based polymer with side-chain content of ~60%.*

1.2.2 Characterization of semiconducting polymer glass transition temperature

Despite these challenges, obtaining the T_g of D-A conjugated polymers is not impossible. Notably, supported DMA,[23–27] AC-chip calorimetry,[23,24,28] UV-Vis,[29,30] and oscillatory shear rheometry[31,32] have been used to characterize the T_g of these rigid semicrystalline systems. In supported DMA, the measurement utilizes 5-20 mg of polymer drop cast onto a woven glass fiber substrate. The substrate elicits a negligible response throughout the measurement, thus allowing the thermal transitions of many conjugated polymers to be elucidated.[19,33] However, as there is no specified geometry of the polymer sample, absolute moduli cannot be obtained and thus careful consideration must be used when classifying thermal transitions. AC-chip calorimetry is a dynamic nanocalorimetry measurement which utilizes periodic temperature oscillations over a

broad frequency range to achieve sensitivities on the order of tenths of a pJ K^{-1}.[34,35] Although AC-chip calorimetry is sensitive to the thermal transitions of conjugated polymers it is not a widely available technique. In contrast, UV-Vis is prevalent throughout polymer science and has been demonstrated to obtain the T_g of conjugated polymers with the propensity to form photo-physical aggregates upon thermal annealing, including DPP-based polymers.[29,30] Despite the effectiveness of this technique for semicrystalline systems, it was not capable of determining the T_g for predominantly amorphous systems. Oscillatory shear rheometry, utilizing a vacuum molded puck, requires only 10 mg of material and is a facile method of measuring semiconducting polymer T_g.[31,32] Impressively, this method has been used to characterize the T_g of 32 semiconducting polymers and develop a relationship to further predict T_g based on the chemical structure of interest. Unfortunately, given the nature of the measurement it cannot be applied to thin films.

Although these techniques have been able to locate these weak thermal transitions, many reports disagree on the phenomenon governing their existence. For instance, utilizing modified DMA and AC-chip calorimetry, Zhang et al. reported the backbone T_g of DPP-polymers to generally reside between -10°C and 65°C, depending on the backbone structure and sidechain content.[23,24] Additionally, a higher transition temperature was observed, although not thoroughly discussed, near 150°C. More recently, using AC-chip calorimetry, Luo et al. observed a similar backbone T_g for DPP-T at 23°C as well as another transition at 118°C which was prescribed as the relaxation response of the rigid amorphous fraction.[28] In contrast, other works using modified DMA have shown similar thermal transitions but were attributed to either an aggregate

transition or left undefined.[25–27] Sugiyama et al. utilized UV-Vis to obtain elevated

transitions (from 90°C to 160°C) for a series of DPP-based polymers with varying side

chains. These transitions were described as the T_g of the polymer and were observed to

decrease with increasing side chain content.[29,30] Although this trend agrees with the

findings from Zhang et al, the prescribed T_g by UV-Vis is more than 100°C greater,

despite their comparable chemical structures. It is currently unclear as to the structural

phenomenon which governs both these low and high thermal transitions, and thus glass

transition temperature remains a subject of much debate. The topic of glass transition

phenomenon is a focus of this dissertation but particularly within Chapter V, whereby in-

situ spectroscopic ellipsometry and an array of thermal characterizations are utilized to

understand these phenomena and their impact on semiconducting polymer performance.

Briefly, the temperature dependence of a few conjugated systems (namely

polyfluorenes, P3ATs, and poly[N-9'-heptadecanyl-2,7-carbazole-alt-5,5-(4', 7'-di-2-

thienyl-2',1',3'-benzothiadiazole)] (PCDTBT)) have been explored with spectroscopic

ellipsometry, but this has primarily been through the analysis of raw ellipsometry data

rather than modeling.[36–41] In the former case, the inflection of the raw data (psi or delta)

can signal a T_g response, but no other information is obtained. In contrast, ellipsometry

modeling can provide the thickness, optical profile, and anisotropic temperature

dependence of films at device relevant thickness. However, this remains a significant

challenge for conjugated polymers as their strong UV-Vis absorption and anisotropic

nature obfuscate the data.[38,42] This challenge is overcome in the work presented in

Chapter V of this dissertation.

1.3 Mechanical analysis of thin films

1.3.1 Background

Due to their sub-100nm thickness, semiconducting polymers possess unique challenges in understanding their mechanical performance. At this size scale, properties may differ significantly from bulk, resulting from geometric confinement and interfacial influences. Thus, it is imperative that the mechanical properties of these polymers are assessed at device relevant thicknesses to ensure an accurate representation of their performance. However, due to this challenging size scale, semiconducting polymers cannot be measured under traditional metrologies such as DMA and bulk tensile testing. Many techniques, from industrially recognized nanoindentation to recent tensile methodologies of free-standing films, have been developed throughout the last few decades to overcome these challenges and providing an understanding of thin film mechanics **(Figure 1.3).** These techniques can be broken down into three classifications based on the utilization of solid substrates, liquid substrates, or free-standing films.

1.3.2 Thin film mechanical analysis on solid substrates

In the production of polymeric films, a polymeric solution is cast (drop-casting, spin casting, shear coating, etc.) onto a solid substrate, achieving a range of thicknesses from the nm to um scale.[43] Removing such a film from the substrate is not a simple task and thus the mechanics of many polymer films have been studied atop a solid substrate, such as silicon.[44–49] In nanoindentation based techniques, a probing tip characterizes the mechanical response of a film by applying a vertical force throughout the depth of the film.[50–55] The modulus of many semiconducting polymers has been studied in this manner.[56–59] However, careful consideration should be given to the tip geometry and

penetration depth, both which can alter the observed mechanical properties.[60] Buckling

metrology, created by Stafford *et al.* in 2004, is a facile technique where a film is

laminated onto a pre-strained PDMS substrate.[49,61–64] Upon release of this strain a

compressive force is applied to the film resulting in periodic buckles/wrinkles, which can

be used to determine modulus and yield stress. Additionally, the film on elastomer may

be stretched followed by observation with optical microscopy to obtain the crack-onset-

strain of the polymer film. This has been applied to many semiconducting polymers, with

notable contributions from Lipomi *et al.*, O'Connor *et al.*, Delongchamp et al., and Bao et

al.[47,65–71] Most recently, the temperature dependent mechanical properties of P3HT

laminated onto PDMS have been measure utilizing conventional DMA.[72] Despite the

facile nature of such measurements, utilizing solid substrates, the influence of these

substrates should be taken into account when characterizing mechanical performance.
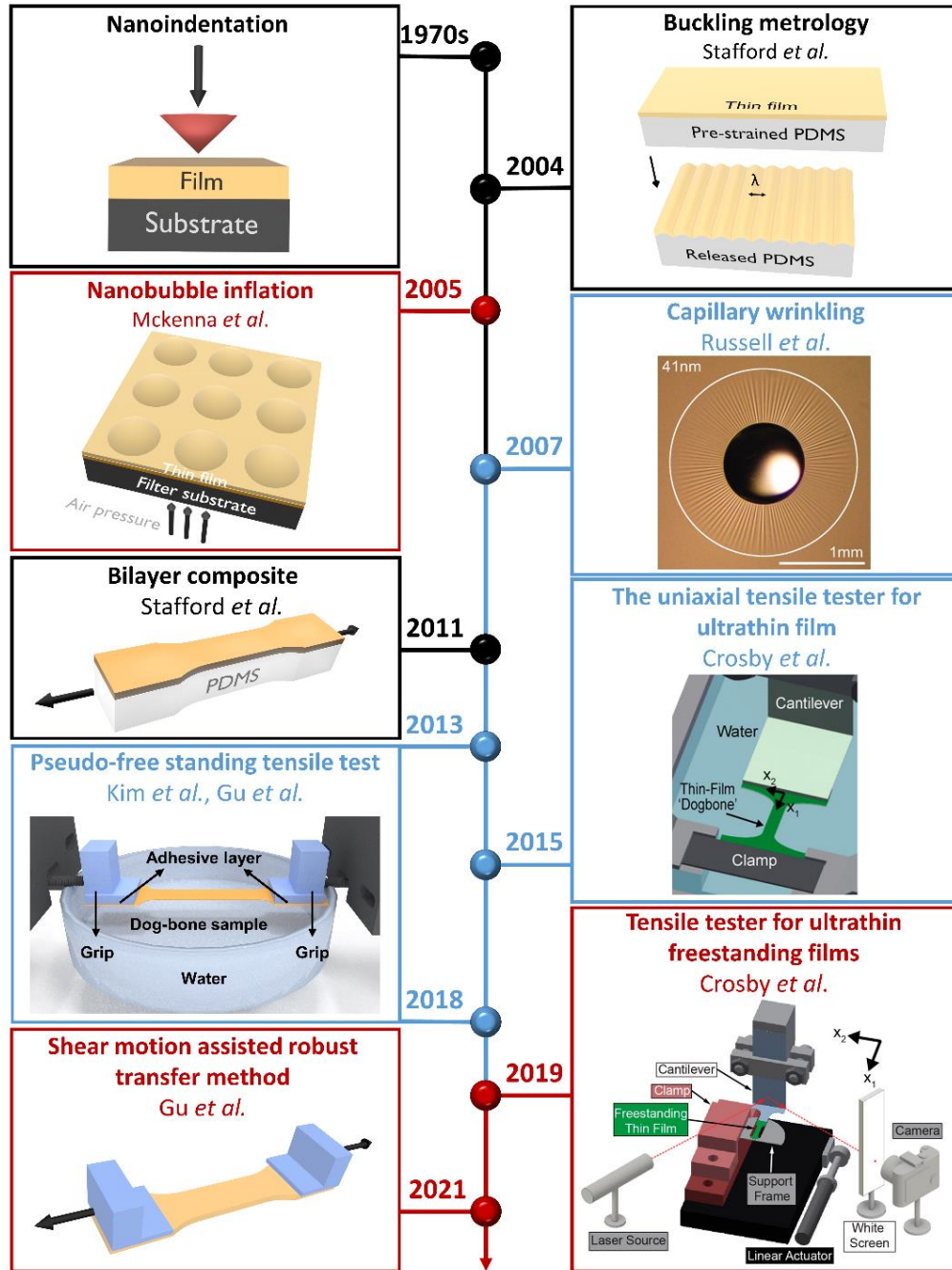
Figure 1.3 *A roadmap showing the development of thin-film mechanical testing techniques. Three categories are divided based on the type of substrates: black color for solid substrate, blue for liquid substrate, and red for free-standing films. Capillary wrinkling. (Reproduced with permission.[73] 2007, American Association for the Advancement of Science.) The uniaxial tensile tester for ultrathin film. (Reproduced with permission.[74] 2018, American Chemical Society.) Pseudo-free standing tensile test. (Reproduced with permission.[75] 2018, John Wiley and Sons.) Tensile tester for ultrathin free-standing films. (Reproduced with permission.[76] 2019, American Chemical Society.)*

1.3.3 Thin film mechanical analysis on liquid substrates

In contrast to solid substrates, which may restrict chain mobility (hard substrates) or promote elevated ductility through force delocalization (soft substrates), liquid substrates offer potential to provide a neutral non-restrictive interface for mechanical investigation. In 2007, Russel *et al.* developed a wrinkling technique, analogous to the previously described buckling metrology by Stafford, whereby a film is suspended across a liquid support and a droplet of water is placed on the film.[73] The force of the droplet results in wrinkling of the film which can be used to extract the film's mechanical response, such as modulus. Beyond wrinkling based techniques, a liquid support, such as water, offers the means to perform a conventional tensile analysis of thin films. This was first demonstrated by Kim *et al.*, in 2013, where gold films were floated onto a water bath and their complete stress-strain profiles were obtained.[77] This technique was expanded to polymer films, by Crosby et al., where polystyrene was first investigated followed by polycarbonate and polymer nanocomposites.[74,78–80] In 2015, this technique was first adopted by Kim *et al.* to explore the mechanical properties of the semiconducting polymer P3HT of varying regioregularity.[81] Lipomi *et al.* further utilized this film-on-water technique and compared the observed mechanical properties of P3HT to that obtained from buckling metrology.[47] The methods provided qualitatively similar trends when comparing P3HT films of increasing molecular weight. However, the modulus was substantially higher for buckling metrology while crack-onset-strain was reduced. These differences were attributed to the differing modes of applied load, tensile vs compression, as well as the strain rate and processing. However, these findings are somewhat incongruent in relation to previous work by O'connor *et al.* where the modulus

of P3HT was determined to be 252 MPa which is analogous to that reported through tensile analysis.[71] Lastly, our own group has used this method extensively to elucidate a myriad of mechanical phenomenon within semiconducting polymers.[23,82–87]

1.3.4 Thin film mechanical analysis on free-standing films

Despite the success of liquid substrates to analyze the mechanical properties of thin films, there remain some concerns, such as plasticization, over potential polymer-liquid interactions. Thus, there is a drive to develop methods to analyze thin film mechanics in a free-standing (two air interfaces) environment. This has been accomplished in several ways. First, nanobubble inflation was developed by Mckenna *et al.* in 2005. utilizing a polymer film laminated across a porous substrate.[88–93] A back pressure is applied, forming bubbles which are subsequently analyzed using AFM, enabling the viscoelastic properties of the film to be investigated. Second, a camphor-enabled transfer method was developed by Wang *et al.* in 2018. The camphor layer enables transfer of the film onto a hollow substrate. The camphor is then sublimed at elevated temperature and the film is characterized via DMA.[94] Third, water-assisted transfer of thin films into a free-standing environment has been reported recently within the Crosby,[76] Okamura,[95] and Gu[83,86] research groups. Currently, such methods have allowed the mechanical properties of polystyrene films, as thin as 19 nm, to be characterized. However, to date, only the Gu research group has investigated the free-standing tensile mechanics of semiconducting polymers. These works are presented in Chapter III and IV of this dissertation.

1.4 Thin film confinement

(Adapted from "Zhang, S.; Galuska, L. A.; Gu, X. Water-assisted Mechanical Testing of Polymeric Thin-films. J. Polym. Sci. 2021, No. April, pol.20210281.")

1.4.1 Background

The primary challenge of polymeric thin films extends from their ability to differ from bulk properties, most notably, the glass transition temperature (T_g) has been studied extensively in literature.[96–105] This area of research is generally known as confinement and has attracted significant attention for nearly three decades. Confinement consists of two primary phenomena: 1) the interfacial effect and 2) geometric restriction, also known as the finite size effect **(Figure 1.4)**. As the film thickness diminishes, the interfacial contribution grows rapidly. In terms of thin films, there are generally two distinct interfaces, namely, the substrate-polymer interface and the polymer-air interface (free surface), which typically supply a restraining and a mobilizing effect, respectively. The ultimate contribution of these two interfaces lies in the strength of the interfacial interaction and the distance this interaction pervades throughout the thickness of the polymer film. Hence a strong interaction with an immobile substrate (silicon) will in turn restrict polymer dynamics and increase the T_g, while the opposite is true for a strong interaction with the polymer-air interface or a relatively mobile substrate. A prime example of this is the thickness dependence T_g for PS and poly(methyl methacrylate) (PMMA) films supported by silicon. As early as 1994, the T_g of silicon supported PS has been shown to decrease with reducing thickness by as much as 40 °C at 10 nm, attributed to the free surface.[96,106] In contrast, PMMA has the potential to form hydrogen bonds with the native oxide surface resulting in strong substrate-polymer interaction,

overcoming that of the free surface, which increases the T_g with decreasing thickness.[97] Fluorescent labeling, originally demonstrated by Ellison and Torkelson in 2003, has proved to be an exemplary method for establishing the interfacial influence on T_g throughout the depth of a film and well demonstrates the potential competing effects between a silicon substrate and free surface.[98] For example, a 36 nm PS film with a 12 nm labeled layer at the substrate, middle or free surface demonstrated a gradient in T_g -T_g (bulk) from -4, -5, to -14 K, respectively. However, T_g -T_g (bulk) for a 14 nm labeled free surface of a 270 nm film was observed to be -32 K while labeling at the substrate surface resulted in T_g (bulk). This indicates that the 36 nm film was under the influence of both interfaces, each with a distinct competing length scale of influence. Similar studies have further assessed the T_g gradient from free-standing films containing two free surfaces, as well as polymer-polymer interfaces of both a hard and soft nature relative to polystyrene.[104,107,108] Thus, the interface has a profound role over the glass transition phenomena of confined polymers.

The finite size effect occurs when the thickness of the film becomes smaller than the end-to-end distance of the polymer chain resulting in a loss of conformational freedom in the out-of-the-plane direction of the film. As such, confined films are compressed throughout the in-plane direction and exhibit a loss of interchain entanglements.[109] This loss of interchain entanglements has been observed to not significantly contribute to the reduction of the thin-film T_g with reducing thickness.[110] In the case of free-standing films, the reduction in T_g has been shown to be molecular weight dependent, with high molecular weight polystyrene exhibiting a stronger reduction in T_g and at progressively greater thicknesses.[99,100,107,111–113] However, this

reduction in T_g does not correlate to the end-to-end distance of the polymer and has further been observed by ellipsometry to only contribute approximately 10% to 20% of the total glass transition response.[102,114] Thus, the finite size effect does not significantly contribute to the reduction in T_g of confined films.

a

Interface 1

h

Interface 2

b

h R_{ee}

h R_{ee}
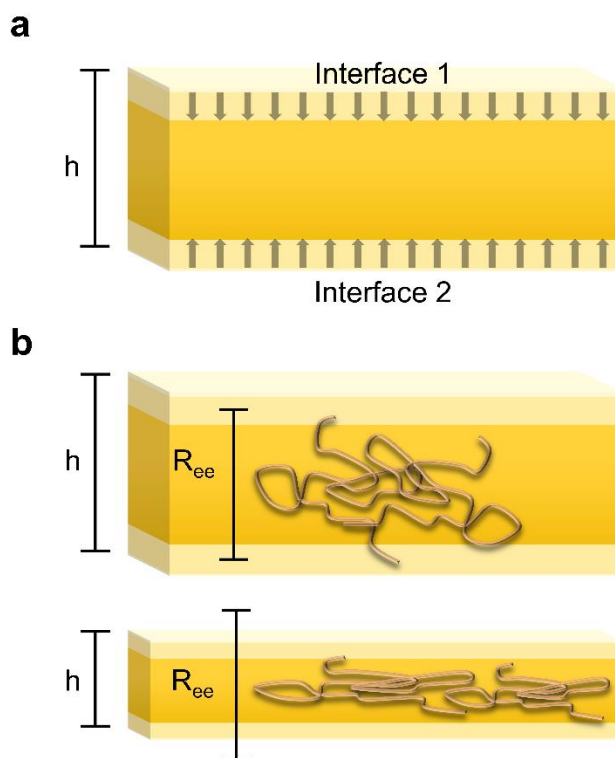
Figure 1.4 *Illustration of thin-film confinement, namely, (a) the interfacial effect and (b) the finite-size effect where thickness (h) becomes smaller than Ree.*

1.4.2 Influence of confinement on thermomechanical properties

When considering the characterization techniques from **Figure 1.3**, it is vital to understand how the interface may influence the apparent thermomechanical properties of the polymer system. These interfaces can be divided into hard/soft substrates, liquid media (water), and air. We first summarized the findings from the literature and compare the measured T_g reduction of confined polystyrene films in **Figure 1.5(a)**. The reduction in T_g for hard substrates is due to the influence of the single free surface and results in the

smallest reduction upon confinement. Soft substrates are represented by PDMS as this is the predominant elastomeric substrate for buckling metrology and supported tensile measurements. Recently, Gagnon and Roth demonstrated the influence of the base to crosslinker ratio of PDMS substrates on the T_g of polystyrene using fluorescence labeling.[108] In this report, a 10−15 nm thick pyrene-labeled probe layer was used to characterize the influential distance of PDMS on the T_g of a bulk (>500 nm) polystyrene film. The PDMS substrate was observed to substantially reduce the T_g of PS at a length scale of 65-90 nm with a higher base to crosslinker ratio of 17:1, demonstrating the most significant influence. For example, there was a dramatic 50-degree reduction in T_g 50 nm from the interface of the 17:1 PDMS. It is important to note that these measurements do not include a free surface air layer and as such measurements such as buckling metrology which are influenced by both the PDMS interface and the free surface, may be subjected to a more rapid decay in T_g. Previously, the Priestley group has determined the influence of water on polystyrene nanoparticles in an aqueous solution using modulated differential scanning calorimetry.[101] The T_g dependence on the characteristic size of the polystyrene nanoparticles was observed to parallel that of free-standing films. This observation is perhaps not surprising as plasticization is not expected given the hydrophobicity of polystyrene and that water is highly mobile, with an estimated T_g of -108°C.[115] Thus, the water film interface may be considered as a free surface given the film of interest is not hydrophilic. Lastly, free-standing polystyrene films have demonstrated significant reductions in T_g with reducing thickness as previously described. What is interesting, however, is the overlap of T_g reduction for free-standing films with that of PDMS 9:1 and water measurements. Given the direct link between T_g and the modulus of the material,

this indicates that the mechanical properties obtained from techniques utilizing these interfaces are likely to be similar.

In the past 15 years, significant strides have been made in the mechanical characterization of confined polymeric films. **Figure 1.5(b)** compares the normalized modulus of polystyrene films obtained from buckling metrology, film-on-water, and free-standing tensile tests. Measurements on silicon via nanoindentation were not included as this technique undergoes a different confinement phenomenon, dependent on indentation depth and tip geometry.[60] Three critical thicknesses are observed at which the modulus begins to decay. The first, which occurs near 25 nm, includes polystyrene films measured by all three techniques (PDMS 10:1) and with molecular weights ranging from 114 to 2062 kDa. This behavior agrees with the expectation that these interfaces provide a similar reduction in the film T_g. Additionally, the end-to-end distance of these polymers ranges from 22 nm to 94 nm, which given the similar decay in modulus, implies that the reduction in modulus of confined films is unrelated to the finite size effect, but primarily dependent on the interfacial phenomenon and thus film T_g. Given this, we have plotted the difference between the measurement temperature and T_g of a 25 nm film overlayed with the dynamic mechanical analysis of bulk polystyrene obtained from the literature (**Figure 1.5(c)**).[118] Thus, an expected modulus can be extracted for these 25 nm films from each technique based on the difference from the measurement conditions and the film T_g. Interestingly, this would suggest a 10% reduction in modulus which agrees well with the 5-10% reduction observed experimentally and further supports the importance of the interfacial influence on T_g. However, upon further confinement, the modulus decays more rapidly than what is expected from the influence of T_g alone. Given that the

5
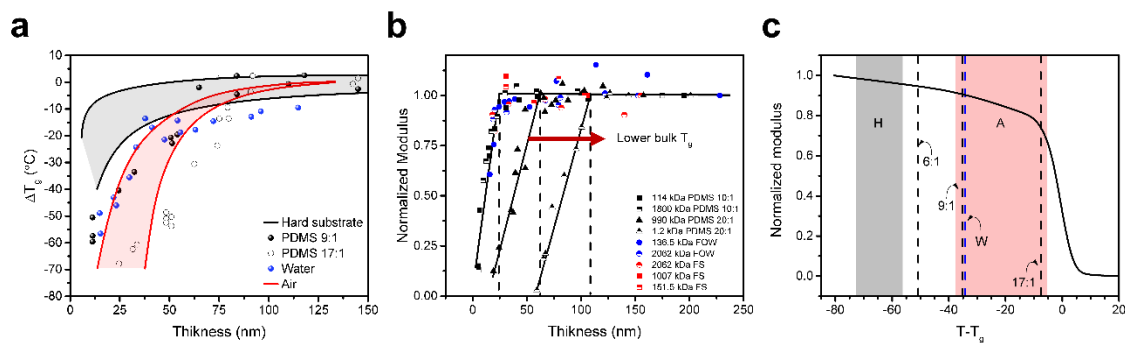
Figure 1.5 *A comparison of the confining interface on polystyrene thermomechanical properties with reducing thickness. a) Reduction in Tg from the bulk state relative to substrate stiffness.*[101,106,108,112] *b) Normalized moduli obtained from buckling metrology, film-on-water, and free-standing tensile tests, demonstrating a reduction in modulus occurring at ~25 nm for film-on-water, FS, and 10:1 PDMS while increasing base to crosslinker to 20:1 shifts the reduction to higher thickness dependent on polymer bulk T_g.* [76,80,86,116,117] *c) Hypothetical moduli of 25 nm PS based on the normalized modulus from DMA in respect to the difference in measurement temperature (25°C) and thin-film Tg.*

polymer at the mobile interface may be regarded as melt-like, the interfacial modulus is

expected to be significantly reduced resulting in a reduction of load bear chains. Thus, the

load bearing thickness is reduced based on the thickness of the mobile layer and may be

attributed to the rapid decay in modulus below 25 nm. The second critical thickness lies

just above 60 nm and occurs for the 990 kDa film measured with PDMS 20:1. Given the

molecular weight range for measurements performed on PDMS 10:1, this difference is

evidently related to the base to crosslinker ratio of the PDMS substrate. Interestingly, this

difference was not highlighted in the original publication.[117] However, this observation is

supported by the previous T_g reduction observed for PDMS 17:1, and this is expected to

be more severe at the buckling metrology ratio of 20:1 as well as the presence of the free

surface. Considering the 25 nm film measured on PDMS 20:1 was reported to have an

approximate 75% reduction in modulus relative to the bulk, compared to DMA, this

would imply a T-T_g close to zero. The third critical thickness lies above 100 nm and

occurs for the 1.2 kDa polystyrene measured with PDMS 20:1. This increase in the critical thickness was attributed to the small quench depth into the bulk glass, where the 1.2 kDa polystyrene was reported to have a bulk T_g of 21.3 ± 3.2 °C. The influence of quench depth on thin-film modulus was previously reported for a series of methacrylate polymers of varying T_g.[119] Confinement effects were observed to shift towards greater film thicknesses as the quench depth from the bulk state decreased. Interestingly, it was also observed that the reduction in modulus of poly(n-propyl methacrylate) was not correlated with thin-film T_g which did not deviate from the bulk. These findings stress the importance of understanding the potential influence of interfacial phenomenon on the polymer's apparent mechanical performance and highlight the need for additional investigation into confined film mechanics and potential dependence on chemical structure. This topic is a focus of Chapter III and IV within this dissertation.

1.5 Current trends in the thermomechanics of semiconducting polymers

1.5.1 Background

Given their heterogenous chemical structure, thickness dependence, poor molecular weight control, and semicrystalline morphology, understanding the thermomechanical properties of semiconducting polymers has been a significant challenge within the field. Regardless, significant progress has been made within the last decade, leading to the following general guidelines. 1) High backbone rigidity, associated with fused aromatic rings, restricts conformational freedom along the backbone increasing T_g and modulus. 2) Flexible sidechains plasticize the conjugated backbone resulting in reduced T_g and modulus, as well as increased ductility, with increasing sidechain content. 3) Sufficient molecular weight is necessary to achieve both high ductility and electrical performance. 4) High crystallinity is not necessary for superior charge transport and is detrimental to mechanical performance (soft and ductile). 5) Confinement can both decrease and raise conjugated polymer T_g depending on the competition between interfacial influence and morphology. These topics are briefly described below.

1.5.2 Backbone structure

Inherent to semiconducting polymers is their conjugated backbone, which provides charge transport, but also restricts the conformational freedom of the system. In 2016, Roth *et al.* assessed a library of 51 semiconducting polymers and studied their mechanical property using the film-on-elastomer technique.[68] Semiconducting polymers with increasing number of fused rings exhibited elevated modulus and low crack-onset-strain. This agrees with more recent work, by Zhang *et al.*, where the number of fused

8

and isolated thiophene rings were shown to substantially influence the thermomechanics of a DPP-based polymer.[23] Altering the chemical structure from an isolated thiophene to fused thienothiophene and then dithienothiophene resulted in an increase in T_g from -11°C to 3.5°C and 22°C, respectively. In turn, modulus increased from 173 MPa to 480 MPa and crack-onset-strain decreased from 53% to 3%. These changes were attributed to the incorporation of high T_g moieties within the backbone as well as reduced content of plasticizing sidechains. In contrast, semiconducting polymers incorporating flexible conjugation break spacers (CBS) within the backbone, exhibit the opposite effect. For example, Savagatrup *et al.* found that incorporation of methylene units (3 carbons long) within the backbone decreased the modulus of a fully conjugated DPP-based polymer from 315 MPa to 174 MPa.[120] However, crack-onset-strain decreased from 3.5% to 3.0% which was attributed to tighter crystalline packing. Galuska *et al.* demonstrated incorporation of methylene-based CBS to greatly decrease the T_g of an NDI-based polymer from 100C to below room temperature.[87] At the same time, backbone rigidity was significantly reduced from 521 to 36Å resulting in a low entanglement molecular weight of 15 kDa and high ductility. This work will be discussed fully in Chapter II of this dissertation.

1.5.3 Sidechain structure

Alkyl sidechains are prevalent throughout semiconducting polymers for their solubilizing power and morphological control. More recently, their critical influence on thermomechanics has come into view. For example, polythiophene, without sidechains, possesses a T_g of 120°C while incorporation of butyl sidechain plasticizes the backbone, reducing T_g to ~ 40°C.[121,122] This trend continues, with diminishing returns, as sidechain

length increases. There are two competing affects with increased sidechain length. 1) As sidechain length increases the content of internal plasticizer increases thus enhancing backbone dynamics and lowering the T_g.[123] 2) Sidechain T_g increases from below -100°C for a butyl chain to -40°C for a dodecyl chain. Thus, the plasticization capability per methylene unit is reduced as sidechain length increases. This trend also occurs for D-A polymers, where sidechain content has been linked as a controlling parameter of backbone T_g.[124] This influence is vital to understand, as sidechain content for such systems can range from 20-70% and thus be a facile method of tuning thermomechanical performance. The structure of the sidechain also plays a role, namely, flexibility and branching position.[30,125] In 2018, Sugiyama *et al.* compared the influence of linear alkyl, branched alkyl, and linear ethylene oxide sidechains on the thermomechanics of a DPP-based polymer.[30] For polymers containing the same total number of atoms, 16 (carbon + oxygen), in the side chain, the T_g was observed to be lowest for the ethylene oxide sidechain (~95°C), termed EO5, followed by the branched (~134°C) and linear alkyl (~155°C) sidechains. Subsequently, the EO5 sidechain demonstrated the lowest modulus, as measured by buckling metrology, as well as high ductility. This improvement on the thermomechanics imparted by the ethylene oxide sidechains was attributed to their greater flexibility and hence plasticization potential. However, it is important to note a discrepancy between the T_g and modulus reported. Given that EO5 side chain had an elevated T_g of ~95°C, the polymer should lie deep within the glassy state and thus the reported modulus of ~50MPa is unlikely. Potential reasonings for this could include interactions by the PDMS substrate during buckling metrology or that the reported backbone T_g is originating from another phenomena, such as the T_g of a rigid amorphous

fraction. Although the influence of the sidechain is most related to T_g and hence the modulus of the material, ductility is also influenced. Balar *et al.* observed that the sidechain T_g may act as a brittle to ductile transition for many semiconducting polymers, above which, the polymers behave in a ductile manner.[26] Such brittle-ductile transitions are common in conventional polymers and have been linked to secondary relaxations of the polymer.[126,127]

1.5.4 Molecular weight

Molecular weight is a key parameter governing the connectivity of polymeric systems. It is this connectivity which allows for load displacement as well as charge transport to occur across large length scales and subsequently impact nearly every aspect of performance.[13,128,129] The impact of molecular weight on the properties of P3HT has been studied extensively. For example, as M_n increases from 20 to 90 kDa, bulk strain at failure shifts from 10% to 300%.[130] The same trend was observed for P3HT measured by the film-on-water technique in the thin-film state.[47] This can be attributed to increased entanglement density in the amorphous state and sufficient tie-chain concentration bridging crystalline domains. The role of tie-chains has been assessed in more detail by Gu *et al.*, whereby varying molecular weights of P3HT were blended and assessed on their mechano-electrical behavior.[131] In the absence of sufficient tie-chain concentration, brittle failure occurred as chains were unable to delocalize the applied force through conformational reorganization as evidenced by the lack of orientation obtained from UV-vis. For D-A systems, Balar *et al.*, demonstrated that increasing molecular weight of both pure and blended systems resulted in increased crack-onset-strain as well as cohesive fracture energy, attributed to enhanced load distribution offered by chain entanglement.[132]

In 2020, Pei *et al.* demonstrated the influence of molecular weight on a DPP-based polymer. Modulus was observed to decrease at elevated M_n, attributed to disruption of crystalline packing, while crack-onset-strain increased. Charge mobility also increased with molecular weight, due to increasing connectivity despite reduced crystalline size. Thus, molecular weight is a key parameter in our understanding of semiconducting polymer thermomechanics.

1.5.5 Crystalline morphology

Most semiconducting polymers are semicrystalline in nature, with a range of crystalline orientations and packing distances dictated by their structure and processing. Previously, the drive within the field was to produce highly crystalline polymers with the hope of improving charge mobility. A great example of this is the development of poly(2,5-bis(3-alkylthiophen-2-yl) thieno[3,2-b]thiophene) (PBTTT), which exhibits large crystallite size and improved charge transport over P3HT.[133] However, high crystallinity effectively robs amorphous domains of entanglements, thus limiting the ductility of the system. This was demonstrated by O'Connor *et al.,* via film-on-elastomer method, where PBTTT exhibited a high modulus of 1.8 GPa and low crack-onset-strain below 2.5%.[71] In contrast P3HT failed above 150% strain. Our recent work also demonstrated the impact of crystallinity on thermomechanics. Upon incorporation of hydrogen bonding urea moieties into the sidechain, a DPP-based polymer exhibited a 48% increase in crystallinity and in turn an approximate decrease in strain at failure by 50%.[134] Amide functionalization resulted in a drop in crystallinity and 100% improvement in ductility. This work is fully discussed in Chapter 4 of this dissertation. Additionally, Qian *et al.* demonstrated the importance of crystallinity on mechanical

performance even in highly flexible systems.[82] Cold crystallization was found to occur at room temperature for an NDI-based polymer containing a flexible CBS along its backbone. Measurement of the mechanical performance within 15 minutes of spin coating resulted in low modulus (~200 MPa) and high ductility (40% strain at failure). Within 24 hours, embrittlement occurred (less than 5% strain at failure) and modulus grew by ~ 250%.

Low crystalline polymers, such as IDT-BT,[135] have demonstrated excellent charge mobility due to planar chemical structures and sufficient tie-chains bridging small crystalline domains.[136] Furthermore, this finding suggests that high mechano-electrical performance may now be achieved in unison. For example, *Zheng et al.* compared mechano-electrical performance of IDT-BT to a more crystalline DPPTT polymer.[137] Despite an elevated modulus of 745 MPa, IDT-BT also demonstrated 2.4 times increase in strain at failure while exhibiting a high charge mobility of 1.8 cm^2 V^{-1} s^{-1}. Beyond the direct impact of crystallinity on mechanical performance, the interaction of crystalline and amorphous domains may lead to the formation of a rigid amorphous fraction (RAF) with reduced conformational freedom and an elevated T_g.[138,139] Currently, only a couple works have identified the existence of elevated thermal transitions, associated with the RAF, within P3HT and DPP-based polymers, but the identity and influence has yet to be fully elucidated on the optoelectronic and mechanical performance of semiconducting polymers. [28,140] Chapter V of this dissertation will focus on identifying the RAF and its role on semiconducting polymers.

1.5.6 Confinement

Unlike conventional glassy systems, of which confinement has primarily been studied, as discussed in section 1.4, semiconducting polymers are semicrystalline and possess a myriad of potential competing phenomenon. Thus, the thermomechanics may be stiffened or softened depending on the competing mechanisms of influence. For example, in 2006, Campoy-Quiles *et al.* explored the thickness dependent thermal transitions of two polyfluorene polymers using temperature dependent ellipsometry and discovered 3 regimes of influence.[40] 1) Above 159 nm, PFO possessed a T_g equivalent to the bulk state. 2) Between 60 nm and 159 nm the T_g was greater than $T_{g,bulk}$ (18°C greater at 70 nm). 3) The T_g decreased 5°C below $T_{g,bulk}$ at 18 nm in thickness. The crystallization temperature followed the same trend. Similar phenomenon was observed with PCDTBT, by Wang *et al.*, which demonstrated an initial T_g reduction with decreasing thickness down to 40 nm.[36] Below 40 nm the T_g plateaued at a value 20°C below $T_{g,bulk}$. This was attributed to favorable π-π stacking at the substrate interface restricting chain mobility and limiting further reductions in T_g. Most recently, thermal transitions of DPPT, DPPTT, and DPPTTT were assessed through AC-chip calorimetry.[28] Three glass transitions were observed for each polymer, representative of the sidechain, backbone, and RAF. The thickness dependence of these transitions was assessed for DPPTTT from bulk polymer to 33 nm films. All three separate transitions were observed to decrease with reducing thickness. This is attributed to increased free volume provided at the air-film interface as well as a reduction in crystallinity which may loosen the segmental restrictions imposed on the RAF. It is also important to recognize that confinement is not just related to thickness, but rather any geometric restriction of a polymer, for instance, a

14

semiconducting polymer orientated into nanoconfined fibers within a soft elastomer. In 2017, Xu *et al.*, investigated the influence of nanoconfinement of a DPP-based polymer within a polystyrene-block-poly(ethylene-ran- butylene)-block-polystyrene (SEBS) matrix.[141] The DPP-polymer formed nanofibers within the SEBS matrix, which were confirmed by AC-chip calorimetry to have a reduced T_g relative to 135 nm and 35 nm thick films. This resulted in a reduction in modulus as well as substantially improved ductility. In 2018, Zhang *et al.* explored the thickness dependent mechanical properties of P3HT and DPP-TVT using the film-on-water method.[142] Modulus remained constant for P3HT from 20 nm to 100 nm, but decreased for DPP-TVT. Additionally, crack-onset-strain decreased for both films with decreasing thickness.

CHAPTER II – IMPACT OF BACKBONE RIGIDITY ON THERMOMECHANICS

(Adapted from "Galuska, L. A.; McNutt, W. W.; Qian, Z.; Zhang, S.; Weller, D. W.; Dhakal, S.; King, E. R.; Morgan, S. E.; Azoulay, J. D.; Mei, J.; Gu, X. Impact of Backbone Rigidity on the Thermomechanical Properties of Semiconducting Polymers with Conjugation Break Spacers. Macromolecules 2020, 53, 6032–6042.")

2.1 Introduction

A main attribute of organic semiconductors is the potential to produce inherently soft and ductile electronics for emerging applications in technology such as wearable and implantable devices.[65,141,10,143] Such applications require an active material with high charge transport and mechanical compliance similar to biological tissues. Conjugated polymers (CPs) have seen vast improvements in charge transport performance in the last three decades[144], this improvement has driven recent research interest towards the investigation of mechanical performance which is still in its infancy.

Despite the high heterogeneity of many CPs, the structural components can be separated into two regions of interest, namely, side chains which offer enhanced solubility and a conjugated backbone which promotes charge transport. Side-chain engineering offers a reliable route for tuning the mechanical properties through moderate influence over backbone chain dynamics. Increasing side chain length promotes plasticization of the backbone resulting in a reduction in the glass transition temperature (T_g) and subsequently the elastic modulus, which has been previously demonstrated with poly(3-alkylthiophenes) (P3ATs).[145,67] More recently, Sugiyama et al. investigated the influence of side-chain length, branching, and chemical structure on a diketopyrrolopyrrole (DPP) based donor-acceptor (D-A) polymer, concluding that

16

increased length and flexibility of the side-chain will result in reduced T_g and increased ductility.[30]

Backbone engineering provides a more direct control over chain flexibility which is a key contributing factor to backbone T_g as well as the propensity of chains to entangle which governs ductility. Solution scattering is the principal route to quantitatively assess chain flexibility, but has primarily been limited to more conventional CPs such as P3ATs[146,147,148],polyfluorene (PF)[149], poly(p-phenylene vinylene) (PPV)[150], and poly(thieno[3,4-b]-thiophene-co-benzodithiophene) PTB7[151]. The general consensus is that D-A CPs containing higher content of fused rings will have greater rigidity due to an increase in the rotational energy barrier thus reducing conformational freedom.[152] Additionally the dihedral angle between different backbone building blocks also affects the chain conformation as the Milner group pointed out.[153] This is evident in the comparison of P3HT and fused PF which exhibit a persistence length of approximately 3 nm[148] and 7 nm[149] respectively. Previous research by Roth et al. explored a broad library of 51 low-bandgap polymers of varying architecture, demonstrating that a higher content of fused rings results in increased stiffness as well as likelihood of fracture.[68] A similar trend was observed in our recent publication where we examined the effect of isolated and fused thiophene content on the thermomechanics of DPP-based polymer.[154] It was discovered that increasing thiophene content exhibited an anti-plasticization effect yielding an increase in elastic modulus and reduced ductility.

Recently, conjugation break spacers (CBS) were introduced to the field of organic electronics to disentangle the effect of intra- and intermolecular transport.[155,156,157,158] For randomly incorporated CBS at small concentration, the charge mobility was found to be

largely maintained relative to the parent poly(2,5-bis(3-tetradecylthiophen-2-yl)thieno[3,2-b] thiophene) (PBTTT) polymer.[155] This is attributed to long range percolation of conjugated units via a robust π-π stacked network. Although no mechanical properties were considered, this study has sparked interest in the CP community for utilizing flexible CBS to reduce backbone rigidity and enhance mechanical performance without compromising charge mobility. The first mechanical study of such systems was performed by Savagatrup et al. in 2016, in which the effect of CBS concentration on a DPP-based polymer was investigated.[120] A reduction in elastic modulus was found upon increasing CBS content. Despite the supposed increase in flexibility offered by incorporation of CBS the strain at failure was observed to be surprisingly low, below 15% strain, regardless of CBS content. This was justified through the solid-state packing, where alkyl packing distance and full width half max (FWHM) decreased with increasing CBS, indicating that morphology and not structure alone are responsible for the deformation mechanics within these systems. However, it should be noted that the molecular weight of the DPP polymer used in this study was generally low (e.g. M_n of 12.5 kDa for fully incorporated CBS) which may also be a significant factor in the poor ductility. Also, in 2016, Zhao et al. investigated the influence of CBS length upon incorporation into the monomer repeat unit itself where previously only random copolymers have been reported.[157] Although, the thermomechanics of these systems were not considered, a surprisingly high charge mobility was maintained for blend systems containing as little as 2% fully conjugated DPP within a matrix of CBS based polymer. For pure CBS polymer, electrical properties are detrimentally affected as conjugation is effectively broken at longer length scales. With further increase of CBS length, the

electrical properties continue to decrease as the concentration of π-π stacked units are effectively diluted and thus weaken intermolecular charge transport. Many more investigations on the utilization of CBS have been reported, including: promotion of solubility and melt processability[156,158,159,160], healable semiconductors[161], and semi-random copolymers.[162,163] However, there remains a fundamental gap in knowledge for these systems, namely a lack of quantitative information regarding the influence of CBS on chain rigidity, propensity to entangle, and ultimately their mechanical property.

Here, we investigate a series of naphthalene diimide (NDI) based polymers as the first n-type polymer to be incorporated with CBS of varying length to ascertain the role of backbone flexibility on thermomechanics as well as morphology. Our findings provide a quantitative verification that increased backbone flexibility results in a softening effect expressed through a reduction in T_g and elastic modulus. An extremely high ductility, upwards of 400% strain for pseudo-freestanding film, is observed at multiple CBS lengths and determined to be directly proportional to the number of entanglements in the system given by oscillatory melt shear rheology and molecular weight dependent mechanical analysis using our unique film on water tensile tester. Given the profound ductility, a high degree of alignment was observed and characterized through an in-depth morphological analysis, including grazing incidence wide angle X-ray scattering (GIWAXS), transmission WAXS, polarized UV-Vis, and atomic force microscopy (AFM). This work sheds light on the important role of backbone rigidity for designing flexible and stretchable conjugated polymer.

2.2 Experimental

2.2.1 Materials and processing

Six PNDI-Cx polymers were synthesized with CBS units incorporated into each repeat unit. The synthesis was performed as previously described by McNutt et al.[164] For GPC analysis, the polymers were dissolved by shaking in 1,2,4-trichlorobenzene (TCB) at a concentration of 1-2 mg/mL for 2 hrs at 160°C through use of an Agilent PL-SP 260VS sample preparation system, the samples were then filtered through a 2 μm stainless steel filter into the 2 mL glass GPC vials and ran in the instrument at 160°C using TCB as an eluent. The high temp (HT)-GPC utilized was an Agilent PL-GPC-220 system, this system is equipped with 3 pLGel Olexis (13 μm particle size) in series in addition to a differential refractive index (RI) detector, a dual angle (15° and 90°) light scattering (LS) detector, and a viscometer (VS) detector. The chromatograms were worked up from the RI signal utilizing a narrow standard polystyrene calibration (14 points, ranging from 162 g/mol to 3,242,000 g/mol). The SEC curves are shown in Figure S10.

2.2.2 Film preparation

PNDI-Cx polymers were dissolved in chlorobenzene at 80 ˚C at a concentration of approximately 25 mg/ml. PNDI-C0 was prepared at 10 mg/ml under identical conditions. Poly(sodium 4-styrenesulfonate) (PSS) was obtained from Sigma Aldrich at a molecular weight of 70 kDa in 30% by volume aqueous solution. PSS was first diluted to 3 wt% in aqueous solution and spun cast onto plasma treated silicon wafer at 4000 rpm for 2 minutes. PNDI-Cx solution was then cast at 2000 rpm for 1 minute forming the composite film.

2.2.3 Solution small angle neutron scattering (SANS)

SANS was performed at both the National Institute of Science and Technology (NGB 30 m SANS) and Oak Ridge National Laboratory (EQSANS). A wavelength of 10 Å was used for two sample-detector distances of 1 and 8 m which was combined for coverage of a wide q vector range. Solution was prepared in deuterated chlorobenzene at 5 mg/ml. Each sample was exposed at both 25 and 85 ˚C with an exposure time of 5 and 30 minutes for sample to detector distances of 1 and 8 m respectively. Data reduction was performed through Wavemetrics Igor. Finally, SasView software was used to fit the scattering data to the flexible cylinder model[165] to calculate the chain rigidity.

2.2.4 Differential scanning calorimetry (DSC)

DSC was performed with a Mettler Toledo DSC 3+ at heating and cooling rates of 30 ˚C/min.

2.2.5 Pseudo-free-standing tensile test

Thin film tensile tests were performed on a water surface through the pseudo-free-standing tensile tester, as described in our previous publication.[166] Briefly speaking, the composite films were patterned into a dog-bone geometry using a laser cutter. Post patterning, the composite film was floated on top of water before being further unidirectionally pulled at a strain rate of 5×10^{-4} s^{-1} until the film fractures. Generally, five independent samples were measured for each conjugated polymer to provide statistically averaged mechanical properties. The elastic modulus was obtained from the slope of the linear fit of the stress–strain curve within the first 0.5% strain.

2.2.6 Oscillatory melt-shear rheometry

Linear rheological measurements of PNDI-C4 to C7 were performed with strain-controlled rheometer Advanced Rheometric Expansion System (ARES-LS) from TA Instruments under dry nitrogen protection. The sample was molded into a 0.5 mm thick bubble-free disk with 8 mm in diameter under vacuum at 30 °C above the relevant melting temperature. The sample was loaded between 8-mm aluminum disposable parallel plates and heated above the melting temperature to ensure good contacts between sample and plates. The dynamic frequency sweep between 100 to 0.1 rad/s were performed in a wide temperature range: 150 °C to 70 °C for C4, 80 °C to 30 °C for C5, and 100 °C to 30 °C for C6 and C7, after the linear viscoelastic strain range was determined with strain sweep measurements.

2.2.7 Grazing incidence wide angle X-ray scattering (GIWAXS)

GIWAXS was performed on beamline 11–3 at the Stanford Synchrotron Radiation Lightsource. Data was collected at a sample to detector distance of ~ 300 mm under a helium environment with an incident beam energy of 12.7 keV and an incidence angle of 0.12°. Diffraction analysis was performed using Nika software package within Wavemetrics Igor, in combination with WAXS tools.[167]

2.2.8 Transmission wide angle X-ray scattering (WAXS)

Transmission WAXS was performed using a Xenocs Xeuss 2.0 SAXS/WAXS lab source instrument. Free-standing films were exposed for 2.5 hours with an incident beam energy of 8.05 keV and a beam geometry of 1.2 x 1.2 mm. The sample to detector distance was approximately 157 mm. Free-standing films were obtained by lifting post tensile drawn films from the pseudo free-standing tensile tester's water bath using a steel

washer with an inner diameter of 3.85 mm. The films were allowed to dry under vacuum at room temperature overnight prior to the obtained scattering. Film thickness was obtained by interferometry and AFM for normalization of the scattering intensity.

2.2.9 Transmission UV-Vis

UV–Vis–NIR transmission spectra were performed with an Agilent Cary 5000 with a specified operating wavelength range of 300 – 1100 nm. Polarized measurements were achieved with a Harrick Glan-Taylor polarizer at 0˚ and 90˚. For tensile drawn samples, measurement was conducted on glass slides after collection and subsequent drying.

2.2.10 Atomic force microscopy (AFM)

AFM images were acquired on an Asylum Research Cypher S operating in AC mode in air. The samples were collected post tensile strain onto bare silicon wafer.

2.3 Results and discussion

2.3.1 The impact of CBS on the chain rigidity characterized by solution small angle neutron scattering.

A series of NDI-based conjugated polymers with CBS directly incorporated into each repeat unit were utilized to systematically evaluate the effect of CBS length on backbone flexibility (**Figure 2.1(a)**). Random incorporation of CBS masks its inherent influence over both electrical and thermomechanical performance due to two factors: 1) While CBS concentration can be relatively maintained, its placement within the polymer structure is unclear and may provide varying effects at the chain end or centrally located along the backbone. This becomes particularly important for low molecular weight polymer systems where it's feasible to consider that only one CBS may be incorporated

into the polymer chain. 2) Packing morphology is greatly affected by structure consistency and upon random CBS insertion, disruption of the morphology is likely to occur and act as defects towards crystallization.[168,169,170] Therefore, the properties obtained from such systems may be dominated by the morphology induced from random addition rather than the CBS itself. Thus, this work opted to investigate 100% incorporation of the CBS to elucidate the effect of backbone flexibility on the thermomechanical properties. The synthesized polymers are listed in **Table 2.1**. The synthesis of these polymers is described in our recent 2019 and 2020 publications.[21,164] C1 and C2 analogues are omitted due to difficulty in synthesis. The C1 analogue suffers from rapid decomposition of C1 linked thiophene and as such has not been studied in previous publications. The general procedure for C2 analogues can be found in a 2016 paper by Zhao et al., but was neglected due to the challenges in synthesis.[157]

The CBS length was varied from PNDI-C0 (fully conjugated) to PNDI-C7 with the purpose of demonstrating the effect of increasing backbone flexibility on the thermomechanics. Despite the notion that CBS offers improved flexibility for conjugated systems, there is currently no quantitative experimental evidence of this in the literature. In order to investigate the polymer chain conformation, solution small angle neutron scattering (SANS) was conducted for each polymer (2D scattering profiles are available in **Figure A.1** in Appendix A). A 5 mg/ml polymer solution in deuterated chlorobenzene was used to provide a strong coherent scattering signal while also being sufficiently dilute to obtain non-interacting polymer chains and thus elucidating the form factor (**Figure 2.1(b)**). Temperature was also controlled at both 25 ˚C and 85 ˚C to consider variable solvent interactions as well as potential aggregation of conjugated polymer,

24
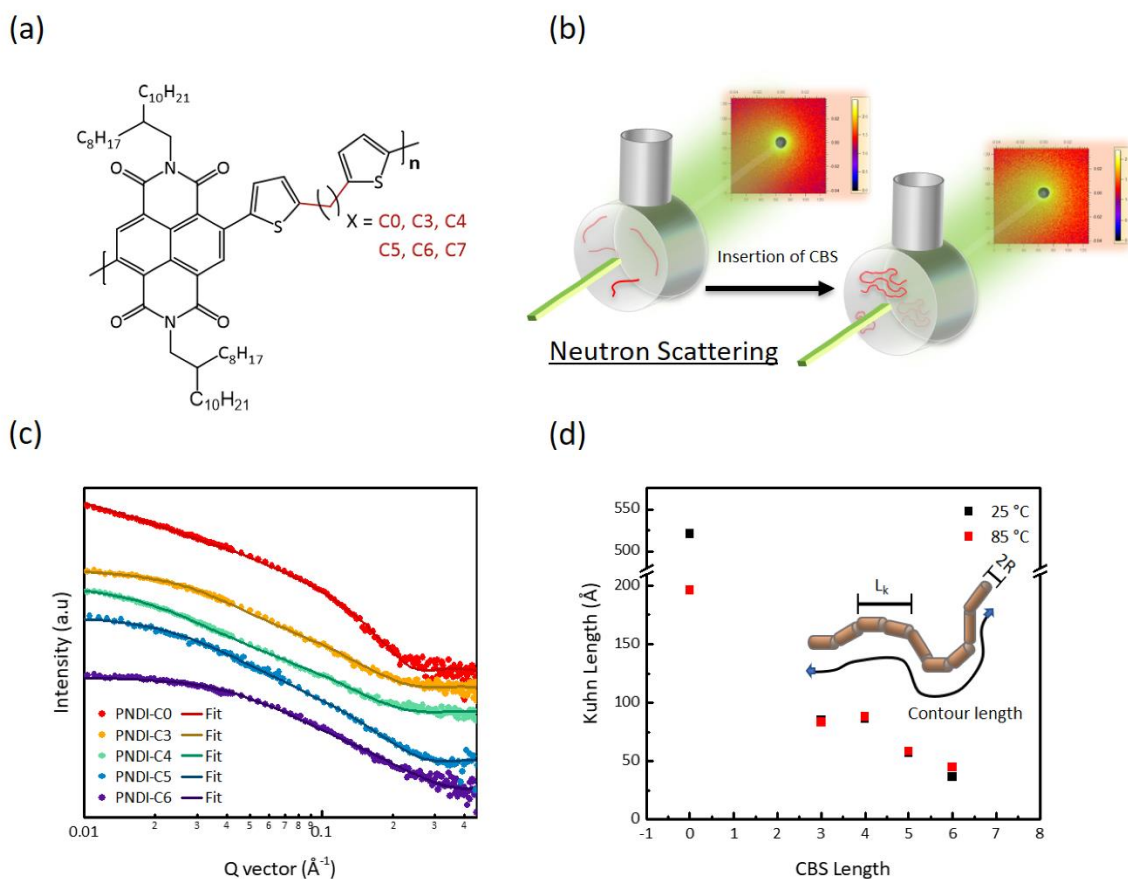
Figure 2.1 *(a) PNDI-Cx polymers under investigation. (b) Illustration of solution SANS upon insertion of CBS. (c) 1D scattering profile obtained at 25 ˚C in deuterated chlorobenzene. (d) Kuhn length dependence on CBS length as fitted using the flexible cylinder model in SasView software.*

especially for fully conjugated PNDI-C0. The scattering data was fitted to the flexible

cylinder model in SasView[171] software which enabled the calculation of the chain rigidity

through the Kuhn length (L_k) (**Figures 2.1(c-d)**, **Figure A.2** and **Table A.1**). The L_k was

shown to dramatically diminish upon insertion of CBS. Take PNDI-C3 for example, the

backbone rigidity reduced from 521 Å (for fully conjugated) to 85 Å at 25 ˚C. This

suggests that introducing flexible linkers into the polymer backbone turned the worm-like

semirigid chain into nearly flexible. Upon further increasing the CBS length, the L_k

continued to reduce indicative of increased flexibility, thus providing the first

experimental evidence that incorporation of CBS does indeed increase the backbone flexibility within conjugated systems. For PNDI-C5 and PNDI-C6, both of their L_k is around 50 Å, indicating they are now as flexible as P3HT.[148]

At room temperature we observed a considerable decrease in the L_k when going from PNDI-C0 to PNDI-C3. Considering the strong intermolecular interactions associated with conjugated polymers, we evaluated these systems at elevated temperatures to verify our findings. It was discovered that the L_k of PNDI-C0 greatly decreased at 85 °C, indicating a strong conformation shift with temperature. Aggregation typically results in enlarged low Q vector scattering intensity which greatly diminishes at high temperature.[148,172] Thus, aggregation effects can be ruled out as the low Q vector scattering intensity remains consistent between the two temperatures and all polymers measured (**Figure A.2(b-c)**). However, it was found that the L_k was still much larger (196 Å) than that that observed in PNDI-Cx polymers which remained consistent with the initial 25 °C experimental results. This independence of temperature indicates that CBS containing PNDI-Cx polymers are highly soluble and interact strongly with the solvent at all measured conditions.

2.3.2 Thermomechanical properties

An in-depth thermomechanical analysis was performed to ascertain the impact of chain flexibility, provided by the CBS, on T_g, entanglement molecular weight (M_e), elastic modulus, and crack-onset strain (COS) for PNDI-Cx thin films. Such parameters ultimately govern the softness and ductility that can be achieved for intrinsically stretchable electronics. The glass transition temperature dictates the physical state of the conjugated polymer, be it in a viscoelastic or glassy state, and exerts a profound impact

26

on the elastic modulus. M_e corresponds to the molecular weight at which entanglements are observed within the melt, while the molecular weight of the conjugated polymer with respect to the M_e determines the degree of interchain entanglements in their solid state and thus affects the failure behavior of the polymeric film, namely COS. COS corresponds to the strain at which a crack appears and begins to propagate throughout the film. This is generally monitored by optical microscopy for film-on-elastomer methods or by force decay, measured by a load cell, in our tensile measurements.

In literature, differential scanning calorimetry (DSC) has shown to be unreliable for the characterization of glass transition phenomena associated with conjugated polymer. This is due to high backbone rigidity, semi-crystalline nature, and high side chain content which ultimately results in a low backbone Δc_p that is nearly imperceptible when using conventional DSC.[173,124] In the case of PNDI-C0, physical aging was used in our previous publication to elucidate the T_g through the associated enthalpy overshoot and further verified with a modified DMA technique.[173,174] The resulting values obtained for PNDI-C0 were 101 and 131 ˚C respectively. In contrast, the enhanced backbone flexibility of PNDI-Cx polymers containing CBS provide a strong T_g signal from conventional DSC. Glass transition temperature for PNDI-Cx was studied with DSC at a heating/cooling rate of 30 ˚C/min, the thermograms are shown in **Figure A.3**. **Figure 2.2(a)** reveals a clear reduction in both T_g and melting temperature (T_m) with increasing CBS length. This demonstrates a strong dependence of backbone flexibility to influence chain dynamics and crystalline packing. The most dramatic change occurs upon introduction of the CBS unit, from PNDI-C0 to PNDI-C3, where backbone flexibility is dramatically enhanced due to the break in conjugation (e.g. T_g reduced from 102 ˚C to

27

around 20 ˚C). While addition of CBS with greater length provides diminishing improvement in flexibility and T_g as chain dynamics are already quite mobile.

From the thermal analysis we hypothesized that a reduction in the elastic modulus would manifest with increasing CBS length due to greater chain dynamics as expressed by the reduction in T_g. This was verified through the use of the pseudo-free-standing tensile tester which as described in our previous publications enables the mechanical properties of an ultrathin film to be directly obtained through stress-strain analysis while supported by a smooth water surface.[154,166,175,176,177] Prior to characterization, each polymer film was annealed under a nitrogen atmosphere for two days at either the operating temperature of the tensile tester (25 ˚C) or 30 ˚C below each polymer's respective T_m, noted as "PA" for post-annealing. The rationale for this is two-fold: 1) The thermal properties of the PNDI-Cx polymers, namely $T_g < T_{operating} < T_m$, allow for isothermal crystallization to take place at room temperature which may yield time-dependent mechanics as the morphology is in a state of flux. 2) The increased flexibility of these systems yields relatively slow crystallization rates as compared to the fully conjugated PNDI-C0, whose crystallization cannot be impeded even when cooling from the melt at rates of more than 10,000 K/s.[173] Thus, the annealing protocol was designed to achieve equilibrated morphologies for deriving structure-property relationships without the obfuscation of time dependence. **Figure 2.2(b)** shows representative curves for the tensile analysis for annealed PNDI-Cx films (see **Figure A.4** for raw curves) where a clear trend in elastic modulus is given by the diminishing slope in the linear elastic regime thus confirming our hypothesis. For fully conjugated PNDI-C0 the elastic modulus is 881 MPa post annealing, while, the PNDI-Cx polymers with flexible linker

range from 664 MPa (PNDI-C3) down to 213 MPa (PNDI-C7). However, for PNDI-Cx films annealed at room temperature the trend in elastic modulus is not as clear, which may be due to different crystallinity in the films as a result of different crystallization rates. A summary of the tensile data from both regimes is given in **Table 2.1**.
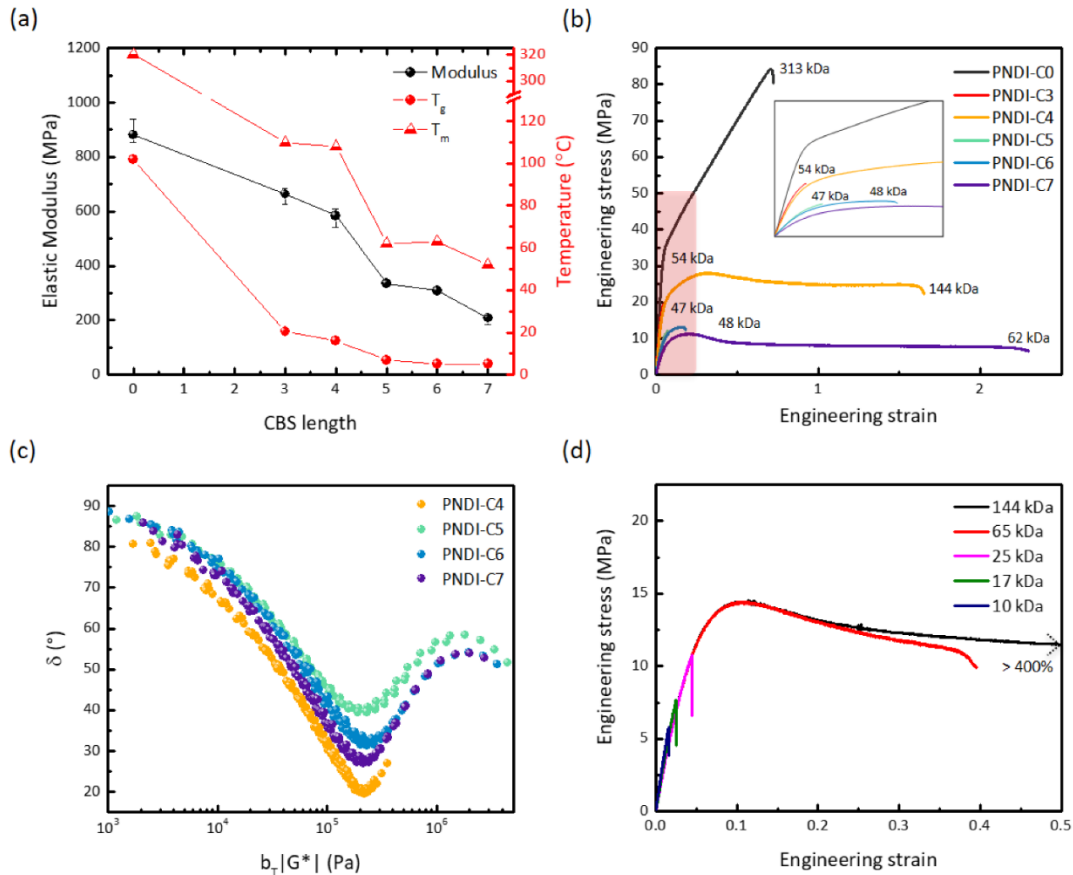
Figure 2.2 *Influence of chain flexibility on thermomechanical and rheological properties. (a) Elastic modulus, backbone T_g, and T_m for all examined PNDI-Cx polymers. Thermal data was obtained from DSC and T_g was verified through physical aging. (b) Comparison of stress-strain curves obtained from the pseudo-free-standing tensile test post a two-day annealing at an undercooling of ~ 30 ˚C. PNDI-C0 was annealed for 8 hours at 200 ˚C. Shaded red area indicates region of interest relative to insert. (c) Van Gurp-Palmen-plots of PNDI-C4 - C7. PNDI-C4 of 144 kDa M_w was used. (d) Molecular weight dependent tensile test of PNDI-C4 post two-day equilibrating at room temperature in nitrogen atmosphere.*

Table 2.1 *Physical and mechanical properties of NDI-Cx polymers*

	M_n (kDa)	M_w (kDa)	PDI	Me (kDa)	Thickness (nm)	Modulus (Mpa)	STDEV	COS	STDEV
PNDI-C0 PA	42.2	104.7	2.5	---	90	652	24	0.02	< 0.01
PNDI-C0	157.5	313.4	2.0	---	97	691	38	0.69	0.05
PNDI-C0 PA	157.5	313.4	2.0	---	115	881	26	0.65	0.11
PNDI-C3	33.2	53.9	1.6	---	83	293	3	0.83	0.53
PNDI-C3 PA	33.2	53.9	1.6	---	135	664	19	0.04	0.01
PNDI-C4	4.73	9.6	2.0	---	67	386	25	< 0.02	NA
PNDI-C4	10.5	17.3	1.6	---	71	364	6	0.03	0.01
PNDI-C4	14.6	24.6	1.7	---	82	320	8	0.04	0.01
PNDI-C4	34.1	63.8	1.9	---	94	312	16	0.43	0.18
PNDI-C4	61.3	144.3	2.4	15.9	78	338	11	4.04	0.27
PNDI-C4 PA	61.3	144.3	2.4	15.9	66	585	25	1.10	0.55
PNDI-C5	15.3	46.5	3.0	15.9	83	335	10	0.06	0.01
PNDI-C6	16.7	48.0	2.9	14.2	99	309	3	0.16	0.02
PNDI-C7	19.0	62.3	3.3	14.8	79	213	7	1.80	0.41

PA: post annealing at 30 ˚C below the respective melting temperature (PA occurs at R.T. for PNDI-C5, C6, C7 and is thus not listed)

Apart from the elastic modulus difference in PNDI polymers, we also studied their COS. The COS for the polymers covers a wide range from below 5% strain to above 400% in the case of high molecular weight PNDI-C4 annealed at 25 ˚C. COS is often found to be proportional to the number of intermolecular entanglements in a polymer system.[178,179,180] As the number of entanglements increase, the distribution of load bearing chains becomes more uniform minimizing the influence of inherent defects and ultimately providing increased elasticity. The entanglement behavior for conjugated polymer can be measured using melt reheology.[181] Due to limited material supply, the sample was molded into disks 8 mm in diameter and 0.5 mm in thickness under vacuum for oscillatory melt shear rheology.[182,183,181,184] The rheological measurements were successful for PNDI-C4 to C7 and the associated master curves are given in **Figure A.5,**

which demonstrate the viscoelastic response of these polymers within the melt state. Van Gurp-Palmen-plots (vGP-plot), an alternate mathematical representation of the data, were constructed to elucidate the entanglement characteristics, namely the M_e and the degree of entanglement (**Figure 2.2(c)**).[185,186,187]

The entanglement plateau modulus (G_N) was obtained from the norm of complex modulus corresponding to the minimum phase angle of the vGP-plot. G_N is shown to be weakly dependent on CBS length with values ranging indiscriminately from 19-23 kPa. This also implies similar M_e through the equation:[188]

$$G_N = \frac{\rho RT}{M_e} \qquad\qquad \text{eq1}$$

which is in the range of 14-16 kDa. Additionally, the position of the minimum in respect to the phase angle describes the molecular weight of the system where higher molecular weight polymer is expressed through a lower phase angle. Considering the relatively consistent M_e, the phase angle will be directly related to the number of entanglements within the system and therefore greatest ductility should be found at the minimum phase angle. This was found to be the case as 144 kDa PNDI-C4 possesses the lowest phase angle followed by PNDI-C7, PNDI-C6, and PNDI-C5 which corresponds well to their relative COS of 400%, 180%, 16%, and 6%.

To illustrate the important role of entanglements on the COS for conjugated polymers, we performed molecular weight dependent mechanical analysis on PNDI-C4 (**Figure 2.2(d)** and **Figure A.6**) with weight average molecular weight (M_w) ranging from 9.6 kDa (below M_e) to 144.3 kDa (well above M_e). Samples with M_w of approximately 65 kDa (~4 times that of M_e) were shown to be relatively ductile with above 40% strain at failure, but not to the extent of 144 kDa M_w which could tolerate

strains above 400%, a record high value for deformable electronics. This transition is justified given that multiple entanglements are generally required for high ductility. Likewise, the influence of molecular weight on fully conjugated PNDI-C0 was briefly studied with a low molecular weight batch of 104.7 kDa M_w (**Figure A.4(b)**). A drastic reduction in COS from 65% to 2% was observed, indicating a significant loss of entanglements consistent with the above analysis on PNDI-C4.

Here we provide rational design guidelines for engineering highly deformable materials by enhancing the number of entanglements. This can be achieved via two distinct approaches: 1) Reduce the M_e while maintaining the molecular weight. 2) Increase the molecular weight while fixing the entanglement molecular weight. The second approach has limitations in that high molecular weight D-A CPs can be hard to obtain as they eventually become insoluble. Regardless, we highlight the importance of scaling the M_e with the M_w of the polymer to obtain your desired mechanical properties. This parameter has generally been overlooked; however, it can be exceedingly useful for the rational design of highly deformable electronic materials and thus should warrant careful consideration.

2.3.3 Morphology for PNDI-Cx polymers

Next, grazing incidence wide angle X-ray scattering (GIWAXS) was used to study the film crystalline morphology (**Figure 2.3 and Table A.2**). PNDI-C0 has predominantly face-on morphology with strong π-π stacking as well as in-plane (100) and (001) scattering peaks corresponding to the alkyl and backbone respectively, consistent with literature.[189,190] Upon addition of CBS we observed a shift from the face-on to edge-on morphology as well as a significant loss of π-π stacking. Additionally, the

in-plane q vector of the (100) peak was shown to increase from 0.258 to 0.337 Å^{-1}

indicating a more closely packed alkyl system and the (001) peak was shown to decrease

from 0.470 to 0.332 Å^{-1} indicative of increasing CBS length which provides the contrast

to elucidate the (001) peak. This trend continues until a CBS length of C6 is reached at

which point the alkyl and backbone scattering become indistinguishable as their

scattering occurs at the same q vector.
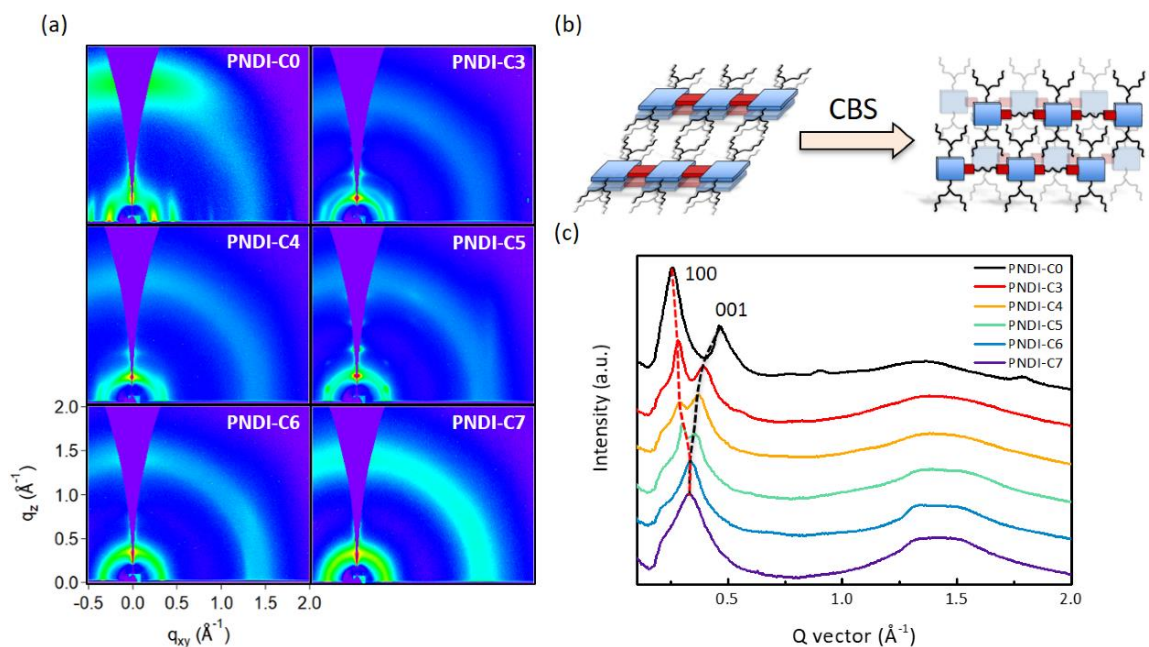
Figure 2.3 *(a) 2D GIWAXS profiles of as cast PNDI-Cx films. PNDI-C0 and PNDI-C4 are of 313 and 144 kDa Mw respectively. (b) Schematic diagram of the shifting solid-state morphology upon addition of CBS. Face-on PNDI-C0 with strong π-π stacking transforms to predominantly edge-on PNDI-Cx with disordered π-π stacking and closer alkyl packing. (c) 1D in-plane line cut profile.*

2.3.4 Deformation mechanism for CPs with CBS and tensile alignment of polymer backbone.

X-ray scattering techniques were extensively used to determine the degree of alignment

in the crystalline region for PNDI-Cx. GIWAXS was performed on tensile strained

PNDI-C0, C3, C4, and C7 to study the effect of tensile alignment on these ductile

33

systems (**Figure 2.4(a)**, **Figures A.7-A.8** and **Table A.3**). The d-spacing of (100) and (001) were largely maintained upon strain and a shift in the orientation of these scattering peaks was evident through comparison of perpendicular and parallel exposures to the strain direction. This suggests the lattice of the crystalline domain is maintained while the orientation of the crystallite changes upon being stretched. High molecular weight PNDI-C4 showed the most dramatic alignment, evident in **Figure 2.4(b)**, where an increase in the (100) intensity occurred with increasing strain along with a reduction in the (001) intensity for exposure parallel to strain. The opposite trend occurs for exposure perpendicular to strain where the (001) scattering is the majority of the detected signal. Such scattering is indicative of a highly aligned system.

Unfortunately, in the grazing incidence geometry, the illuminated volume as well as the beam intensity was not well accounted for, thus preventing highly accurate normalization and quantitative understanding of the alignment. To quantify the degree of alignment we transitioned towards ex-situ transmission WAXS which provides enhanced elucidation of the in-plane morphology which encompasses the (100) and (001) peaks of interest. The transmission 2D profiles are given in **Figure** 2.**4(c)** and were achieved for free standing films with thickness ranging from 192 to 120 nm depending on extent of strain. Through circular integration of the scattering signal, (**Figure 2.5(a-b)**) the peak area was determined to increase with strain up to 150% upon which the area decays towards 300% strain. This corresponds to a crystallinity enhancement in the early stage of the stretching (up to 150%) process, then the crystallinity drops which is potentially due to a breakup of the crystallites from the mechanical stress imposed on the film.
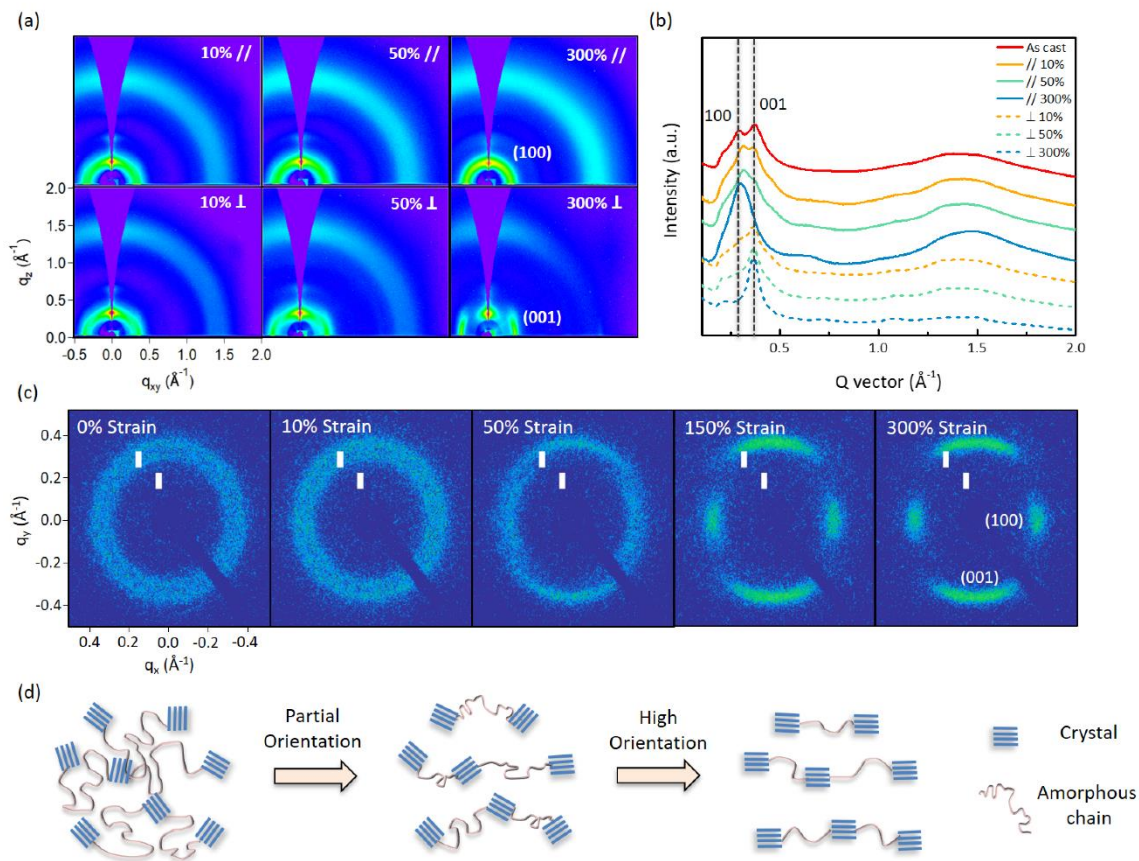
Figure 2.4 *X-ray characterization for deformed 144.3 kDa M_w PNDI-C4 polymer. (a) 2D GIWAXS profile of PNDI-C4 under tensile strain for both parallel and perpendicular exposures relative to strain direction. (b) 1D in-plane line cut scattering profile. (c) 2D transmission WAXS profiles of free-standing thin film (192-119 nm thickness) PNDI-C4 under ex-situ tensile strain. (d) Diagram showing an increase in orientation corresponding to transmission WAXS at 0, 50 and 300% strain.*

The FWMH of (001) peak was determined to decrease with increasing strain (**Table A.4-A.5**). Together the increase in area and reduction in FWHM imply an increased backbone contribution and a greater long-range order pervading throughout the system. Pole figure analysis was performed for both (100) and (001) scattering peaks to assess the contribution of scattering at each azimuthal angle and analyzed using Walker/Wagner alignment factor methodology to quantitatively determine the degree of tensile induced alignment (**Figure 2.5(c-d)**).[191] We note a high degree of alignment upwards of 0.3 and -

0.5 for (100) and (001) regimes respectively which plateaus post 150% strain; this is in agreement with both observed area and FWHM trends. A value of 1 or -1 represents a perfectly aligned system orientated in the horizontal and vertical directions respectively and agrees with (100) and (001) orientation direction. For plotting purposes, the absolute value of the alignment factor was taken, as the direction of orientation is inconsequential for quantitative confirmation of alignment.

While the X-ray technique discussed above only probes the crystalline regions, the alignment of amorphous domains must also be considered.[192] To confirm the highly aligned system of PNDI-C4 we then performed polarized UV-Vis (**Figure 2.5(e-f)**) to study the chain alignment in both amorphous and crystalline regions as well as atomic force microscopy (AFM) (**Figure A.9**) for topographical investigation. Polarized UV-Vis is unique for conjugated polymers as the transition dipole moment (π-π*) lies parallel to the backbone thus enabling elucidation of alignment through comparison of parallel and perpendicular absorption intensities, also known as the dichroic ratio.[193] This is demonstrated in **Figure 2.5(e)** where the parallel to strain absorption is normalized for each strain and we note the perpendicular to strain absorption diminishes with increasing strain. This correlates to a linearly increasing dichroic ratio up to a value of 3.35 in the case of 300% strain. Although more qualitative, AFM does show an aligned morphology at 300% strain. Considering the high amorphous content in the PNDI-C4 system, it stands to reason that at relatively low strains the relaxation of the surface would prevent significant visual alignment.
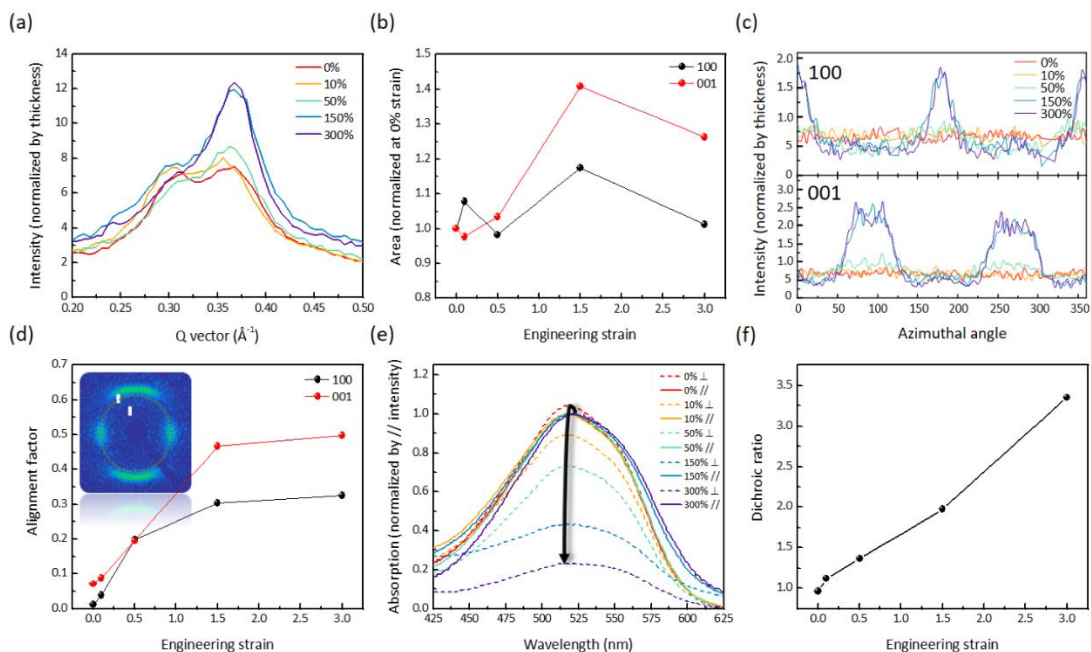
Figure 2.5 *Alignment analysis of 144.3 kDa Mw PNDI-C4 under tensile strain. (a) 1D circle gathering plot obtained from transmission WAXS and (b) fitted peak area. (c) Pole figure analysis of 100 and 001 peaks at q vectors of 0.305 and 0.366 Å-1 respectively and (d) resulting alignment factor analysis. (e) Polarized UV-Vis parallel and perpendicular to strain normalized by the absorption in the parallel to strain direction and (f) the corresponding dichroic ratio.*

Based on the X-ray scattering and polarized UV-Vis result, the deformation of the PNDI-C4 polymer can be described as follows (Shown in **Figure 2.4(d)**): 1) At low degree of strain, the mobile amorphous domains accommodate the applied stress by reorganizing in the strain direction. 2) Upon additional strain, amorphous segments unravel from a coil-like state and begin to become restricted by rigid crystallites. Force is then transferred into the crystalline units which initiates their alignment. Both crystalline and amorphous domains continue to align up to 150% strain in a near linear fashion. 3) Further deformation of the polymer leads to a plateau in crystalline alignment and relative degree of crystallinity (RDOC) followed by a breakdown of crystallites. Such disruption of the crystallites eases the physical restriction placed on the amorphous chains

which continue to align to the final strain of 300% due to significant interchain entanglements.

2.3.5 The important role of backbone rigidity in deformable electronics

Taken together, the following reasons are responsible for the very high crack on-set strain value, up to 400%, for PNDI-Cx polymers.

1) The highly flexible CP backbone results in a substantially lower T_g. The lower T_g allows the polymer to have a lower modulus and places the sample into the viscoelastic state. Within this state, chains are highly mobile and may accommodate stress through conformational reorganization. This significantly reduces the stress in the film which lowers the tendency for crack propagation near defect sites, thus promoting ductility.

2) The reduced backbone rigidity lowers the M_e and allows the polymer chains to entangle more easily relative to stiffer polymers at similar molecular weight. An increase in the number of entanglements leads to a more uniform load distribution throughout the semiconductor which deters crack propagation. Entanglements then undergo chain pullout to accommodate stress which promotes ductility. This deformation mechanism is further enhanced by the significant chain mobility in the system which acts as lubricant towards deformation.

Thus, for engineering highly deformable CPs, the backbone rigidity should be an important parameter to consider.

2.4 Conclusion

In summary, a suite of characterization methodologies was performed on PNDI-Cx polymers to provide a holistic perspective into the role of backbone flexibility on thin

film thermomechanics and morphology. For the first time, backbone flexibility was quantitatively shown to significantly reduce upon addition of CBS into the conjugated backbone. Such increase in flexibility was evident through the T_g, T_m and elastic modulus which all demonstrated a reduction with increasing CBS length. A high ductility was observed for high molecular weight PNDI-C4 which was rationalized through the large number of entanglements expressed by oscillating melt-shear rheology. The M_e was discovered to be weakly dependent on CBS length and therefore ductility was directly proportional to the molecular weight. In-depth morphological analysis was conducted indicating strong in-plane scattering which was exploited to evaluate the degree of tensile alignment for PNDI-C4. Currently, we are exploring the effect of chain alignment on their electrical properties and the possibility of coalignment with a fully conjugated tie-chain.

CHAPTER III – DEVLOPING A FREE-STANDING TENSILE METHOD TO STUDY

ULTRATHIN-FILM CONFINEMENT AND INTERFACIAL INFLUENCE

(Adapted from "Galuska, L. A.; Muckley, E. S.; Cao, Z.; Ehlenberg, D. F.; Qian, Z.;

Zhang, S.; Rondeau-Gagné, S.; Phan, M. D.; Ankner, J. F.; Ivanov, I. N.; Gu, X. SMART

Transfer Method to Directly Compare the Mechanical Response of Water-Supported and

Free-Standing Ultrathin Polymeric Films. Nat. Commun. 2021, 12, 2347.")

3.1 Introduction

The future of coatings, membranes, and organic electronics (thin film transistors,

photovoltaics, sensors, and bioelectronics) relies on a thorough understanding of polymer

thin film structure and mechanical response. Mechanical characterization of sub-100 nm

films has been an ongoing challenge throughout the field and has gained tremendous

interest with the growing prospects of organic electronics which, at the device scale,

possess an active layer of 100-nm or less.[141,9,194,13,195] To complicate matters, the

properties of such nm-thin polymer films tend to deviate from their bulk properties due to

an increasing contribution of the polymer interface[196,197]. This accompanies a phenomena

known as the finite size effect which describes the geometrical constraints that occur

when the thickness of a polymer film is of the same length scale as the dimensions of an

individual polymer coil, characterized by its polymer chain end-to-end distance

(R_{ee}).[111,109] A prime example of such a thickness dependent property is the glass transition

phenomena in polystyrene (PS).[96,198,98,106] For instance, reductions in the glass transition

temperature (T_g) as large as 10 and 80 ˚C have been reported for supported and free-

standing (FS) 30-nm PS films.[96,114] More recently, the reduction in T_g with film thickness

has been correlated to a decrease in film elastic modulus (E) which has not only

invigorated interest in thin film mechanics but also fundamental investigations surrounding T_g phenomena.[116,199,80,142]

Nanoindentation[200,56] and buckling techniques[116,71] have been used to measure the mechanical properties of ultrathin films deposited on silicon wafer or poly(dimethylsiloxane), respectively. However, the intrinsic properties of the film may be obscured by the underlying substrate due to sample-substrate interactions as well as a low signal to noise ratio. More recently, the pseudo-free-standing tensile test, referred to as film-on-water tensile test (FOW), has been used extensively in the study of both conventional and conjugated polymers (CPs). The FOW technique utilizes water as a nearly frictionless thin film support allowing the acquisition of complete stress-strain profiles.[80,142,77,201,23] However, there remains some concerns that the water support may influence such measurements, for instance water acting as plasticizer. Hence there is a need for mechanical characterization without the supporting substrate while maintaining the ability to analyze a wide range of polymer films with stiff (glassy) and soft (rubbery) characteristics.

Currently there are three primary methods for the mechanical characterization of ultrathin (sub-100 nm) free-standing films. These include nanobubble inflation[88,92,89], camphor-enabled transfer[94], Tensile Tester for Ultrathin Freestanding Films (TUFF)[76] technique, and a more recent guide frame technique.[95] Nanobubble inflation is performed by placing a thin film across an etched silicon nitride substrate with defined holes. Applied pressure forms nanobubbles while atomic force microscopy monitors the thermoviscoelastic response of the film. Creep compliance as a function of time and temperature has been measured for films as thin as 3-nm (polycarbonate) revealing

reductions in T_g by over 120 ˚C.[93] The main drawback for nanobubble inflation is that the

length scale of the measurement (micron hole diameter) prevents observation of large

scale deformation which is of particular interest within the growing field of deformable

electronics. Camphor-enabled transfer is a uniaxial tensile test whereby a composite film

is fabricated utilizing camphor as a sacrificial substrate. At elevated temperatures, the

camphor sublimes leaving the intact thin film behind. This technique has primarily been

used to study the mechanics of graphene but polycarbonate films as thin as 100-nm have

been successfully measured. The TUFF method is an extension of the FOW tensile test,

whereby a film floating on water is connected to a support frame and translated vertically

into air. The film is subsequently laser etched into a dog-bone geometry and mechanical

properties measured using uniaxial tensile testing. Currently, moduli of ~ 30-nm PS films

can be measured by this technique. The guide frame technique relies on transfer of the

film to a wax paper substrate, evaporation of water, followed by pick up with a

polyethylene terephthalate guide frame with supports. The frame is then connected to a

tensile stage and the supports are melted prior to testing. This technique was utilized to

study PS films with thickness ranging from 45–4319 nm and a wide variety of gauge

dimensions, thus providing insight in how film geometries alter the apparent mechanical

properties observed. The advantages and disadvantages of each measurement technique

are summarized in **Table B.1**.

Here we present an innovative s̲hear m̲otion a̲ssisted r̲obust t̲ransfer (SMART)

process as a reliable technique to measure FS mechanics for both stiff glassy and soft

viscoelastic polymers. We then compare the influence of water and air interfaces on the

mechanics of ultrathin films (**Figure 3.1(a)**) characterized by both FOW and FS

techniques. The mechanical properties of three FS polymers, PS, poly(3-hexylthiophene) (P3HT), and 5-dialkyl-3,6-di(thiophen-2-yl)-2,5-dihydro-pyrrolo[3,4-c]pyrrole-1,4-dione (DPP)-containing polymer incorporating a linear thieno[3,2-b]thiophene donor (PDPP-TT), were measured and compared to results from the FOW test to assess the influence of water. We observed minor differences in modulus, while yield stress (maximum strength) and strain at failure were slightly elevated for the FOW method which is attributed to a force dissipating mechanism provided by the capillary forces of the water. Independent measurements using quartz crystal microbalance (QCM) and neutron reflectometry (NR) demonstrated water uptake within PS and P3HT films to be as high as 9.79% and 9.13% by volume respectively. This uptake in water supports that the mechanical properties of these hydrophobic polymer films are influenced by water to a minor extent, validating previous mechanical analysis using the FOW technique.

3.2 Experimental

3.2.1 Materials

Polystyrene was obtained from Polymer Source with weight-average molecular weights/dispersity of 183 kDa/1.06 (low molecular weight) and 2062 kDa/2.9 (high molecular weight). The weight-average molecular weight for 2062 kDA was characterized by GPC using trichlorobenzene as the eluent at 160 °C, polystyrene for calibration, viscometer, and light scattering as the detectors (**Figure B.15**). P3HT and PSS were obtained from Sigma-Aldrich with weight-average molecular weights/dispersity of 54 kDa/2.74, and 70 kDa respectively. PS was annealed under vacuum to remove solvent impurities, while the other samples were used as received without additional purification or GPC measurement. PDPP-TT, was synthesized

following previously established procedures.[202] The weight-average molecular weight was determined to be 184 kDa with a dispersity of 3.62 via characterization by GPC as described above for 2062 kDa PS.

3.2.2 Dog-bone film preparation

The composite films were fabricated by first spin casting 3 wt% PSS in aqueous solution onto plasma treated silicon wafer at 4000 rpm for 1 minute. The polymers of interest were then spun cast from their respective solutions at 2000 rpm for 2 minutes. Concentrations are as follows, 183 kDa PS: 25, 20, 15, 10, and 7.5 mg/ml solution in toluene. 2062 kDa PS: 15, 13, 10, 7.5, 5, and 3.5 mg/ml solution in toluene. P3HT: 25 and 20 mg/mL solution in chlorobenzene. DPP-TT: 10 mg/ml solution in chlorobenzene.

Unless stated within the discussion, all samples were measured as cast without annealing. Some samples were annealed in a vacuum oven at 115 ˚C for 1-hour and allowed to naturally cool to room temperature while under vacuum.

Once the composite films were fabricated, they were then laser etched using a Ytterbium 20 W laser with a wavelength of 1064-nm. The dog-bone gauge length and width were etched to either 8x2-mm and 4x2-mm respectively with a 3.25-mm wide support on each side of the gauge. Microfibers connecting the dog-bone to the side supports were then laser etched. Samples were then separated into individual dog-bones for testing.

3.2.3 Thickness measurement and film uniformity

After creating the composite film, a representative portion was floated on water, removing the PSS layer, and collected on fresh silicon. Film thickness was determined using atomic force microscopy for all polymer materials. Additionally, a F20-UVX

interferometer was used to measure the thickness of PS films, utilizing a probing wavelength from 325-1700 nm, refractive index of 1.5865, and a spot size of 1.5 mm in diameter.

Film uniformity is assessed in **Figure B.16**. To assess the uniformity of the thinnest 19 nm film, a fresh 3.5 mg/ml solution of polystyrene in toluene was spun cast onto a 4x4 cm wafer with PSS layer. The film was divided into 9 1x1 cm squares as demonstrated below where each PS film was floated on water, removing the PSS layer, and collected on fresh silicon. Both AFM and interferometry were used to assess thickness throughout each coordinate. Three measurements were performed at different locations within each 1x1 cm coordinate. Additionally, NR was performed on 19 nm PS film without PSS verifying that spin coating on a 5x5 cm wafer provides a uniform thickness.

3.2.4 Free-standing tensile test

Each sample was connected to a motorized x-stage using a vacuum pen for easy sample handling. DI-water droplets were then placed at each corner of the film to dissolve the PSS underlayer and lift the film from the silicon surface. Once lifted the linear stage and load cell PDMS clamps were attached to the pads at each end of the dog-bone film. An approximate shear speed of 0.15 mm/s was then applied with the motorized x-stage while monitoring the water meniscus across the film. Generally, residual water on the film was minimal at this shear speed and resulted in a pristine free-standing film. A tweezer was then used to remove the outer film supports which was facilitated by the laser etched microfibers. The film was then left in air to dry and equilibrate prior to tensile testing. During the tensile test, each film was elongated with an

applied strain rate of $5*10^{-4}$ s^{-1} while simultaneous measurement of the force was conducted at a frequency of 10 Hz. The force-displacement data was then converted into the representative stress-strain plots.

The pseudo-free-standing tensile test is similar to that reported here and is described in great detail in our previous publications.[142,23] However, in this report laser etching was utilized as the primary means of dog-bone patterning rather than oxygen plasma etching. The laser etching process provides equivalent mechanical properties to films prepared by oxygen plasma etching, as shown in **Figure B.17**, despite differences in edge appearance.

The correction factor for the 4 mm dog-bones was determined by dividing the modulus of the 8 mm films measured on water to that of the 4 mm films of similar thickness. An average correction of 1.314 with standard deviation of 0.056 was determined. For the thinnest films, only the annealed measurements were compared to discount the influence of processing conditions. This correction factor was then multiplied by the gauge length of 4 mm to yield an apparent gauge length of 5.256 mm. This apparent gauge length corrects the strain values of the 4 mm films and in turn provides an accurate comparison of modulus and strain at failure for the 8 mm films. Yield stress is not influenced by this correction but rather the strain at which yielding occurs.

3.2.5 Quartz crystal microbalance

P3HT and PS films of 100 nm thickness were deposited on Au-coated 5 MHz Au-coated quartz crystal microbalance (QCM) crystals by spin-coating at 2000 RPM for 30 seconds. QCM measurements were carried out by tracking frequency shift and change in

peak width of the first 9 off crystal harmonics using a SARK-110 vector impedance analyzer controlled using custom software written in Python. Gravimetric/viscoelastic response of films was measured while the film was transferred from air and submerged in Milli-Q water, and then transferred back to air. Values of Δf and ΔD were calculated by fitting QCM conductance peaks to a Lorentz distribution and extracting position and width. [203,204]

3.2.6 Neutron reflectometry

NR measurements were performed on the Liquids Reflectometer (LIQREF), BL-4B, at the Spallation Neutron Source (SNS) in Oak Ridge National Laboratory (ORNL) with a two dimensional position-sensitive ^{3}He detector.[205] The reflected intensity was measured as a function of the momentum transfer $Q = 4\pi \sin\theta/\lambda$, where θ and λ are the incident angle and wavelength of the neutron beam, respectively. A 6.8-Å bandwidth, selected from a wavelength range of 5.95-15.68-Å, is used in conjunction with measurement angles of $\theta = 0.60$, 0.75, 1.1, and 1.62 to span a Q range of 0.008 to 0.060-Å^{-1}. The footprint of the beam was 35x20 mm^2, smaller than the 50x50 mm^2 dimension of the films and was kept constant by increasing the beam-defining slit openings proportional to the neutron angle of incidence. PS or P3HT films were floated onto the meniscus of a DI-water Langmuir trough through the release of a PSS layer, identical to the process in the free-standing tensile test. A small scratch was made along each edge of the square film and DI-water droplets were placed at each corner to allow a gentle release from the silicon substrate as the PSS layer dissolved. Once fully lifted, the floated sample (still on silicon) was deposited into the Langmuir trough, which was then sealed to minimize air vibration and water evaporation. The entire system was supported by the

antivibration table (Accurion Halcyonics, MD, U.S.A.). Each sample was exposed to the room temperature water surface for 1 hour during the alignment procedure and subsequently scanned with a Q-vector range from 0.008 Å^{-1} to 0.060 Å^{-1}. Data reduction and fitting was performed through the online reflectivity modeling software provided by BL-4B.[206]

3.3 Results and discussion

3.3.1 SMART (shear motion assisted robust transfer) to obtain free-standing ultrathin films

The making of FS films for tensile measurements usually involves the transfer from a supporting substrate (silicon, glass) to the tensile stage. This is difficult because the films are fragile and cannot easily be lifted off the supporting substrate. This remains true even for films supported by a water surface. If a 2 x 8 mm rectangular polymer film undergoes a vertical lift, the surface tension of water (~ 73 mN/m) results in an approximate downward/inward force of 1.5 mN, primarily along the perimeter of the film, causing local stress, bending, fracture, and ultimately rupture of the film. This effect is exacerbated in thin or brittle films which have a tendency to fracture as seen with 60-nm PS (**Movie B.1**) and 300-nm graphene oxide films.[94]

Figure 3.1(b) and **Movie B.2** demonstrate the SMART process used to obtain FS films. This approach is simple and includes the following steps. A laser etched composite film (polymer of interest with outer microfiber support and poly(sodium 4-styrenesulfonate) (PSS) water soluble sacrificial layer and silicon substrate) is attached to
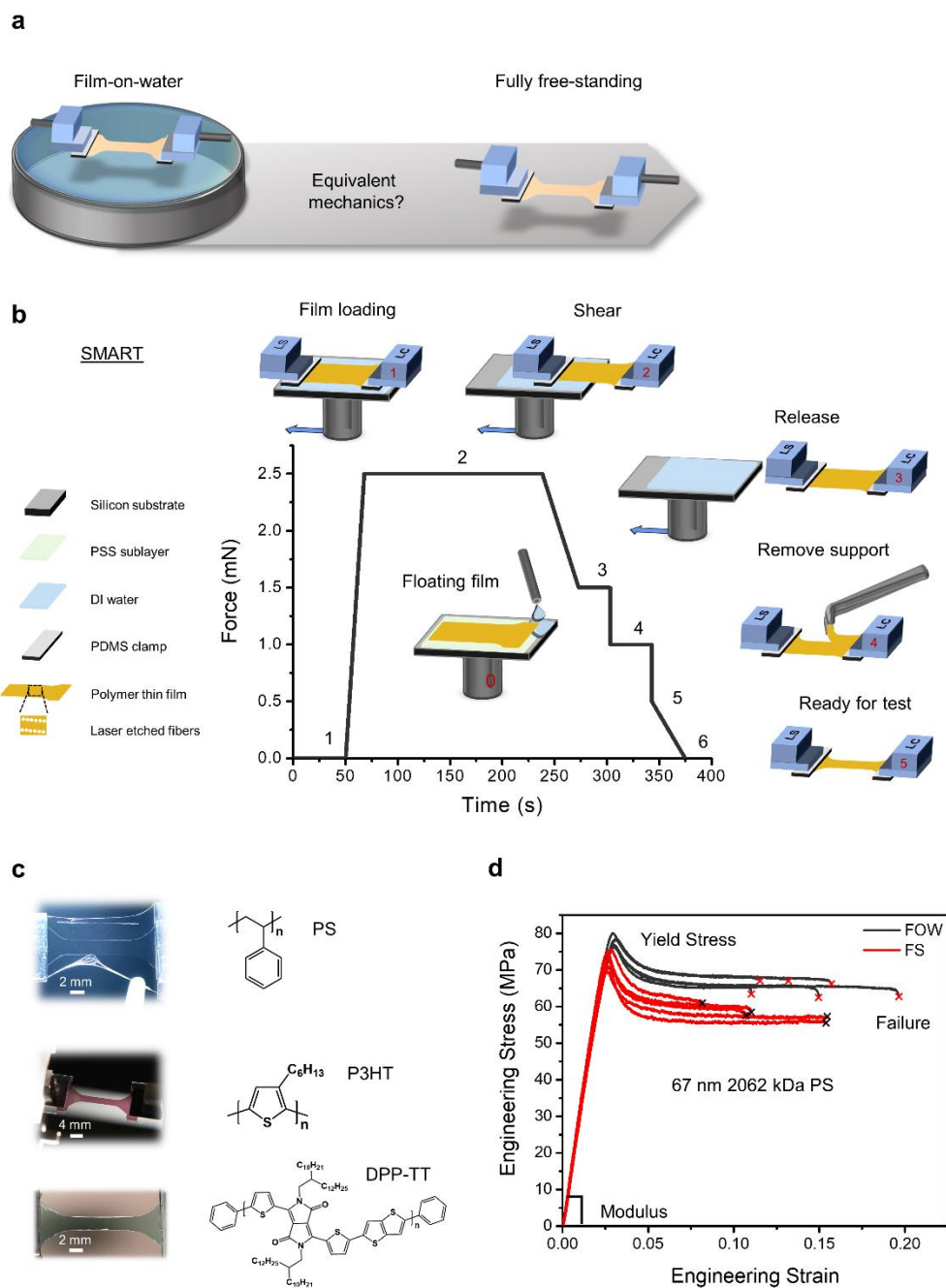
Figure 3.1 *Use of shear motion assisted robust transfer (SMART) method to obtain ultrathin films. a) Illustration of the FOW and FS tensile tests. b) SMART process and representative force applied to the film for obtaining a free-standing dog-bone for tensile analysis. c) The three polymers investigated within this study and representative free-standing films with a dog-bone gauge of 8 x 2 mm. From top-down: support removal from 19-nm high molecular weight PS, 80-nm P3HT prior to strain, DPP-TT prior to strain. d) Representative stress-strain profiles for a 67-nm 2062 kDa PS film from both FS and FOW techniques.*

a motorized stage which provides precise continuous shear speeds along the in-plane direction. Water droplets are placed at the corners of the silicon substrate which then propagate throughout and dissolve the PSS sacrificial layer lifting the polymer thin film to a floating position. A linear stage and load cell are then attached to opposite ends of the film at which time a shear of 0.15 mm/s is applied to the silicon substrate parallel to the lateral dimension of the film, which is held stationary. At this speed, minimal lag exists between the water layer and the silicon substrate, which allows the removal of water from under the film while only forming a small mobile meniscus which exerts minimal force on the film. Water-film contact angle, and subsequently, the force exerted on the film, can be further reduced by adding ethanol to the water solution. Once a free-standing film is obtained, the laser etched microfiber supports (example optical images are shown in **Figure B.1-2**) are removed prior to mechanical analysis of the dog-bone patterned film. The temporary supports help minimize wrinkling near the edges of the film as shown in supporting **Movie B.2**.

The force exerted on the polymer thin film was monitored throughout the SMART process by the attached load cell and is generally less than 3 mN. The shear process distributes this force more uniformly across the film and utilizing sacrificial side supports maintains the geometry of the dog-bone. Upon removal of the side supports an approximate 0.5 mN of force is estimated to have been applied to the final dog-bone-shaped film. A restoring force is then applied to the film to remove any residual stress prior to measurement. For PS films we demonstrate the potential of this technique to transfer films as thin as 19-nm (**Movie B.3**). Successful measurement of the thinnest films is further dependent upon removing defects which may initiate failure during

50

transfer or tensile testing. A facile method to mitigate such defects is to shorten the gauge

length thereby reducing the available area for defects during film formation as well as the

length of travel during the SMART process. Dog-bones with a gauge length of 4-mm

(**Movie B.3**), as compared to longer gauge length of 8-mm (**Movie B.2**), were shown to

provide a more efficient transfer thus enabling increased data fidelity and successful

transfer of the thinnest 19-nm films (success rate ~ 80%).

Here we demonstrate successful transfer and measurement of mechanical

properties for a broad range of polymer films, including PS films (as thin as 19 ± 1.5-nm)

as well as the viscoelastic CPs P3HT and PDPP-TT, as thin as 80 ± 3 and 75 ± 2-nm

respectively (**Figure 3.1(c)**). Thus, this method can be applied to a broad range of thin

film materials.

3.3.2 Free-standing thin film mechanics

Here we discuss the thin film mechanics of rigid glassy and soft viscoelastic

polymers, focusing on confinement and interfacial effects. PS, a glassy polymer with

high T_g, possesses fundamental interest as it has been reported that sub-100 nm FS PS

films, in excess of 350 kDa, exhibit a sharp reduction in T_g, the severity of which

increases with molecular weight. Sub-350 kDa PS features a more gradual T_g decay as

seen with substrate supported measurements.[106,107,207] The molecular weight dependent

T_g for FS PS is consistent with the finite size effect. In contrast, PS films with silicon

support are independent of molecular weight, and thus reductions in the T_g with reducing

thickness more accurately represent the influence of the free surface mobile layer. The

origins of the molecular weight dependence for FS T_g are not yet understood, and attracts

significant attention.[208] In this report, we first explore the effect of PS molecular weight (

183 and 2062 kDa) and gauge length (8 mm and 4 mm) on thin film mechanics, using both FOW and FS techniques. **Figure 3.1(d)** shows representative stress-strain profiles for a 67-nm film measured with both techniques in the 4 mm gauge length dog-bone sample geometry. Particular attention is paid to 2062 kDa PS in hopes of observing mechanical properties with increased sensitivity towards the sample-interface (air and water) given the range of viable thicknesses below the polymer's large R_{ee} of ~ 94-nm.

Tensile tests of 2062 kDa PS were performed for a series of films with thickness from 155 to 19-nm, exhibiting yielding and plastic deformation behavior **(Figure 3.2(a)**, **Figure B.3-B.5)**. Large scale deformation of a 19-nm thick PS film was monitored by optical microscopy, demonstrating wrinkling and then shear deformation zones post yielding **(Movie B.3 and Figure B.6)**. To the best of our knowledge, this measurement is the thinnest free-standing PS film to undergo tensile testing, an approximate 40% reduction in thickness from the previous record of 30-nm.[76]

Regardless of molecular weight, a near equivalent modulus was observed between the FS and FOW techniques at all film thicknesses **(Figure 3.2(b), Figures B.3(b) and B.7(a))**, indicating that polymer-water and polymer-air interfaces have similar effects on the thin film's mechanical properties. This observation is consistent with measurements of PS nanoparticles in aqueous solution, which have demonstrated equivalent T_g reductions to those of sub-350 kDa FS films.[101] Both techniques, in the 8 mm gauge length dog-bone sample geometry, demonstrate a reduction in modulus lower than the bulk value for sub 40-nm thin films, consistent with a previous study using buckling metrology.[116]

Films were subjected to vacuum thermal annealing at 115 ˚C for one hour to eliminate residual stress. Post annealing, the modulus of 8 mm sub-40 nm PS films increased to the bulk value of ~ 3 GPa, excluding FS 19-nm PS which remained just under the bulk E. This increase in modulus upon annealing indicates that the previously observed reduction originates from a process driven phenomenon, unrelated to T_g.[209] We attribute this effect to residual stress from rapid evaporation of solvent during spin casting which results in radially aligned polymer chains, thus reducing the number of loadbearing chains in the tensile direction and lowering the apparent E.[110,69] Upon annealing above the bulk T_g, the polymer chains relax isotropically leading to reduced orientation and an increased number of load bearing chains. PS films exceeding 40-nm in thickness, excluding 153-nm, were not annealed as bulk modulus was maintained. This implies a critical thickness for PS films at which residual stress begins to influence the apparent E. Previous mechanical analysis of as cast ~ 220-nm PS films also demonstrated identical modulus to films annealed at 115 ˚C for 15 hours.[80] We note that 4 mm thin films do not demonstrate a strong dependence on annealing which may be due to the reduced size scale limiting the influence of anisotropy, further investigation is warranted.

From a T_g perspective, the increase in E, post annealing, for 183 kDa PS is expected as at 38-nm in thickness, the anticipated T_g from literature is near 80 ˚C[112], sufficiently above the measuring temperature of 25 ˚C, and thus should express bulk-like behavior. In contrast, the bulk modulus of the 19-nm 2062 kDa FS PS film is particularly interesting given that at such high confinement (21% of R_{ee}) the T_g is expected to lie below room temperature[106] where the film would reside within the rubbery regime and

modulus should exhibit a considerable reduction.[210] That is not the case here, and thus points to an alternative T_g phenomenon.
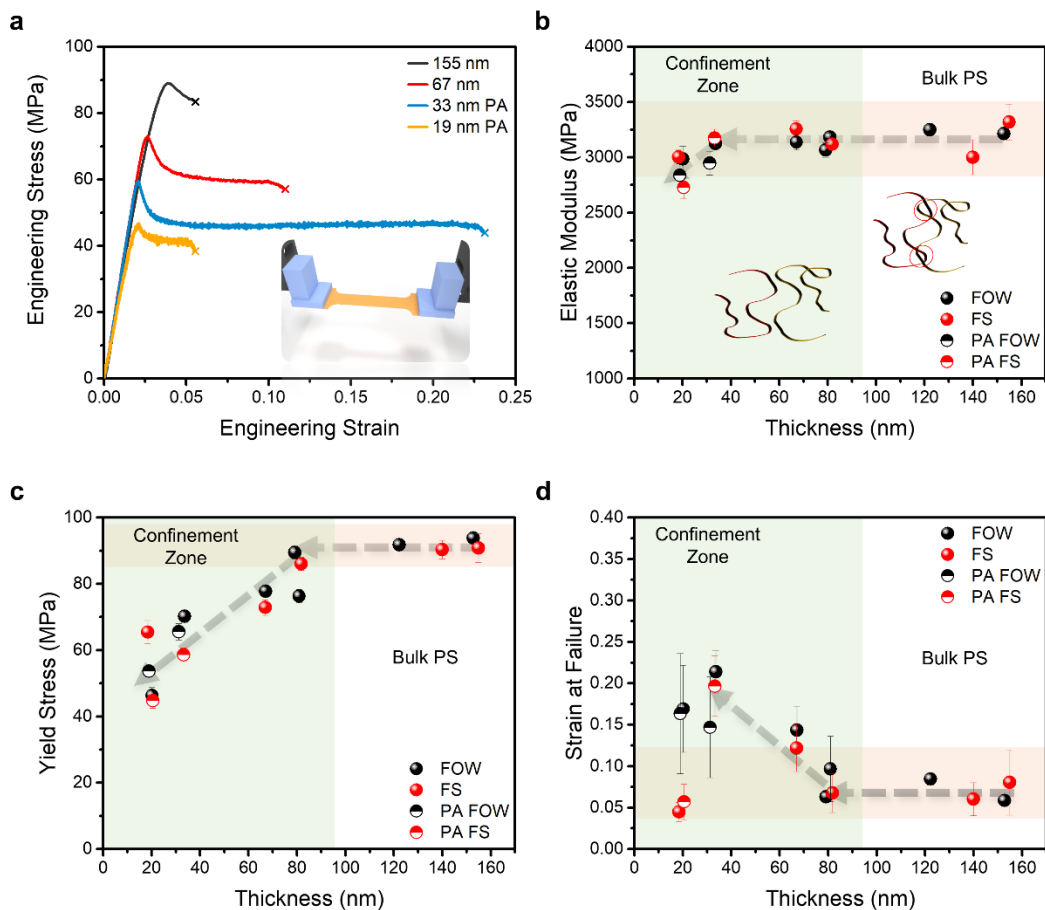
Figure 3.2 *Comparison of 2062 kDa PS FS and FOW mechanical properties with reducing film thickness. Gauge length is 4 mm. a) Representative stress vs strain profiles of FS PS from 155 nm to 19 nm. b) Elastic modulus thickness dependence of both FS and FOW PS films. Insert represents the loss of inter-entanglements upon confinement at thicknesses below the end-to-end distance of a polymer chain. c) Yield stress thickness dependence of both FS and FOW PS films. d) Strain at failure thickness dependence of both FS and FOW PS films. "PA" corresponds to samples characterized post vacuum annealing at 115 °C for 1 hr. Error bars represent the standard deviation of the characterized mechanical properties.*

Here we seek to explain why the modulus of the 19-nm FS PS film maintained its high value despite heavy confinement. Seminal work by Forrest et al. utilized Brillouin light scattering to investigate the high frequency mechanics of FS 767 kDa and 2240 kDa

PS films as thin as 29-nm which surprisingly demonstrated bulk-like properties.[211] This finding is congruent with more recent T_g investigations of FS PS by Connie Roth where ellipsometry covering a wider temperature range revealed two T_g's.[114,102] The lower T_g, approximately 20 ˚C for 30-nm films of 934 kDa PS, was found to be molecular weight dependent, consistent with previous T_g measurements of high molecular weight FS PS[112,113], while the higher T_g, approximately 85 ˚C, was observed to be molecular weight independent, consistent with both supported PS and sub-350 kDa FS PS films.[106] The high T_g fraction, independent of molecular weight, was determined to contribute up to 90% of the thermal expansion, making it the dominant transition. This observation is consistent with work by O'Connel et al. using nanobubble inflation which demonstrated a similar trend in T_g, approximately 80 ˚C and 60 ˚C for 994 kDa PS films with thicknesses of 30-nm and 20-nm respectively, as well as an independence of molecular weight.[89] Considering these works, the measurement temperature (~ 25 ˚C) for our 19-nm FS PS films lies significantly within the glassy state and is thus congruent with our mechanical analysis demonstrating high modulus and molecular weight independence. Furthermore, there is a discrepancy between the enhanced local dynamics observed with FS films and large-scale chain motion which has been shown to express bulk-like behavior. McKenna et al. have reported rubbery stiffening, as well as glassy stiffening, of thin PS films at reduced thicknesses despite reductions in the thin film T_g.[88,89] This indicates that long range and local chain dynamics respond differently when confined and may potentially obfuscate the expected mechanical response from T_g alone. Hole formation, an indicator of large-scale chain mobility, has also been shown to occur near the bulk T_g for FS PS films , regardless of the apparent T_g reduction occurring in such thin

films.[212,213] Considering that tensile deformation also represents large-scale chain motion, it is possible that FS films experiencing tensile deformation, as within this work, may similarly be negligibly affected by the apparent thin film T_g as in hole formation. Ediger et al., measured the molecular motion of FS PS films, greater than 14-nm thick, which were seen to possess a bulk-like interior with a maximum mobile layer thickness of 7-nm at elevated temperatures near the bulk T_g. Experiments performed below ~ 80 ˚C demonstrated a mobile layer thickness of less than 1-nm. This finding was conjectured to support the resistance of thin films toward hole formation.[214] In regards to the current study, this suggests that the mobile layer contributes less than 5.3% of the polymer volume for a 19-nm thin film and thus would minimally impact modulus in most instances. Although bulk-like modulus is observed, we note a 10 % average reduction in modulus for confined 19 nm films relative to the unconfined state **(Figure 3.2(b))**, congruent with the above discussion. Previously, a reduction of modulus for 136.5 kDa PS was observed near a thickness of 25 nm and was correlated to the R_{ee} of 25 nm.[80] Since the reduction in modulus in this work also occurs near this thickness despite a greater R_{ee} of 94 nm, we hypothesize that such reduction is due to the mobile interface and not geometric constraints associated with confinement below the R_{ee}. Lastly, the bulk modulus observed in this report agrees with previous results from FOW and TUFF measurements despite heavy confinement.[201,76] Thus, we conclude that the thickness dependent modulus values seen in FS PS films are 1) independent of molecular weight, 2) independent of conformational restrictions associated with confinement below the R_{ee} of a polymer chain, and 3) primarily dictated by the polymer-surface interface, as is the case for supported thin film T_g measurements.

Beyond the modulus of 2062 kDa PS, a near linear reduction in yield stress was observed throughout the confined films regardless of the technique employed (**Figure 3.2(c) and Figure B.3(c)**). For the 8 mm films, the yield stress and strain at failure were reduced relative to the FOW technique (**Figure B.3-B.4**). We believe this is due to potential defects along the transferred films, which upon reducing the gauge to 4 mm was mitigated (**Figure B.5**). For 183 kDa PS, average strain at failure was observed to be greater in the FOW measurements, while yield stress did not show a strong trend (**Figure B.7-B.8**). It is important to note that although modulus does not correlate to the polymer R_{ee}, yield stress and strain at failure are marked by a clear transition to lower and higher values, respectively, upon confinement (**Figure 3.2(d)**). The 19 nm films demonstrate a difference of 43% in the yield stress and the 30 nm films demonstrate a 160% difference in strain at failure relative to the unconfined films. Additionally, confined FOW measurements have an average increase in yield stress and strain at failure by 4.3% and 3%, respectively. The difference in strain at failure does not include the 19 nm films which show disagreement between the two techniques. This difference may be associated with a loss of inter-entanglements resulting in the reduced strain at failure for the free-standing film, while in the case of FOW measurements this is mitigated by the water interface. We note significant wrinkle formation within the FS films under tensile strain relative to the FOW measurements (**Figure B.9**). This may indicate that the surface tension of water is sufficient to retard strain localization in thin films resulting in a more uniform deformation, similar to films stretched on an elastomeric substrate, and thus deter crack propagation. Although small, these results support the concept of a force dissipating mechanism provided by the water interface resulting in elevated yield stress

and strain at failure for confined films. This makes conceptual sense as the polymer-water interface begins to play a greater role at reduced thicknesses but may be overcome by the loss of inter-entanglements when significantly confined. Both the trend in modulus and strain at failure are in agreement with that reported by the Crosby group using their TUFF technique.[76] However, we note that a distinguishing feature between these data sets is the low strain at failure exhibited from the TUFF technique thereby limiting the observable deformation of 151.5 kDa PS to the onset of the yielding regime ($< 2.5\%$ strain); while in the SMART process, strain at failure upwards of 15% strain (85 nm 183 kDa) is observed, surpassing the yielding point and fully within the plastic deformation zone. Considering that these techniques, as well as the PS materials used, are fundamentally similar, it is important to ascertain the cause for such variations in ductility. We propose two potential origins for the low ductility found through the TUFF technique. 1) PS films were annealed at 170 ˚C for 25 minutes which may result in hole formation as previously shown for 71-nm PS on Krytox oil after annealing at 160 °C.[215] To further explore this possibility, we annealed ~ 40-nm PS on both mica and silicon substrates at 170 ˚C for 25 minutes resulting in partial de-wetting of the PS film **(Figure B.10)**. 2) Previous measurements by our group using the FOW technique, have shown the strain at failure for PS to decrease at elevated strain-rates.[142] Considering that the strain-rate used through the TUFF methodology is sixteen times greater than the strain rate of $5*10^{-4}\,s^{-1}$ used in the current study, this may be a significant causative factor in the relatively low strain at failure. Regardless, the enhanced ductility from the FOW measurements may be due to a force dissipating mechanism provided by the water interface. If this is the case, then it is expected that similar phenomena may occur in other hydrophobic polymer thin films.

58

Mechanical analysis was performed on a more challenging ductile polymer, P3HT, the benchmark CP. P3HT is a soft viscoelastic polymer which has a bulk T_g near room temperature[122] and consequently a relatively low modulus of 100-350 MPa, depending on measurement technique, sample crystallinity, regioregularity, and molecular weight.[142,216,81,72] As such, this polymer represents a significant challenge as the forces applied during any transfer process may lead to irreversible deformation and thus alter the measured mechanical properties. In this study we investigated the mechanics of 105-nm and 80-nm thick P3HT films, which to our knowledge is the first sub-100-nm FS mechanical analysis for any CP reported to-date. All measurements were performed without annealing given that the sub-room temperature T_g of P3HT should limit anisotropy from spin coating. **Figure 3.3(a)** and **Figure B.11(a)** show the stress-strain profiles for 80-nm and 105-nm films respectively under both FOW and FS techniques. From these curves it is readily apparent that the yield stress and strain at failure are lower for the FS measurement while the difference in modulus is less noticeable with a value ~ 6% greater **(Figure 3.3(b-c))**. These values track the trends seen in the PS films, although more significantly, and support the notion of water providing a mitigating mechanism towards crack propagation. As stated previously, it is possible, given the viscoelastic characteristics of P3HT, that some form of plastic deformation throughout the SMART process may lead to a reduction in yield stress or strain at failure. This is not believed to be the case given that a significant reduction in apparent modulus would also be expected, while we note a ~ 6% increase in FS compared to FOW, from 309-332 MPa and 310-326 MPa for 80 and 105-nm respectively. However, this difference could imply a slight plasticization effect from the

59

water which may explain the decreasing differences in mechanical properties at the greater thickness of 105-nm (i.e., lower Δ *modulus*, Δ strain at failure, and Δ yield stress between FS and FOW). Considering the hydrophobic nature of P3HT, this would seem unlikely at first glance.[217] Thus, we will also discuss the diffusion of water into such polymer films in a later section.
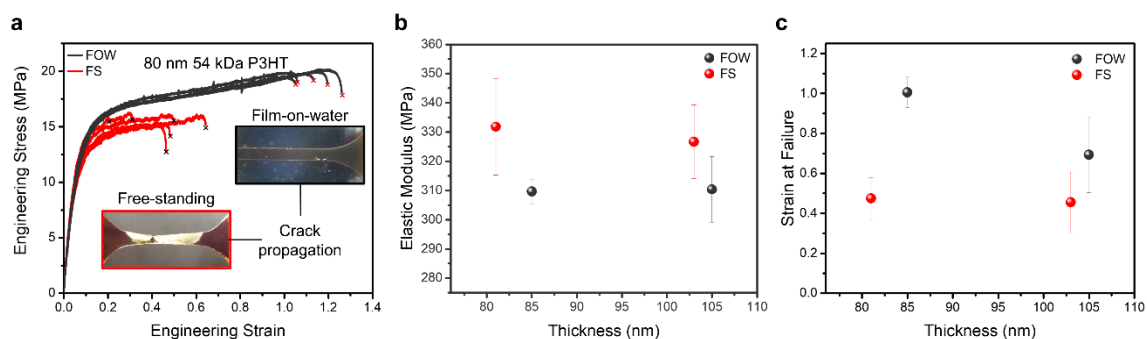
Figure 3.3 *Comparison of 25 kDa P3HT FS and FOW mechanical properties at ~105 and ~80 nm using the 8 mm gauge geometry. a) Representative stress vs strain profiles of 80 nm P3HT for both FOW and FS tensile test. Insert is an optical comparison of a FS and FOW P3HT at failure. b) Modulus and c) Strain at failure of P3HT in both FOW and FS measurements. Error bars represent the standard deviation of the characterized mechanical properties.*

Preliminary mechanics of PDPP-TT, a high-performance donor-acceptor (DA) CP, was also investigated at 75-nm in thickness for both methods **(Figure B.11(b))**. PDPP-TT possesses a variety of chemical functional groups **(Figure 3.1(c))**, different than PS or P3HT, which may lead to altered mechanical performance depending on interactions at the interface. Of most concern, is the carbonyl group which may form hydrogen bonds with water and potentially plasticize the film. However, similar modulus was observed between the two techniques and strain at failure was found to be slightly greater in the FOW measurements. Further investigation is necessary to confirm this, but preliminary results parallel our previous analysis on PS and P3HT polymers, where

60

modulus was observed to change less significantly than COS or YS. Thus, both methods are viable, particularly for modulus measurement, for DA polymers which often possess carbonyl functionalities. However, this is not to suggest that this would be the case regardless of composition, as side chain content and concentration of such functional groups differ considerably among synthesized CP's, such as hydrophilic functionality for bioelectronic applications.

3.3.3 Characterizing the presence of water

To ascertain the presence of water in these hydrophobic films (PS and P3HT), we utilized QCM and NR. QCM is a technique which can provide a qualitative understanding of both mass uptake and energy dissipation (change in stiffness) throughout the depth of a film with particular sensitivity towards the interface.[218,203] This is accomplished through tracking the response of multiple crystal harmonics (n) whereby low n harmonics correspond to regions closer to the film-water interface of interest and higher n harmonics probe the film-substrate interface. The QCM measurement was conducted with each film submerged in water, using the initial air response as a reference **(Figure 3.4(a-b))**. **Figure 3.4(c)** shows an immediate reduction in the normalized frequency shift ($\Delta f/n$) of 100-nm PS upon submersion. This shift corresponds to a gain in mass from the water which primarily occurs at the film-water interface given that the lowest harmonic $n = 3$ has the largest frequency shift. Furthermore, the full width half max (FWHM), which is a measure of the normalized energy dissipation ($\Delta D/n$), was found to increase towards the film-water interface, signaling a softening or plasticization effect from the water **(Figure 3.4(d))**. Throughout the experiment, there was a slow gain in mass and continuous softening of the film throughout its thickness. Upon drying, $\Delta D/n$

returns to the initial reference value, indicative of the reversibility of the transition. P3HT (100-nm) shows a rapid response and stabilization in water **(Figure 3.4(e-f))**. Most significant mass gain and softening occur near the film-water interface (indicated by lower n), suggesting a diffusion-limited process. Response is not reversible at low harmonics (3rd harmonic trace does not return to $\Delta f/n=0$ after removal from water), suggesting possible morphological or structural change during the interaction with water. QCM results confirm the presence of water within the bulk PS and P3HT films and indicates that water softens these hydrophobic films to some extent and does so primarily at the film-water interface. This may explain the 6% difference in modulus observed for P3HT FS and FOW measurements. In contrast, the value of modulus of PS thin film is relatively stable, even when strongly confined, and thus we consider the following possibilities. 1) Water may be penetrating through the film via pinhole defects originating through sample preparation. Given a small enough number of defects, the mechanical properties may not be influenced despite detection by QCM. 2) The softening effect shown by QCM may be small, and thus not influence the large modulus of PS. For example, an approximate reduction of 20 MPa was observed for the modulus of P3HT, but for PS this same reduction would be indistinguishable given the typical modulus of 3 GPa and uncertainty of ~ 100 MPa. Thus, glassy hydrophobic thin films with high modulus may be less influenced by diffusion of water. To investigate further, 90 nm and 70 nm PS films, 183 kDa and 2062 kDa respectively, were exposed to water for 48-hours prior to tensile measurement. Modulus and yield stress did not deviate significantly from the standard measurement, while strain at failure significantly increased in both cases **(Figure B.12)**. Although enhanced ductility is often a side effect of plasticization, the

small influence on modulus and yield stress suggests some other mechanism may be at work. This coincides well with the QCM response at 24 hours, where water uptake doubles but the energy dissipation (softening) remains relatively stable compared to the initial response upon submersion. Thus, the increase in water content at extended times and the subsequently greater ductility indicates that water mitigates crack propagation. In this respect, we chose to further explore NR which has high sensitivity with nanometer resolution in the film thickness direction, to quantify the uptake of water.
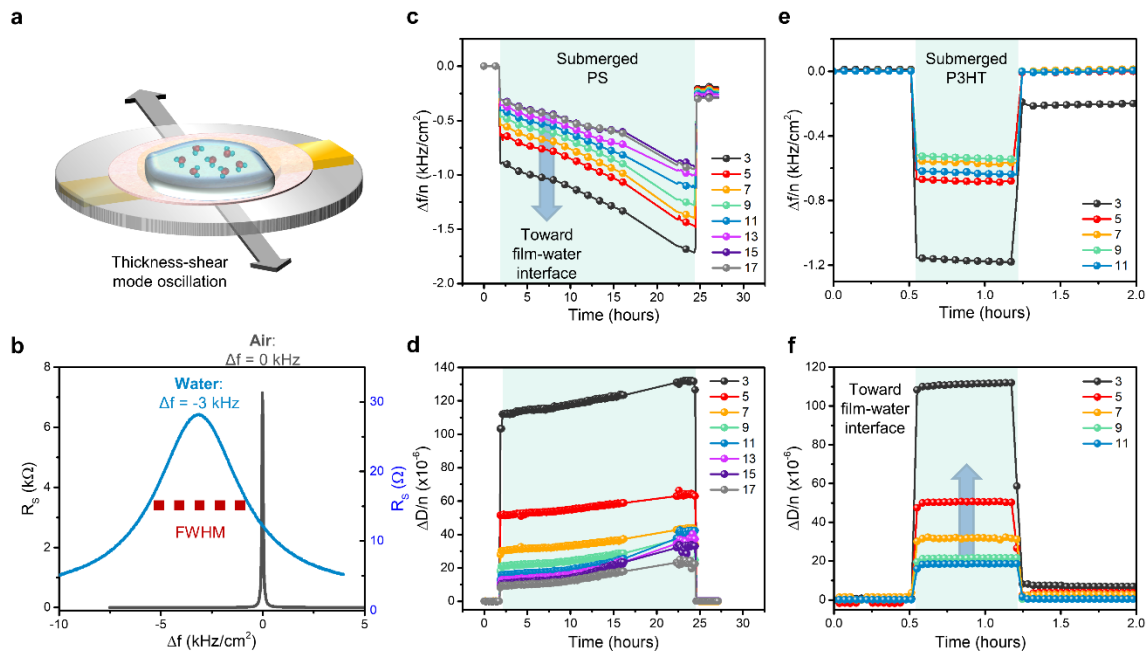
Figure 3.4 *Quartz crystal microbalance analysis of PS and P3HT films submerged in DI-water. a) Illustration of film (pink) on the quartz sensor submerged in water. b) Representative response of QCM coated with P3HT during transfer from air to water. FWHM corresponds to full width at half the maximum intensity. c-d) Normalized frequency shift and change in energy dissipation of ~ 100-nm PS submerged in water for 20+ hours. e-f) Normalized frequency shift and change in energy dissipation of ~ 100-nm P3HT submerged in water for ~ 40 minutes.*

To more accurately match the environmental conditions of our FOW tensile test, NR measurements were performed at room temperature with a 5x5 cm film floated onto a

water trough, thus mimicking the water-sample and sample-air interfaces present in the FOW test (**Figure 3.5(a-c)**). **Figure 3.5(d)** shows the NR results and best fits for PS with thickness ranging from 118 nm to 39-nm. Each film was interpreted using a two-layer model, layer 1 adjacent to the water interface (sublayer) and layer 2 adjacent to the air interface (top layer). This two-layer model was supported by the previous QCM analysis, which demonstrated the film-water interface to have the most significant response while higher n harmonics revealed a more gradual response. The thickness, scattering length density (SLD), and roughness of the layers were systematically varied and optimized until the sum of the χ^2-values for all the data points was minimized (**Table B.2** for fitting results).[206] The thickness of the films were determined by h = 2π/ ΔQ, where ΔQ is the wave vector difference between fringes. The obtained SLD profile is provided in **Figure 3.5(e)** and directly describes the water uptake within the films given the following equation:

$$ EQ\ 1 \qquad SLD_{film} = SLD_{PS} * (1-x) + SLD_{H2O} * x $$

where x represents the volume fraction of water within the film, and the calculated values for SLD_{PS} and SLD_{H2O} are $1.42*10^{-6}/Å^2$ and $-0.56*10^{-6}/Å^2$, respectively. Reflectivity data of the dry films (**Figure B.13**) demonstrated a reduction in SLD with thickness from $1.42*10^{-6}/Å^2$ to $1.33*10^{-6}/Å^2$, which was attributed to the growing contribution of the mobile interface. We observe a reduction in the SLD_{film} with decreasing thickness, from $1.321*10^{-6}/Å^2$ to $1.146*10^{-6}/Å^2$ for the 118 nm and 39 nm films respectively. These values correspond to an increase in the volume fraction of water, present in the top layer, from 5.04% to 9.79%, a significant amount given the

64

hydrophobicity of PS. This is in contrast to previous work on deuterated PS where no

water uptake was observed.[219] The primary difference between these measurements and
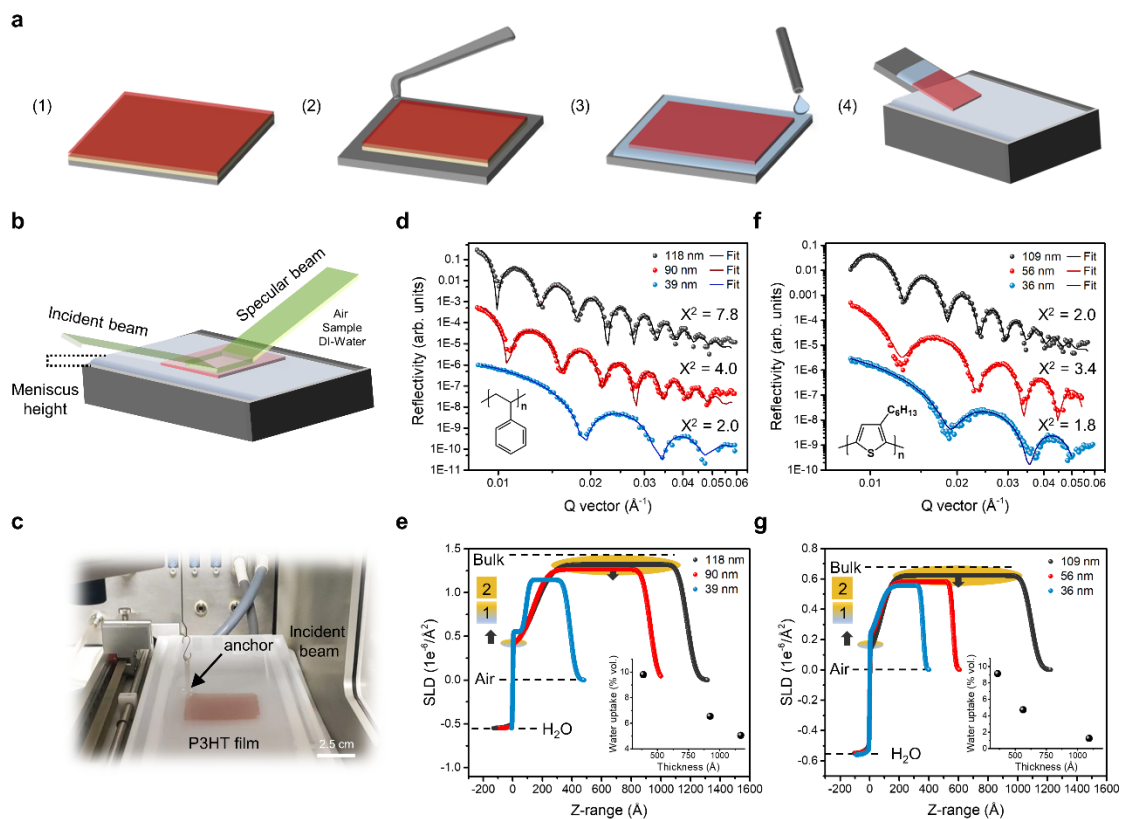
Figure 3.5 *Monitoring water uptake within PS and P3HT thin films via neutron liquid reflectometry. a) Sample loading with (1) spun cast composite film with PSS underlayer, (2) removal of film edge, (3) floating of film, (4) transfer into trough. b) Illustration of NR experiment with film floating on water surface. c) Photograph of a 5x5 cm P3HT film of 36-nm in thickness anchored within the DI-water trough. d) Reflectivity vs. wave vector for PS films of varying thickness. e) PS SLD profile in Z-direction. Insert is of PS water uptake dependence on thickness. f) Reflectivity vs. wave vector for P3HT films of varying thickness. g) P3HT SLD profile in Z-direction. Insert is of P3HT water uptake dependence on thickness. The shaded regions corresponding to the sublayer and top layer represent the layers 1 and 2 depicted in Figure 6.*

those reported by Tanaka and co-workers are the environmental conditions at the

interface of the polymer. The previous work was performed with deuterated PS supported

by quartz substrate, meaning that there is both an air-polymer and polymer-quartz

interface. In the current work, the polystyrene film is directly floated on water where two

mobile interfaces exist, air-polymer and polymer-water. This may facilitate water uptake given the potential for enhanced dynamics exhibited by both interfaces. Additionally, the uptake in water for PS is also supported by the previously discussed QCM results.   The water-film interface or sublayer is more complex, as an increase in SLD is observed (0.361 to $0.552*10^{-6}/\text{Å}^2$) with reducing thickness. We attribute this to a reduction in roughness with decreasing film thickness (**Table B.2**), as greater roughness will raise the apparent water concentration across the film interface leading to the lower SLD. Time-dependent measurements were also conducted with the same PS films after a 4-hour exposure to water. No significant changes were observed in the thicknesses of the films, and SLD_{film} exhibited a marginal reduction (**Figure B.14**). This stability supports the QCM findings, indicating that the diffusion of water into PS films is relatively slow after the initial exposure to the surface.

Similarly, P3HT was also studied using NR with film thicknesses from 109 to 36-nm (**Figure 3.5(f-g)**). The results are comparable to those of PS. We observe a reduction of the SLD_{film} from 0.622 to $0.558*10^{-6}/\text{Å}^2$ with decreasing thickness which corresponds to water volume fractions of 1.24 and 9.13%, respectively. Thus, from QCM and NR, we were able to confirm that water does penetrate these hydrophobic films and that plasticization, and its effect on modulus, is relatively small at the film thicknesses used in our mechanical measurements. This fact is illustrated in **Figure 3.6** where water primarily resides near the rough film-water interface but also diffuses throughout the film with a decreasing gradient. We hypothesize that the water primarily lies within voids throughout the film but does not significantly swell adjacent polymer chains, given the slight influence on modulus as previously observed. However, the presence of water

within these films, especially the increased volume fraction observed at low thicknesses, supports the claim that water is responsible for the elevated COS and YS found throughout our FOW tensile measurements.
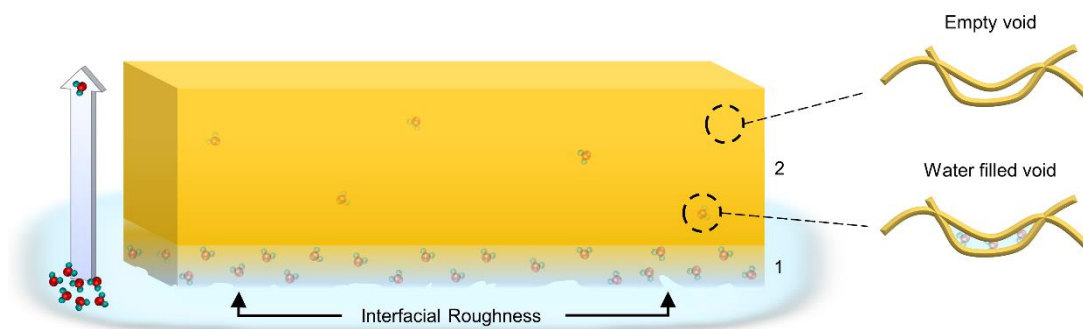
Figure 3.6 *Illustration of water residing within a representative hydrophobic film, with the majority of water present at the relatively rough polymer-water interface. Layer 1 depicts decreasing water content with increasing distance from the film-water interface followed by a reduced water content in layer 2. "Wet" and "dry" polymer chains are depicted on the right, illustrating that the water resides within pre-existing voids throughout the film and does not swell the polymer chains.*

3.4 Conclusion

In this work we have introduced the SMART method to measure FS thin-film mechanics. First, the influence of confinement on FS PS thin films was explored. Despite heavy confinement, only the thinnest FS PS film of 19 nm demonstrated a reduction in modulus (10%). Our results indicate that film modulus is dependent upon a mobile interface rather than geometric confinement below R_{ee}. This is in contrast with previous reports of high molecular weight 20 nm FS PS films exhibiting sub-room temperature T_g. However, yield stress and strain at failure show a transition to lower and higher values, respectively, when confined below the R_{ee}. Second, the difference between FS and FOW mechanics was then explored for three polymer systems (PS, P3HT, and PDPP-TT) representing both stiff glassy and soft viscoelastic materials. Modulus and yield stress did

67

not differ considerably between the two measurements, while strain at failure were consistently greater for the FOW measurements. This difference increased with both softer polymer films (P3HT) as well as increased water exposure time (PS). Despite the hydrophobic nature of these films, water content as high as 9.79% by volume was observed with a primary contribution occurring at the film-water interface. Upon tensile strain, the water interface provides force delocalization resulting in elevated yield stress and strain at failure. This SMART technique provides a new means of studying the mechanics of thin films and 2D materials inaccessible to existing techniques.

CHAPTER IV – ROLE OF HYDROGEN BOND STRENGTH ON

THERMOMECHANICS AND MORPHOLOGY

(Adapted from "Galuska, L. A.; Ocheje, M. U.; Ahmad, Z. C.; Rondeau-Gagné, S.; Gu, X. Elucidating the Role of Hydrogen Bonds for Improved Mechanical Properties in a High-Performance Semiconducting Polymer. Chem. Mater. 2022, acs.chemmater.1c04055.")

4.1 Introduction

Electronics are getting more interconnected and integrated to everyday objects through flexible and conformable devices in order to grow an expansive quantity of data, the interest and need for mechanically robust materials has been steadily increasing.[13,48,220–224] As improved mechanical properties result in devices with increased lifetimes, new materials are currently being developed to confer emerging electronics with the ability to be incorporated into (and onto) more complex topographies. Among the different electroactive materials that can be used to fabricate and develop stretchable/flexible electronics, organic π-conjugated polymers are particularly promising. Compared to their inorganic counterparts, these organic semiconductors have the advantage of possessing superior thermomechanical properties that can easily be modified and enhanced even further.[225–228] Recent π-conjugated polymers have also been shown to possess good charge transport and the possibility of being deposited in solution, opening new avenues for the large-scale manufacturing of soft electronics.

Many strategies have been implemented by researchers to develop semiconducting polymers capable of accommodating large strains and with favorable thermomechanical properties.[229–231] One popular method is to blend the semiconducting

material with soft and stretchable elastomers. Many recent examples focus on this physical blending with poly(dimethylsiloxane) (PDMS), styrene-ethylene-butadiene-styrene (SEBS), polyethylene (PE), or butyl rubber (BR) to control and improve the thermomechanical properties of rigid semicrystalline semiconducting polymers, principally occurring through a nanoconfinement of the conjugated polymer chains in a soft matrix.[85,141,195,232–234] This method is straightforward, but comes with the inherent disadvantage of introducing insulating material into the active layer of an electronic device.

To circumvent this drawback, strategies for the synthesis of intrinsically stretchable conjugated polymers through precise molecular engineering have been explored in the recent literature.[87,235–237] Performed through the insertion of bulky soft side chains or through the utilization of conjugation breaking units, the molecular design of π-conjugated polymers is an effective approach to generate materials with increased amorphous content, reduced crystallinity and improved resistance to mechanical failure all while maintaining good charge transport properties. One particularly promising approach to generate intrinsically stretchable semiconducting polymers with new properties is through the utilization of dynamic supramolecular interactions. Non-covalent interactions, either inserted on the polymer's side chains or backbone, have been shown to significantly impact the polymer solid-state morphology and to help tensile strain dissipation and chain alignment upon strain. Among the different types of noncovalent interactions used in semicrystalline conjugated polymers, hydrogen bonds have been especially investigated. For example, Oh *et al.* implemented a backbone engineering approach by synthesizing and incorporating a pyridine dicarboxamide

(PDCA) moiety as a conjugation-break spacer into DPP-based polymers.[238] Although the charge mobility decreased slightly with increasing incorporation of these non-conjugated segments, the novel polymers still exhibited high stretchability as well as high conductivity, achieving a hole mobility of greater than 0.1 $cm^2V^{-1}s^{-1}$ while being stretched to 100% elongation and demonstrated their viability in fully functional, fully-stretchable devices. In a similar manner, Gasperini *et al.* expanded on this work by instead using the PDCA unit in side-chain engineered DPP polymers.[239] Through extensive characterizations, they showed that the location and the amount of hydrogen-bonding units in conjugated polymers have an important influence on the thermal and mechanical properties. Finally, hydrogen bonding has been shown to lead to particularly impressive charge transport values in organic field-effect transistors (OFETs).[240,241]

Although the use of hydrogen bonds to dissipate tensile strain is a strategy that has been employed to great effect, some challenges remain to fully unveil and predict their influence on the optoelectronic and thermomechanical properties of high-performance semiconducting polymers. First, only a relatively low content of hydrogen-bonding moieties (typically between 10-20 mol%) can be typically incorporated in semiconducting polymers through side chain engineering to avoid a drastic reduction of the polymer solubility, which makes a direct observation and quantification of the effect of these hydrogen bonds on the thermomechanical properties rather challenging. Moreover, most techniques used to evaluate the thermomechanical properties of conjugated polymers in ultrathin films rely on support (elastomer or water), which can influence the formation of intermolecular hydrogen bonds. Finally, the effect of moisture on these materials in the solid-state is still not well known and difficult to control.

71

Herein, an in-depth characterization of semiconducting polymers incorporating urea and amide moieties allowing for intermolecular hydrogen bonding is performed to fully unravel the impact of hydrogen bonds on the optoelectronic and thermomechanical properties of semicrystalline π-conjugated polymers. A careful investigation of the effect of water molecules on hydrogen-bond functionalized DPP-based conjugated polymers is also performed by using a shear motion-assisted robust transfer method for fabricating free-standing ultrathin films, thus allowing for the direct observation and quantification of the effect of water on the mechanical properties of intermolecularly hydrogen-bonded films. Our work suggests that hydrogen bonding strength alone is not a good indicator of mechanical performance. The resulting influence on crystalline packing plays a significant role in performance and may out way any benefit provided via energy dissipation of hydrogen bonds.

4.2 Experimental

4.2.1 Materials

DPP-TVT based polymers were synthesized as previously described.[242] Nuclear magnetic resonance (NMR) spectra were recorded on a Bruker 300 MHz with variable temperature controller and are available in **Figures C.10-C.12**. Spectra for polymers were obtained in deuterated 1,1,2,2-tetrachlotoethane (TCE-d_2) at 120°C. High temperature GPC at 160°C, with trichlorobenzene as the eluent, was utilized to obtain the molecular weight and distribution of the polymers. Poly(sodium 4-styrenesulfonic acid) (PSS) was obtained from Sigma-Aldrich at a molecular weight of 75 kDa in 18% by volume aqueous solution and diluted to 3% for spin casting.

4.2.2 Film preparation

All polymers were dissolved at 7 mg/ml in chlorobenzene at 80 °C overnight. For all measurements, the polymer solution was spun cast at 2000 rpm for a minimum of 2 minutes onto plasma treated silicon wafer.

4.2.3 Pseudo-free-standing tensile test

Uniaxial tensile tests were performed on top of a supporting water bath as described in our previous publication.[142] Composite films were first created by spin coating the polymer solution onto a sacrificial PSS layer. The PSS layer was formed by spin coating at 4000 rpm for 2 min. The composite films were then laser etched into dogbone geometries with a gauge width of 2 mm and length of 8 mm. Individually, the dogbones were dipped into water, dissolving the PSS sacrificial layer, and subsequently attached to a linear stage and load cell. A strain rate of $5*10^{-4}s^{-1}$ was then applied until the film broke. Force data was collected at a frequency of 10 Hz.

4.2.4 Free-standing tensile test

Uniaxial tensile tests were performed in air via the SMART technique as described in our previous publication.[86] A composite film is laser etched into a dogbone geometry (4 mm long, 2 mm wide) with an outer film support connected by etched microfibers. The composite film is then loaded onto a motorized stage at which water is deposited at the parameter of the film causing the PSS layer to dissolve and lift the film of interest. The film is then connected to the linear stage and load cell followed by translation of the motorized stage at 0.15 mm/s. This enables the film to be sheared from the water surface and into an air environment. The side supports are then removed, and

73

the film is ready for the tensile measurement. This was performed at the same strain rate as previously described.

4.2.5 Ellipsometry characterization

Ellipsometry was performed with a M-2000® UI Ellipsometer from J.A. Woollam. Dry films were measured from 55°-75° at increments of 5°. Each angle was scanned for 2 seconds with a wavelength range from 245-1700 nm. To assist in the model development each film was spun cast onto a thermal oxide layer of ~500 nm to provide interference enhancement for increased sensitivity to absorbing films.[38,243] The oxide layer was measured prior to spin coating to ensure an accurate thickness of each layer. The data was modeled in CompleteEase software package. The samples were initially modeled using an anisotropic B-spline to establish a reference model. The B-spline was then converted to a series of gaussian oscillators (Gen-Osc) to minimize the number of variables required to fit the data and thus obtain an accurate assessment of the film optical constants and thickness. In the case of the composite films for tensile testing, the PSS layer was first measured followed by the composite film. The PSS layer was modeled using an isotropic Gen-Osc model. Thus, the model for the composite film uses known thickness from the PSS layer and allows for facile calculation of the thickness of the active polymer layer.

The *in-situ* film swelling experiments were performed at 23°C using a 500μL variable temperature liquid cell at a fixed incidence beam angle of 70°. The modeled wavelength range was reduced to 245-1100 nm due to the absorption of water in the infrared regime. Given this reduced spectral range, each film was spun cast onto a thermal oxide layer of known thickness for the swelling measurement. The films were

exposed to de-ionized water for a period of 24 hours and measured every 2 seconds. The H$_2$O Pribil (temperature library) material file provided in the CompleteEase software package was used to model the ambient environment. Less than 20 parameters were allowed to vary with time to appropriately model the data yielding excellent fidelity.

Temperature dependent ellipsometry measurements were performed using a Linkam heat cell at an incidence angle of 70° while under a nitrogen atmosphere. Unlike the swelling measurements, the full spectral range (245-1700 nm) is assessable with the heat cell to increase model fidelity. Each polymer was heated to 300°C to remove thermal history from spin coating and subsequently cooled to -25°C at a rate of 5°C/min. The data was fitted with the previously described GEN-Osc models along with a material file of the silicon substrate and thermal oxide layer with known optical constants across the temperature profile. The oxide thickness was held constant. This helps to ensure accurate modeling of the film of interest as the optical constants of the substrate and interference oxide layer were already accounted for. The T_g was obtained from the cooling ramp based on the change in slope of the thickness dependence on temperature.

4.2.6 Grazing incidence wide angle X-ray scattering (GIWAXS)

GIWAXS was performed using a Xenocs Xeuss 2.0 SAXS/WAXS lab source instrument. All samples were exposed under vacuum for 2 hours with an incident beam energy of 8.05 keV, an incident angle of 0.2°and a beam geometry of 0.8×1.2 mm. The sample-to-detector distance was approximately 154 mm as determined by fitting a silver behenate standard. The 1D data and peak fitting were processed using Nika and WAXS tools software packages within Igor Pro from Wavemetrics.

The rDoC was determined as previously described from literature. [244,245] The (200) scattering peaks were fitted to determine the Q vector from each polymer sample. A pole figure analysis was then performed using the WAXS tools software package within Igor Pro to determine the integrated intensity across all crystalline orientations. Each pole figure was centered at the fitted Q vector of the representative sample with an analysis width of 0.2 Å^{-1}. Background scattering was then subtracted and the intensity across each azimuthal angle (χ) was normalized by thickness, exposure time, and beam path length. A geometric correction, $\sin(\chi)I(\chi)$, was then applied to obtain the relative orientation of the crystallite followed by integration of the area below each curve.

4.2.7 Strain dependent charge transport measurements

Conjugated polymer semiconductors were processed through transfer printing according to the method described by Bao and co-workers.[9] First, the polymer inks were spun cast onto octadecyltrimethoxysilane (OTMS)-modified silicon wafers[41] and annealed at 150°C for 10 minutes in a nitrogen filled glovebox with <0.5 ppm of both O_2 and H_2O. Next, the annealed films were transferred onto a rectangular slab of poly(dimethylsiloxane) (PDMS) elastomer (base: crosslinker ratio = 20:1 w/w, crosslinked overnight at 70 °C in an oven). Each transferred film was stretched to a particular strain between 0-75% and subsequently transferred back to a p^+-doped 300 nm SiO_2 OTMS-modified wafer. Following film transfer, 50 nm of top contact Au source and drain electrodes were evaporated onto the wafers through a stencil shadow mask with 100 μm channel length and 1000 μm channel width oriented both parallel and perpendicular to the strain direction. The completed devices were then brought into the glovebox for testing with a Keithley 4200-SCS analyzer. Mobility calculations were

performed in the saturation regime through linear fitting of the square root of drain

current vs gate voltage, and inputting into the equation $\mu_{sat} = 2L/CW\ (\delta(I_D)^{1/2}/\delta V_G)^2$.

4.3 Results and Discussion

4.3.1 Mechanical analysis via supporting mediums

Here we discuss the thin film mechanics of four DPP-TVT based polymers

(**Figure 4.1 and Table 4.1**). The polymers consist of DPP-TVT copolymer and three

statistical copolymers with either linear alkyl, amide, or urea moieties incorporated at 10

mol% ratio in the sidechains. Detailed synthesis of those four polymers can be found in

the supporting information. These alterations to the DPP-TVT parent polymer have three

primary modes of influence, namely 1) Interfacial interaction with supporting medium, 2)

morphological changes and particularly to the crystalline domain and 3) chain dynamics

or the glass transition phenomena, all of which dictate mechanical performance.
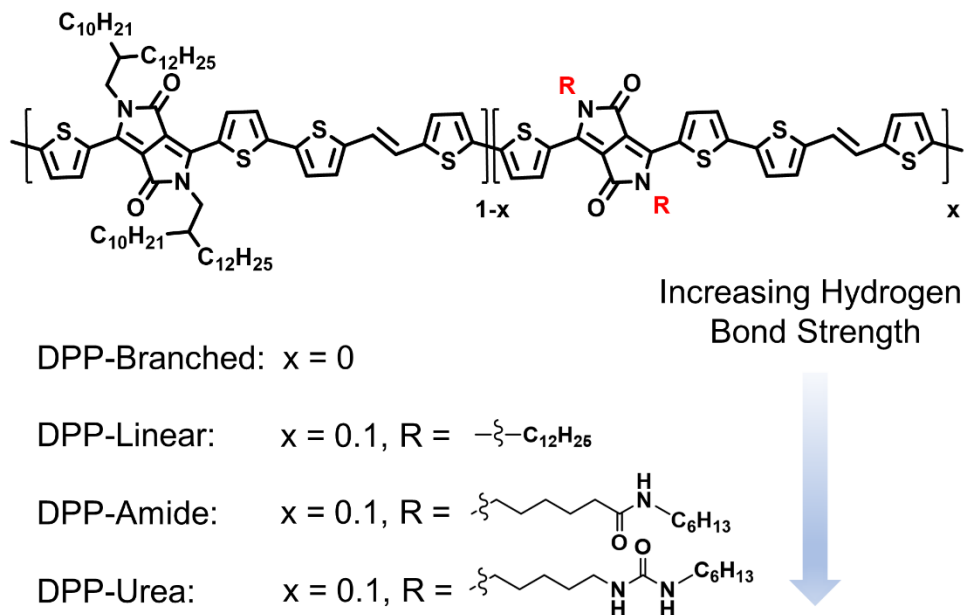
Figure 4.1 *Chemical structures of DPP-TVT based conjugated polymers investigated in this study.*

We note that there are several factors that should be carefully evaluated to compare the mechanical property of hydrogen-bonded conjugated polymers. Firstly, when dealing with ultra-thin films it is paramount to understand how the measurement process dictates the observed mechanical properties. The supporting interface may either stiffen or soften a polymer film depending on their interaction.[246] As this work relies on water as a support, increased hydrogen bonding may result in plasticization at the film-water interface and lead to a reduced modulus. However, this is unexpected for the measurement as the concentration of hydrogen bonding moieties is limited to 10 mol% incorporation and the contact time with water is less than 5 minutes. Secondly, statistical copolymers are likely to have reduced modulus as random incorporation disrupts the crystalline packing behavior resulting in increased amorphous content.[81,247,248]The intermolecular interactions of hydrogen bonding may further disrupt or promote the packing behavior, as previously observed for amide and urea incorporation, respectively.[59,240] Lastly, hydrogen bonding is expected to increase the glass transition temperature (T_g), reducing the conformational freedom of the system, resulting in increased modulus. Additionally, H-bonding offers additional routes for energy dissipation which may increase ductility.

Table 4.1 *Polymer material and mechanical properties*

Polymer	M_n(kDa)	Đ	E (MPa)	SAF[b]	COS[c]
Branched	29.0	3.1	$380.7_{(21.9)}$[a]	$0.10_{(0.03)}$	N/A
Linear	31.4	4.2	$416.7_{(5.4)}$	$0.09_{(0.01)}$	0.25
Amide	35.7	2.1	$357.4_{(18.5)}$	$0.22_{(0.02)}$	0.5
Urea	31.3	1.8	$371.6_{(7.4)}$	$0.05_{(0.01)}$	0.5

[a] Standard deviation from a minimum of four individual tensile measurements. [b] Abbreviation for strain at failure. [c] Abbreviation for crack onset strain.

The film-on-water tensile test was first used to assess the mechanics of these polymers in the thin film state. This technique can be found in our recent review article.[246] **Figure 4.2(a)** shows representative stress-strain profiles for each polymer under an applied strain rate of $5*10^{-4}s^{-1}$. All polymers demonstrate similar elastic modulus with a trend in average modulus as follows: DPP-Linear > DPP-Branched > DPP-Urea > DPP-Amide > **(Figure 4.2(b))**. The increased modulus for DPP-Linear over the branched counterpart was expected given the reduced side chain content which acts as an internal plasticizer.[24] Interestingly, DPP-Amide and DPP-Urea demonstrated a lower modulus than DPP-Linear despite their ability to form hydrogen bonds which would result in an increased T_g. This implies that either the influence of water or their crystalline structure may be responsible for the reduced modulus. In terms of DPP-Amide and DPP-Urea, their modulus agrees with the expected trend in hydrogen bond strength. The strength of hydrogen bonding can be quantified by the hydrogen bonding cohesion parameter which is 25.5 $(J/cm^3)^{1/2}$ and 34.2 $(J/cm^3)^{1/2}$for amide and urea moieties respectively.[249] The difference in ductility of these films was pronounced

79

(Figure 4.2(c)). DPP-Amide demonstrated the highest strain at failure of 22% followed by DPP-Branched at 10%, DPP-Urea at 5%, and DPP-Linear at 3%. This was quite interesting as DPP-Urea exhibited poor ductility despite having the greatest hydrogen bonding strength.

One question that emerges is the influence of water on the previous film-on-water tensile test, as increased hydrogen bonding moieties may result in plasticization by the water support. In our previous work DPP-Amide was observed to have a lower modulus than DPP-TVT attributed to reduced crystallinity as a result of intermolecular hydrogen bonds.[59] Verification of such hydrogen bonds was performed via FTIR and NMR analysis.[242] The same trend in modulus was observed for both the film-on-water technique and nanoindentation. This indicates plasticization by water is not the reason for the reduced modulus in the statistical copolymers relative to DPP-Branched.

To explore this further, we performed two additional thin film tensile measurements to preferentially exclude or exacerbate the interaction of the hydrogen bonds with the supporting media. First, tensile measurements using the film-on-elastomer method were used to assess the ductility of each polymer **(Figure 4.2(d))**. In this method the potential energy dissipation provided by the hydrogen bonds should be fully available resulting in extended ductility. Like the film-on-water measurement, the crack onset strain (COS) was greatest for DPP-Amide, with an even greater value of ~ 50% strain. In contrast to the film-on-water measurement, DPP-Urea exhibited increased ductility, like that of DPP-Amide, which was attributed to the energy dissipation provided by the urea moieties. Second, we kept each polymer film on water for a period of 24 hours prior to

a | **b** | **c**

d

Stretching direction
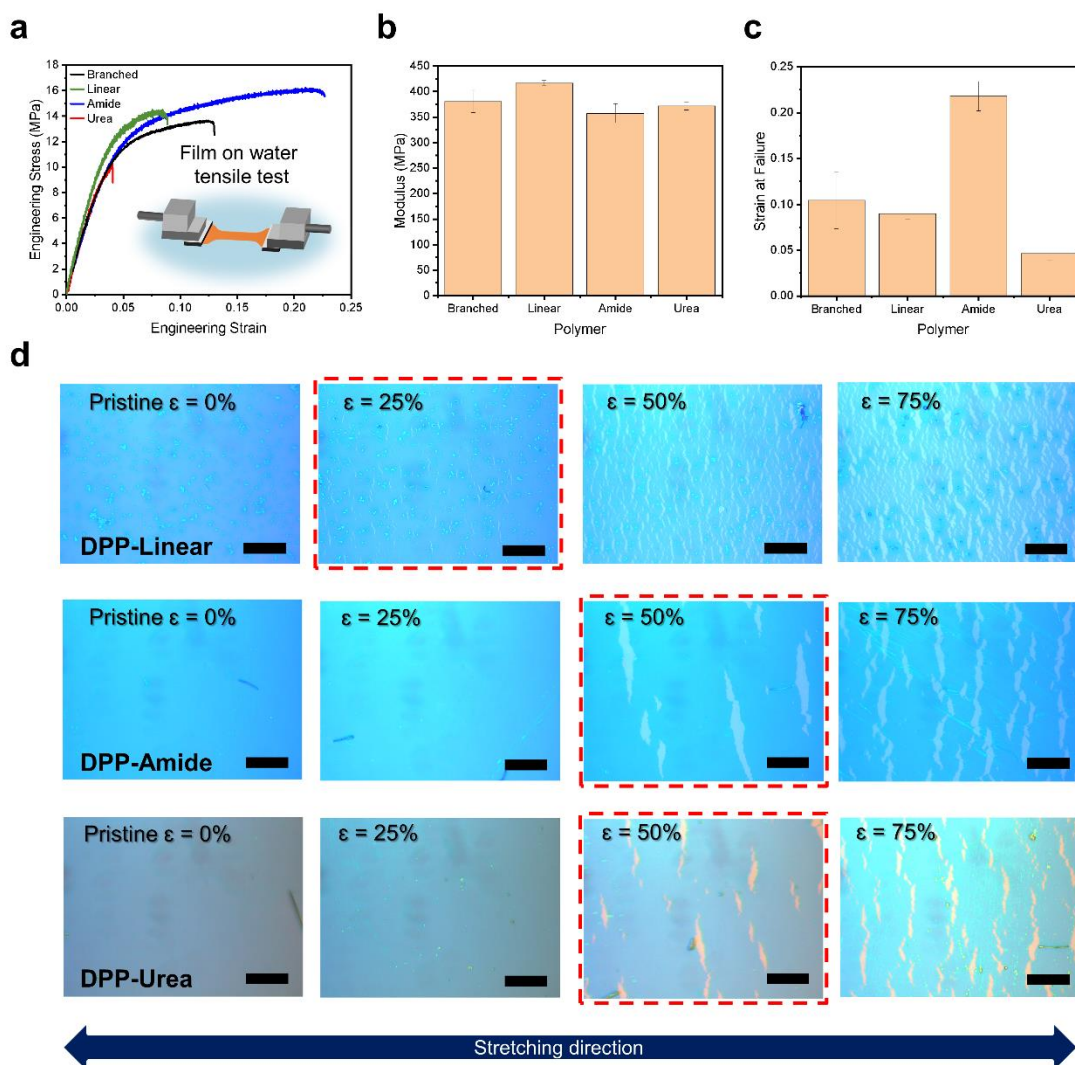
Figure 4.2 *Thin film mechanical properties as measured by the film-on-water and film -on -elastomer techniques. (a) Representative stress-strain plots of DPP-TVT-based polymers. Insert is an illustration of the film on water tensile measurement. (b) Modulus of each polymer measured in the standard film-on-water process. (c) Strain at failure of each polymer measured in the standard film-on-water process. (d) Representative optical images of the three statistical copolymers strained via the film on elastomer technique. The dashed red outline indicates the crack onset strain for each polymer. Scale bar is 25 microns. Error bars represent the standard deviation of the data from a minimum of four consecutive measurements.*

tensile testing **(Figure C.1(a))**. All the polymers exhibited a reduction in modulus, and

this was most dramatic in the case of DPP-Amide films **(Figure C.1(b))**. DPP-Amide

exhibits a 34% reduction in modulus while DPP-Urea, DPP-Branched, and DPP-Linear

exhibit a 23%, 20%, and 28% reduction respectively. Despite the reduction in modulus, DPP-Amide exhibits near identical strain at failure relative to the conventional film-on-water method **(Figure C.1(c))**. Given that the hydrogen bonds are likely disrupted by the presence of the water, as evidenced by the reduced modulus, it is unlikely that energy dissipation via hydrogen bond disassociation is solely responsible for the high ductility of DPP-Amide. Rather, we surmise that the full impact of these hydrogen bonds lies within the initial film formation through disruption of the crystalline morphology and promotion of amorphous entanglements. In contrast, DPP-Urea exhibited both low and high ductility depending on the measurement condition. This indicates two competing mechanisms which dictate its mechanical performance, that is, energy dissipation via hydrogen bonding (increasing ductility) and potentially high crystallinity (reducing ductility). In the case of the film-on-water measurement, hydrogen bonds were disrupted resulting in crystallinity dictating the films ductility.

To further elucidate the mechanism by which hydrogen bonding influences the mechanics, we explored the free-standing mechanics, followed by the swelling behavior, morphology characterization with an emphasis on the crystalline packing, glass transition temperature, and strain dependent charge transport.

4.3.2 Free-standing Measurements

To assess the water molecule's potential influence on the mechanical properties we performed fully free-standing tensile measurements of DPP-Amide. The general exposure time during the film-on-water method is approximately 5 minutes, where the water could impact thin film mechanics. The free-standing films (in air) were obtained via the shear motion assisted robust transfer method (SMART) outlined in our previous

publication.[86] DPP-Amide, 80 nm in thickness, was successfully transferred and measured using the SMART technique **(Figure 4.3(a) and Movie C.1)**. DPP-Urea was also attempted but failed due to its brittle nature and limited thickness **(Movie C.2)**. Figure 3b shows the representative stress-strain profile of DPP-Amide obtained from the free-standing tensile tests relative to the film-on-water and post 24-hour measurements. The modulus was observed to be identical for the free-standing and film-on-water methods **(Figure 4.3(c))** while the strain at failure was reduced. Such a trend was previously observed for free-standing polystyrene films and attributed to a crack mitigation mechanism provided by the water interface.[76,86]

a

b

c
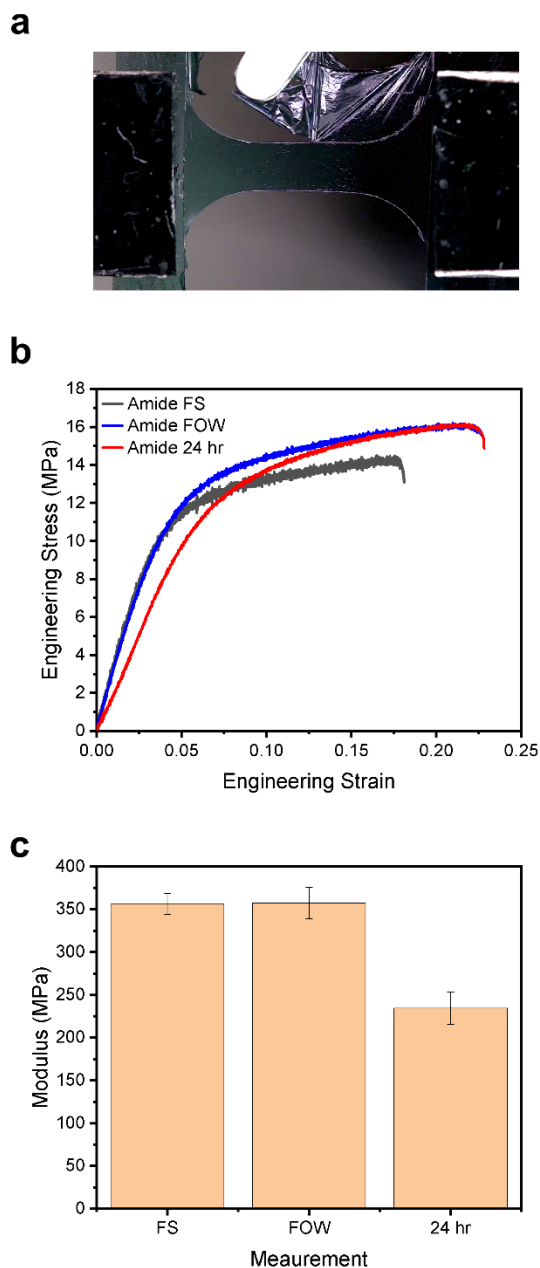
Figure 4.3 *Free-standing tensile measurement and comparison with the film on water techniques. (a) Optical image of a free-standing (in air) DPP-Amide 80nm film with side supports being re-moved prior to the tensile measurement. (b) Representative stress-strain plots comparing the three tensile measurements for DPP-Amide. (c) Modulus comparison of DPP-Amide films measured in the free-standing environment, film on water, and after prolonged exposure to water. Error bars represent the standard deviation of the data from a minimum of four consecutive measurements.*

4.3.3 Swelling Measurement

The swelling of polymer films was assessed over a 24-hour period using *in situ* ellipsometry in an aqueous environment **(Figure 4.4(a))**. In this experiment, we spin coated conjugated polymers onto silicon substates with a 500nm silicon dioxide layer and sealed the film in a liquid cell filled with deionized water and monitored film thickness change continuously. Ellipsometry uses two components of polarized light, Ψ and Δ, to obtain high sensitivity to film thickness and optical constants. Ψ is the ratio of the amplitude change of the polarized light while Δ is the phase difference. Representative raw data for Ψ is shown in **Figure 4.4(b)** for DPP-Amide. There is a slight red shift of the data from 0 to 24 hours which indicates a small increase in thickness. The raw Ψ and Δ data were successfully fitted using an anisotropic model consisting of a series of gaussian oscillators to appropriately model the data with low mean square error (MSE) and statistically unique thickness **(Figures C.2(a))**.[42] The modeled thickness profiles for each polymer film are shown in **Figure C.2(b)**. We observed a notable difference in swelling behavior with increased hydrogen bond strength **(Figure 4.4(c))**. DPP-Branched exhibited low swelling over 24 hours and had the slowest initial swelling rate. This indicates that the interaction between DPP-Branched, and water was relatively limited. Linear DPP has an accelerated swelling rate and plateaus with a swelling of 2.8%. Such an increase in the swelling behavior can be attributed to the relative increase of carbonyl functionality as the side chain content is reduced from the branched to linear motif. DPP-Amide exhibited the highest swelling of 3.5% and demonstrated a high initial swelling rate. In contrast, DPP-Urea has the most rapid initial swelling, but plateaus in less than 1 hour. The initial rapid swelling by DPP-Urea is attributed to the stronger hydrogen bond

85
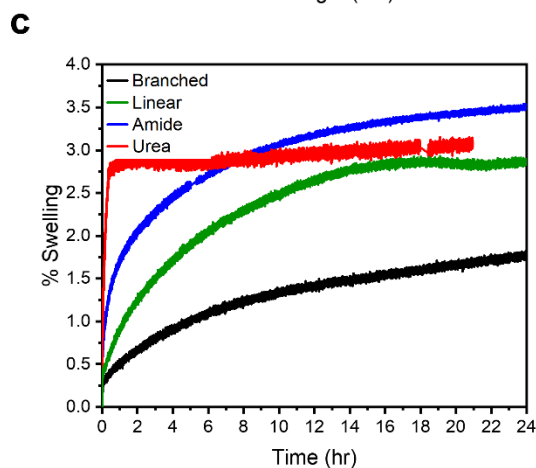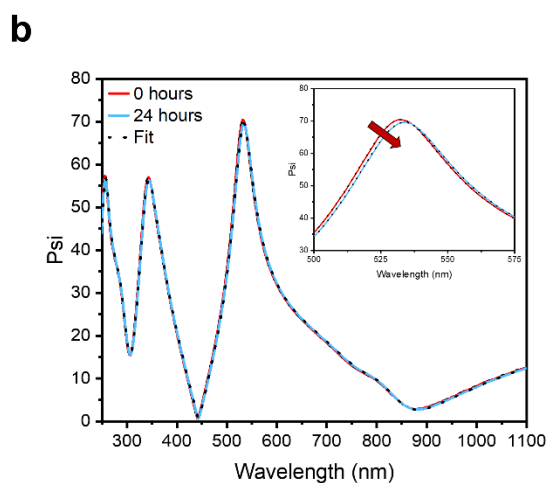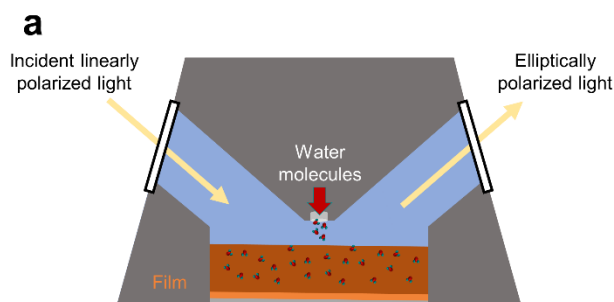
Figure 4.4 *Thin film swelling as measured by ellipsometry in an aqueous environment. (a) Illustration of the liquid cell measurement to monitor film water uptake. (b) Comparison of the raw Psi data for DPP-Amide upon initial water contact and after 24 hours. The insert demonstrates the red shift of the Psi peak at ~ 530 nm indicating a small increase in thickness. (c) Percent swelling occurring in each film throughout 24 hours of exposure to a water environment at room temperature.*

interaction of urea moieties with water. It has been observed that upon addition of water, urea dimers are destroyed due to the preferential association between urea and water.[250] Given that our tensile measurement requires approximately five minutes of exposure of the film to water, DPP-Urea would exhibit over half of its swelling in this time. Thus, such a rapid initial swelling may result in plasticization leading to the reduced modulus exhibited by DPP-Urea in the film-on-water tensile test. The plateau in the swelling of DPP-Urea indicates that there are no more urea moieties assessable to the water. This seems counterintuitive as we would generally expect a greater degree of swelling to occur given the increase in hydrogen bonding functionality. However, the inclusion of urea moieties has been known to promote crystallization in DPP-based polymers which would decrease the available urea moieties for plasticization as the penetration of water into such crystalline regions may be diffusion limited.[240] This hypothesis agrees with our mechanical property observations in that DPP-Amide shows not only greater ductility than DPP-Urea but also a more dramatic reduction in modulus upon extended exposure to water, both of which may be attributed to reduced crystallinity. Additionally, we were able to extract the thin film optical constants throughout the swelling process **(Figure C.2(c))**. There is negligible change to the absorption profile of these polymers even after 24 hours of exposure to water. This indicates that plasticization of water does not significantly influence the conjugated polymer backbone but lies solely on the side chain as is expected. It is also worth noting, all the polymers studied here consisted mostly of branched alkyl sidechains, thus rendering a hydrophobic film. Thus, all the films showed limited swelling which is in agreement with previous neutron reflectivity data for thin film floated on a water surface.[86]

87

4.3.4 Influence of hydrogen bonding on morphology and dynamics

The crystalline packing of each polymer film was assessed through grazing incidence wide angle X-ray scattering (GIWAXS). All polymers exhibited similar alkyl and π-π scattering peaks with D-spacings on the order of 22Å and 3.6Å, respectively **(Figure C.3-C.4 and Table C.1-C.2)**. This is not unexpected as the only difference lies in the statistically incorporated side chain moieties at 10% concentration. What does change however is the orientation of the crystalline packing and the relative degree of crystallinity (rDoC). The crystalline orientation is primarily edge-on for DPP-Branched, DPP-Linear, and DPP-Urea, while DPP-Amide exhibits a more isotropic orientation. To further assess the packing behavior, we performed a pole figure analysis of the (200) scattering peaks to obtain the rDoC of each polymer.[244,245] The rDoC is highly related to the mechanical performance of the films whereby a higher rDoC would be expected to yield a higher modulus and reduced ductility. Relative to pure DPP-Branched, with an assigned rDoC of 1, DPP-Linear and DPP-Urea observed an increase in the rDoC to 1.18 and 1.48 respectively. In contrast, DPP-Amide demonstrated a reduction in the rDoC to a value of 0.95 **(Figure 4.5)**. The trend in rDoC strongly matches the ductility of these polymers. For example, DPP-Amide and DPP-Branched exhibited the highest ductility's yet have the lowest rDoC values. The trend in modulus matched that of the rDoC for all the polymers expect DPP-Urea which exhibited the highest rDoC yet possessed a reduced modulus relative to DPP-Branched and DPP-Linear. This further confirms the plasticization of DPP-Urea by water molecules.

We further asses the crystalline packing of each film by exposure to water for 24 hours followed by GIWAXS measurement in the dry state **(Figure C.3-C.4 and Table**

C.1-C.2). The purpose was to determine if there was any influence of the water on the crystalline nature of these films. We observed an increase in the rDoC of these films which decreased with increasing hydrogen bond strength. DPP-Urea exhibited the only reduction in rDoC. The change in rDoC was attributed to plasticization by water over the 24 hr exposure period. This further supports the previous trends in mechanics and swelling behavior.
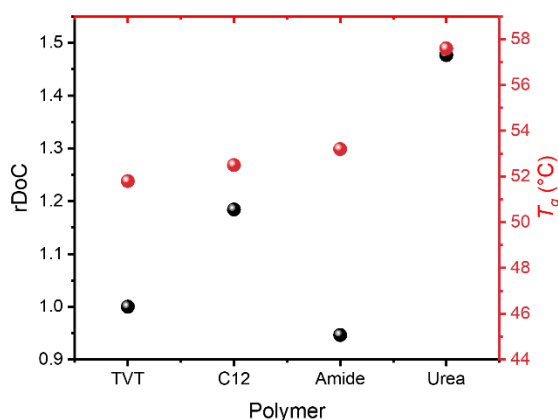
Figure 4.5 *Relative degree of crystallinity and glass transition temperature of each polymer measured by GIWAXS and temperature dependent ellipsometry respectively.*

Glass transition temperature is a primary parameter which governs conjugated polymer mechanical performance. As T_g increases modulus increases resulting from the restriction of chain dynamics, which, may in turn also reduce the ductility of the system.[23,24,30,87] Here an increase in T_g is expected with increasing hydrogen bond strength. We elucidated the T_g of these polymers through temperature dependent ellipsometry, whereby a discontinuity in the thermal expansion (thickness), as the films are heated at a constant rate, is indicative of the T_g (**Figure 4.5 and Figure C.5**).[41,96,124] The polymers observed a clear trend in T_g as follows: DPP-Urea > DPP-Amide > DPP-Linear > DPP-Branched. It is important to note, that the change in T_g for the polymers is

relatively low compared to the rDoC and thus we conclude that the crystalline packing

dominated the observed mechanical performance and in particular the strain at failure.

4.3.5 Strain Dependent Charge Transport

OFET devices were fabricated to assess the charge transport dependence on strain

(Figures 4.6 and C.6-C.9). At 0% strain the charge mobility was 0.148, 0.199, and

0.0154 cm^2/Vs for DPP-Linear, DPP-Amide, and DPP-Urea respectively. The charge

mobility was further assessed parallel and perpendicular to the strain direction up to 75%

strain. DPP-Urea demonstrated the greatest reduction in charge transport upon applied

strain, with a 94% reduction in charge mobility at 25% strain in the parallel

configuration. Regarding the previous FOE measurements this is quite interesting as the

COS for DPP-Urea was equivalent to that of DPP-Amide. This indicates that the charge

pathways were easily broken upon applied strain in DPP-Urea, prior to visible crack

formation. In contrast, the charge transport of DPP-Amide decayed only 14% at 25 %

strain. Considering the typical maximal strain experienced by human skin is 33%, amide

functionalization may be a suitable synthetic strategy to achieve the tolerable strain for

wearable devices while maintaining charge transport. These results indicate that the

greater hydrogen bonding strength of the urea moiety was not advantageous as an energy

dissipation mechanism, but rather detrimental due to the promotion of crystallite

formation.
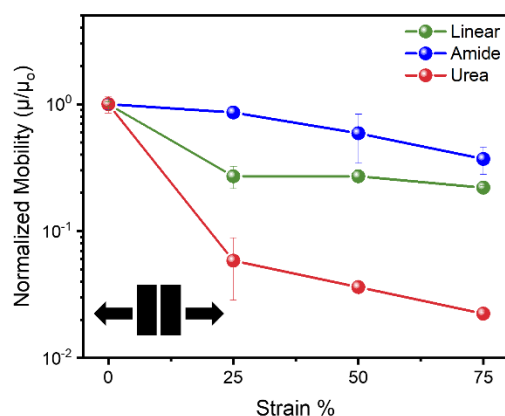
Figure 4.6 *Strain dependence on the normalized mobility of the statis-tical copolymers in the parallel to strain direction. Error bars represent the standard deviation of the data from a minimum of four consecutive measurements.*

4.4 Conclusion

In summary, three DPP-TVT based statistical copolymers (with 10% linear alkyl side chain, amide functional sidechains, and urea functional sidechains) were assessed relative to DPP-TVT with branched sidechains to elucidate the role of hydrogen bonding on thin film mechanics. Amide and urea moieties demonstrated strikingly different effects, with amide functionalization yielding the highest ductility while urea functionalization resulted in embrittlement of the polymer. This is attributed to the diverging influence on crystalline packing. Amide functionalization disrupts crystallite orientation resulting in a highly beneficial response to tensile deformation, while urea incorporation results in directed crystallization and an inability to accommodate stress. This was further assessed by characterization of the polymer swelling behavior, whereby, DPP-Amide exhibited the greatest swelling of 3.5% after prolonged exposure, indicating the greater availability of amide moieties for interaction with water resulting from the disruption of crystalline packing. In contrast DPP-Urea possessed an initially rapid

91

swelling behavior, but quickly plateaued due to the greater crystallinity. We further

validated our film-on-water measurements by performing a free-standing tensile

characterization of DPP-Amide, using our SMART technique, which exhibited identical

modulus to the film-on-water technique. This indicates that the polymers must be

exposed for prolonged periods in water (e.g., tens of hours) for water plasticization effect

to occur. To conclude, hydrogen bond moieties offer a novel route to improve conjugated

polymer mechanical performance (DPP-Amide), but the intermolecular interactions must

be carefully appraised as they may also be detrimental to device performance (DPP-

Urea). Expanding from this work, we envision that both mechanical and electrical

performance will continue to be improved through the further optimization of the side

chain structure and positioning of hydrogen bonding moieties. For instance, placement of

amide moieties at increasing distance from the backbone may provide enhanced

hydrogen bonding interaction with continued control over crystallization.

CHAPTER V – A GENERAL RELATIONSHIP BETWEEN THE RIGID

AMORPHOUS FRACTION AND OPTOLECTRONIC PERFORMANCE OF

CONJUGATED POLYMERS

5.1 Introduction

The morphological landscape of conjugated polymers is intricate, containing

varying length scales of crystalline order, chain conformation, and domain connectivity

by which the optoelectronic and mechanical performance are governed. Previously,

obtaining high crystallinity was the principal driving force for enhancing charge mobility,

such as the progression from poly(3- hexylthiophene) (P3HT) to poly(2,5-bis(3-

alkylthiophen-2-yl) thieno[3,2-b]thiophene) (PBTTT).[133] However, the dawn of high-

performing donor-acceptor polymers, such as indacenodithiophene copolymer with

benzothiadiazole (IDT-BT) with low crystallinity, has resulted in a paradigm shift.[135,251]

(In either case, the nanoscopic crystalline domains for all conjugated polymers typically

possess high paracrystalline disorder, limiting long-range charge transport.[136,252] Tie-

chains bridge ordered domains by traversing a sea of amorphous chains providing a

pathway for long-range charge transport.[131,136,253] Thus charge transport for conjugated

polymeric thin films rely on the conformational stability of the tie-chain as it traverses the

amorphous domain to serve as a charge highway, as outlined by Salleo *et al.*

It is well documented that nearly all semicrystalline polymers possess two

amorphous domains which exhibit distinct conformational freedom, chain dynamics, and

thus greatly impact material performance.[138,139,254,255] They are termed mobile amorphous

fraction (MAF) and rigid amorphous fraction (RAF) respectively. The MAF corresponds

to the traditional amorphous domain while the RAF corresponds to domains that consist

of amorphous chains which interact strongly with the crystalline segments of the polymer

(Figure 5.1(a)). Such interactions result in slower chain dynamics, as reflected by an

elevated thermal transition (T_{RAF}), which typically lies between that of the MAF glass

transition temperature (T_g) and the melting temperature (T_m) of the crystallites. The RAF

enhances amorphous-crystalline interactions and provides connectivity throughout the

polymer.[256,257] Tie-chains by their definition are part of the RAF and as such have

reduced chain dynamics and conformational freedom near interacting crystallites. Thus,

tie chains and the RAF are prevalent in donor-acceptor polymers due to their strong

tendency towards rapid crystallization rates because of their rigid backbone, and

subsequently high paracrystalline disorder of π-π stacked units.[82]

The existence of the RAF within semiconducting polymers was first identified in

poly(3-alkylthiophenes) through temperature modulated differential scanning calorimetry

(TMDSC), Flash DSC, and most recently AC chip calorimetry.[28,140,258,259] Specifically,

T_{RAF} of P3HT was observed at 55°C for TMDSC, between 40°C and 180°C for Flash

DSC utilizing an aging protocol, and 81°C for AC chip calorimetry. However, the

discovery of RAF within donor-acceptor semiconducting polymers remains notoriously

challenging due to weak transition signal.[87,140,259] To the best of our knowledge, only Luo

et al. has reported RAF relaxation for donor-acceptor polymers. Using AC chip

calorimetry, PDPPT-C2C10C12 was determined to have a T_{RAF} of 118°C.[28] Other

techniques, such as modified DMA[23–27], and an aging protocol with UV-Vis[29,30] have

been utilized to obtain similar elevated thermal transitions for donor-acceptor polymers

but there is little agreement within the literature as to what these transitions represent.

Modified DMA has demonstrated transitions at 175°C for PDPPTT-C2C8C10,[27] 200-

220°C for N2200,[27] 129°C for PDPP2T-C2C8C10 and PDPPTT-C2C8C10,[26] and 100°C

for P3HT[26,260]. However, these were attributed to either an aggregate transition or left

undefined.[25–27] Sugiyama *et al.* utilized UV-Vis to obtain thermal transitions (from 90°C

to 160°C) for a series of DPP-based polymers with varying side chains.[30] These

transitions were described as the general T_g of the polymer. However, this is

contradictory to others work suggesting DPP-based polymers to possess a backbone T_g

near/below room temperature.[23,24,27,28] Despite these disparities, most of these works

agree that there is both a low (-10°C to 65°C) and a high transition temperature (100°C+)

for DPP-based polymers. Although these techniques can provide the position of these

transitions, there is little information about their morphological landscape, particularly

the RAF, at device relevant thickness and hence their identity and the role they play in

device performance is obscured and of great debate.[28,140,258,259,261]

Interestingly, a decay in charge transport has been observed for semiconducting

polymers near these elevated thermal transitions, yet to the best of our knowledge this has

yet to be linked to the stability of the RAF. For example, the charge mobility of high

molecular weight P3HT was observed to decay above 120°C despite both increased

crystallinity and reduced π-π stacking distance with increasing temperature.[262] Given that

charge mobility decayed despite the improved crystalline structure, this reduction was

attributed to increased backbone torsion within the amorphous domain bridging

crystallites, evident through blue-shifting of the absorption spectra. Unfortunately, for

pure donor-acceptor polymers, there is limited literature sources regarding charge

mobility at such elevated temperatures.[263] Isoindigo based polymer and N2200 have

been observed to maintain their electrical performance up to 220°C and 180°C,

respectively.[263,264] While charge mobility of PDPP2T-C4C10C10 has been observed to decay above 150°C, which lies in between the thermal transitions (118°C to 175°C) previously discussed for DPP-based polymers.[265] Thus, the RAF may play a pivotal role in the optoelectronic performance of semiconducting polymers by governing the conformational stability of tie chains, which dictate intercrystalline charge transport.

5.2 Experimental

5.2.1 Materials

Regioregular (Mw 50-70 kDa) and regiorandom (Mw 30-90 kDa) P3HT were obtained from Reike Metals. N2200 (Mw 125.1 kDa and Đ 2.3) and PFFBT-4T (Mw 123.8 kDa and Đ 1.7) were obtained from Ossila. PDPPT (Mw 250.8 kDa and Đ 3.3),[266] PDPPTT (NA),[267] PDPPT-4 (NA),[268] NDI-C5 (Mw 60.8 kDa and Đ 3.1),[269] IDT-BT (Mw 295.4 kDa and Đ 2.7),[135] and C16CDT-QxMe (Mw 54.3 kDa and Đ 1.3)[270] were synthesized following previous literature procedures. Chemical structures of the semiconducting polymers are shown in **Figure D.1**. PLLA was obtained from Nature Works.

5.2.2 Film preparation

All polymers were dissolved in chlorobenzene at 80 °C overnight. Concentrations ranged from 5 – 20 mg/ml depending on the polymer and desired thickness. For all measurements, the polymer solution was spun cast at 2000 rpm for 2 minutes onto either a plasma-treated silicon wafer or a 500 nm thermally grown oxide.

5.2.3 Multi-sample spectroscopic ellipsometry

Spectroscopic ellipsometry was performed using an M-2000® UI Ellipsometer from J.A. Woollam with a spectral range of 245 nm to 1700 nm. Multi-sample analysis

was first employed on as-cast films to establish a reliable model. Each polymer was measured on both a silicon substrate, containing a native oxide layer with an assumed thickness of 15 Å, and one with a ~500 nm oxide layer. The thickness of the 500 nm oxide was assessed independently from the coated polymer films to reduce the number of unknowns within each model. Each measurement was performed at five angles from 55°-75° at room temperature, with an exposure time of two seconds per angle. The polymer film thickness of the two consecutive measurements was ensured to be within a difference of 10%. Thus, the optical profiles could be assumed to be equivalent which was confirmed by the low MSE and uniqueness of each model.

Model development was performed within the CompleteEase software package using multi-sample analysis. An anisotropic Cauchy model was first used to describe the transparent region of the polymer film. This was then converted into a Kramer Kroning consistent transparent B-spline using the existing Cauchy data as the initial parameters. The anisotropic B-spline was then expanded into the absorbing spectral range using a sequential fitting procedure within the software. The in-plane resolution of the B-spline was held at 0.05 eV (87 variables), while the out-of-plane resolution was held at 0.3 eV (15 variables). This B-spline model was then used as a frame of reference to develop a more robust model using a series of gaussian oscillators (Gen-Osc) to describe each polymer's absorption profile. The Gen-Osc model was then optimized to minimize the MSE with the fewest variables.

The temperature measurements were performed with a Linkam heating cell in conjunction with the M-2000® UI Ellipsometer at a fixed incidence angle of 70°. All measurements were performed under a nitrogen atmosphere with continuous exposure at

two-second intervals. To perform a temperature scan of the polymer films, the silicon substrate and oxide films' temperature-dependent optical profile was first assessed independently. A library of the optical profiles of both silicon and thermal oxide was developed and utilized to model the polymer films with known substrate parameters at each temperature **(Figure D.2)**. Both the native oxide and ~ 500 nm oxide layer were assumed to have a constant thickness throughout the temperature profile. This was justified by the low MSE obtained throughout the temperature scan. Each semiconducting polymer was first heated above its melt temperature to remove thermal history, followed by cooling to -50 °C at a rate of 5 °C/min. The sample was then heated to above its melting temperature at a rate of 5 °C/min. This was performed for each polymer cast onto both silicon and the 500 nm thermal oxide layer. Using the previously developed Gen-Osc model, the data from both samples were fitted simultaneously throughout the measurement time **(Figure D.3)**. Specifically, the amplitude and energy of the Gaussian curves were allowed to vary to provide the best fit for the data. Variables that did not lower the MSE of the fit were not used. Unless stated, roughness was neglected throughout the modeling due to an insignificant influence on MSE.

The glass transition for both the mobile and rigid amorphous fractions were determined through the step change in the 1st derivative of the thickness and optical data obtained from spectroscopic ellipsometry. The melting temperature was determined by fitting the peak in the 1st derivative of the data. In general, a locally weighted scatterplot smoothing of 0.1 was applied to the data prior to taking the 1st derivative to remove noise and ensure an accurate assessment of all transitions.

5.2.4 Wide angle X-ray scattering (WAXS)

Both grazing incidence wide angle X-ray scattering (GIWAXS), and temperature dependent transmission WAXS were performed using a Xenocs Xeuss 2.0 SAXS/WAXS lab source instrument under a vacuum environment. For the GIWAXS measurements, samples were subject to two hours of exposure with an incident beam energy of 8.05 keV, an incident angle of 0.2°and a beam geometry of 0.8×1.2 mm. Two consecutive measurements were performed using the line eraser feature to remove grid lines between detectors. The sample-to-detector distance was ~150 mm as determined by fitting a silver behenate standard. The 1D data and peak fitting were processed using Nika and WAXS tools software packages within Igor Pro from Wavemetrics.

For the temperature dependent WAXS measurements, bulk samples were placed into a 2 mm wide glass capillary tube and loaded within a Linkam heating cell. The samples were first heated above the melt temperature and subsequently cooled to -50 °C. The samples were then exposed to X-rays at 10 °C increments with and exposure time of 5 minutes. Between each measurement the subsequent temperature was allowed to equilibrate for 5 minutes. The temperature of the stage was calibrated using a K-type thermocouple. All 1D-data and peak fitting were processed as described previously.

5.2.5 Organic field-effect transistors

Device fabrication: N-doped Si wafers with 300nm SiO_2 surface dielectric layer (capacitance of 11.5nF/cm2) were cut into smaller substrates by a diamond cutter. These substrates were washed with soap water, acetone, and isopropanol before cleaning with hot piranha solution (98% H_2SO_4:30% H_2O_2 = 7:3). This step was used to clean all the organic residue and make the surface hydrophilic for octadecyltrichlorosilane (OTS)

modification. The substrates were then sonicated in water, acetone, and isopropanol sequentially for 5 minutes each. After drying, they were placed in a small petri dish surrounding a tiny drop of OTS. The dish was covered and put in a vacuum oven at 120°C for 3 hours to form an OTS self-assembled layer on the substrate surface. After three hours, the $SiO2$ was fully covered by OTS and became hydrophobic (the contact angle with $H2O$ was 105-110°). The OTS modified substrates were rinsed with hexane, isopropanol, chloroform and dried by nitrogen gun before transferring into the glovebox for spin coating.

The solutions were spin-coated at 2000RPM for 60s followed by 4000RPM for 30s to remove excess solution at the edges. The thin films were annealed in an N2 glovebox at 150°C to remove solvent residue for 30 minutes and allowed to cool down to room temperature slowly. Then the substrates were transferred into the evaporation chamber for source/drain electrode deposition. Here, a 40 nm Au was thermally evaporated through shadow masks on top of the polymer thin film under a high vacuum (10-6 mbar) at a small rate (0.1 Å/s) for the first 10nm and higher rate (0.5-0.6 Å/s) for the rest.

Electrical measurements: For P3HT, the devices were measured in a nitrogen atmosphere. The substrates were transferred into the Linkam HFS600E-PB4 stage. Thermal paste was applied between the substrates and the heating stage to ensure good thermal contact. At each temperature step, the devices were kept at equilibrium for 20 minutes before applying voltage using two Keithley 2450.

For the rest of the polymers, the devices were measured in ambient atmosphere. The substrates were transferred into the Linkam HFS600E-PB4 stage. Thermal paste was

also used to make good thermal contact between substrates and the heating block. The

temperature was increased at 20°C/min and kept constant for 10 minutes before each

measurement. The electrical characterization was carried out using a Keithley 4200. The

effective mobility μ_{eff} is calculated based on this reference.[271]

5.3 Results and discussion

5.3.1 Variable temperature spectroscopic ellipsometry analysis of PDPPT

Here, we ascertained the existence of the RAF domain within a broad range of

semiconducting polymers **(Figure D.1)** and its subsequent influence on their

optoelectronic performance, especially regarding to device stability. This was

accomplished through a holistic array of *in situ* characterization techniques **(Figure

5.1(a))** whereby, thermal expansion, optical profile, crystallinity, charge transport, and

chain conformation were all assessed. Each of these techniques indicated the existence of

the RAF domain and its impact on the morphological stability of the semiconducting

polymer (representative PDPPT-C2C8C10 in **Figure 5.1(b))** and subsequently device

stability. Four stages of thermal transitions were observed **(Figure 5.1(c))** and assigned

by the onset of the transition obtained by thermal expansion from spectroscopic

ellipsometry. Stage 1) All chains lie within the glassy state with mobility present only in

low T_g (e.g. T_g of sidechain around -50°C)[23,24] alkyl side chains. Stage 2) MAF

mobilization occurs once above the backbone T_g of the polymer. Charge mobility

increases due to temperature activated hopping.[272–274] Stage 3) At elevated temperature,

prior to melting, RAF mobilization occurs leading to significant morphological changes,

such as a loss of anisotropy and rapid blue-shifting of the absorption spectra. Notably, the

conformational stability of tie-chains becomes destabilized resulting in a detrimental loss

towards charge transport. Stage 4) Melting of crystallites occurs resulting in complete

isotropy of the system, consisting only of amorphous chains. Notably, several polymers,

PDPPTT, IDT-BT, and CDT-QxMe, in this work did not exhibit melting behavior before

polymer degradation at high temperature.
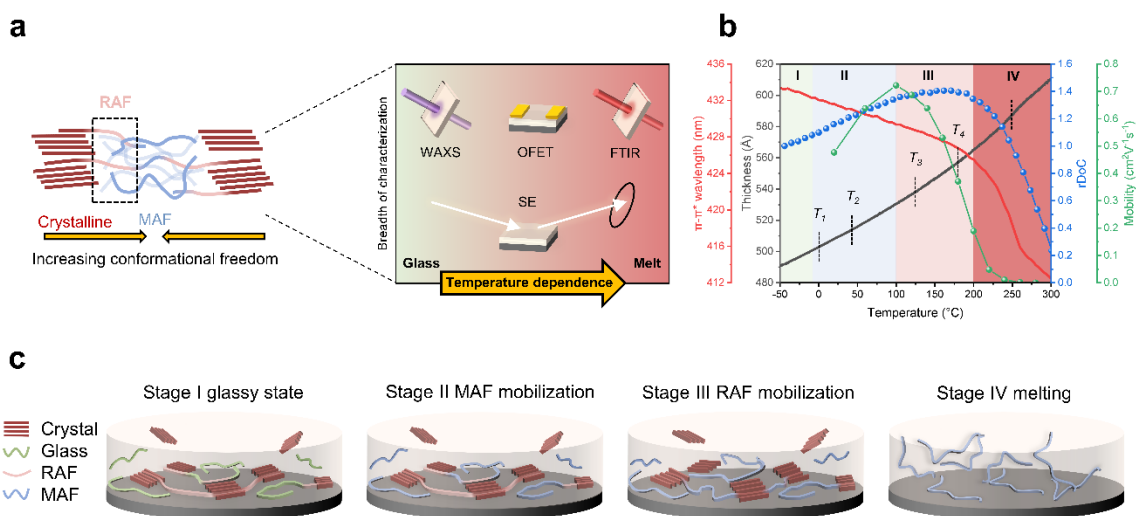
Figure 5.1 *a) In-situ characterization techniques to investigate the thermal transitions of the three domains within semiconducting polymers: crystalline, rigid amorphous fraction (RAF), and mobile amorphous fraction (MAF). Emphasis is on the RAF. The green, blue, pink, and red shaded regions represent the polymer's glassy state, MAF mobilization, RAF mobilization, and crystalline melting, respectively. b) Temperature-dependent parameters illustrating the thermal transitions of a representative semiconducting polymer DPPT-C2C8C10. c) Illustration of each thermal transition's impact on morphology. Red, green, pink, and blue colors correspond to crystalline, glassy, RAF, and mobile polymer segments, respectively.*

We employed temperature dependent multi sample spectroscopic ellipsometry

(SE) to simultaneously illuminate the thermal transitions of donor-acceptor conjugated

polymers while extracting their temperature dependent optical response with high fidelity

(Figure 5.2(a-b)). Previously, SE characterization of semiconducting polymer thermal

transitions was primarily limited to analysis of the raw ellipsometry signals (Ψ and

Δ).[36,40,41] Thus the anisotropy and optical constants were unexplored. This was due to the

102

difficulty in modeling the temperature dependent anisotropic and absorbing nature of semiconducting polymers, which this work has now overcome. In short, temperature dependent multi-sample SE measures the ellipsometry signal of an identical semiconducting polymer film on two separate substrates whose temperature dependent optical profiles were already known. The polymer film from both measurements was simultaneously modeled to yield a single optical profile that provided the best fit to the data from each measurement. The procedure is discussed in detail in Appendix D (**Figure D.2-D.3**). To the best of our knowledge, SE has not been utilized to observe the RAF of any semicrystalline polymer. Thus, to ensure efficacy of the measurement we first characterized the RAF transition of PLLA, a commodity polymer with a known T_g for MAF and RAF. We observed T_g and T_{RAF} at 63°C and 133°C (**Figure D.4**), respectively. The result agreed with recent findings from literature.[138,275]

Here, we first focus our discussion on the SE characterization of a representative p-type donor-acceptor semiconducting polymer PDPPT (**Figure 5.2**). Details on the sample preparation and thermal program can be found in supporting information. From modeling of the 2nd heating ramp of the SE data, we were able to obtain six parameters to verify the T_g response from both MAF and RAF. These were 1) thermal expansion, 2) refractive index, 3) anisotropy, 4) wavelength of 0-0 absorption peak, 5) wavelength of the π-π* absorption peak, and 6) optical bandgap (**Figure 5.2(b-f)**). As the temperature increases the rate of thermal expansion increases with each glass transition response.[22] For PDPPT, we observed a modest change in film thickness expansion at 0°C (T_1) which was previously prescribed as the backbone T_g via DMA.[24] Another transition (T_2) was observed at 41°C and attributed to the thiophene-thiophene bond which exhibits less

internal plasticization by the side chain due to its increased separation from the alkyl chain. Previously, this bond was demonstrated to be more thermally stable than the diketopyrrolopyrrole -thiophene bond through MD simulation.[265] Two elevated transitions (T_3, T_4) were observed at 124°C and 181°C followed by melting at 250°C. These elevated thermal transitions were attributed to RAF mobilization and their vitrification were also observed upon cooling from the melt in a subsequent experiment (**Figure D.5**). Given that two backbone transitions were observed at 0°C and 41°C, it is probable that the two RAF transitions were exhibited from the differing conformational freedom of these bonds, subjected to crystalline constraint on the RAF. The analysis of the optical constants yields a similar conclusion, albeit with somewhat shifted transition temperatures due to their differing sensing mechanisms. Values for those transitions are listed in **Table 5.1**. Both the averaged refractive index and anisotropy (Δn)[42] were observed to decrease more rapidly upon mobilization of the RAF rather than MAF. This indicates that the RAF provides the dominant stabilizing mechanism to the film's solid-state morphology. This agreed with the modeled absorption spectra during the temperature variable experiments, which observed a broad blue shift of the 0-0 peak upon mobilization of the RAF at 94°C and subsequently sharp transitions at 154°C and 187°C. Such blue-shifts, along with the reduction in 0-0 intensity, are indicative of increased torsional disorder of the polymer backbone.[276,277] A blue shift was also observed within the π-π* peak which represents the electron delocalization between diketopyrrolopyrrole and thiophene units.[278] The most prominent blue shift occurred within the mobile RAF regime at 137°C. This indicates that upon mobilization of the RAF the length scale of electron delocalization becomes rapidly reduced. Additionally, the optical band gap was

assessed throughout the temperature profile and resulted in a T_4 of 161°C, indicating both

a reduction in the conjugation length and the planarity of the system.[279]
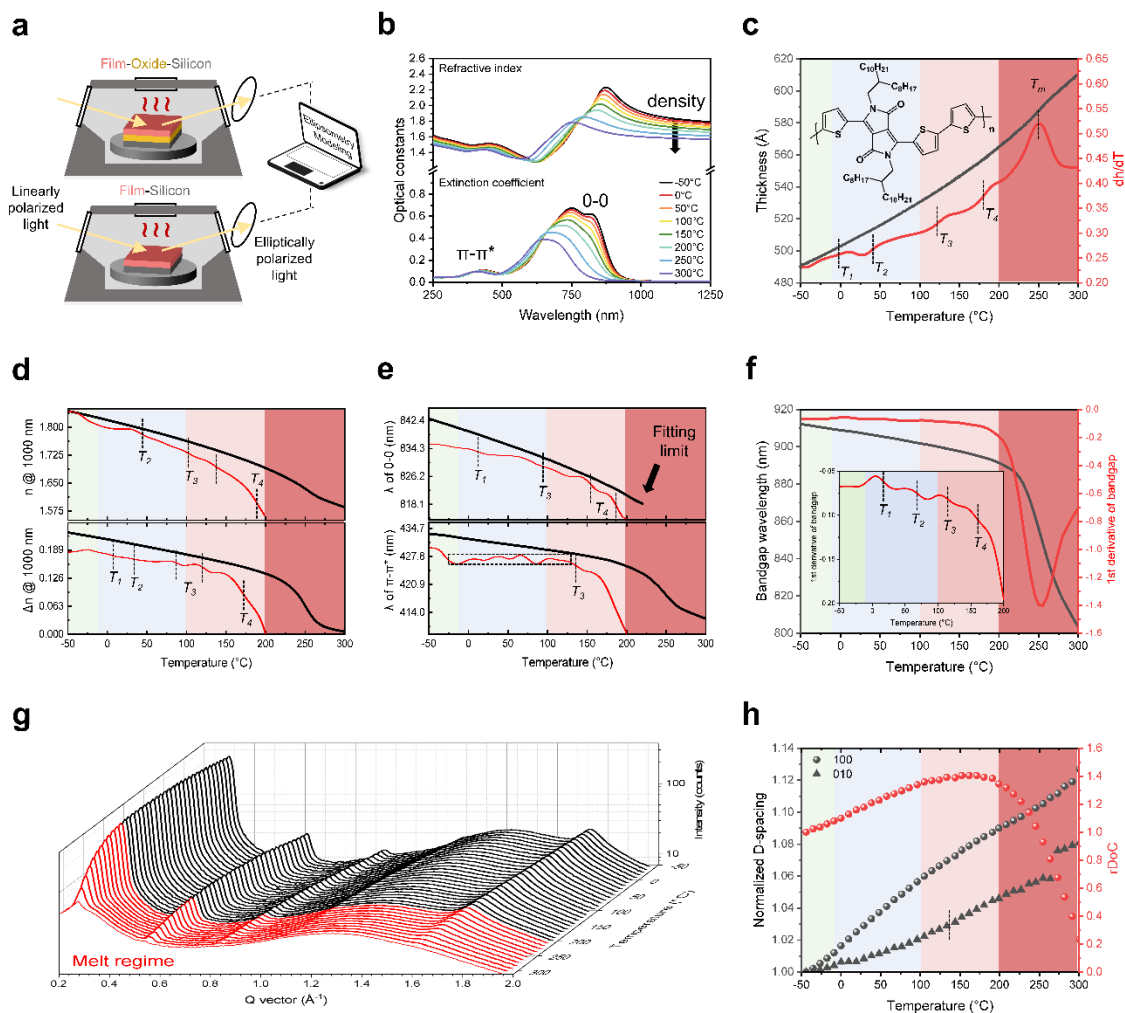
Figure 5.2 *Temperature dependent spectroscopic ellipsometry (SE) and Wide-angle X-ray scattering (WAXS) for a representative semiconducting polymer PDPPT. a) Illustration of temperature dependent SE utilizing multiple sample analysis. b) SE obtained optical constants (2/3 * Ordinary + 1/3 * Extra-ordinary) as a function of temperature. c) Thermal expansion profile and 1st derivative. Insert is the chemical structure of PDPPT. Vertical line segments indicate each transition. d) Refractive index and anisotropy, analyzed at a wavelength of 1000 nm, as a function of temperature. Insert is the 1st derivative with arbitrary y-axis. e) Fitted 0-0 and π-π* peak positions as a function of temperature. Insert is the 1st derivative with arbitrary y-axis. f) Optical bandgap wavelength as a function of temperature. Insert is an expanded view of the 1st derivative. h) Relative degree of crystallinity (rDoC) of (100) peak and normalized D-spacing of (100) alkyl and (010) π-π scattering peaks.*

105

Table 5.1 *Summary of PDPPT thermal transitions from SE*

	T_1 (°C)	T_2 (°C)	T_3 (°C)	T_4 (°C)	T_m (°C)
Thickness	-2	41	124	181	250
Refractive index (n)	NA	43	103 & 138	191	251
Anisotropy (Δn)	4	31	88 & 122	169	250
0-0 peak	11	NA	94	154 & 187	NA
π-π*	10	45	137	NA	247
Bandgap	19	70	118	161	254

5.3.2 Variable temperature wide angle X-ray scattering of PDPPT

Since the RAF depends on its interaction with the crystalline domain, we performed grazing incidence and temperature variable transmission wide-angle X-ray scattering (GIWAXS and WAXS) to assess the crystalline packing of PDPPT and other polymers **(Figure 5.2(g) and Figure D.6-D.7)**. The relative degree of crystallinity (rDoC), calculated based on literature reported method,[244] was observed to initially increase with temperature, followed by a plateau within the mobile RAF regime and subsequent reduction upon onset of melting, near 200°C for PDPPT. Since rDoC did not decay within the prescribed mobile RAF regime from SE, this supports the assertion that the transition is indeed from the RAF rather than melting of the crystalline domain. The D-spacing of the (100) alkyl peak and (010) π-π peak both increased with temperature due to thermal expansion. However, the rate of alkyl expansion decayed within the mobile RAF regime, while the rate of expansion of π-π stacked units increased for all polymers measured. The rate of expansion in the π-π stacking direction increased most rapidly at 138°C for PDPPT, indicated by the 1st derivate in **Figure D.6**, within the mobile RAF regime specified from SE. Given that GIWAXS confirms a predominantly edge-on morphology (alkyl lies parallel to thickness) for these polymers **(Figure D.7)**

this has two implications. 1) Neither the crystalline alkyl nor the π-π expansion are a major contributor to the rapid rate of thermal expansion (z-axis), prescribed as RAF mobilization from SE and thus relaxation of crystallites remains unlikely. 2) The expansion of π-π stacking may correlate with weaker intermolecular interaction of the RAF with the crystalline domain and thus signal RAF relaxation.

5.3.3 Variable temperature charge transport of PDPPT

Given that mobilization of the RAF corresponds to increased backbone torsion as well as increased π-π stacking distance, such morphological change is likely to dictate charge transport, resulting from increased activation energy to transport charge across a mobile RAF (**Figure 5.3(a)**). Thus, we explored the temperature dependent charge carrier mobility for PDPPT (**Figure 5.3(b-c)**) using organic field-effect transistors (OFET). Charge mobility (μ_{eff}) and on current (I_{on}) increased initially, due to thermal activated hopping, followed by a plateau at 100°C and subsequent decay at 140°C, coinciding with the onset of the mobile RAF regime measured by temperature dependent SE. Threshold gate voltage (V_T) decreased slowly until 140°C followed by a rapid negative shift with increasing temperature, indicative of deepening traps along the polymer backbone, which was attributed to RAF mobilization. Interestingly, the decay in charge transport occurred between T_3 and T_4, which may support the claim that T_3 is exhibited from the diketopyrrolopyrrole - thiophene bond within the RAF while T_4 may originate from the thiophene - thiophene bond, agreeing with their susceptibility to torsion, as indicated through MD simulation.[265]
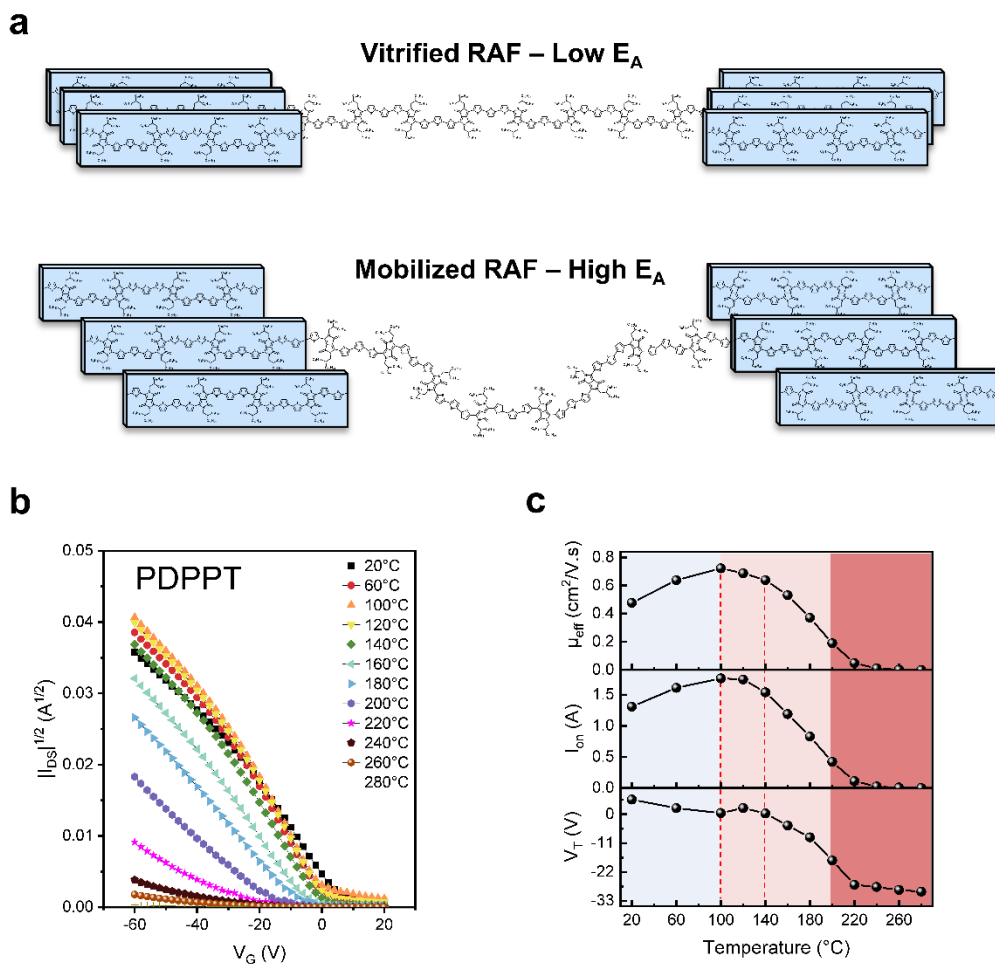
Figure 5.3 *Assessment of the RAF's influence on charge transport. a) Illustration of vitrified RAF, providing an effective bridge for charge delocalization (top) and RAF mobilization resulting in a change in backbone conformation and impediment of charge transport between two crystalline units (bottom). b) Transfer plots of PDPPT polymer as a function of temperature. c) Charge transport characteristics of PDPPT as a function of temperature.*

5.3.4 Comparison of T_{RAF} within 10 semiconducting polymers

Beyond PDPPT, we observed T_{RAF} in all 8 representative semicrystalline polymers which we characterized (**Figure 5.4 and Figure D.8-D.16**). T_{RAF} was observed to increase with T_m (**Figure D.17**), which agrees with literature expectations of the RAF. IDT-BT, C16CDT-QxMe, and PDPPTT were not included in this assessment as their melting temperature was not observed with either DSC or SE due to degradation

temperature lower than melting temperature. However, all three of these polymers

exhibited an elevated T_{RAF} which is congruent with their expectedly high melt

temperatures, despite these values being unknown. Unfortunately, it is challenging to

quantitatively compare T_{RAF} based on chemical structure, due to obfuscation from

differences in crystallinity, T_m, and molecular weight. However, we can qualitatively

assert that increased backbone rigidity/planarity is correlated to increasing T_{RAF}. For

instance, T_{RAF} increased for DPP-based polymers upon increasing backbone rigidity.

PDPP-C4, with broken conjugation, exhibited a T_{RAF} of 119°C followed by fully

conjugated PDPPT with a T_{RAF} of 181°C and then PDPPTT, incorporating a rigid

thienothiophene, with a T_{RAF} of 228°C. Additionally, N2200, IDT-BT, and CDT-QxMe

all possess high planarity, evident by (001) backbone scattering in literature,[87,135,137,270]

and exhibit a T_{RAF} above 220°C. The only flexible polymer which exhibited an elevated

T_{RAF} was PFFBT-4T, persistence length of 3.4 nm, which we postulate is due to increased

crystallinity. In contrast, regio-random P3HT and PNDI polymer with nonconjugated

linker (PNDI-C5) with low crystallinity, did not demonstrate a RAF transition **(Figure

5.5(a))**. This was expected given that the RAF forms from the interaction of an imperfect

crystal with amorphous chains, thus low crystallinity would yield negligible content of

the RAF.
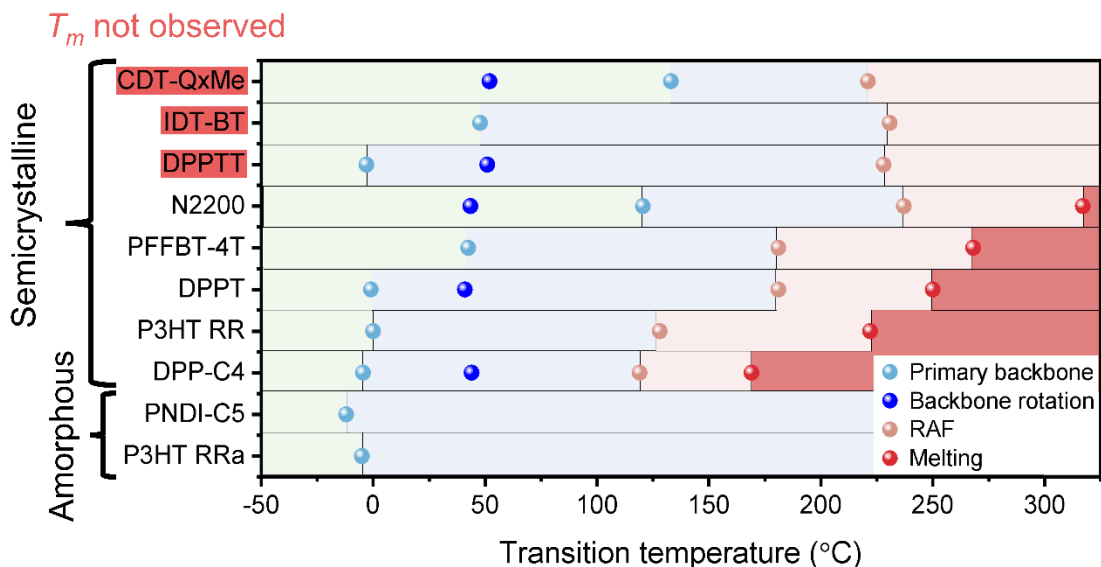
Figure 5.4 *Thermal transitions of all polymers characterized by spectroscopic ellipsometry, based on thermal expansion.*

To further verify the impact of the RAF on charge transport, we then investigated the temperature-dependent charge mobility of four additional polymers with thiophene moiety in their backbone, PDPPTT, PDPP2T, PFFBT-4T, and P3HT, (**Figure D.18-D.19**). All four polymers exhibited a rapid decay in charge mobility within the mobile RAF regime (**Figure 5.4 and Figure D.10-D.12**). PDPP2T was not characterized by SE. In comparison to PDPPT, the charge mobility of PDPPTT decayed above 180°C, demonstrating increased thermal stability relative to PDPPT. Analysis of the temperature-dependent bandgap confirms an increase in T_3 and T_4 to 158°C and 230° C for PDPPTT (**Figure 5.5(c)**), respectively, indicative of increased backbone stability. Given that the diketopyrrolopyrrole -thiophene bond is more susceptible to torsion,[265] it is unlikely that the loss of the thiophene-thiophene bond, resulted in this increased stability. Rather, we postulate that the improved intermolecular interaction of PDPPTT, evident by high crystallinity (**Figure D.7**) and T_m above 300°C,[23,280] provides a stronger restricting force
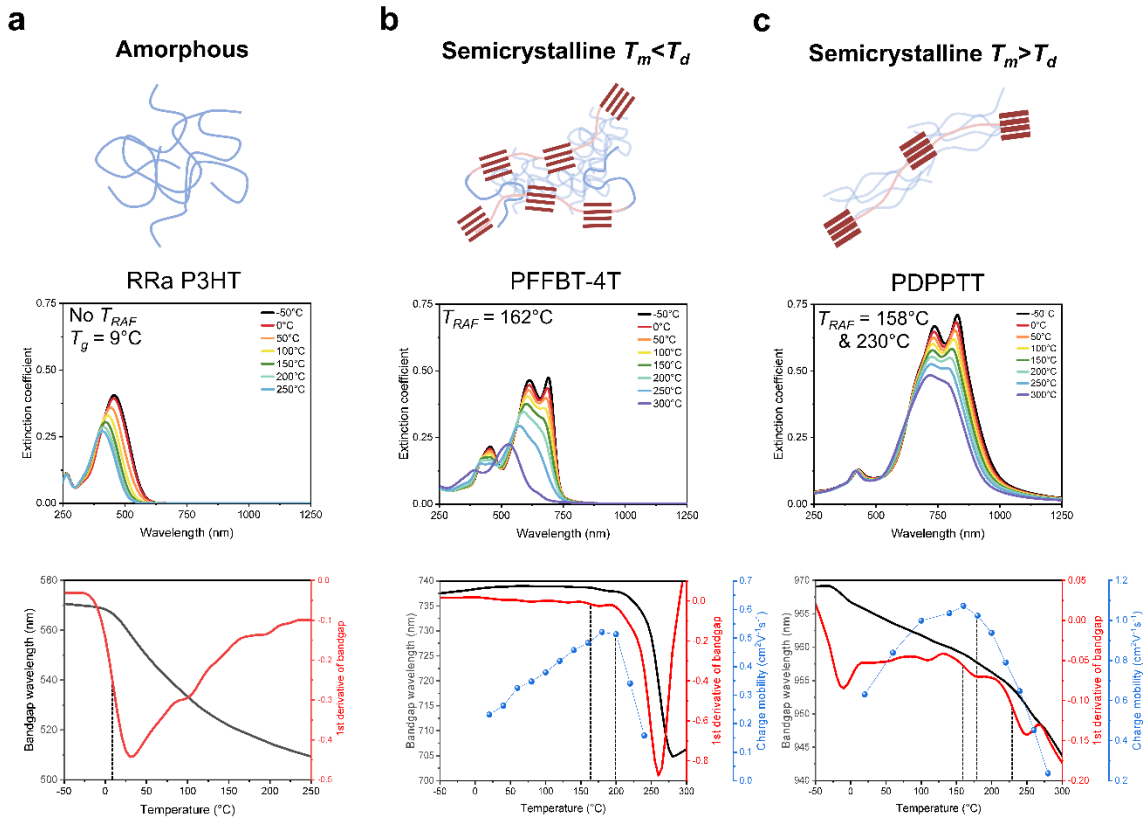
Figure 5.5 *Comparison of the optoelectronic property of three representative polymers, a) amorphous P3HT, b) semicrystalline PFFBT-4T with observable Tm and flexible backbone, and c) semicrystalline PDPPTT with unknown Tm and rigid backbone. Illustration of each polymers' morphology (top), followed by the variable temperature absorption profile obtained from SE (middle), and the temperature dependence of the optical bandgap compared to the variable temperature OFET charge mobility (bottom). OFET characterization was not performed for RRa P3HT.*

upon the RAF. This was verified through OFET measurements of PDPP2T, containing an additional thiophene-thiophene bond relative to PDPPT, which observed a decay in charge mobility above 180°C, analogous to PDPPTT. These findings are in line with conventional semicrystalline polymers, which exhibit both an elevated RAF transition and greater RAF content with increasing T_m and crystallinity.[138,139] PFFBT-4T also exhibited elevated thermal stability. Intriguingly, the bandgap of PFFBT-4T increased with temperature until ~ 100°C **(Figure 5.5(b))**, indicating planarization of the backbone

with increasing temperature, followed by T_{RAF} at 162°C and a decay in charge mobility at 200°C. Given the greater rotational freedom along the backbone of PFFBT-4T (persistence length of 3.4 nm),[281] this exemplifies the crystalline amorphous interaction to promote RAF stability. This was confirmed with temperature dependent WAXS (**Figure D.6**) which demonstrated a large increase in rDoC upon heating of PFFBT-4T and thus likely improved RAF content as well. This is congruent with our findings for P3HT which, despite its generally low charge mobility and backbone flexibility (persistence length of 3 nm), exhibited the same trend as PDPPT. Thus, for the five polymers measured here, OFET stability was observed to increase with increasing T_{RAF}. Together, these findings, not only validate the existence of RAF in donor-acceptor polymers but highlight its significance in governing the conformational stability of the system which in turn dictates optoelectronic performance.

5.4 Conclusion

In summary, the thermal transitions of ten semiconducting polymers of varying chemical structure were investigated to elucidate the existence and impact of the rigid amorphous fraction on optoelectronic performance. All the semicrystalline polymers studied here, were observed to possess a RAF T_g, as determined through temperature-dependent multi-sample spectroscopic ellipsometry. Notably, regiorandom P3HT and PNDI-C5 did not exhibit a RAF T_g due to their lack of crystallinity, thus RAF formation was hindered. Mobilization of the RAF was demonstrated to be detrimental towards charge transport, which was attributed to increased backbone torsion. Crystalline stability, crystallinity, and backbone rigidity were demonstrated as key factors governing the thermal stability of the RAF. These findings not only demonstrated the existence of

RAF within semiconducting polymers, but their role in governing the conformational

stability of the system and subsequently optoelectronic performance.

CHAPTER VI – FUTURE DIRECTIONS

To conclude, this dissertation investigated the structure-property-processing relationships of semiconducting polymers to gain insight into their themomechanical performance. This was accomplished through four projects, through which, the role of backbone rigidity, confinement, hydrogen bonding, and the rigid amorphous fraction were all assessed. Additionally, new characterization techniques were developed to 1) enable tensile analysis of free-standing ultrathin films and 2) to evaluate weak thermal transitions at device relevant thicknesses. However, within the field of semiconducting polymers, there remains a vast library of chemical building blocks and phenomenon to explore. Some potential directions are outlined below.

1) Achieving both high electrical and mechanical performance of semiconducting polymers remains a challenge. Flexible conjugation break spacers, like that reported in Chapter II, may offer a route to achieve a best of both worlds scenario if incorporated correctly. For instance, incorporation of flexible CBS at the length scale of the effective conjugation length of the polymer would enable improved mechanical performance and solubility while maintaining the electrical performance of the pure polymer. In this manner, the CBS moiety may then be tuned to achieve a wide array of mechanical attributes, such as elasticity in the case of crosslinked CBS. Although statistical polymers of a similar nature have been explored,[65,282,283] the length scale of incorporation has yet to be investigated thoroughly.

2) To date, the mechanical performance of only a few ultrathin polymer films have been explored under a free-standing environment. The work of Chapter III opens the door for many more polymers and phenomenon to be investigated as well as the potential

to study 2D materials like graphene. [284–288] For instance, the role of fragility on thin film mechanics has yet to be explored. Fragility describes the breadth of the T_g response. A high fragility indicates a sharp response and has been linked to more significant reductions in T_g from confinement.[90,289,290] Thus, conventional polymers, such as, poly(vinyl chloride), polycarbonate, polysulfonone, and polystyrene which possess known bulk fragilities may offer a facile route of study.[289] Additionally, continued development of such free-standing techniques would be highly advantageous for multi-modal characterization platforms (ex. *In-situ* X-ray, FTIR, UV-Vis) to provide a holistic understanding of the deformation mechanisms of semiconducting polymer films.

3) Our understanding of the thermomechanical phenomena of semiconducting polymers is growing rapidly, but this has primarily been limited to hydrophobic systems. Thus, polymers for organic electrochemical transistor (OECTs) applications have been neglected. Such polymers are engineered to swell in aqueous or biological media, enabling volumetric doping and high transconductance.[291–296] Considering that OECTs are prime candidates for biocompatible applications it is of paramount importance that their mechanical performance and doping mechanisms be assessed under biologically relevant environments. Such mechanical analysis of polymers for OECT applications has yet to occur. The pseudo-free-standing tensile test is a facile method for such investigation as the supporting media can be designed utilizing a wide array of electrolyte solutions and even various degrees of applied voltage, thus mimicking a myriad of biological environments.

4) Despite a focus of this work being on the T_g and rigid amorphous fraction there are many systems which have not been explored. Development of an encompassing T_g

library would be highly beneficial for the community towards unraveling such phenomenon. For instance, our group has already begun the development of an empirical model to predict the glass transition of conjugated polymers by their structure.[24] Continuation of this endeavor towards more complex systems, at device relevant thickness, and incorporation of the rigid amorphous fraction's T_g response would be highly advantageous for guiding the semiconducting polymer community.

APPENDIX A
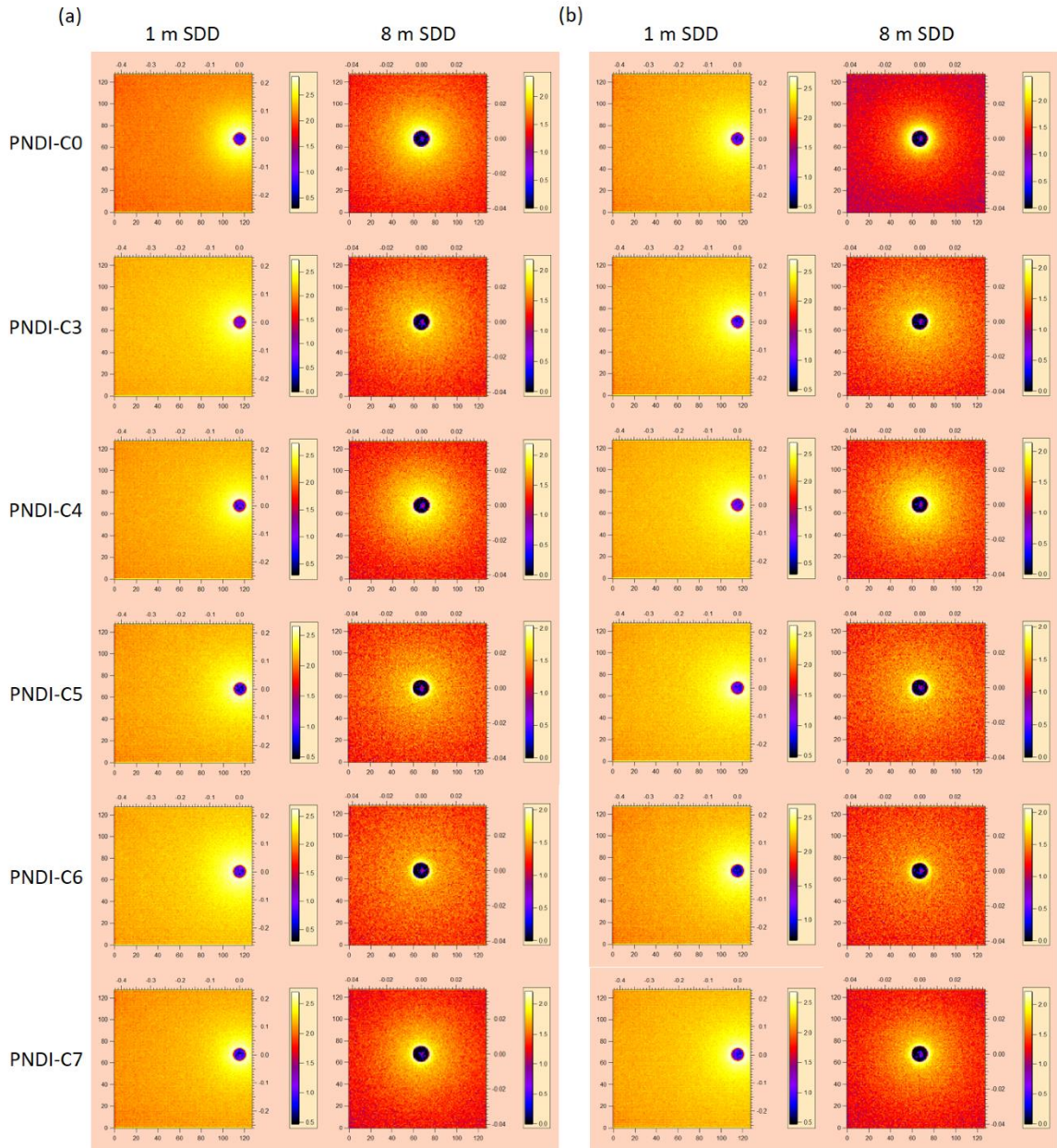
Figure A.1 *2D images from solution SANS of PNDI-Cx polymers at (a) 25 ˚C and (b) 85*

˚C for sample to detector distances of 1 m and 8 m.
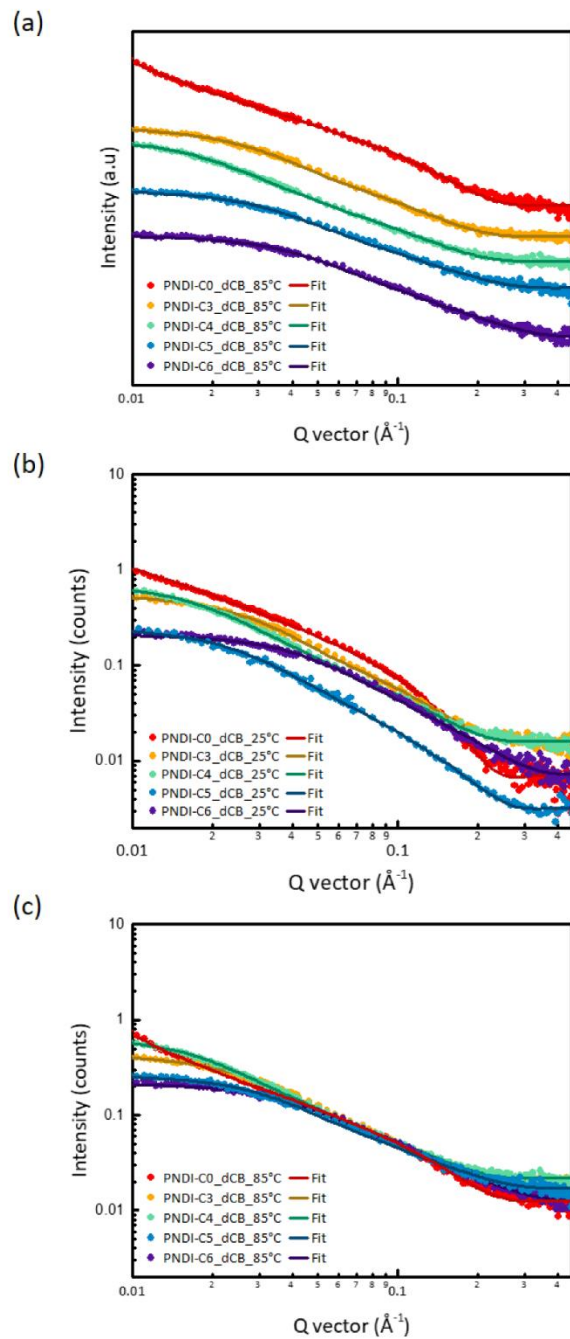
Figure A.2 *a) 1D scattering profile obtained at 85 ˚C in deuterated chlorobenzene b-c) SANS scattering profile at 25 and 85 ˚C with absolute intensity.*
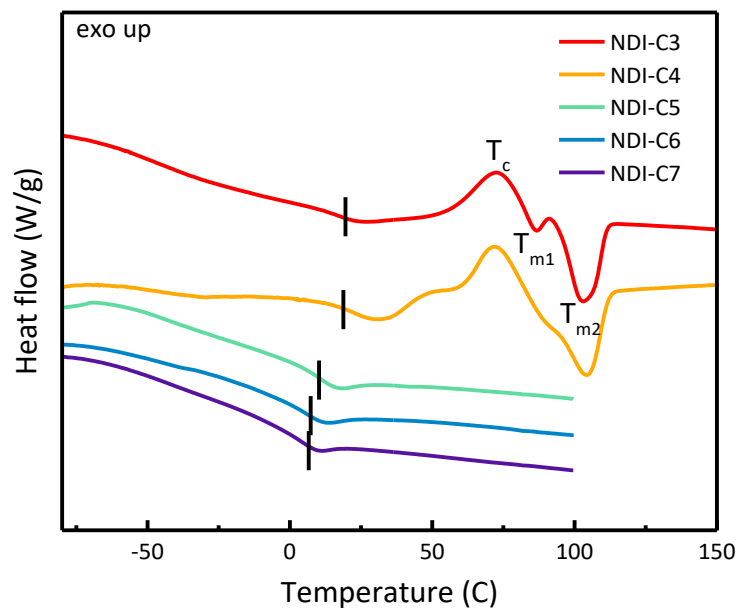
Figure A.3 *DSC thermogram of 2nd heat cycle for polymers C3-C7.*
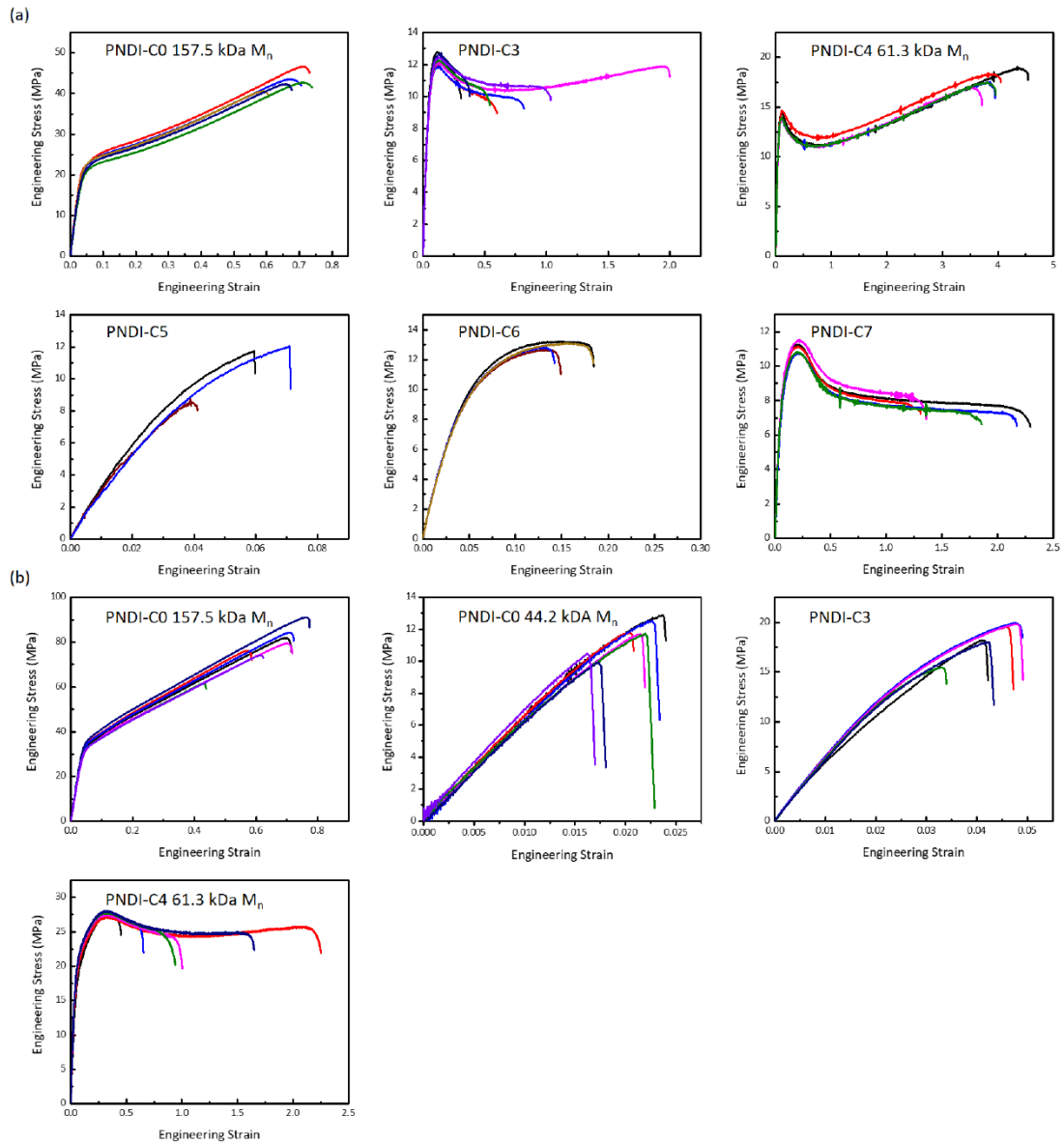
Figure A.4 *Raw tensile data (a) post two-day isotherm at room temperature under nitrogen atmosphere, (b) post two day annealing at 30 ℃ undercooling under nitrogen atmosphere (PNDI-C0 was annealed at 200 ℃ for eight hours)*
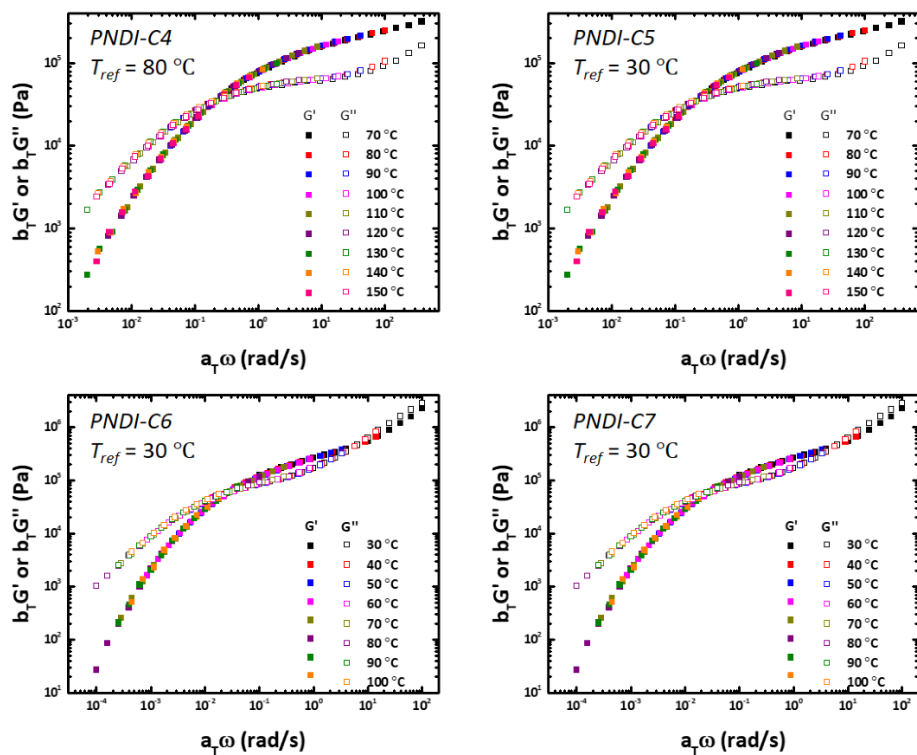
Figure A.5 *Master curves of PNDI-C4-7 obtained from oscillating melt shear rheology*
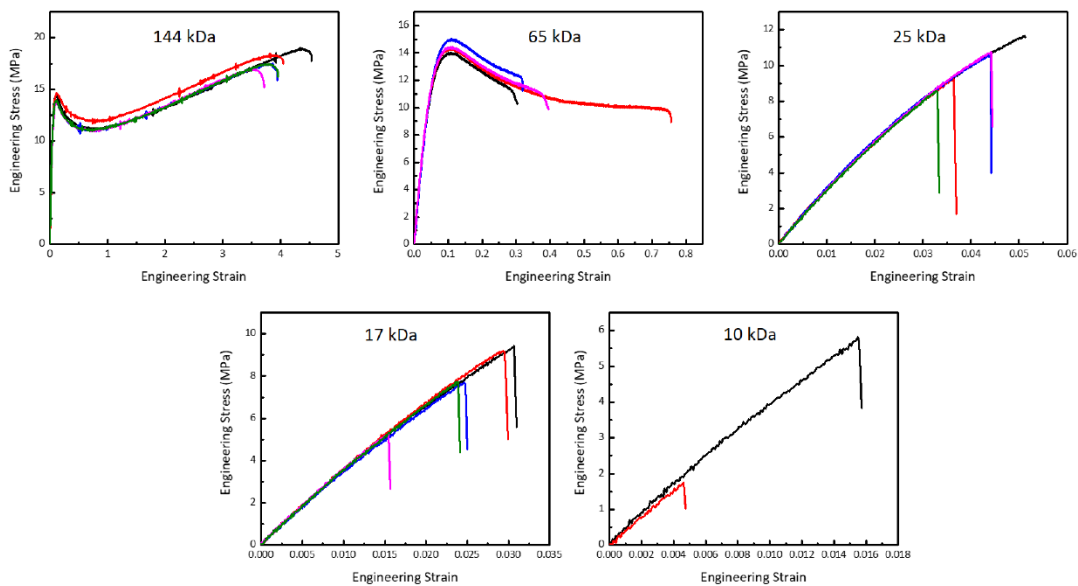
Figure A.6 *Raw PNDI-C4 molecular weight dependent tensile data post two-day*

isotherm at room temperature under nitrogen atmosphere
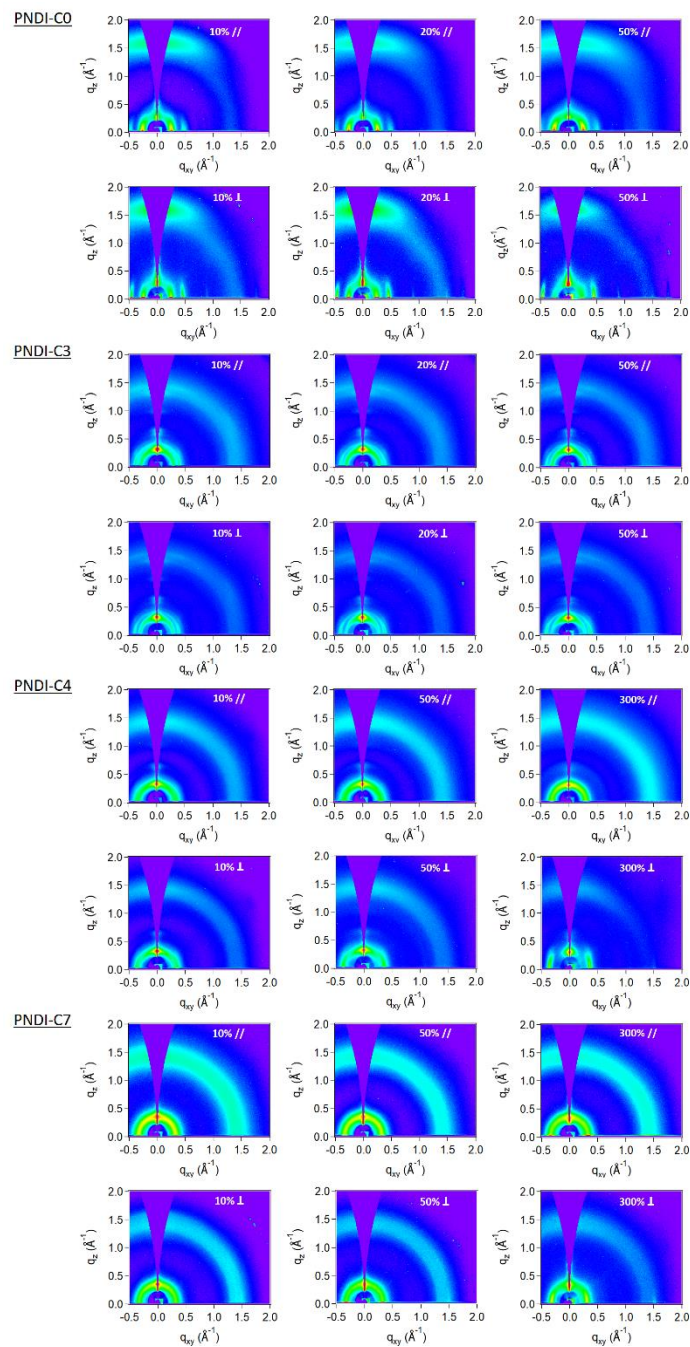
Figure A.7 *2D GIWAXS scattering profiles of PNDI-C0, PNDI-C3, PNDI-C4, and PNDI-C7 under tensile strain for both parallel and perpendicular exposures relative to strain direction.*
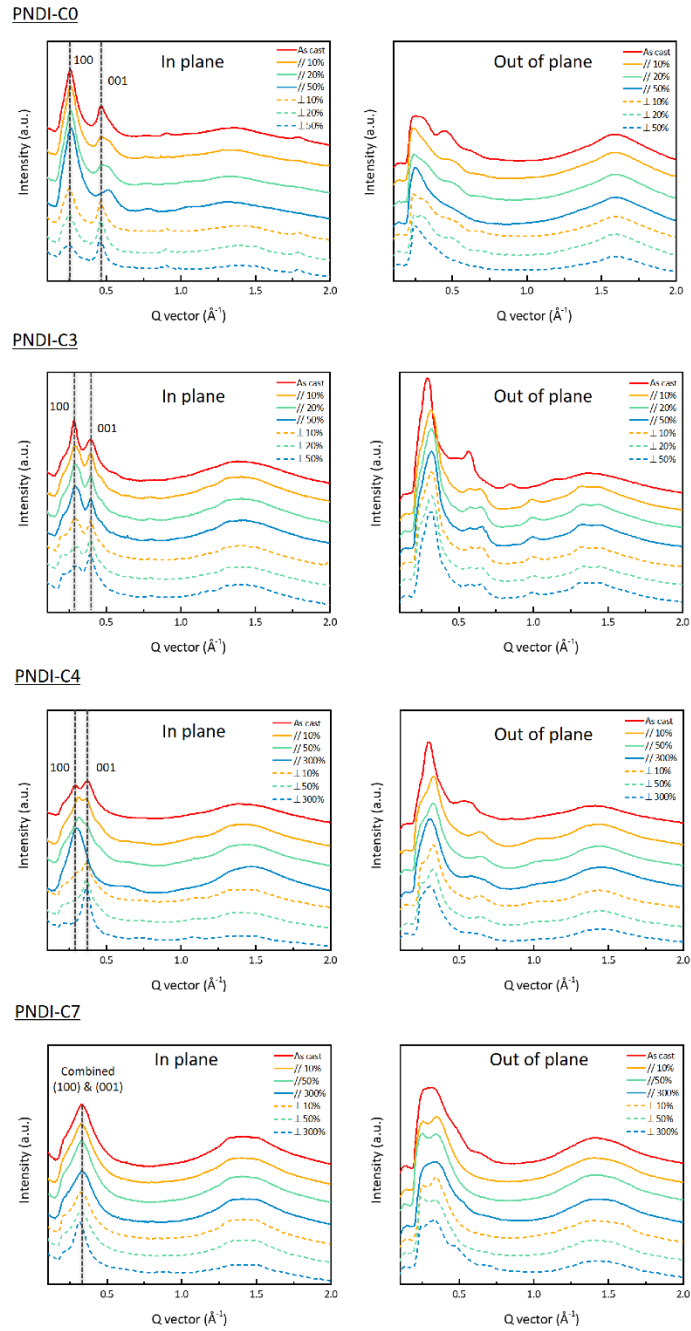
Figure A.8 *1D in-plane and out of plane GIWAXS scattering profiles of PNDI-C0, PNDI-C3, PNDI-C4, and PNDI-C7 under tensile strain for both parallel and perpendicular exposures relative to strain direction.*
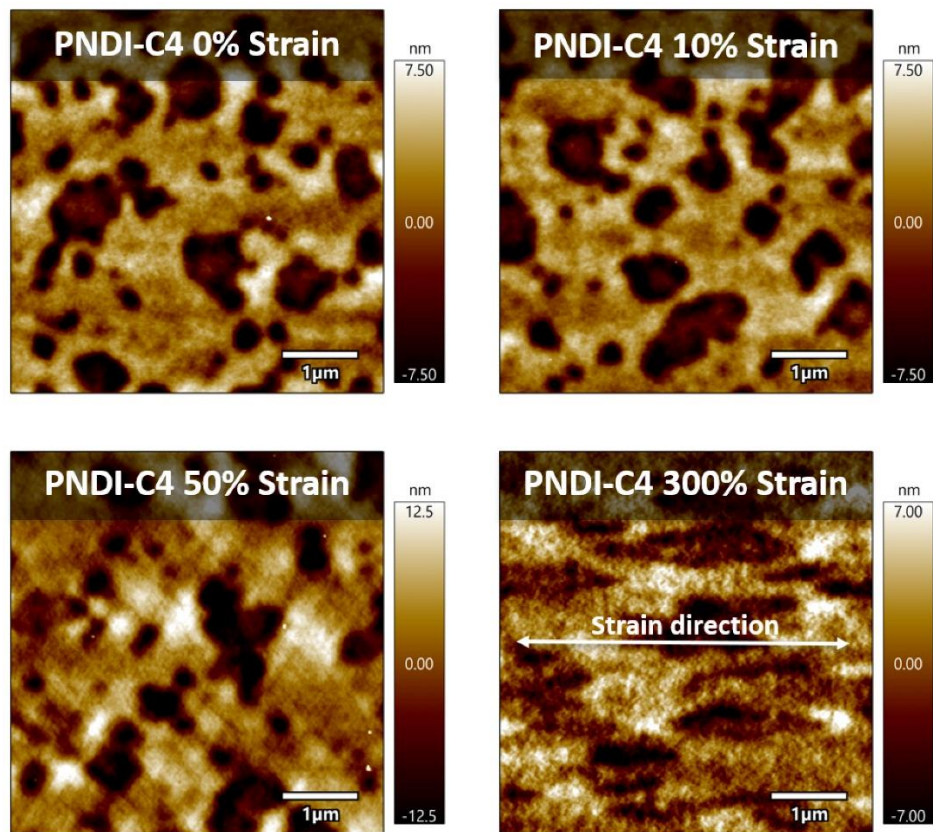
Figure A.9 *Atomic force microscopy of PNDI-C4 under tensile strain*
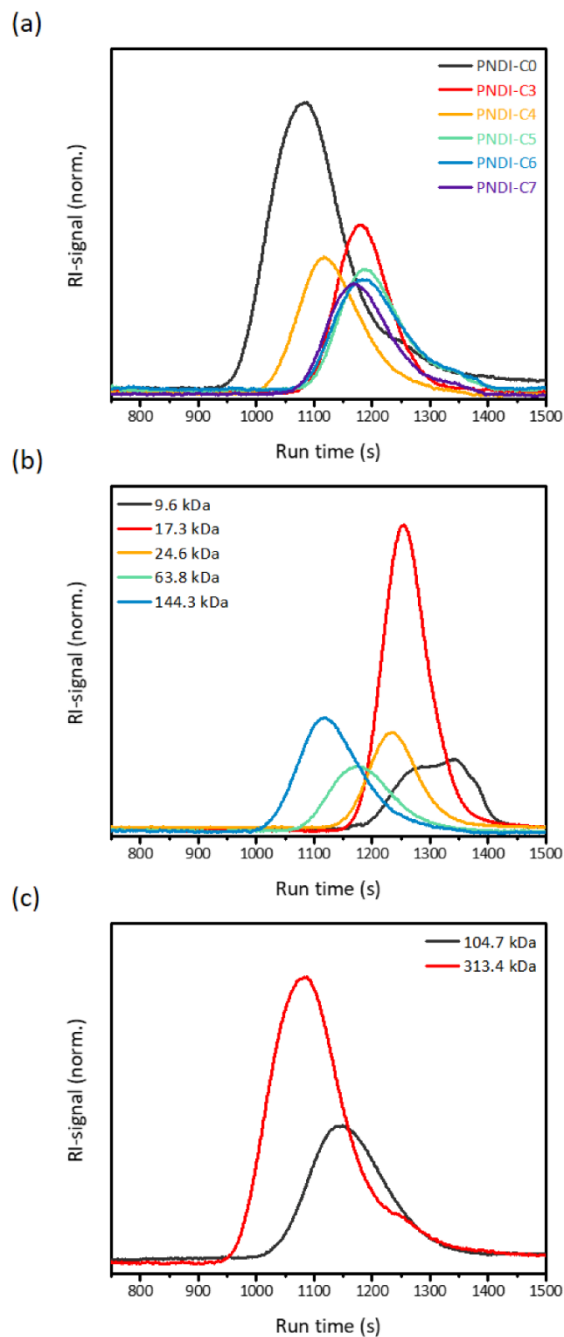
Figure A.10 *High-temperature size exclusion chromatography of PNDI polymers in 1,2,4-trichlorobenzene at 160 ˚C. a) SEC curves for all lengths of CBS incorporation. b) SEC curves of PNDI-C4 of varying molecular weight. c) SEC curves of PNDI-C0 of two molecular weights. All molecular weights shown are weight average molecular weight.*

Table A.1 *SANS fitting parameters and goodness of fitting obtained from SasView*

modeling

	Contour length (Å)	Kuhn length (Å)	Radius (Å)	X2 (Goodness of fitting)
NDI_C0 (25C)	476	521	14	4
NDI_C0 (85C)	310	196	12	2
NDI_C3 (25C)	271	85	13	4
NDI_C3 (85C)	276	84	13	2
NDI_C4 (25C)	447	86	13	2
NDI_C4 (85C)	449	88	13	2
NDI_C5 (25C)	221	86	10	2
NDI_C5 (85C)	233	58	10	2
NDI_C6 (25C)	180	36	9	2
NDI_C6 (85C)	180	45	8	2

Table A.2 *Fitting results for in-plane 1D GIWAXS profiles*

	q (Å^{-1}) [100]	q (Å^{-1}) [001]	q (Å^{-1}) [010]	D-spacing (Å) [100]	D-spacing (Å) [001]	D-spacing (Å) [001]
NDI-C0	0.258	0.470	1.791	24.329	13.358	3.509
NDI-C3	0.284	0.395	NA	22.155	15.919	NA
NDI-C4	0.289	0.371	NA	21.734	16.939	NA
NDI-C5	0.301	0.355	1.551	20.847	17.680	4.051
NDI-C6	0.337		1.454	18.628		4.321
NDI-C7	0.332		1.439	18.927		4.365

Table A.3 *Fitting results for in-plane 1D GIWAXS profiles post tensile strain*

	Parallel Exposure				Perpendicular Exposure			
	q (Å⁻¹) [100]	q (Å⁻¹) [001]	D-spacing (Å) [100]	D-spacing (Å) [001]	q (Å⁻¹) [100]	q (Å⁻¹) [001]	D-spacing (Å) [100]	D-spacing (Å) [001]
NDI-C0	0.258	0.470	24.329	13.358	0.258	0.470	24.329	13.358
10%	0.261	0.485	24.034	12.948	0.252	0.465	24.969	13.525
20%	0.261	0.499	24.086	12.589	0.252	0.465	24.948	13.499
50%	0.263	0.511	23.862	12.290	0.251	0.462	25.043	13.612
NDI-C3	0.284	0.395	22.155	15.919	0.284	0.395	22.155	15.919
10%	0.293	0.394	21.425	15.947	0.292	0.394	21.492	15.945
20%	0.295	0.394	21.292	15.935	0.294	0.394	21.387	15.967
50%	0.296	0.395	21.257	15.916	0.294	0.441	21.360	14.235
NDI-C4	0.289	0.371	21.734	16.939	0.289	0.371	21.734	16.939
10%	0.312	0.368	20.135	17.080	0.301	0.364	20.888	17.253
50%	0.316	0.370	19.855	16.983	NA	0.368	NA	17.087
300%	0.304	NA	20.702	NA	NA	0.366	NA	17.184
NDI-C5	0.301	0.355	20.847	17.680	0.301	0.355	20.847	17.680
NDI-C6	0.337		18.628		0.337		18.628	
NDI-C7	0.332		18.927		0.332		18.927	
10%	0.330		19.023		0.328		19.147	
50%	0.331		18.959		0.328		19.180	
300%	0.334		18.821		0.318		19.745	

Table A.4 *Circle gathering analysis of (100) peak for transmission WAXS of PNDI-C4 under tensile strain*

Strain	Q vector	D-spacing	FWHM	Area	Normalized area
0%	0.304	20.691	0.068	0.419	0.419
10%	0.304	20.664	0.071	0.457	0.470
50%	0.306	20.51	0.083	0.350	0.412
150%	0.299	21.048	0.090	0.323	0.492
300%	0.314	19.983	0.106	0.363	0.583

Table A.5 *Circle gathering analysis of (001) peak for transmission WAXS of PNDI-C4*

under tensile strain

Strain	Q vector	D-spacing	FWHM	Area	Normalized area
0%	0.367	17.105	0.077	0.601	0.601
10%	0.366	17.148	0.076	0.578	0.595
50%	0.366	17.163	0.069	0.528	0.621
150%	0.369	17.032	0.063	0.554	0.846
300%	0.369	17.031	0.049	0.400	0.642
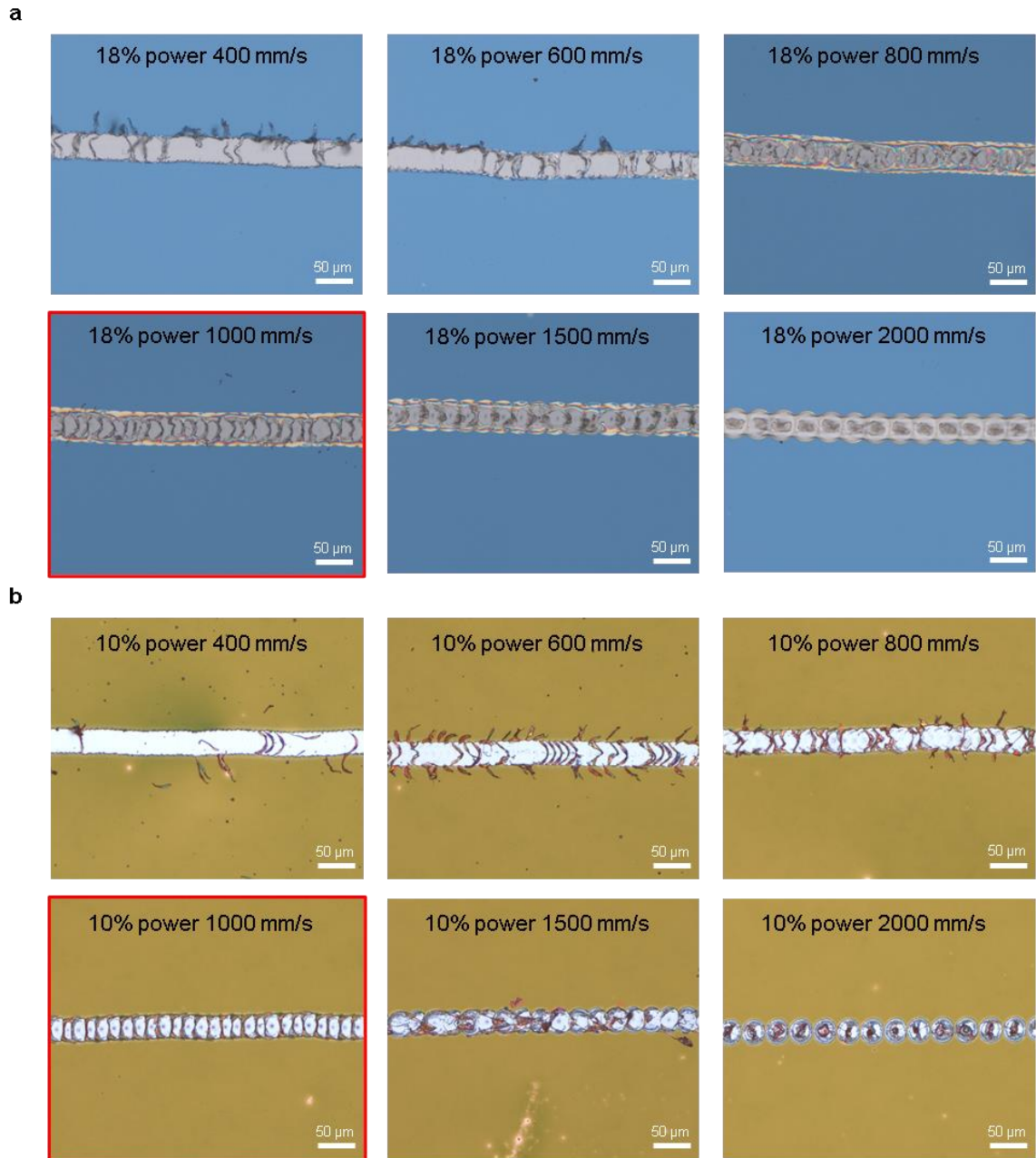
Figure B.1 *Optical images of a) 80 nm PS and b) 80 nm P3HT laser etched under different parameters to create the desired microfiber support. Outlined in red are the desired laser etched fibers for sufficient support throughout the transfer process but weak enough for smooth removal.*

a

b
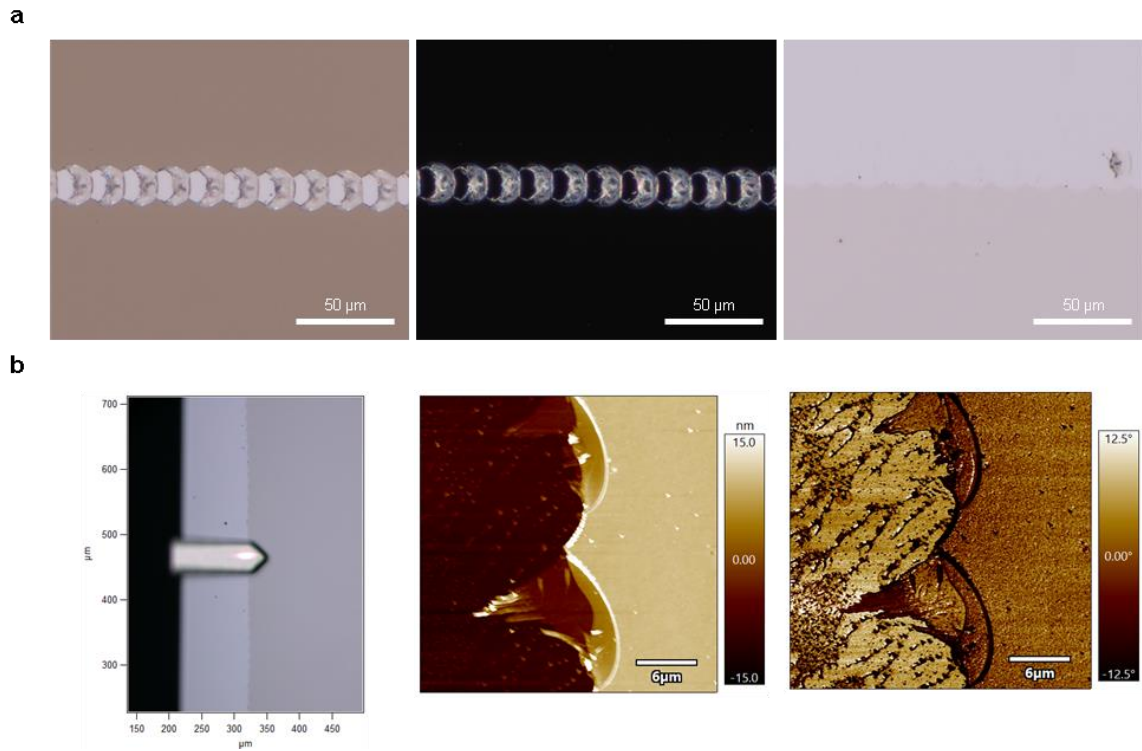
Figure B.2 *Evaluation of 19 nm film integrity before and after side support removal. a) Optical microscopy images of laser etched (4% power) 19 nm PS prior to removal (bright field and dark field) and after removal (right). b) Atomic force microscopy of film edge after removal of side support (optical, height, phase).*
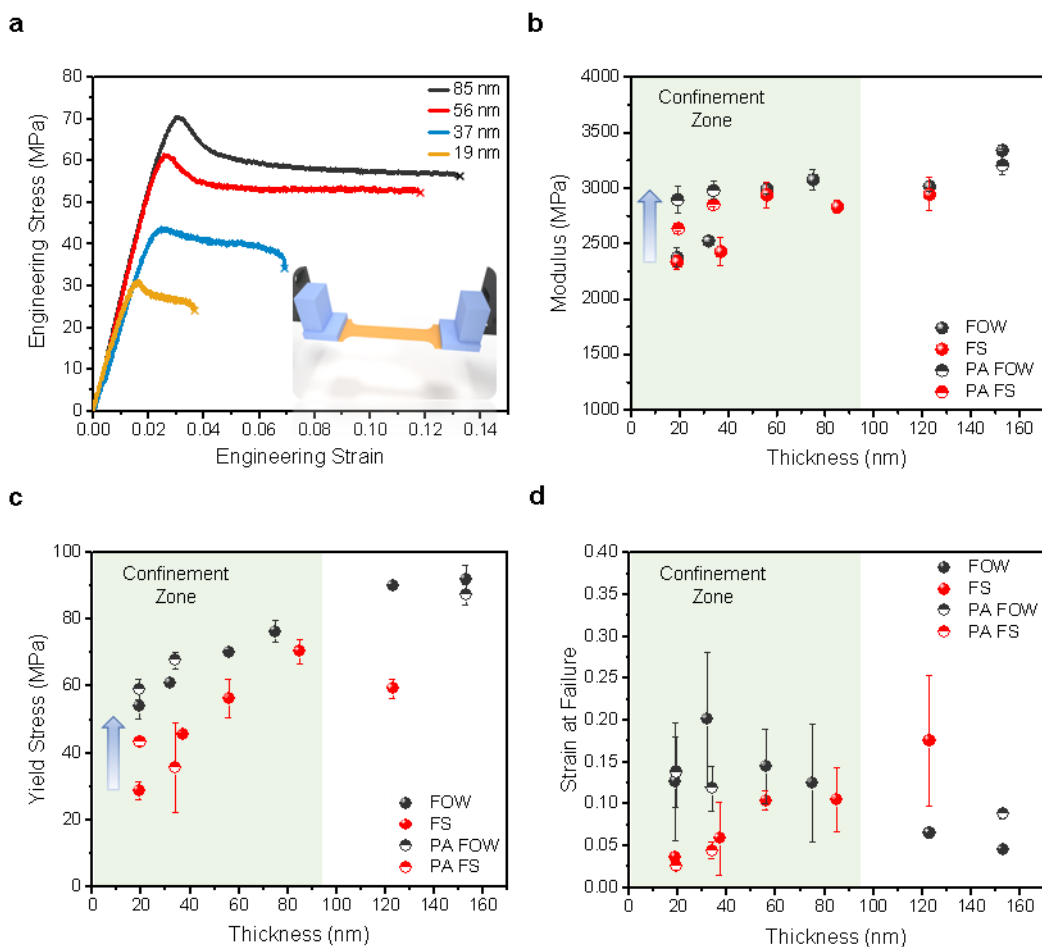
Figure B.3 *Comparison of 2062 kDa PS FS and FOW mechanical properties with reducing film thickness. Gage length is 8 mm. a) Representative stress vs strain profiles of FS PS from 85 nm to 19 nm. b) Elastic modulus thickness dependence of both FS and FOW PS films. Insert represents the loss of inter-entanglements upon confinement at thicknesses below the end-to-end distance of a polymer chain. c) Yield stress thickness dependence of both FS and FOW PS films. d) Strain at failure thickness dependence of both FS and FOW PS films. PA corresponds to samples characterized post vacuum annealing at 115 °C for 1 hr. Yield stress and strain at failure of FS PS differs with that discussed for 4 mm length films due to increased defect density exhibited by the longer*

131

gauge length of 8 mm. Error bars represent the standard deviation of the characterized

mechanical properties.
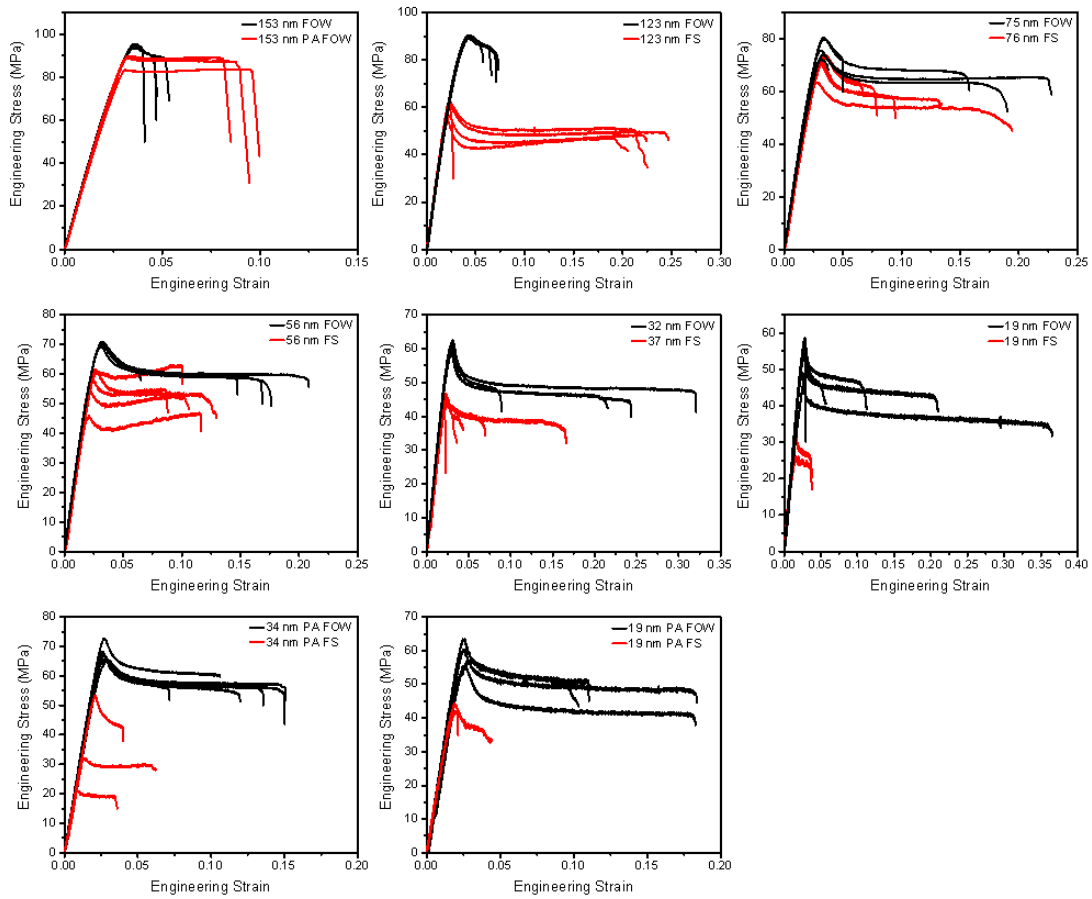
Figure B.4 *Stress - strain profiles of 2062 kDa PS from 153 to 19 nm. PA corresponds to post annealing at 115 °C for 1 hour under vacuum and slow cooled. Gage length of all films is 8 mm.*
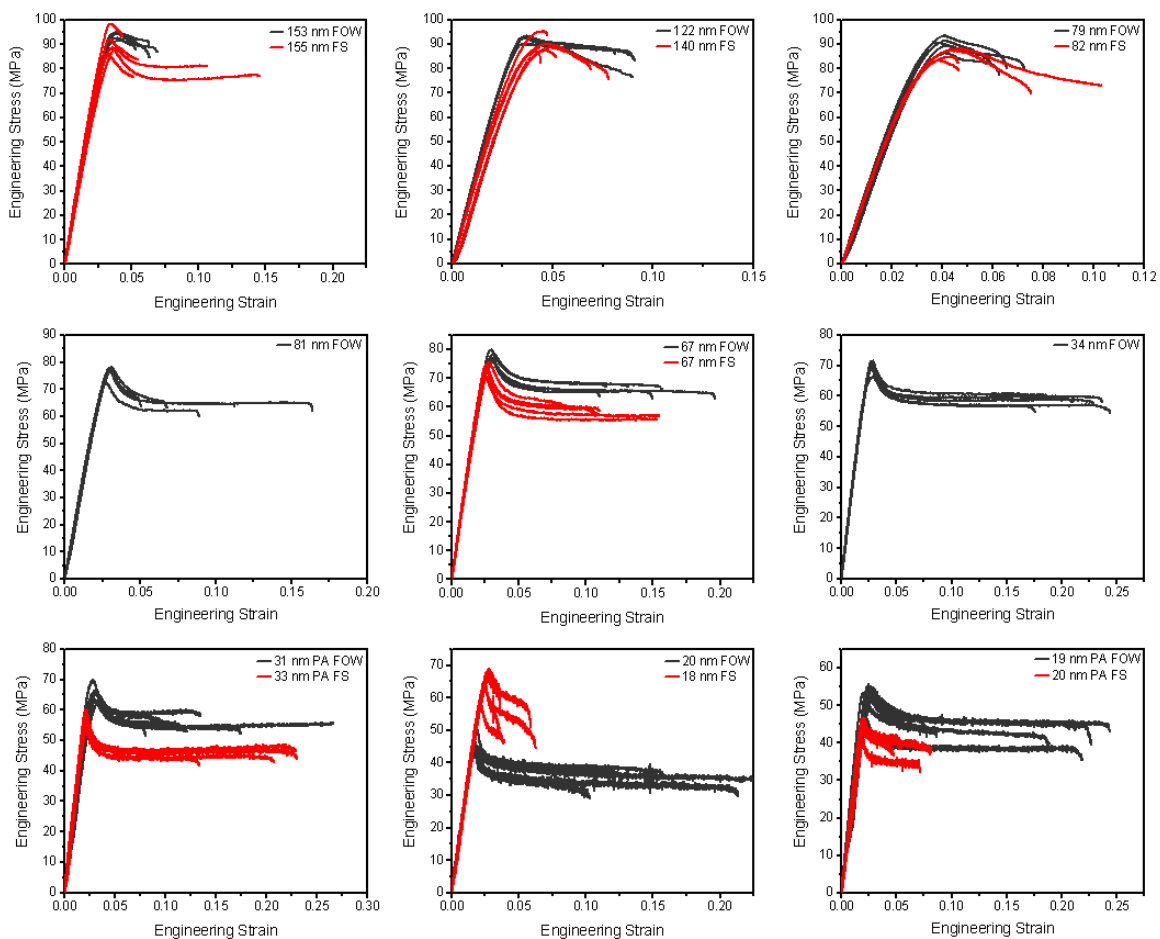
Figure B.5 *Stress - strain profiles of 2062 kDa PS from 155 to 19 nm. PA corresponds to post annealing at 115 ˚C for 1 hour under vacuum and slow cooled. Gage length of all films is 4 mm.*

Figure B.6 *Optical images of 19 nm FS PS with tensile strain of a) 1.6%, b) 2.3%, and c) 3.5%. Gage length is 8 mm.*
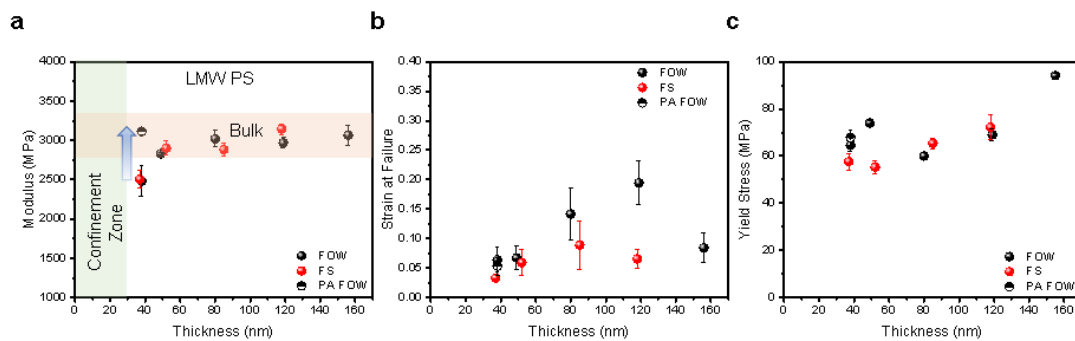
Figure B.7 *a) Modulus b) strain at failure and c) yield stress thickness dependence of 183 kDa PS using both FS and FOW techniques. PA corresponds to samples characterized post vacuum annealing at 115 ˚C for 1 hr. Error bars represent the standard deviation of the characterized mechanical properties.*
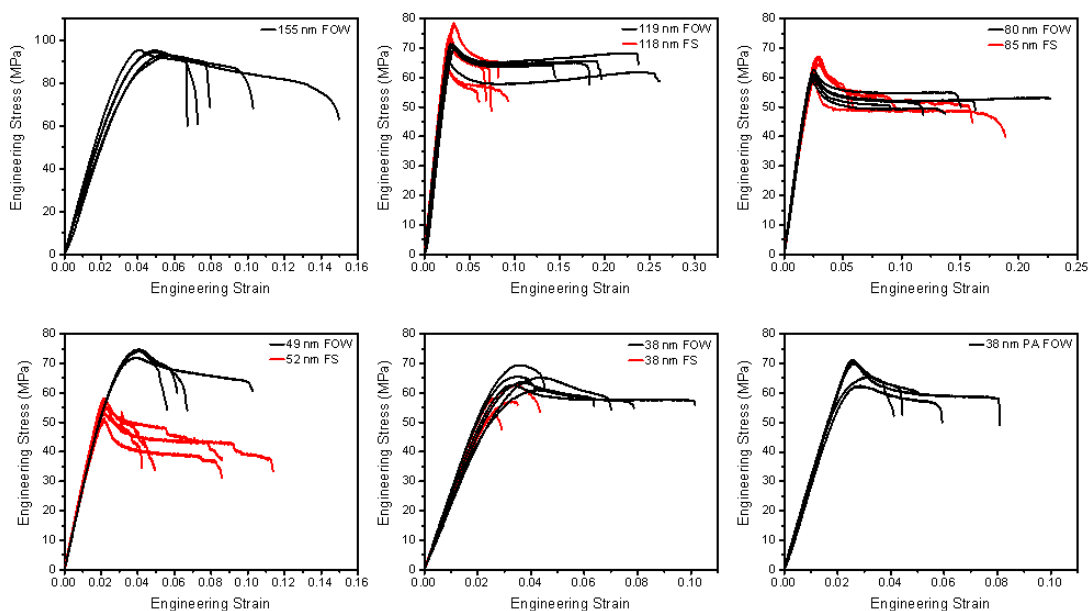
Figure B.8 *Stress - strain profiles of 183 kDa PS from 155 to 38 nm. PA corresponds to post annealing at 115 ˚C for 1 hour under vacuum and slow cooled.*
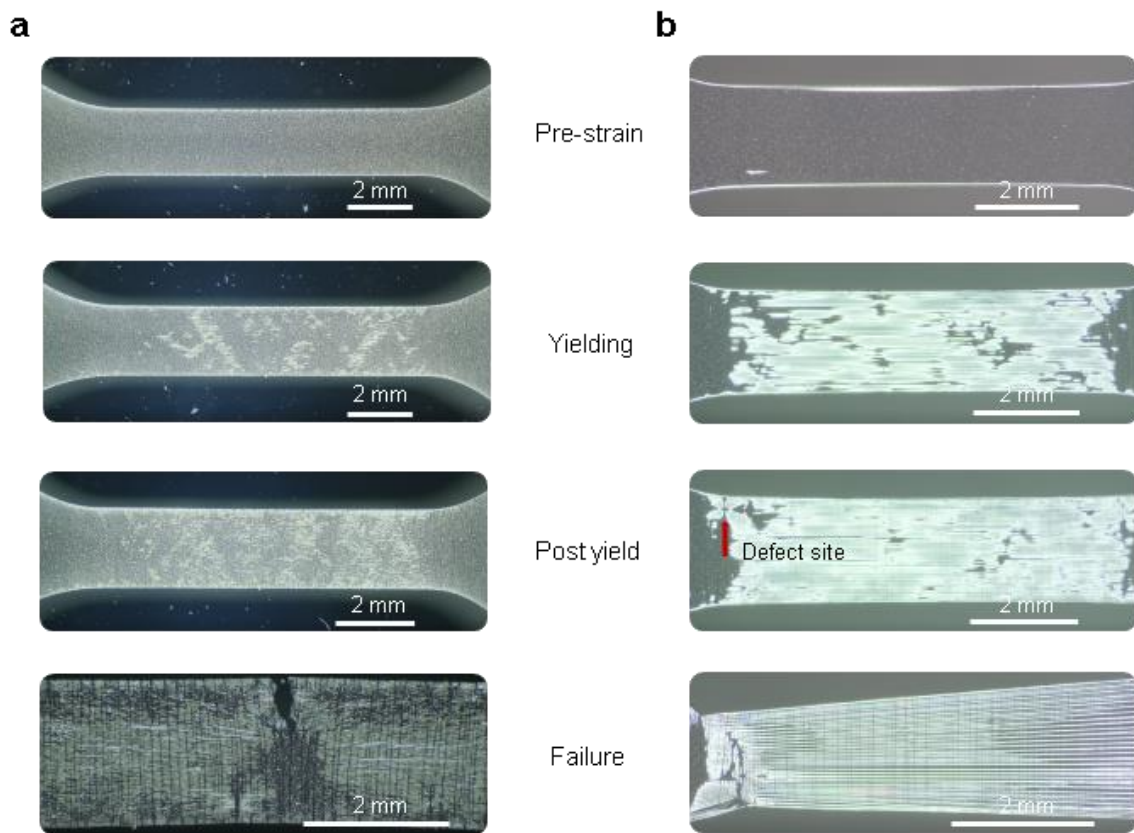
Figure B.9 *Optical microscopy images of 85 nm PS throughout a) on water and b) free-standing tensile strain. The free-standing film fails at the site of a defect seen in the upper left of the post yield image.*

	25x – as cast	25x – 170 °C	500x – 170 °C
Mica			
Silicon			
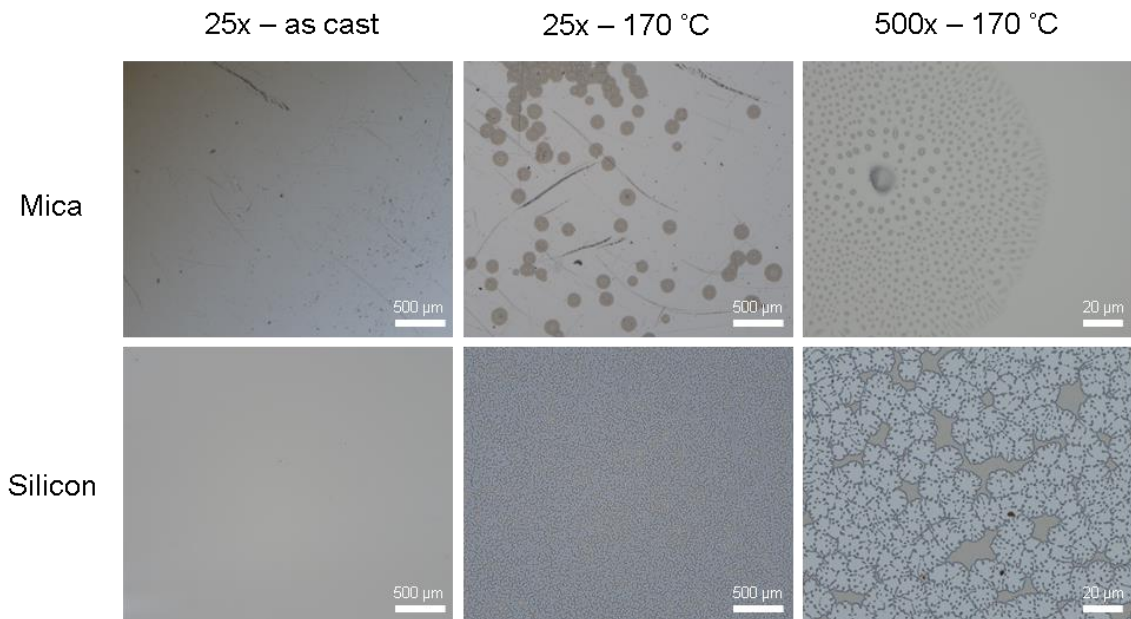
Optical microscopy images of polystyrene spun cast onto both mica and Si substrates followed by annealing at 170 ˚C for 25 minutes, resulting in de-wetting of the film.
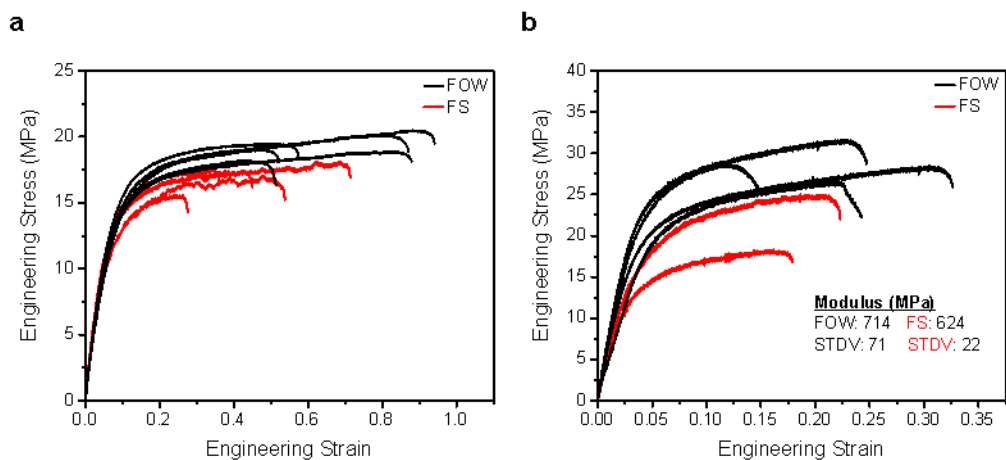
Figure B.10 *a) Representative stress vs strain profiles of 105 nm P3HT for both FOW and FS tensile test. b) Representative stress vs strain profiles of 75 nm DPP-TT for both FOW and FS tensile test. Insert shows the calculated modulus and standard deviation of the profiles shown.*

136
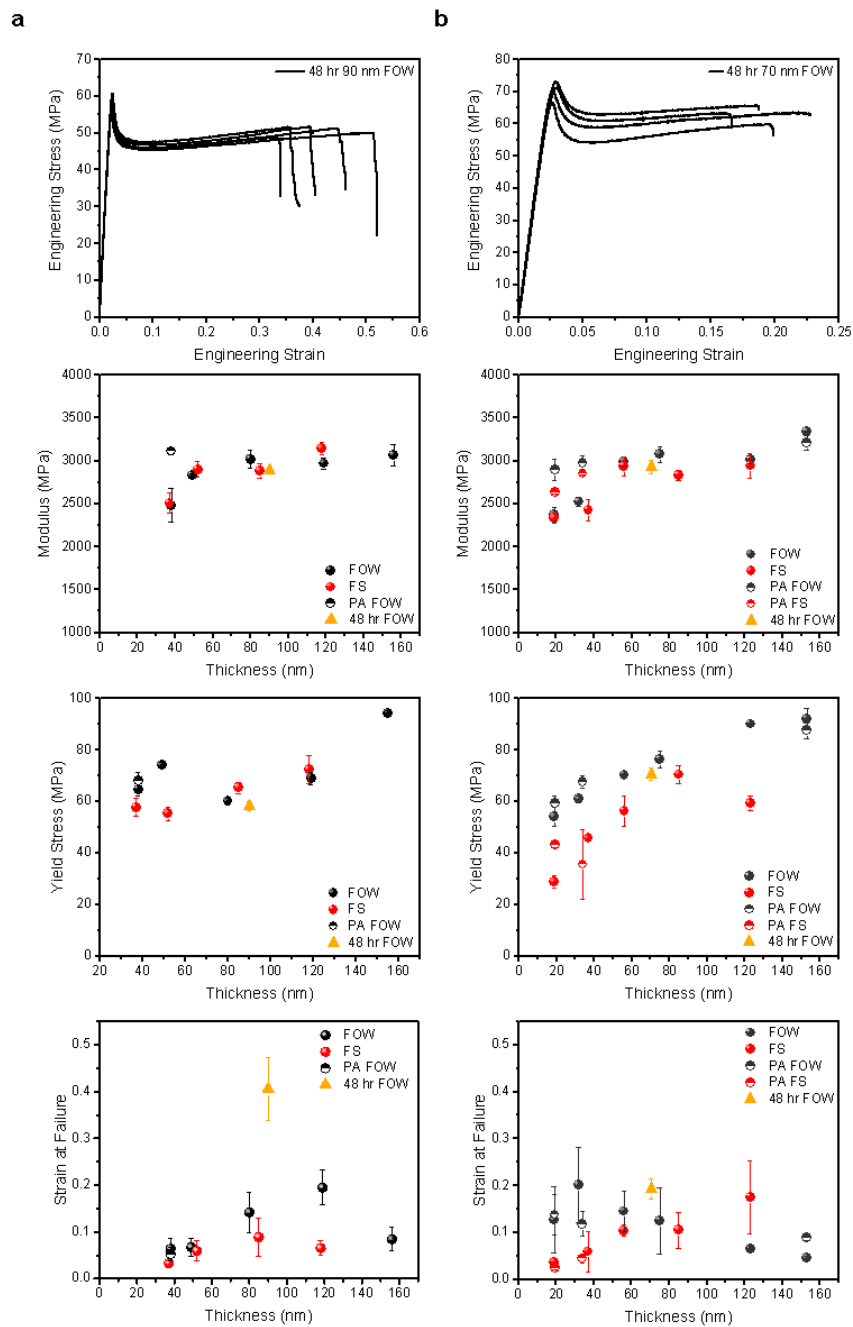
Figure B.11 *Measured mechanical properties of a) 90 nm 183 kDa PS and b) 70 nm 1000*

kDa PS after floating on water for 48 hours compared to original tensile measurements.

PA corresponds to samples characterized post vacuum annealing at 115 ˚C for 1 hr.

Error bars represent the standard deviation of the characterized mechanical properties.
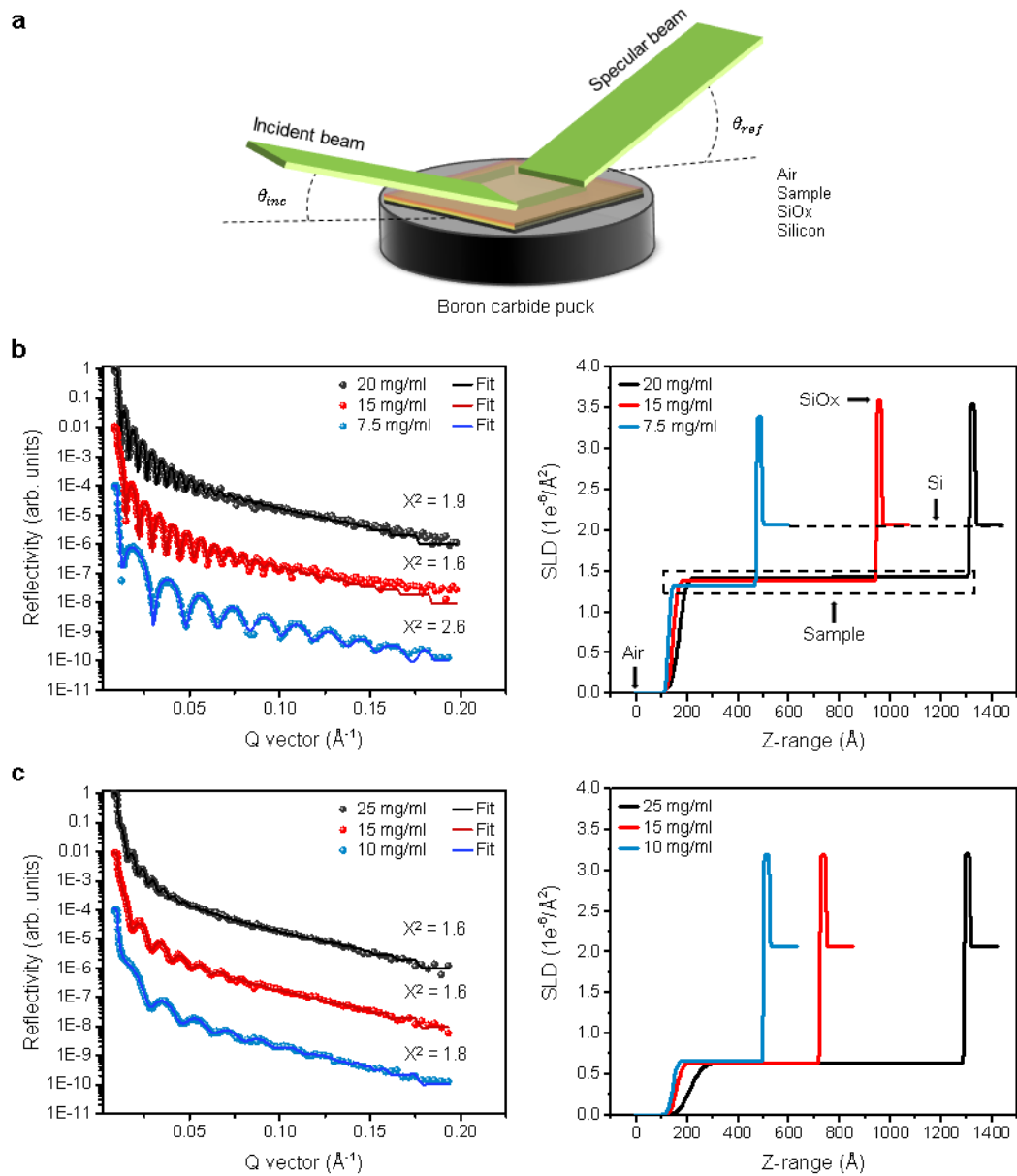
Figure B.12 *a) Representative illustration of the Neutron reflectivity measurement of a dry polymer sample and its associated underlying layers. Reflectivity vs. wave vector and SLD profile for b) dry PS and c) P3HT films of varying thickness. The red and blue curves in each reflectivity plot are shifted downwards by two and four orders of magnitude, respectively.*

138
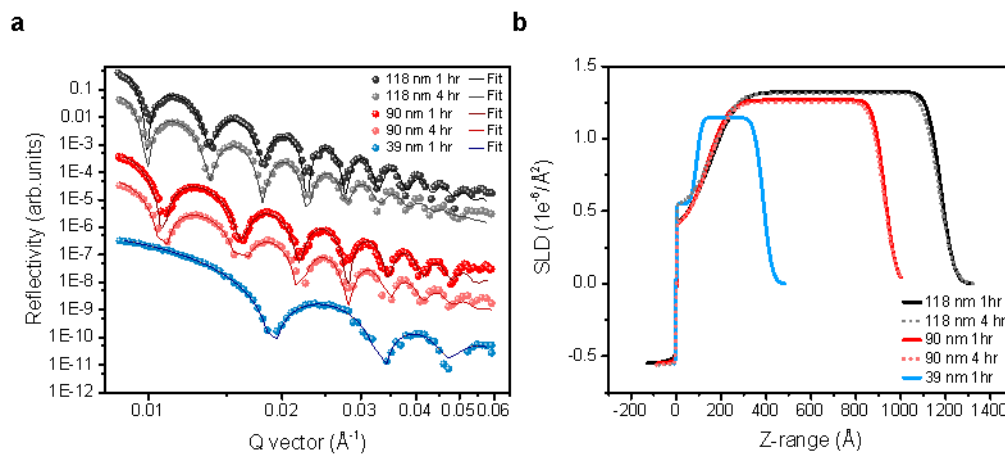
Figure B.13 *Time dependent neutron reflectivity a) fittings and b) SLD profile of 183 kDa PS floating on DI-water for 1 and 4 hours.*
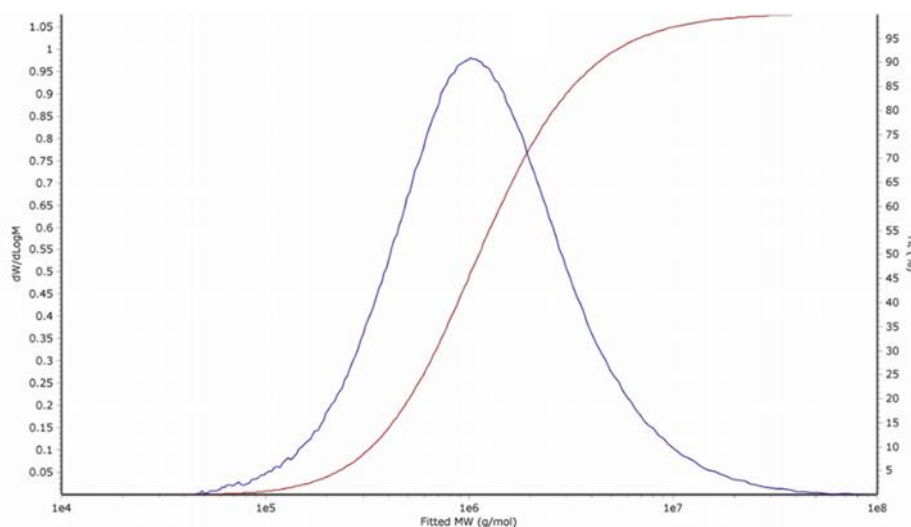
Figure B.14 *Molecular weight distribution of 2062 kDa PS as measured by high temperature GPC.*
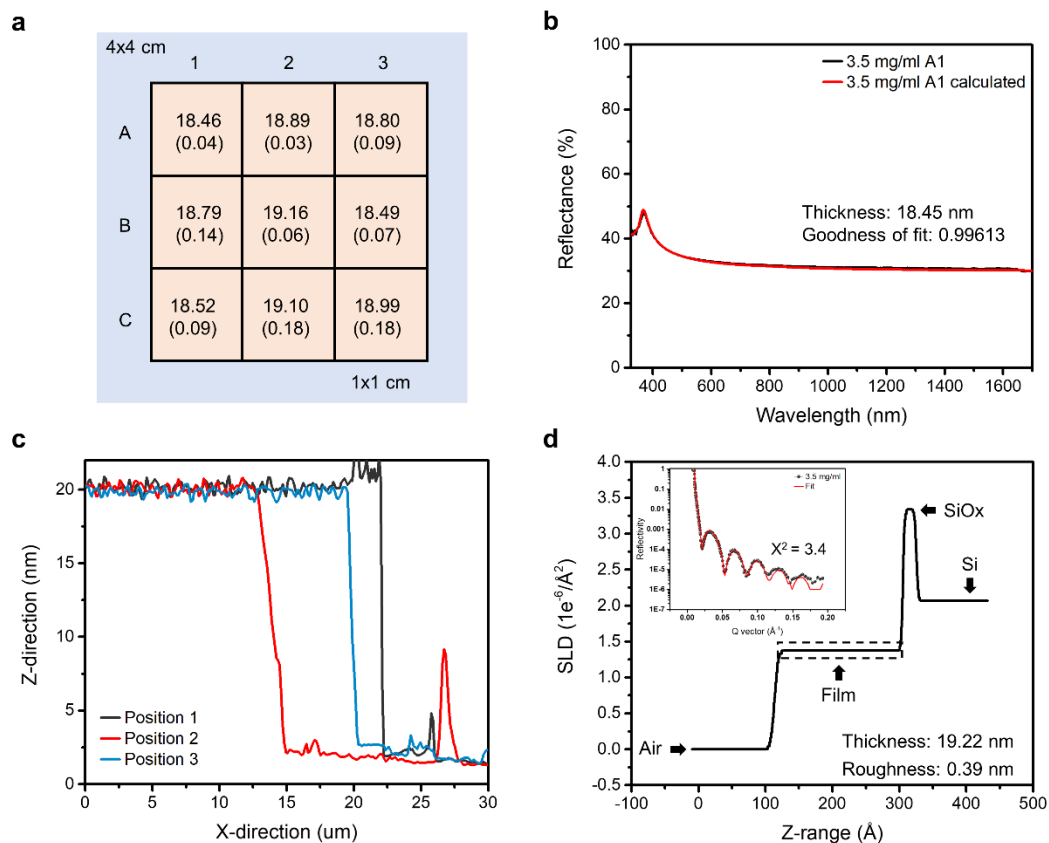
Figure B.15 *Film uniformity of "19" nm PS. a) Measured thickness of 1x1 cm coordinates within a parent 4x4 cm film using interferometry. Standard deviation is in parenthesis and is obtained from three separate measurements and locations within each coordinate. b) Example fitting of interferometer reflectance data of coordinate A1. c) Thickness verification using AFM within coordinate A1, 18.52 nm with a STDEV of 0.23 nm. d) Neutron reflectometry of a separate 5x5 cm PS film, without PSS release layer, demonstrating an average thickness of 19.22 nm and a roughness of 0.39 nm. Insert is of reflectometry fitting quality.*
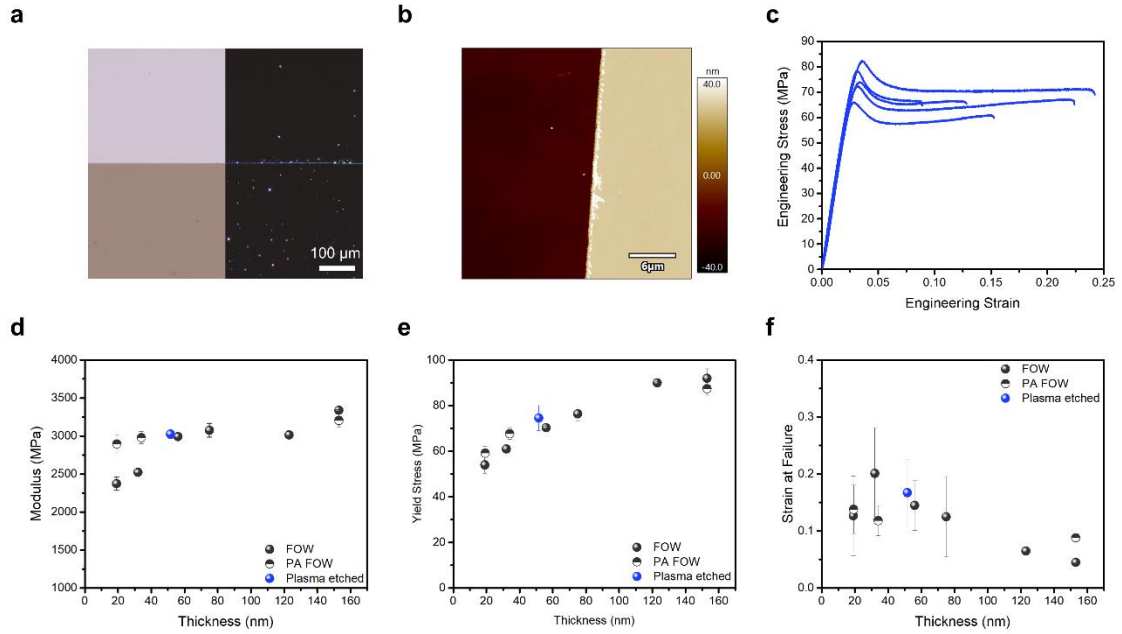
Figure B.16 *Plasma etched 52 nm PS film mechanical properties and comparison to the laser etched process. a) Bright and dark field optical microscopy images of plasma etched PS floated onto clean silicon. b) AFM height image of film edge. c) Stress-strain profile of five consecutive FOW tensile measurements. d-f) Modulus, yield stress, and strain at failure comparison of 52 nm plasma etched PS to that of the laser etched films. Error bars represent the standard deviation of the characterized mechanical properties.*

Table B.1 *Comparison of known methods for measuring the mechanical response of free-standing polymeric thin films.*

Experimental technique	Current capabilities	Disadvantages
Nanobubble inflation	a. Viscoelastic response of films down to 3 nm b. Environmental control	a. Large scale deformation mechanics are not obtainable (micron scale)
Camphor release	a. PC thin film mechanics down to 100 nm b. Full stress-strain profile	a. Transfer process takes 24+ hours b. Sub-100 nm films may not be feasible
TUFF	a. PS thin film mechanics down to 31 nm b. Full stress-strain profile	a. Currently limited to 31 nm b. Full yielding behavior not observed
Guide Frame	a. PS thin film mechanics down to 45 nm b. Full stress-strain profile	a. Limited to 45 nm with relatively low gauge L:W ratio of 0.5 b. 45 nm film shows edge defects
SMART*	a. PS thin film mechanics *sub-20 nm* b. Organic semiconductor mechanics *sub-100 nm* c. Full stress-strain profile with *complete yielding behavior*	

*Method employed in this report

Table B.2 *LIQREF fitting results for 183 kDa PS and P3HT using the Amoeba/Nelder-Mead algorithm engine provided by ORNL*

Polymer	Concentration (mg/ml)	Top layer thickness (Å)	Surface roughness (Å)	Top layer SLD ($1e^{-6}/Å^2$)	Sublayer thickness (Å)	Sublayer roughness (Å)	Sublayer SLD ($1e^{-6}/Å^2$)
PS	20	1026.0	46.1	1.321	151.4	93.5	0.361
	15	789.1	40.0	1.266	138.4	74.8	0.385
	7.5	296.3	31.0	1.146	91.3	18.4	0.552
P3HT	25	1016.0	43.5	0.622	75.8	60.2	0.071
	15	494.9	15.0	0.581	68.6	55.0	0.173
	10	300.7	14.0	0.558	59.3	50.4	0.192
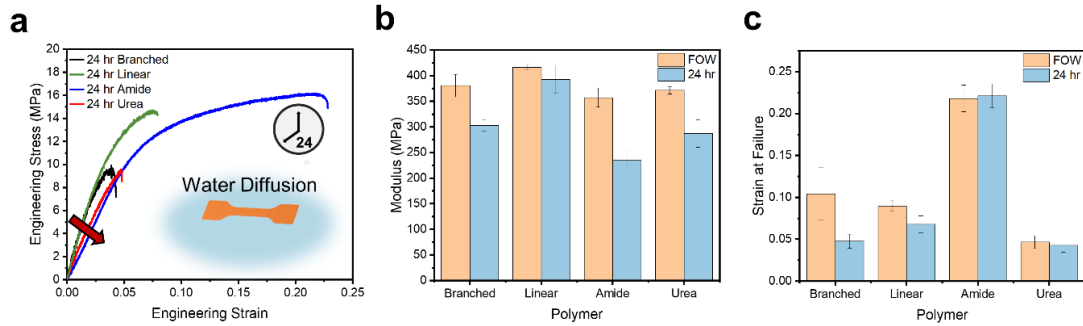
Figure C.1 *Thin film mechanics of DPP-TVT-based polymers after prolonged exposure to water. a) Representative stress-strain plots after exposure to water for a 24-hour period. Insert is an illustration of water diffusion into the dogbone films during prolonged exposure prior to tensile measurement. (b) Modulus of each polymer measured in the standard FOW process compared to films exposed to water for 24 hours. (c) Strain at failure of each polymer measured in the standard FOW process compared to films exposed to water for 24 hours. Error bars represent the standard deviation of the data from a minimum of four consecutive measurements.*
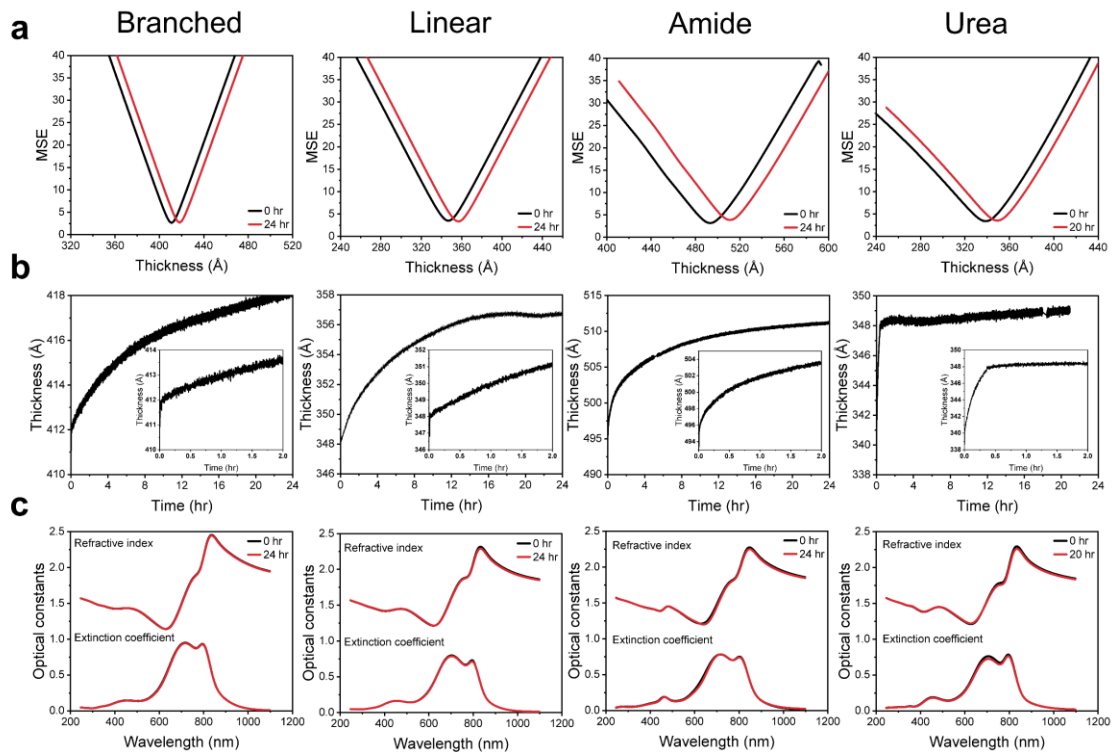
Figure C.2 *In-situ ellipsometry to monitor the swelling behavior of DPP-TVT-based polymers in a water environment. a) Validation of thickness uniqueness obtained from ellipsometry modeling. The minimum MSE provides the thickness used at the 0 and 24 hr time intervals. b) Thickness throughout the swelling measurement. The inserts are of the 1st 2 hours of swelling. c) In-plane optical constants at the 0 and 24 hr time intervals.*
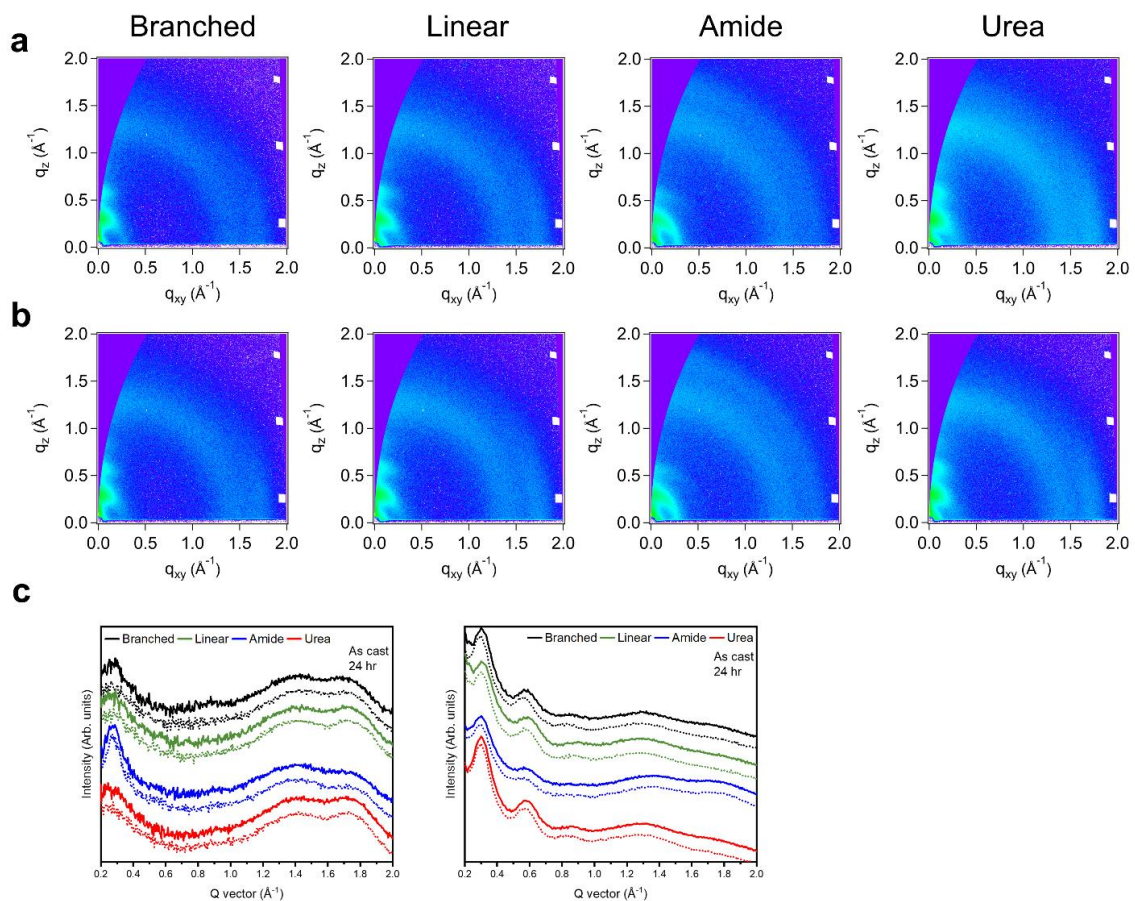
Figure C.3 *Crystalline packing behavior. a) 2D GIWAXS images from the as cast*

polymers. b) 2D GIWAXS images from the polymers after exposing to water for 24 hrs

and subsequently air drying. c) In-plane and out-of-plane line cuts (left to right)
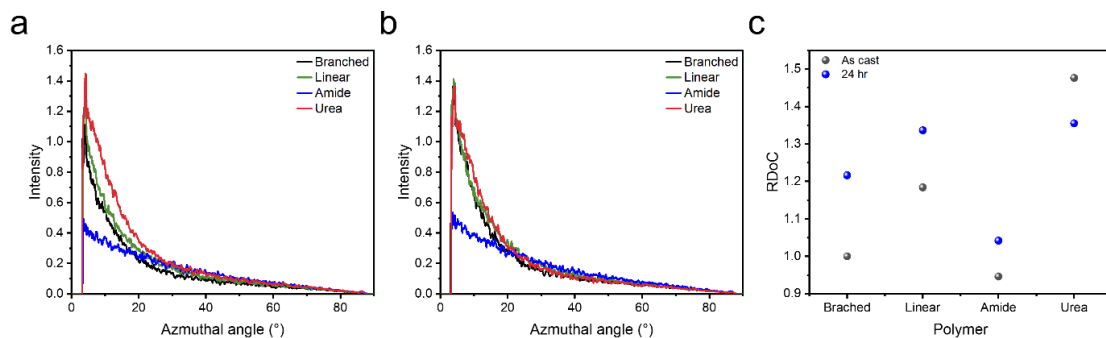
Figure C.4 *Pole figure analysis of the (200) scattering peak from 0 to 90°. a) As cast films. b) Films exposed to water for 24 hours. c) rDoC comparison of as cast films and those exposed to water for 24 hrs.*
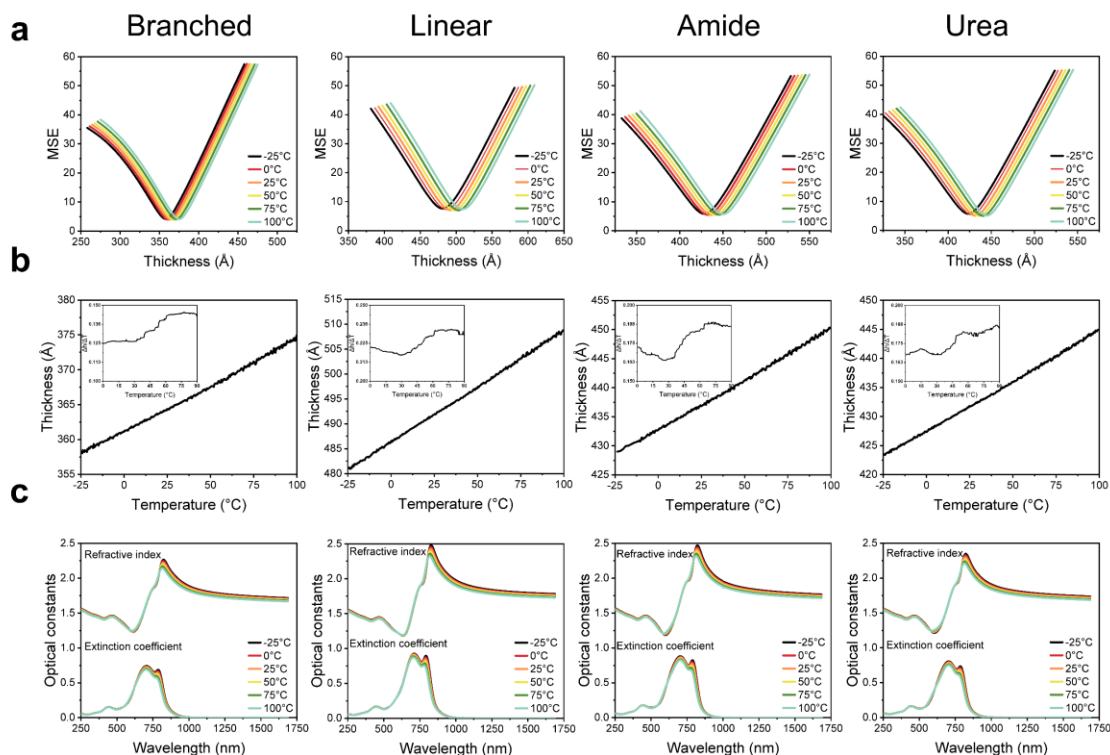
Figure C.5 *Temperature dependent ellipsometry to assess thin film Tg. a) Validation of thickness uniqueness obtained from ellipsometry modeling. The minimum MSE provides the thickness used at each of the representative temperature intervals. b) Temperature dependent thickness of each film. The inserts are the derivative of the thickness as a*

146

function of temperature. c) In-plane optical constants at each of the representative

temperature intervals.

% ε	0%			25%			50%			75%		
	μ (cm^2/Vs)	V_{th} (V)	$I_{ON/OFF}$	μ (cm^2/Vs)	V_{th} (V)	$I_{ON/OFF}$	μ (cm^2/Vs)	V_{th} (V)	$I_{ON/OFF}$	μ (cm^2/Vs)	V_{th} (V)	$I_{ON/OFF}$
‖	**0.148 ±** 0.039	-19.6	10^7	0.039 ± 0.054	-20.8	10^6	0.041 ± 0.009	-4.57	10^6	0.033 ± 0.009	-6.66	10^3
⊥				0.054 ± 0.005	-17.0	10^6	0.053 ± 0.002	-5.59	10^6	0.057 ± 0.006	-7.82	10^6
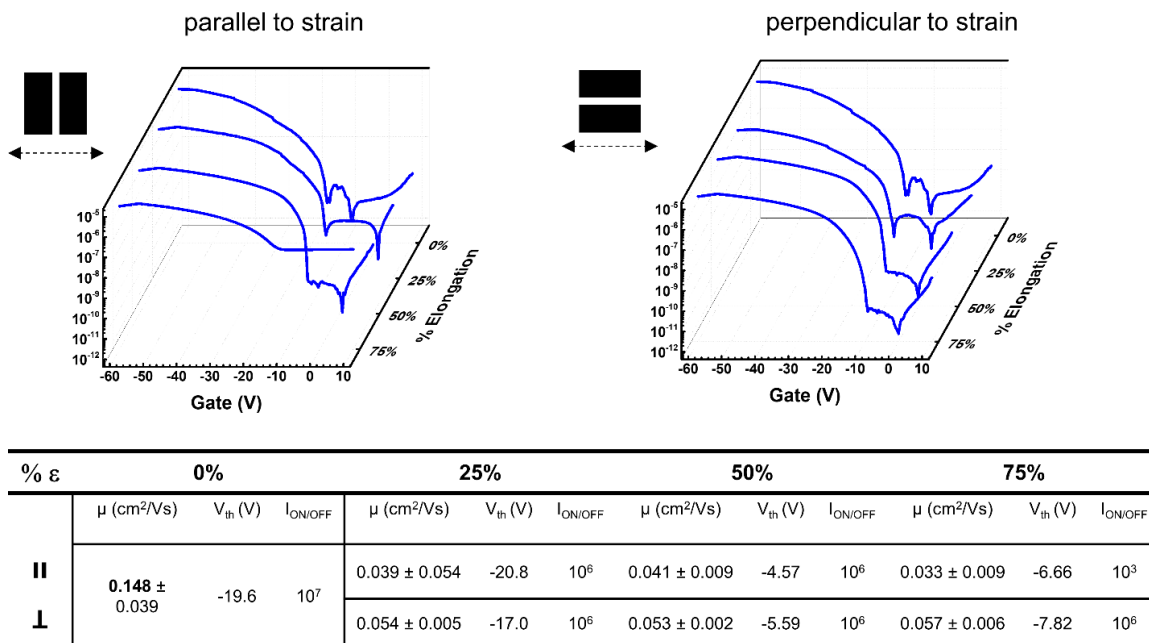
Figure C.6 *Strain dependent charge transport properties of DPP-Linear taken parallel*

and perpendicular to the strain direction.

parallel to strain   perpendicular to strain

% ε	0%			25%			50%			75%		
	μ (cm^2/Vs)	V_{th} (V)	$I_{ON/OFF}$	μ (cm^2/Vs)	V_{th} (V)	$I_{ON/OFF}$	μ (cm^2/Vs)	V_{th} (V)	$I_{ON/OFF}$	μ (cm^2/Vs)	V_{th} (V)	$I_{ON/OFF}$
‖	**0.199** ± 0.020	**-9.93**	10^6	0.171 ± 0.018	-10.8	10^6	0.117 ± 0.049	-10.3	10^6	0.073 ± 0.018	-9.27	10^5
⊥				0.088 ± 0.022	-9.95	10^5	0.053 ± 0.020	-8.63	10^6	0.057 ± 0.006	-9.63	10^5
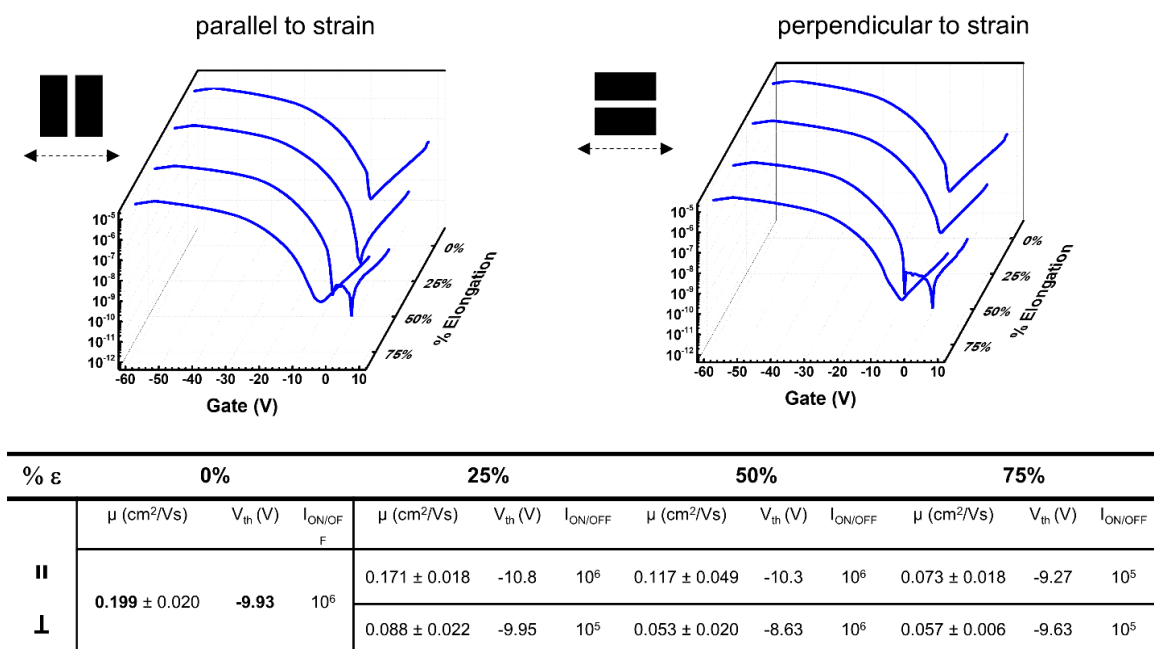
Figure C.7 *Strain dependent charge transport properties of DPP-Amide taken parallel and perpendicular to the strain direction.*

% ε	0%			25%			50%			75%		
	μ (cm²/Vs)	V_{th}(V)	$I_{ON/OFF}$	μ (cm²/Vs)	V_{th}(V)	$I_{ON/OFF}$	μ (cm²/Vs)	V_{th}(V)	$I_{ON/OFF}$	μ (cm²/Vs)	V_{th}(V)	$I_{ON/OFF}$
∥	**0.0154** ± 0.0023	**-7.76**	10^5	0.0009 ± 0.0005	-8.81	10^4	0.0006 ± 0.00003	-8.68	10^3	0.0003 ± 0.00001	-5.40	10^3
⊥				0.0011 ± 0.0005	-9.02	10^3	0.0008 ±0.00007	-7.05	10^3	0.0006 ±0.0004	-10.03	10^3
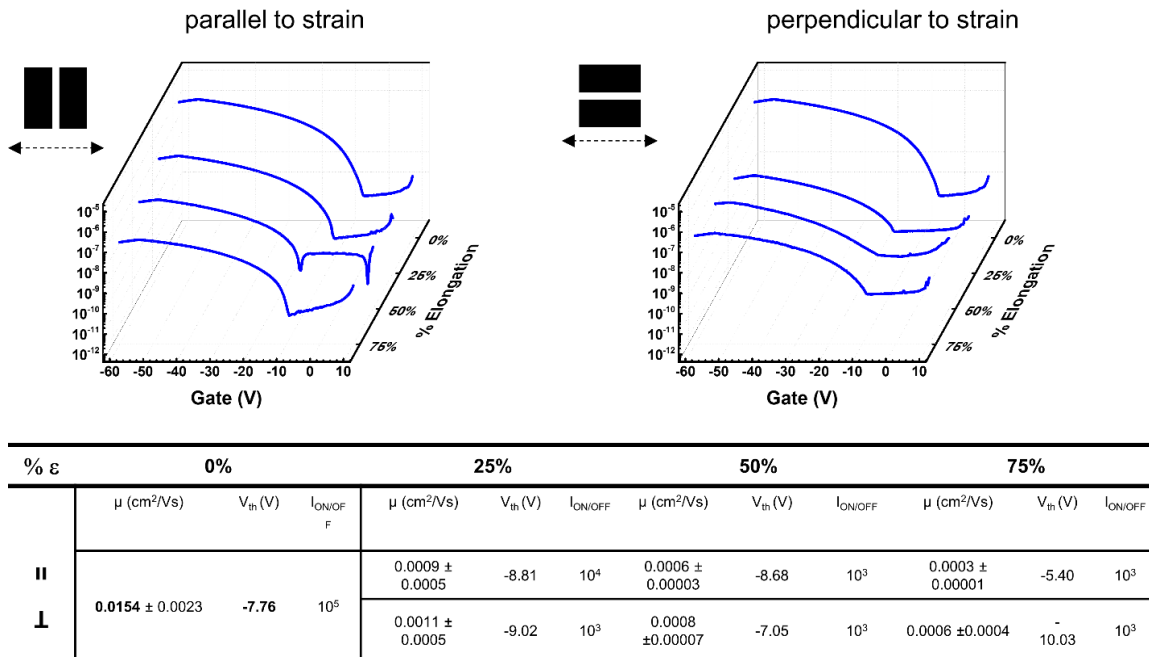
Figure C.8 *Strain dependent charge transport properties of DPP-Urea taken parallel and perpendicular to the strain direction.*
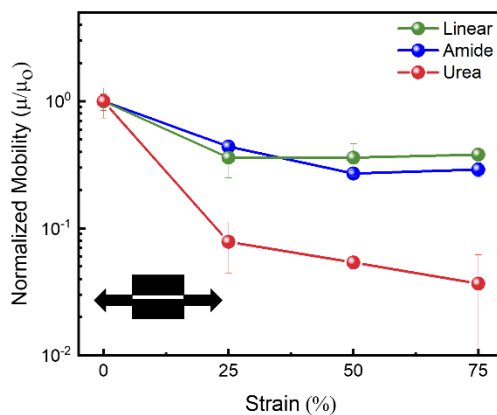
Figure C.9 *Strain dependence on the normalized mobility of the statistical copolymers in perpendicular to strain direction.*

149

Materials synthesis

Variable Temperature-Nuclear Magnetic Resonance (VT-NMR) spectra were recorded on a Bruker 300 MHz. The spectra for all polymers were obtained in deuterated 1,1,2,2-tetrachlotoethane (TCE-d_2) at 120°C. Chemical shifts are given in parts per million (ppm). Number average molecular weight (M_n), weight average molecular weight (M_w), and polydispersity index (PDI) were evaluated by high-temperature size exclusion chromatography (SEC) using 1,2,4-trichlorobenzene and performed on an EcoSEC HLC-8321GPC/HT (Tosoh Bioscience) equipped with a single TSKgel GPC column (GMHHR-H; 300 mm × 7.8 mm) calibrated with monodisperse polystyrene standards. The samples were prepared using 1 mg/mL concentrations in trichlorobenzene (TCB), which were stirred for 12 h at 80 °C prior to injection. The analysis of the samples was performed at 180 °C with a flow rate of 1.0 mL/min with injection quantities of 300 μL. The data were collected and integrated using EcoSEC. 8321GPC HT software suite. A microwave vessel equipped with a stir bar was charged with the appropriate amount of, 3,6- bis(5-bromothiophen-2-yl)-2,5-bis(2-decyltetradecyl)-2,5-dihydropyrrolo[3,4-c]pyrrole-1,4- dione (88.48 mg, 0.078 mmol), and DPP-Urea monomer1 (7.91 mg, 0.0087 mmol), followed by the addition of anhydrous chlorobenzene (3.48 mL). The solution was then bubbled with N2 gas for 30 minutes, followed by addition of Pd2dba3 (1.60 mg, 0.0017 mmol) and P(o-tolyl)3 (2.39 mg, 0.0078 mmol). The vessel was then immediately sealed with a snap cap and microwave irradiated under the following conditions with ramping temperature (Microwave Setup: Biotage Microwave Reactor; Power, 300 W; Temperature and Time, 2 minutes at 100 oC, 2 minutes at 120 oC, 5 minutes at 140 oC, 5 minutes at 160 oC, and 40 minutes at 180 oC; Pressure, 17 bar;

Stirring, 720). After completion, the polymer was end-capped with trimethylphenyl tin

(20.98 mg, 0.087 mmol) and bromobenzene (13.7 mg, 0.087 mmol), successively

(Microwave Setup: Biotage Microwave Reactor; Power, 300 W; Temperature and Time,

1 minute at 100 oC, 1 minute at 120 oC, 2 minutes at 140 oC, 3 minutes at 160 oC;

Pressure, 17 bar; Stirring, 720). The reaction was then cooled to room temperature and

dissolved in 1,1,2,2-tetrachloroethane (TCE). This solution was then precipitated in

methanol and the solid was collected by filtration into a glass thimble. The contents of the

thimble were then extracted successively in a Soxhlet extractor with methanol, acetone,

hexane and finally chlorobenzene. The chlorobenzene fraction was then concentrated

under reduced pressure and re-precipitated in methanol, followed by filtration, and drying

under vacuum. Molecular weight estimated from high temperature GPC: Mn = 31, 316

Da, Mw = 56, 880 Da, PDI = 1.82. 1 H NMR (300 MHz, 1,1,2,2-TCE-d2, 393 K): 13C

NMR could not be attained due to low solubility of the polymer.
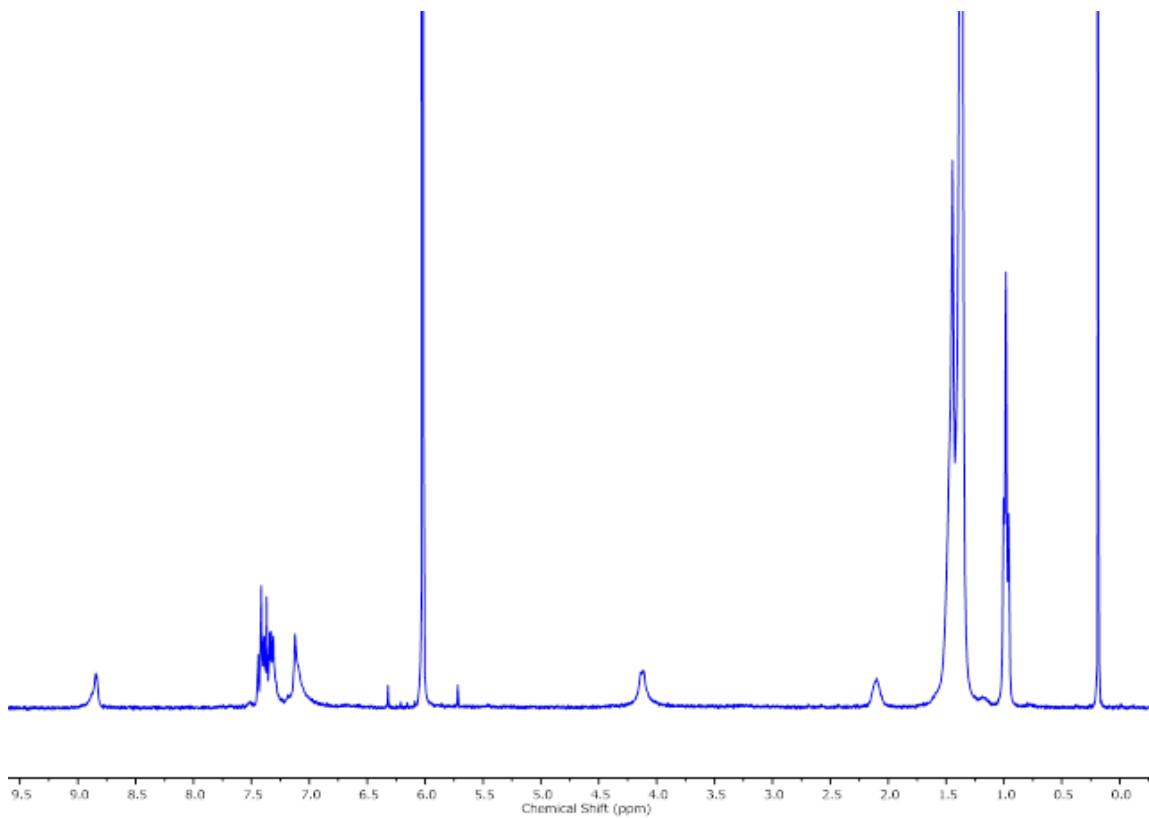
Figure C.10 *¹H NMR spectrum of DPP-Urea in 1,1,2,2-tetrachloroethane-d₂ at 120 °C*

Polymer (y:x)	Theoretical ratio (a:b)	Calculated ratio (a:b)
P(DPP-TVT) 10% Amide	40:4	40:4.4
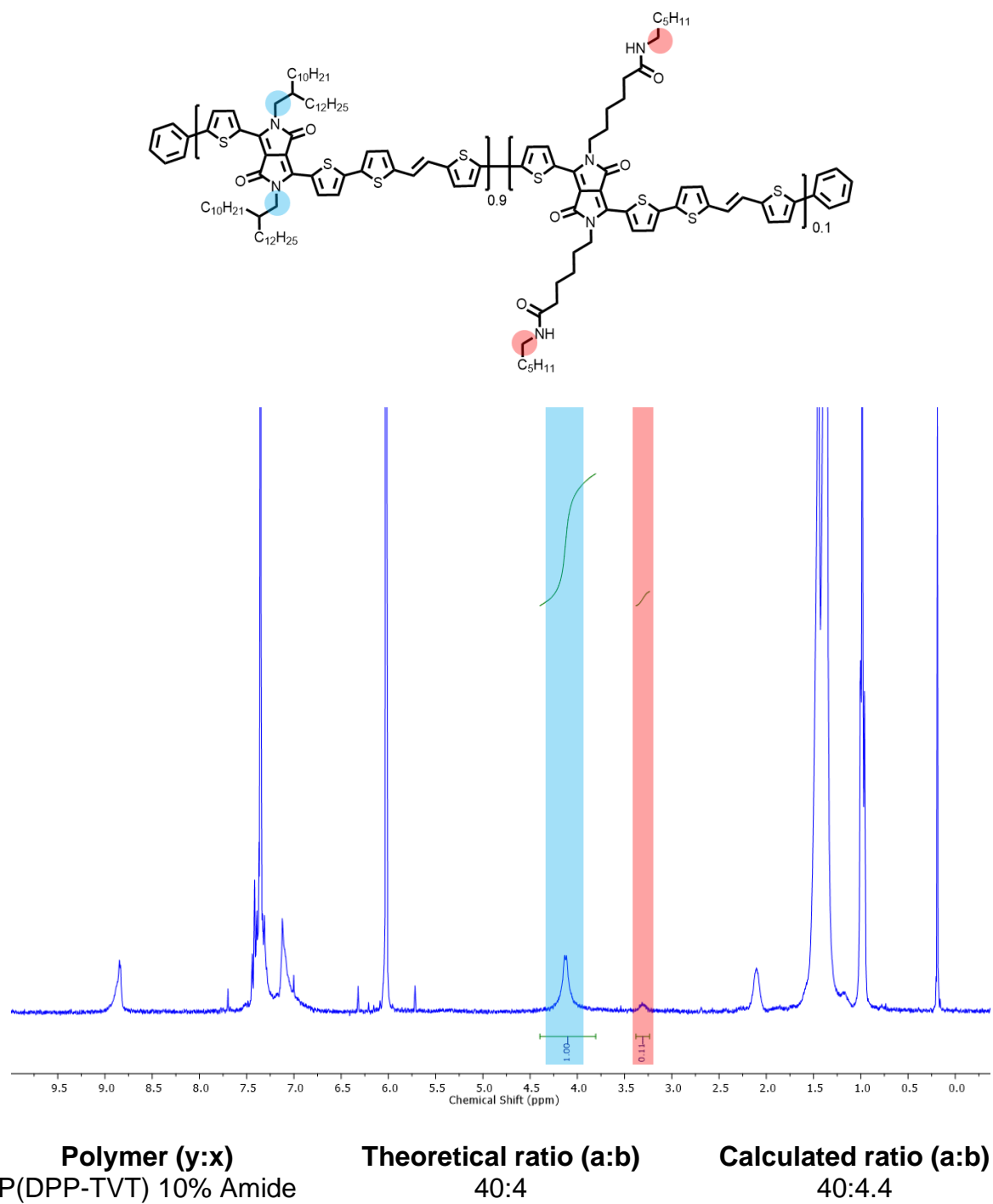
Figure C.11 *1H NMR spectrum of DPP-Amide in 1,1,2,2-tetrachloroethane-d2 at 120 °C with experimental and calculated theorical ratios assuming 10 repeat units*
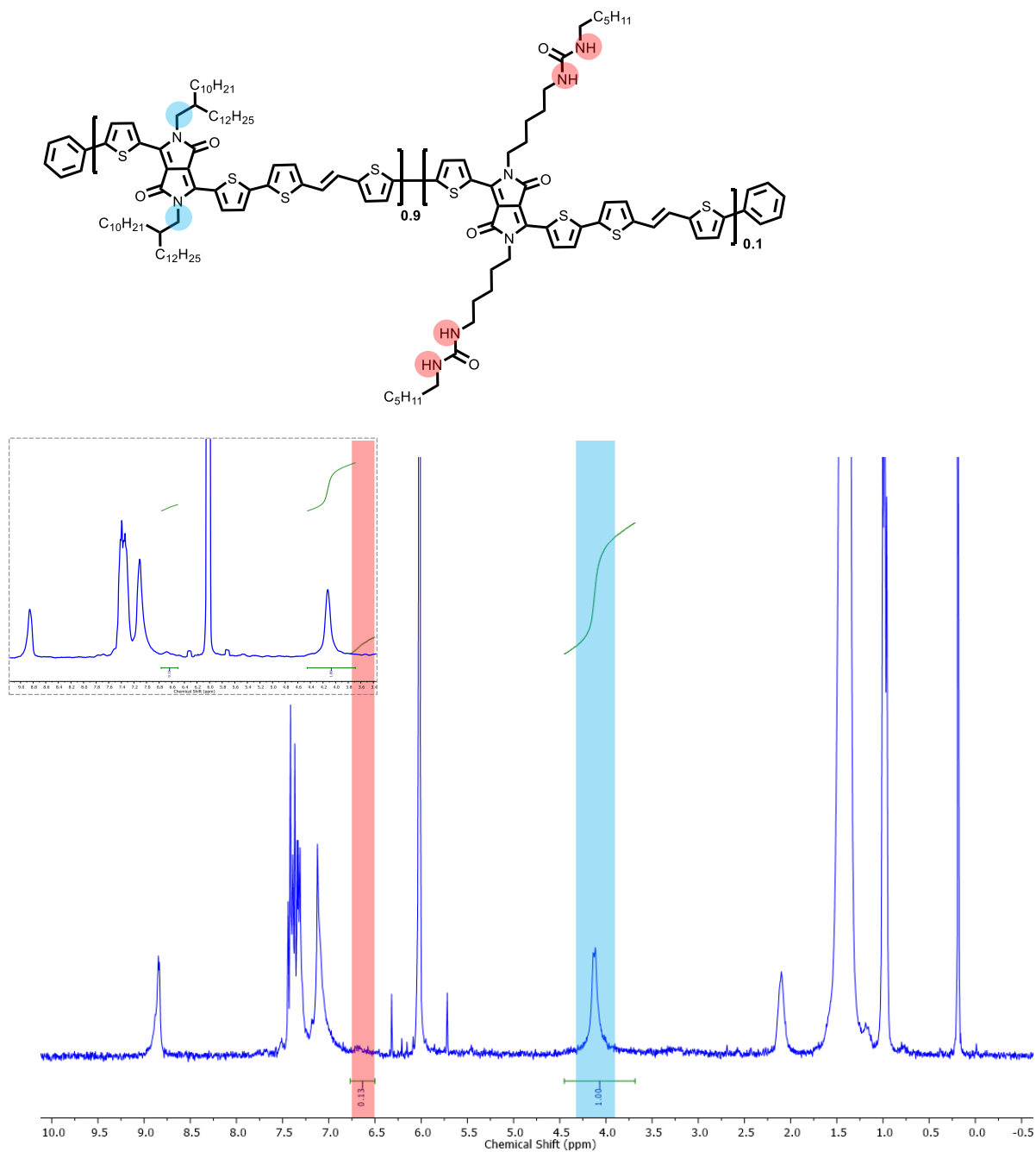
Figure C.12 *1H NMR spectrum of DPP-Urea in 1,1,2,2-tetrachloroethane-d2 at 120 °C with experimental and calculated theorical ratios assuming 10 repeat units. Urea protons were used for experimental ratio calculation. as opposed to the protons alpha to the*

carbonyl, due to the absence of these protons in the NMR. This is consistent with NMR

spectra collected for similar DPP-Urea containing polymers.

Table C.1 *GIWAXS fitting results from the in-plane 1D scattering profile.*

Polymer	Q (010)	FWHM (010)	D-spacing	Δ D	Δ FWHM
Branched	1.738	0.218	3.616	-0.030	-0.015
Branched 24 hr	1.752	0.203	3.585		
Linear	1.758	0.222	3.574	-0.014	0.006
Linear 24 hr	1.765	0.228	3.560		
Amide	1.766	0.212	3.557	-0.010	-0.015
Amide 24 hr	1.771	0.197	3.547		
Urea	1.757	0.227	3.576	0.000	-0.013
Urea 24 hr	1.757	0.214	3.576		

Table C.2 *GIWAXS fitting results from the out-of-plane 1D scattering profile.*

Polymer	Q (200)	FWHM (200)	D-spacing	Δ D	Δ FWHM
Branched	0.581	0.093	21.620	0.595	-0.002
Branched 24 hr	0.566	0.091	22.215		
Linear	0.594	0.098	21.143	0.450	-0.003
Linear 24 hr	0.582	0.095	21.592		
Amide	0.586	0.083	21.451	0.335	0.001
Amide 24 hr	0.577	0.084	21.787		
Urea	0.583	0.098	21.561	0.344	0.000
Urea 24 hr	0.574	0.098	21.905		

It is important to note that for anisotropic samples, the optical signal is comprised of both an in-plane (Ordinary) and out of plane (Extra-ordinary) component. The optical data presented in Chapter V is the average optical profile which is obtained from two-thirds of the Ordinary and one-third of the Extra-ordinary data. In contrast, PLLA, RRa P3HT, and NDI-C5 were able to be fitted using an isotropic model due to their lack of crystalline orientation. This, in turn, reduced the number of variables in the model significantly. Thus, the dual measurement process was not required for an accurate model to be obtained.
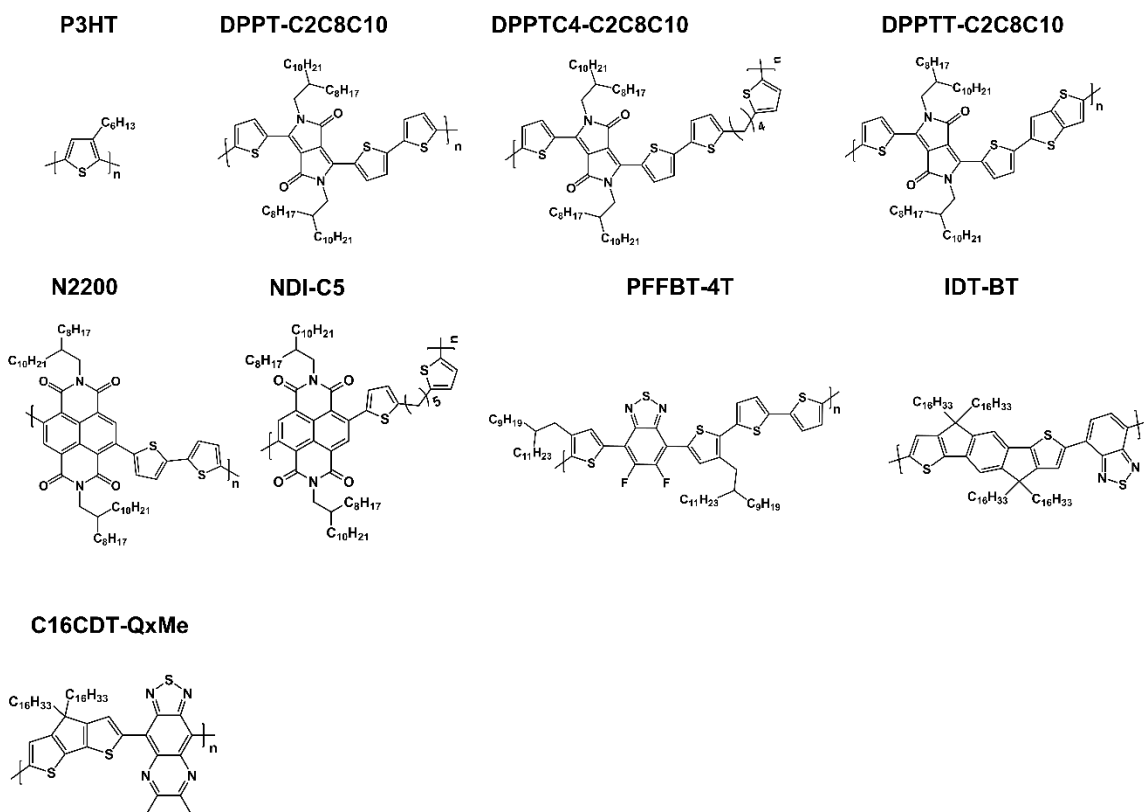
Figure D.1 *Chemical structures of all semiconducting polymers investigated in this study.*

Figure D.2 *Spectral library of a) silicon substrate and b) oxide interference layer as a function of temperature. Inserts are of the mean square error associated with each dynamic fit. Thickness of the oxide interference layer was held constant.*

Film-oxide-silicon @ -50 °C   Film-silicon @ -50 °C

a

Sample measurement

b

Simultaneous modeling

Iterative process

c

Low MSE & uniqueness

Layer # 4 = Biaxial	Thickness # 4 = 505.90 Å (MSA)	**Film of interest**
Layer # 3 = Thermal Oxide Temp Profile	Thickness # 3 = 0.00 Å (MSA)	
Layer # 2 = INTR_JAW2	Thickness # 2 = 0.00 Å (MSA)	
Layer # 1 = NTVE_JAW2	Thickness # 1 = 15.00 Å (MSA)	
Substrate = Silicon Temp Profile		

Knowns

Data Set	Thickness # 4	Thickness # 3	Thickness # 2	Thickness # 1
#1	490.91 Å	5255.86 Å	19.96 Å	0.00 Å
#2	505.90 Å	0.00 Å	0.00 Å	15.00 Å

d

Modeled optical profile

Figure D.3 *Protocol used for the temperature-dependent ellipsometry measurement. Data is representative of the onset of the heating scan at -50 °C. a) Raw ellipsometry data of representative DPPT measured on both a 500 nm thermal oxide layer and bare silicon. b) A four-layer model used to describe DPPT's temperature-dependent optical profile and thickness. The optical profile of the film is assumed to be identical for the two measurements, while the thickness of each is assessed independently. The substrate optical profiles and thickness are all known parameters previously measured. The model*

158

goes through 50 iterations at each temperature until c) the best fit is achieved with the

lowest MSE. The insert represents the uniqueness of the model. d) The anisotropic optical

profile of the polymer film is then obtained at throughout the temperature ramp.
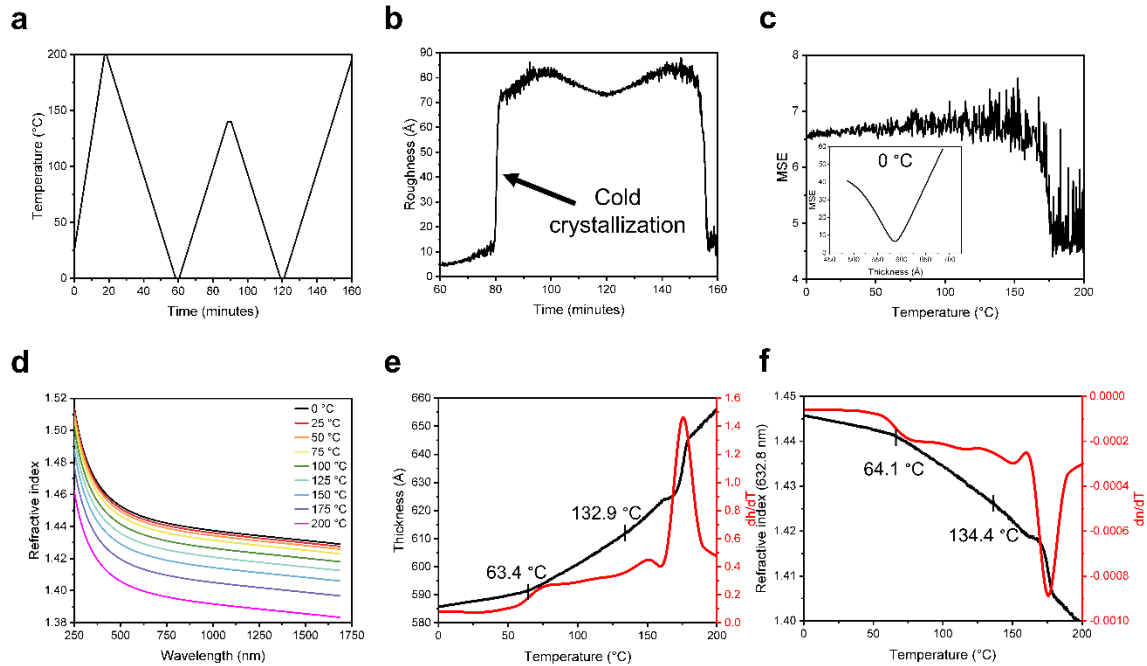
Figure D.4 *Temperature-dependent spectroscopic ellipsometry of PLLA. a) Heat/cool*

protocol to deconvolute RAF from cold crystallization. b) Film roughness indicating cold

crystallization. c) MSE throughout the final heating cycle. Insert is the model's

uniqueness at 0 °C. d) Refractive index profile as a function of temperature. e-f)

Thickness and refractive index of the PLLA film throughout the heating ramp. The lower

temperature is that of the backbone Tg and the higher temperature is that of the RAF.

159
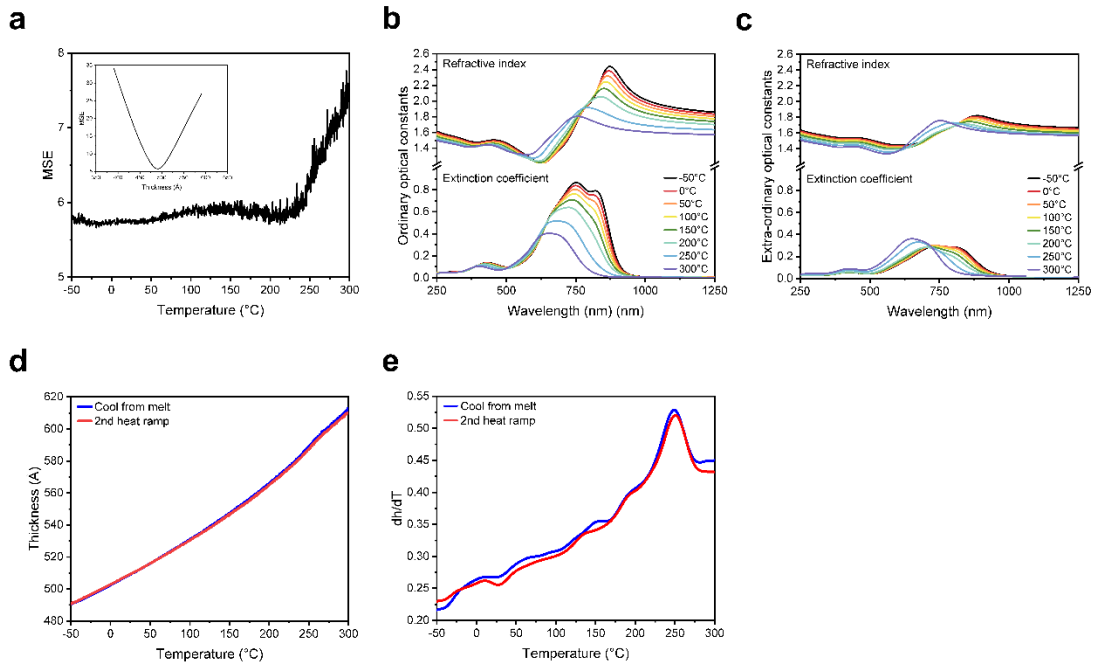
Figure D.5 *Temperature-dependent spectroscopic ellipsometry of DPPT from main manuscript. a) MSE as a function of temperature. Insert is the model's uniqueness at - 50°C. b) Ordinary optical profile and c) Extra-ordinary optical profile of the film at representative temperatures.*

160
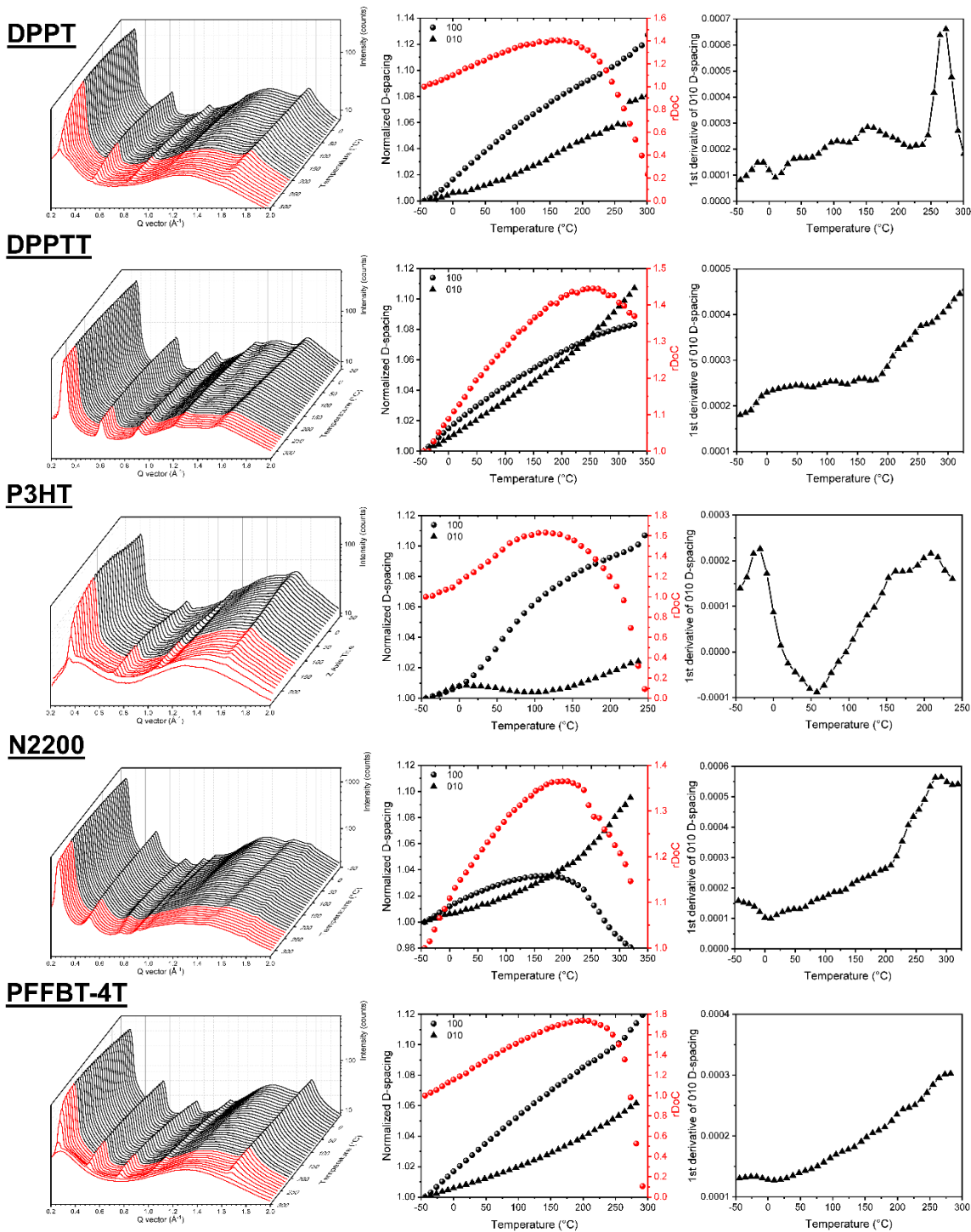
Figure D.6 *Temperature-dependent ellipsometry WAXS 1-D scattering profile (Left).*

Normalized 100 and 010 D-spacing and the relative degree of crystallinity as a function

of temperature (middle). The first derivative of the normalized 010 D-spacing (right).

161
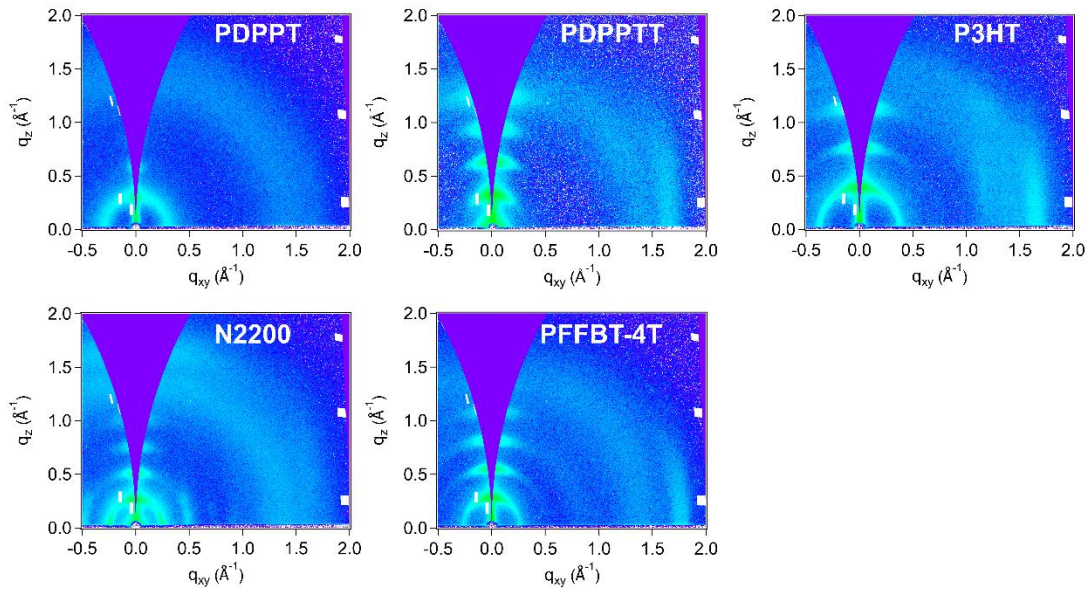
Figure D.7 *Room temperature GIWAXS after thermal processing.*
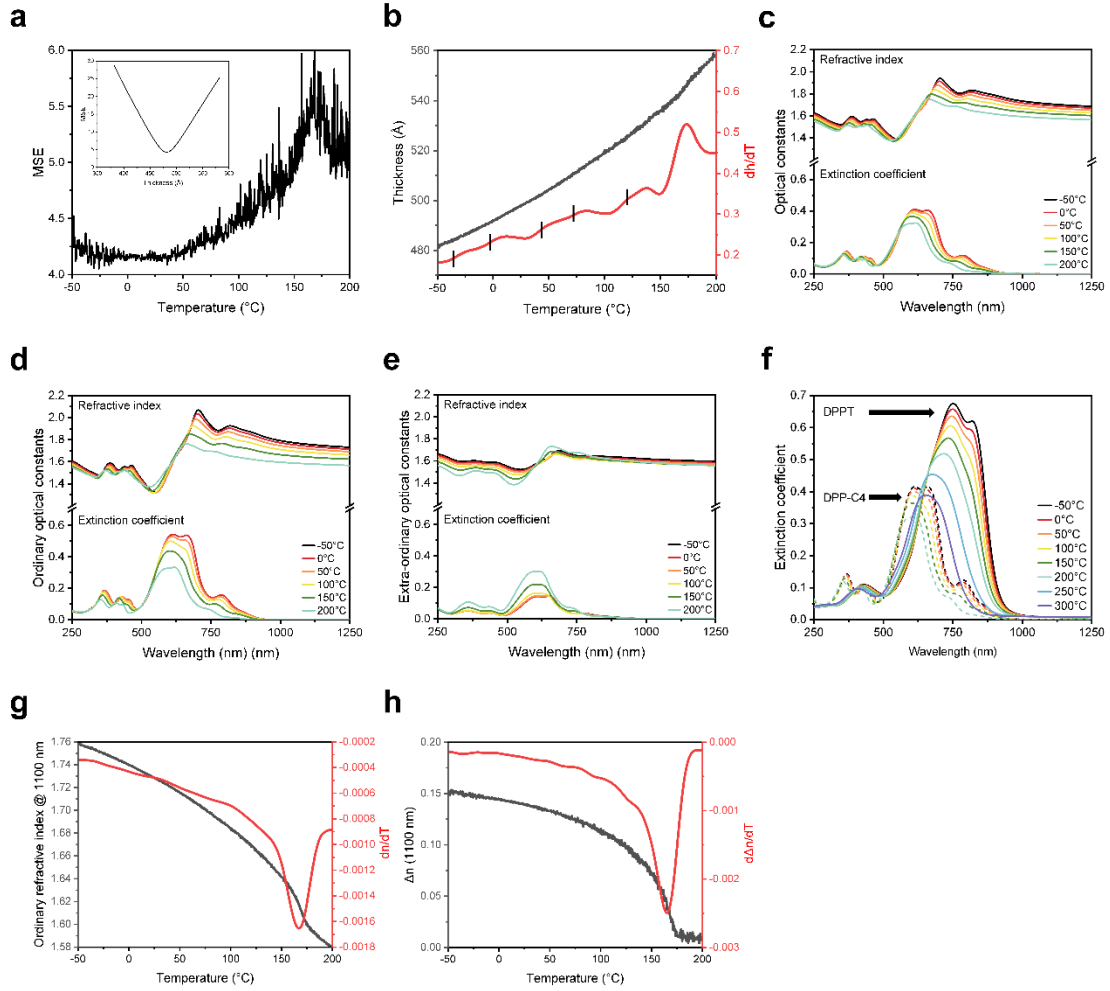
Figure D.8 *Temperature-dependent ellipsometry of DPP-C4. a) MSE as a function of temperature. Insert is the model's uniqueness at -50 °C. b) Thickness and rate of thermal expansion (dh/dT) of the film throughout the heating ramp. c) Averaged optical profile, d) Ordinary optical profile, and e) Extra-ordinary optical profile of the film at representative temperatures. f) Comparison of the temperature-dependent extinction coefficients for DPP-C4 and DPPT. g) Ordinary refractive index at 1100 nm as a function of temperature and its 1st derivative. h) Anisotropy of refractive index at 1100 nm as a function of temperature and its 1st derivative.*

163
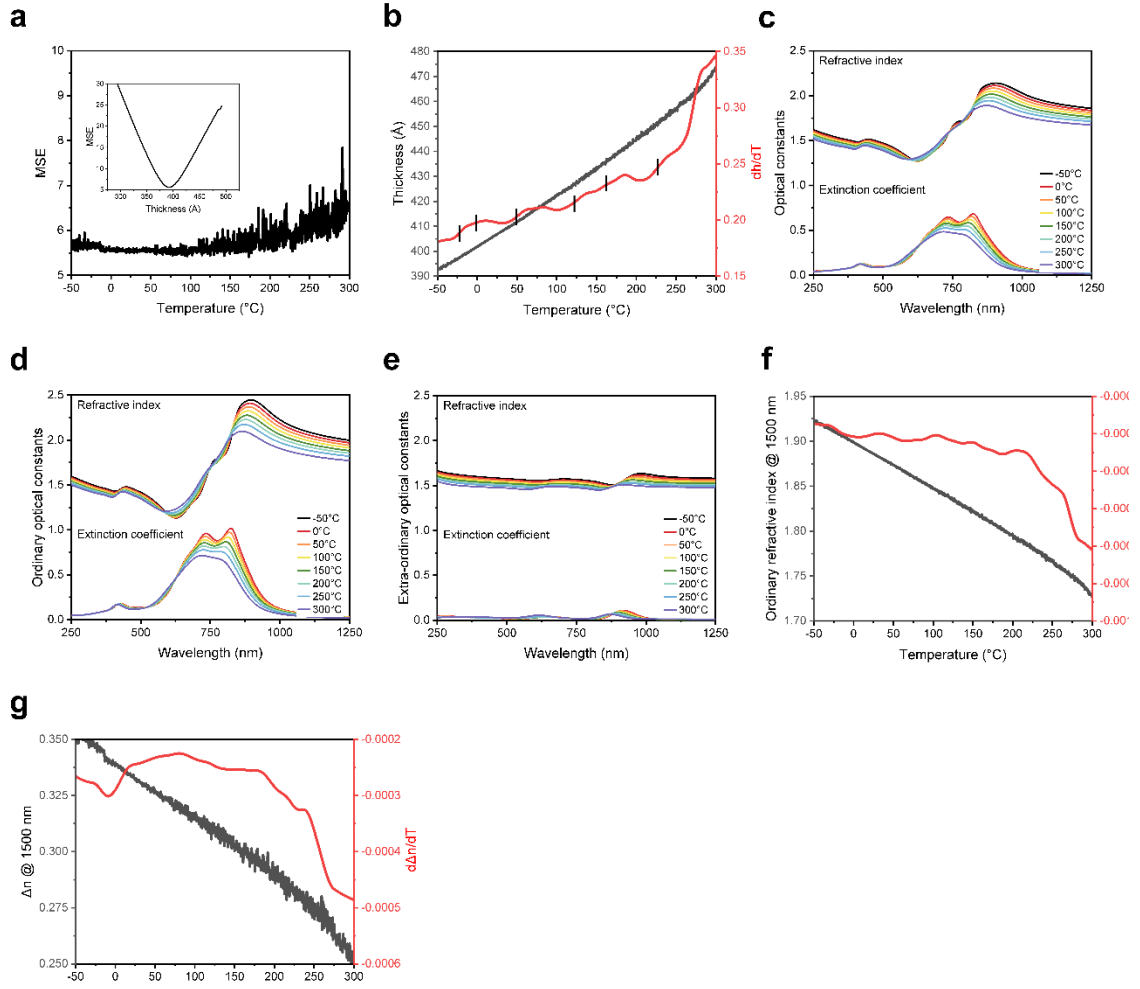
Figure D.9 *Temperature-dependent ellipsometry of DPPTT. a) MSE as a function of temperature. Insert is the model's uniqueness at -50 °C. b) Thickness and rate of thermal expansion (dh/dT) of the film throughout the heating ramp. c) Averaged optical profile, d) Ordinary optical profile, and e) Extra-ordinary optical profile of the film at representative temperatures. f) Ordinary refractive index at 1500 nm as a function of temperature and its 1st derivative. g) Anisotropy of refractive index at 1500 nm as a function of temperature and its 1st derivative.*

164
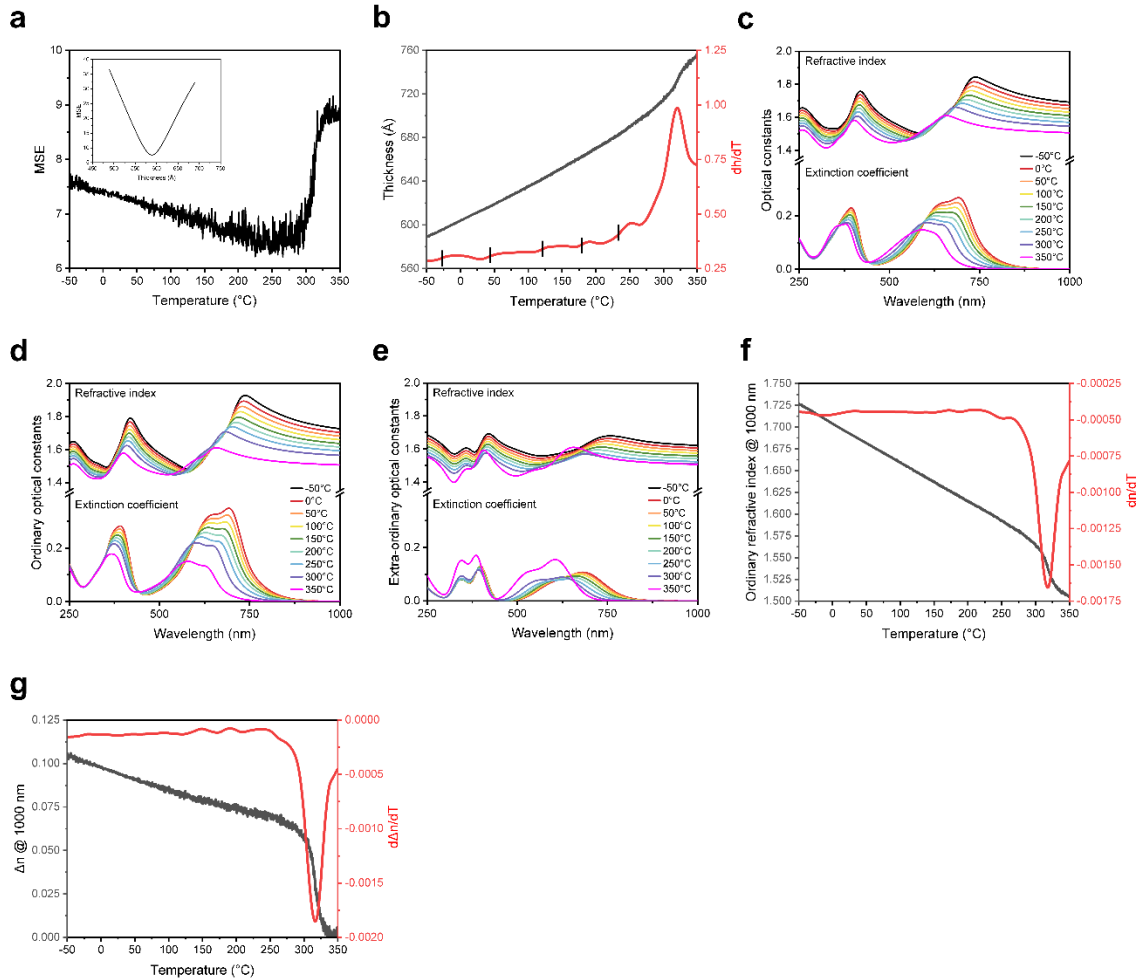
Figure D.10 *Temperature-dependent ellipsometry of N2200. a) MSE as a function of temperature. Insert is the model's uniqueness at -50 °C. b) Thickness and rate of thermal expansion (dh/dT) of the film throughout the heating ramp. c) Averaged optical profile, d) Ordinary optical profile, and e) Extra-ordinary optical profile of the film at representative temperatures. f) Ordinary refractive index at 1000 nm as a function of temperature and its 1st derivative. g) Anisotropy of refractive index at 1000 nm as a function of temperature and its 1st derivative.*
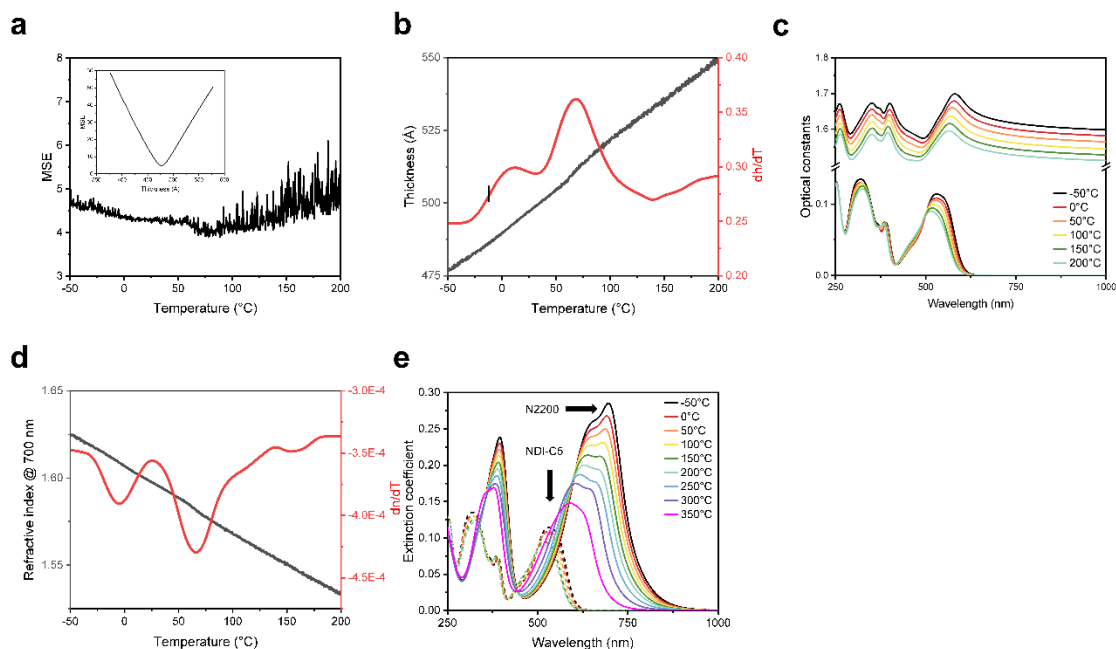
Figure D.11 *Temperature-dependent ellipsometry of PNDI-C5. a) MSE as a function of temperature. Insert is the model's uniqueness at -50 °C. b) Thickness and rate of thermal expansion (dh/dT) of the film throughout the heating ramp. c) Optical profile of the film at representative temperatures. d) Refractive index of the film throughout the heating ramp and its first derivative. e) Comparison of the temperature-dependent extinction coefficients for NDI-C5 and N2200.*
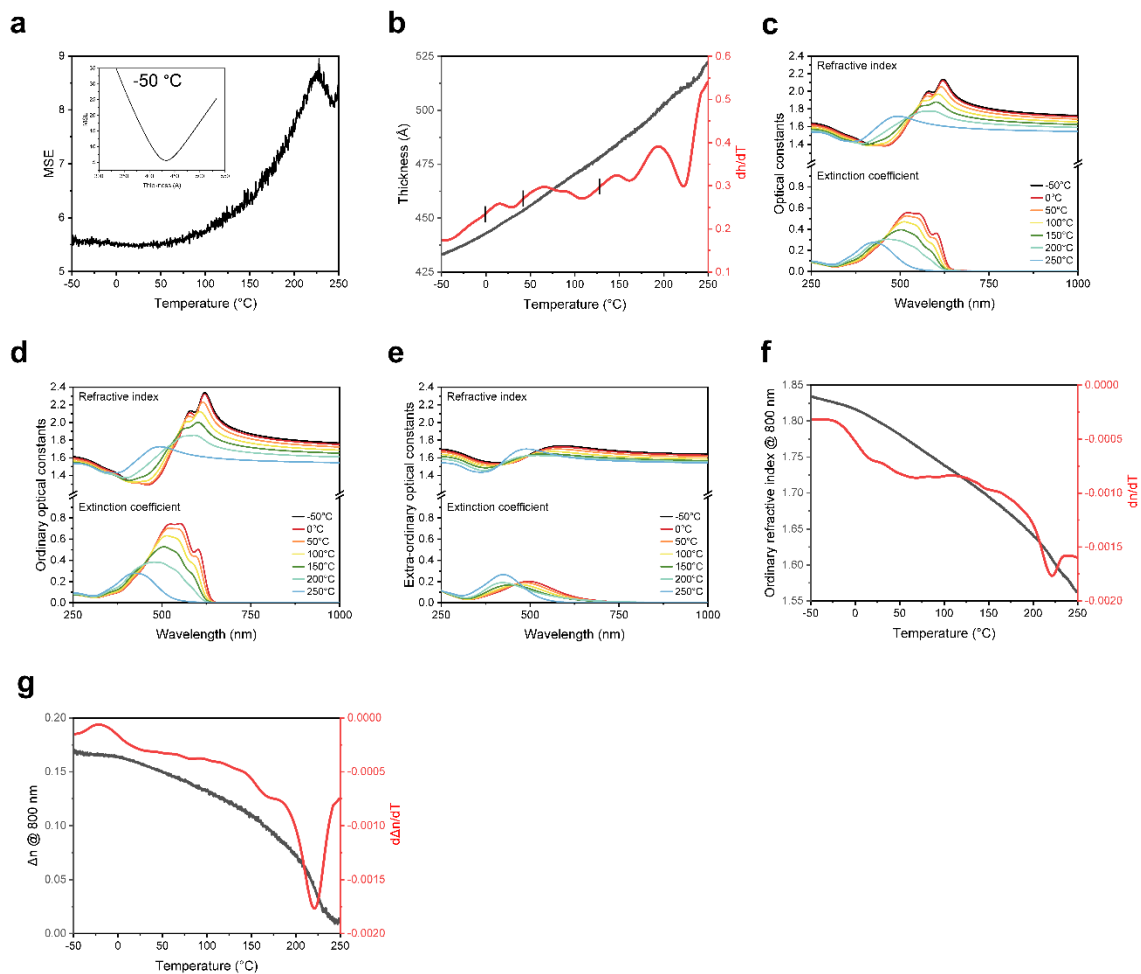
Figure D.12 *Temperature-dependent ellipsometry of regioregular P3HT. a) MSE as a function of temperature. Insert is the model's uniqueness at -50 °C. b) Thickness and rate of thermal expansion (dh/dT) of the film throughout the heating ramp. c) Averaged optical profile, d) Ordinary optical profile, and e) Extra-ordinary optical profile of the film at representative temperatures. f) Ordinary refractive index at 800 nm as a function of temperature. g) Anisotropy of refractive index at 800 nm as a function of temperature.*
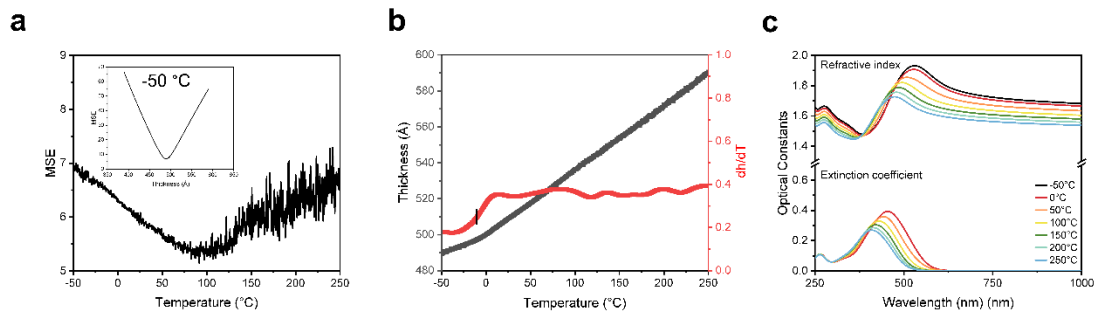
Figure D.13 *Temperature-dependent ellipsometry of regiorandom P3HT. a) MSE as a function of temperature. Insert is the model's uniqueness at -50 °C. b) Thickness and rate of thermal expansion (dh/dT) of the film throughout the heating ramp. c) Optical profile of the film at representative temperatures.*
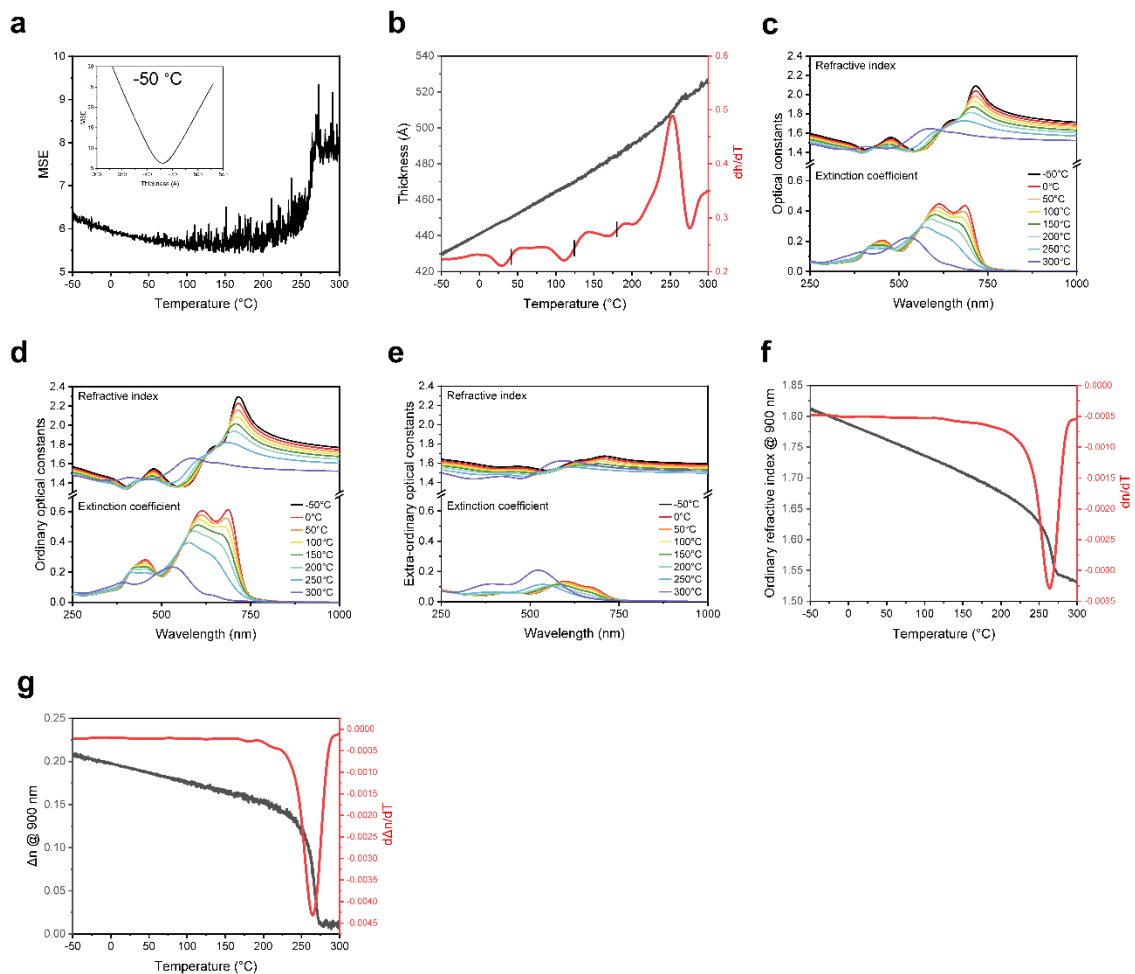
Figure D.14 *Temperature-dependent ellipsometry of PFFBT-4T. a) MSE as a function of temperature. Insert is the model's uniqueness at -50 °C. b) Thickness and rate of thermal expansion (dh/dT) of the film throughout the heating ramp. c) Averaged optical profile, d) Ordinary optical profile, and e) Extra-ordinary optical profile of the film at representative temperatures. f) Ordinary refractive index at 900 nm as a function of temperature. g) Anisotropy of refractive index at 900 nm as a function of temperature.*

169
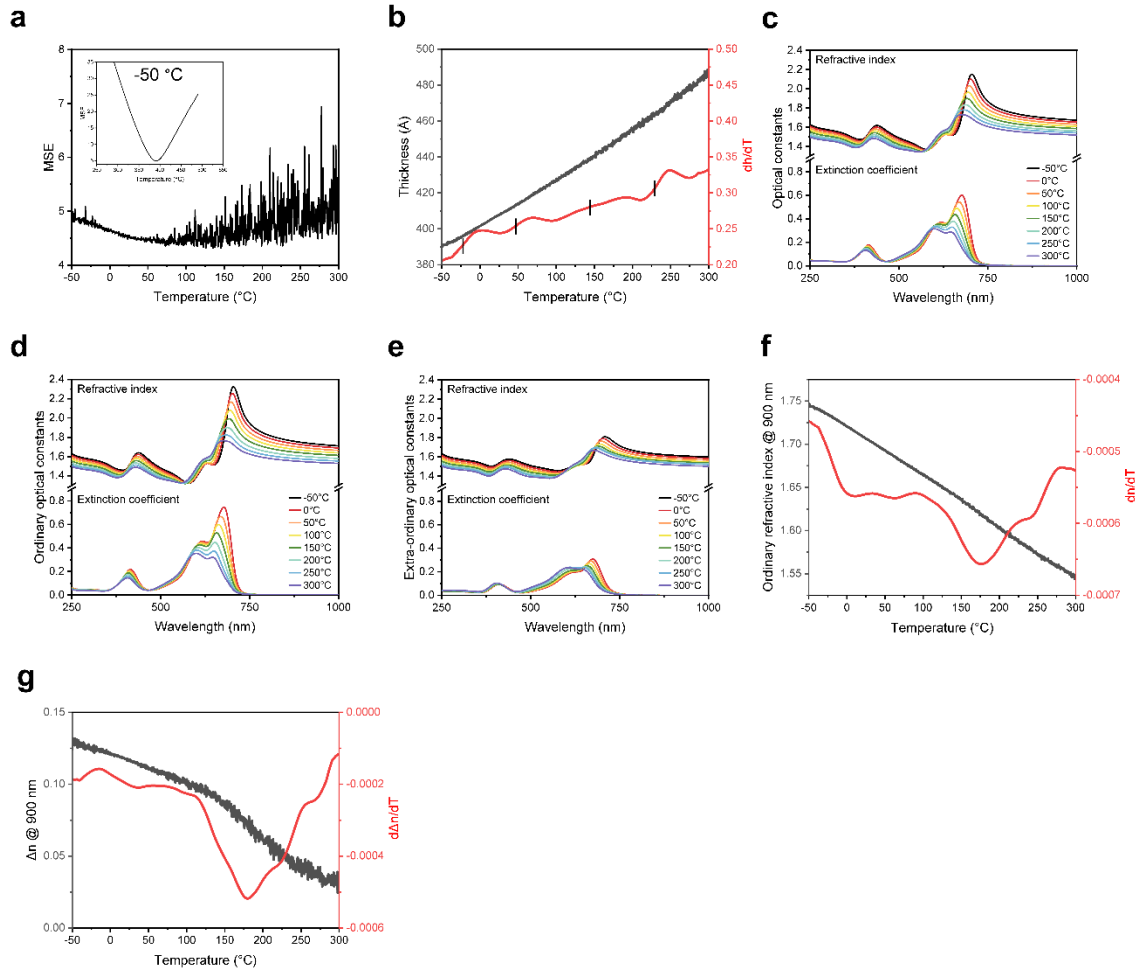
Figure D.15 *Temperature-dependent ellipsometry of IDT-BT. a) MSE as a function of temperature. Insert is the model's uniqueness at -50 °C. b) Thickness and rate of thermal expansion (dh/dT) of the film throughout the heating ramp. c) Averaged optical profile, d) Ordinary optical profile, and e) Extra-ordinary optical profile of the film at representative temperatures. f) Ordinary refractive index at 900 nm as a function of temperature. g) Anisotropy of refractive index at 900 nm as a function of temperature.*
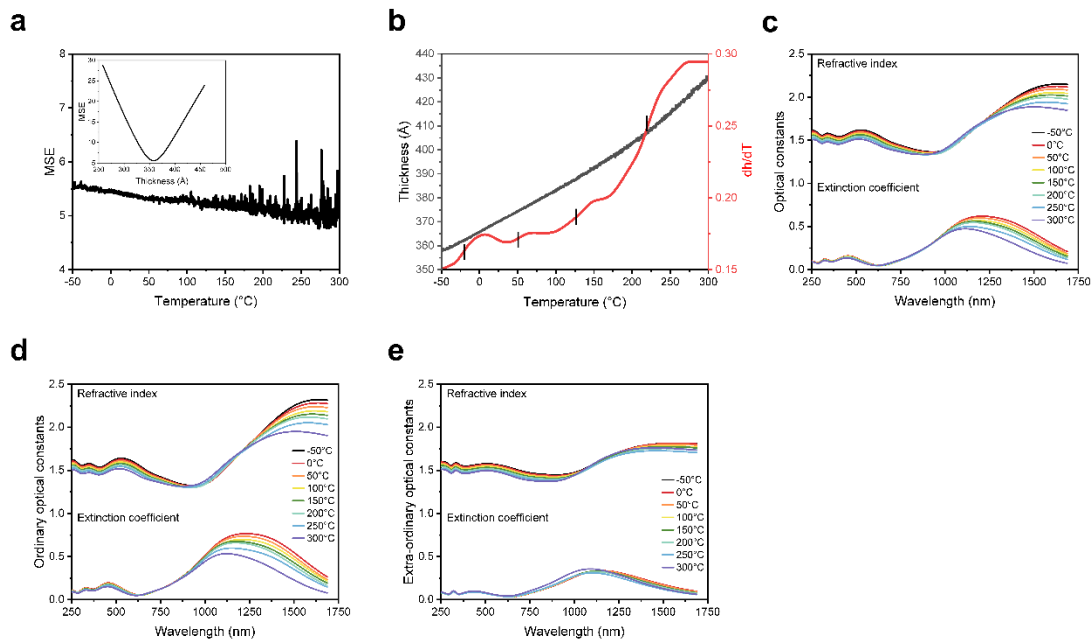
Figure D.16 *Temperature-dependent ellipsometry of C16CDT-QxMe. a) MSE as a function of temperature. Insert is the model's uniqueness at -50 °C. b) Thickness and rate of thermal expansion (dh/dT) of the film throughout the heating ramp. c) Averaged optical profile, d) Ordinary optical profile, and e) Extra-ordinary optical profile of the film at representative temperatures.*
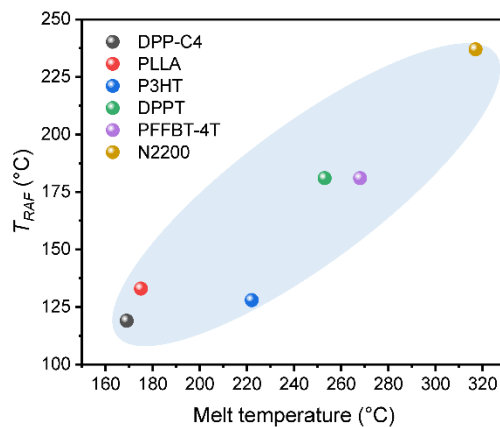
Figure D.17 *Observed trend between TRAF and melting temperature of the polymer.*
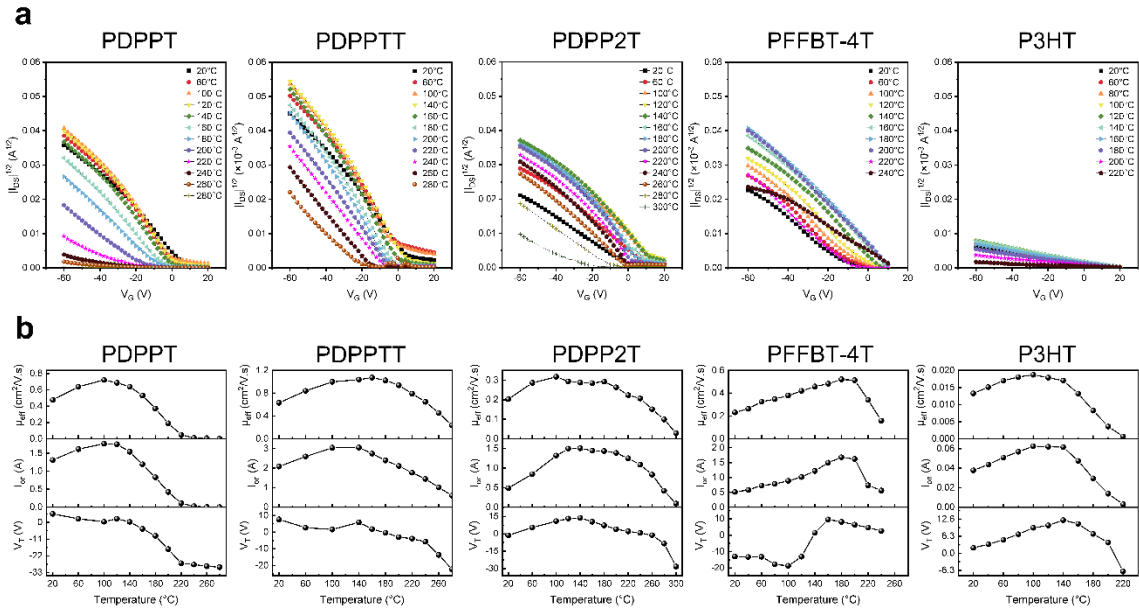
Figure D.18 *Temperature-dependent OFET measurements of 5 representative*

semiconducting polymers. a) Transfer curves and b) Charge transport characteristics

(charge mobility, on current, and threshold gate voltage) for each polymer.
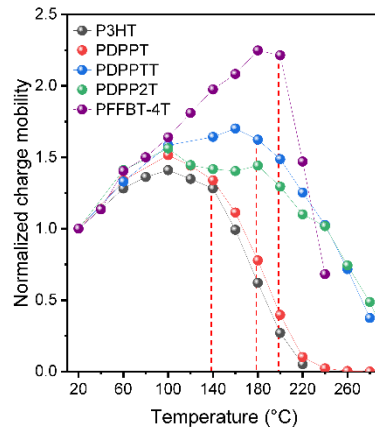
Figure D.19 *Comparison of the normalized charge mobility as a function of temperature*

for P3HT, DPPT, PDPPTT, PDPP2T and PFFBT-4T.

172

REFERENCES

.(1)   Tseng, H. R.; Phan, H.; Luo, C.; Wang, M.; Perez, L. A.; Patel, S. N.; Ying, L.;
        Kramer, E. J.; Nguyen, T. Q.; Bazan, G. C.; Heeger, A. J. High-Mobility Field-
        Effect Transistors Fabricated with Macroscopic Aligned Semiconducting
        Polymers. *Adv. Mater.* **2014**, *26*, 2993–2998.

(2)   Luo, C.; Ko, A.; Kyaw, K.; Perez, L. a.; Patel, S.; Wang, M.; Grimm, B.; Bazan,
        G. C.; Kramer, E. J.; Heeger, A. J.; Kyaw, A. K. K.; Perez, L. a.; Patel, S.; Wang,
        M.; Grimm, B.; Bazan, G. C.; Kramer, E. J.; Heeger, A. J. General Strategy for
        Self-Assembly of Highly Oriented Nanocrystalline Semiconducting Polymers with
        High Mobility. *Nano Lett.* **2014**, *14*, 2764–2771.

(3)   Yao, J.; Yu, C.; Liu, Z.; Luo, H.; Yang, Y.; Zhang, G.; Zhang, D. Significant
        Improvement of Semiconducting Performance of the Diketopyrrolopyrrole-
        Quaterthiophene Conjugated Polymer through Side-Chain Engineering via
        Hydrogen-Bonding. *J. Am. Chem. Soc.* **2016**, *138*, 173–185.

(4)   Zhang, A.; Xiao, C.; Wu, Y.; Li, C.; Ji, Y.; Li, L.; Hu, W.; Wang, Z.; Ma, W.; Li,
        W. Effect of Fluorination on Molecular Orientation of Conjugated Polymers in
        High Performance Field-Effect Transistors. *Macromolecules* **2016**, *49*, 6431–6438.

(5)   Khim, D.; Luzio, A.; Bonacchini, G. E.; Pace, G.; Lee, M.-J.; Noh, Y.-Y.; Caironi,
        M. Uniaxial Alignment of Conjugated Polymer Films for High-Performance
        Organic Field-Effect Transistors. *Adv. Mater.* **2018**, *30*, 1705463.

(6)   Kang, I.; Yun, H. J.; Chung, D. S.; Kwon, S. K.; Kim, Y. H. Record High Hole
        Mobility in Polymer Semiconductors via Side-Chain Engineering. *J. Am. Chem.
        Soc.* **2013**, *135*, 14896–14899.

(7)   Quinn, J. T. E.; Zhu, J.; Li, X.; Wang, J.; Li, Y. Recent Progress in the
        Development of N-Type Organic Semiconductors for Organic Field Effect
        Transistors. *J. Mater. Chem. C* **2017**, *5*, 8654–8681.

(8)   Nielsen, C. B.; Turbiez, M.; McCulloch, I. Recent Advances in the Development
        of Semiconducting DPP-Containing Polymers for Transistor Applications. *Adv.
        Mater.* **2013**, *25*, 1859–1880.

(9)   Wang, Y.; Zhu, C.; Pfattner, R.; Yan, H.; Jin, L.; Chen, S.; Molina-Lopez, F.;
        Lissel, F.; Liu, J.; Rabiah, N. I.; Chen, Z.; Chung, J. W.; Linder, C.; Toney, M. F.;
        Murmann, B.; Bao, Z. A Highly Stretchable, Transparent, and Conductive
        Polymer. *Sci. Adv.* **2017**, *3*, e1602076.

(10)   Wang, S.; Xu, J.; Wang, W.; Wang, G.-J. N.; Rastak, R.; Molina-Lopez, F.;
        Chung, J. W.; Niu, S.; Feig, V. R.; Lopez, J.; et al. Skin Electronics from Scalable
        Fabrication of an Intrinsically Stretchable Transistor Array. *Nature* **2018**, *555*, 83–
        88.

(11)   Chortos, A.; Liu, J.; Bao, Z. Pursuing Prosthetic Electronic Skin. *Nat. Mater.* **2016**,
        15, 937–950.

(12)   Someya, T.; Bao, Z.; Malliaras, G. G. The Rise of Plastic Bioelectronics. *Nature*
        2016, *540*, 379–385.

(13)   Wang, G.-J. N.; Gasperini, A.; Bao, Z. Stretchable Polymer Semiconductors for
        Plastic Electronics. *Adv. Electron. Mater.* **2018**, *4*, 1700429.

(14)   Li, S.; Zhao, H.; Shepherd, R. F. Flexible and Stretchable Sensors for Fluidic
        Elastomer Actuated Soft Robots. *MRS Bull.* **2017**, *42*, 138–142.

(15)   Someya, T.; Bauer, S.; Kaltenbrunner, M. Imperceptible Organic Electronics. *MRS*

Bull. **2017**, *42*, 124–130.

(16) Liang, J.; Tong, K.; Sun, H.; Pei, Q. Intrinsically Stretchable Field-Effect

Transistors. *MRS Bull.* **2017**, *42*, 131–137.

(17) Lipomi, D. J.; Bao, Z. Stretchable and Ultraflexible Organic Electronics. *MRS*

Bull. **2017**, *42*, 93–97.

(18) O'Connor, B. T.; Awartani, O. M.; Balar, N. Morphological Considerations of

Organic Electronic Films for Flexible and Stretchable Devices. *MRS Bull.* **2017**,

42, 108–114.

(19) Schroeder, B. C.; Chiu, Y. C.; Gu, X.; Zhou, Y.; Xu, J.; Lopez, J.; Lu, C.; Toney,

M. F.; Bao, Z. Non-Conjugated Flexible Linkers in Semiconducting Polymers: A

Pathway to Improved Processability without Compromising Device Performance.

Adv. Electron. Mater. **2016**, *2*.

(20) Gu, X.; Shaw, L.; Mun, J.; Chiu, Y.-C.; Toney, M. F.; Fu, T.; Wang, G.-J. N.; Bao,

Z.; Kurosawa, T.; Schroeder, B. C.; Kneller, J. W. E.; Kreouzis, T. Taming Charge

Transport in Semiconducting Polymers with Branched Alkyl Side Chains. *Adv.*

Funct. Mater. **2017**, *27*, 1701973.

(21) Qian, Z.; Galuska, L.; McNutt, W. W.; Ocheje, M. U.; He, Y.; Cao, Z.; Zhang, S.;

Xu, J.; Hong, K.; Goodman, R. B.; Rondeau-Gagné, S.; Mei, J.; Gu, X. Challenge

and Solution of Characterizing Glass Transition Temperature for Conjugated

Polymers by Differential Scanning Calorimetry. *J. Polym. Sci. Part B Polym.*

Phys. **2019**, *57*, 1635–1644.

(22) Cao, Z.; Galuska, L.; Qian, Z.; Zhang, S.; Huang, L.; Prine, N.; Li, T.; He, Y.;

Hong, K.; Gu, X. The Effect of Side-Chain Branch Position on the Thermal

Properties of Poly(3-Alkylthiophenes). *Polym. Chem.* **2020**, *11*, 517–526.

(23)   Zhang, S.; Ocheje, M. U.; Huang, L.; Galuska, L.; Cao, Z.; Luo, S.; Cheng, Y.;

Ehlenberg, D.; Goodman, R. B.; Zhou, D.; Liu, Y.; Chiu, Y.; Azoulay, J. D.;

Rondeau-Gagné, S.; Gu, X. The Critical Role of Electron-Donating Thiophene

Groups on the Mechanical and Thermal Properties of Donor–Acceptor

Semiconducting Polymers. *Adv. Electron. Mater.* **2019**, *5*, 1800899.

(24)   Zhang, S.; Alesadi, A.; Selivanova, M.; Cao, Z.; Qian, Z.; Luo, S.; Galuska, L.;

Teh, C.; Ocheje, M. U.; Mason, G. T.; St. Onge, P. B. J.; Zhou, D.; Rondeau-

Gagné, S.; Xia, W.; Gu, X. Toward the Prediction and Control of Glass Transition

Temperature for Donor–Acceptor Polymers. *Adv. Funct. Mater.* **2020**, *30*,

2002221.

(25)   Sharma, A.; Pan, X.; Bjuggren, J. M.; Gedefaw, D.; Xu, X.; Kroon, R.; Wang, E.;

Campbell, J. A.; Lewis, D. A.; Andersson, M. R. Probing the Relationship between

Molecular Structures, Thermal Transitions, and Morphology in Polymer

Semiconductors Using a Woven Glass-Mesh-Based DMTA Technique. *Chem.*

Mater. **2019**, *31*, 6740–6749.

(26)   Balar, N.; Siddika, S.; Kashani, S.; Peng, Z.; Rech, J. J.; Ye, L.; You, W.; Ade, H.;

O'Connor, B. T. Role of Secondary Thermal Relaxations in Conjugated Polymer

Film Toughness. *Chem. Mater.* **2020**, *32*, 6540–6549.

(27)   Xiao, M.; Sadhanala, A.; Abdi-Jalebi, M.; Thomas, T. H.; Ren, X.; Zhang, T.;

Chen, H.; Carey, R. L.; Wang, Q.; Senanayak, S. P.; Jellett, C.; Onwubiko, A.;

Moser, M.; Liao, H.; Yue, W.; McCulloch, I.; Nikolka, M.; Sirringhaus, H.

Linking Glass-Transition Behavior to Photophysical and Charge Transport

Properties of High-Mobility Conjugated Polymers. *Adv. Funct. Mater.* **2021**, *31*, 1–11.

(28)   Luo, S.; Wang, T.; Ocheje, M. U.; Zhang, S.; Xu, J.; Qian, Z.; Gu, X.; Xue, G.; Rondeau-Gagné, S.; Jiang, J.; Hu, W.; Zhuravlev, E.; Zhou, D. Multiamorphous Phases in Diketopyrrolopyrrole-Based Conjugated Polymers: From Bulk to Ultrathin Films. *Macromolecules* **2020**, *53*, 4480–4489.

(29)   Root, S. E.; Alkhadra, M. A.; Rodriquez, D.; Printz, A. D.; Lipomi, D. J. Measuring the Glass Transition Temperature of Conjugated Polymer Films with Ultraviolet–Visible Spectroscopy. *Chem. Mater.* **2017**, *29*, 2646–2654.

(30)   Sugiyama, F.; Kleinschmidt, A. T.; Kayser, L. V.; Rodriquez, D.; Finn, M.; Alkhadra, M. A.; Wan, J. M.-H.; Ramírez, J.; Chiang, A. S.-C.; Root, S. E.; Savagatrup, S.; Lipomi, D. J. Effects of Flexibility and Branching of Side Chains on the Mechanical Properties of Low-Bandgap Conjugated Polymers. *Polym. Chem.* **2018**, *9*, 4354–4363.

(31)   Xie, R.; Weisen, A. R.; Lee, Y.; Aplan, M. A.; Fenton, A. M.; Masucci, A. E.; Kempe, F.; Sommer, M.; Pester, C. W.; Colby, R. H.; Gomez, E. D. Glass Transition Temperature from the Chemical Structure of Conjugated Polymers. *Nat. Commun.* **2020**, *11*, 893.

(32)   Xie, R.; Lee, Y.; Aplan, M. P.; Caggiano, N. J.; Müller, C.; Colby, R. H.; Gomez, E. D. Glass Transition Temperature of Conjugated Polymers by Oscillatory Shear Rheometry. *Macromolecules* **2017**, *50*, 5146–5154.

(33)   Sharma, A.; Pan, X.; Campbell, J. A.; Andersson, M. R.; Lewis, D. A. Unravelling the Thermomechanical Properties of Bulk Heterojunction Blends in Polymer Solar

Cells. *Macromolecules* **2017**, *50*, 3347–3354.

(34) Huth, H.; Minakov, A. A.; Schick, C. Differential AC-Chip Calorimeter for Glass

Transition Measurements in Ultrathin Films. *J. Polym. Sci. Part B Polym. Phys.*

2006, *44*, 2996–3005.

(35) Zhou, D.; Huth, H.; Gao, Y.; Xue, G.; Schick, C. Calorimetric Glass Transition of

Poly(2,6-Dimethyl-1,5-Phenylene Oxide) Thin Films. *Macromolecules* **2008**, *41*,

7662–7666.

(36) Wang, T.; Pearson, A. J.; Dunbar, A. D. F.; Staniec, P. A.; Watters, D. C.; Coles,

D.; Yi, H.; Iraqi, A.; Lidzey, D. G.; Jones, R. A. L. Competition between

Substrate-Mediated π-π Stacking and Surface-Mediated Tg Depression in Ultrathin

Conjugated Polymer Films. *Eur. Phys. J. E* **2012**, *35*, 129.

(37) Müller, C.; Andersson, L. M.; Peña-Rodríguez, O.; Garriga, M.; Inganäs, O.;

Campoy-Quiles, M. Determination of Thermal Transition Depth Profiles in

Polymer Semiconductor Films with Ellipsometry. *Macromolecules* **2013**, *46*,

7325–7331.

(38) Campoy-Quiles, M.; Alonso, M. I.; Bradley, D. D. C.; Richter, L. J. Advanced

Ellipsometric Characterization of Conjugated Polymer Films. *Adv. Funct. Mater.*

2014, *24*, 2116–2134.

(39) Campoy-Quiles, M.; Etchegoin, P. G.; Bradley, D. D. C. Exploring the Potential of

Ellipsometry for the Characterisation of Electronic, Optical, Morphologic and

Thermodynamic Properties of Polyfluorene Thin Films. *Synth. Met.* **2005**, *155*,

279–282.

(40) Campoy-Quiles, M.; Sims, M.; Etchegoin, P. G.; Bradley, D. D. C. Thickness-

Dependent Thermal Transition Temperatures in Thin Conjugated Polymer Films. *Macromolecules* **2006**, *39*, 7673–7680.

(41) Hajduk, B.; Bednarski, H.; Trzebicka, B. Temperature-Dependent Spectroscopic Ellipsometry of Thin Polymer Films. *J. Phys. Chem. B* **2020**, *124*, 3229–3251.

(42) Campoy-Quiles, M.; Etchegoin, P. G.; Bradley, D. D. C. On the Optical Anisotropy of Conjugated Polymer Thin Films. *Phys. Rev. B* **2005**, *72*, 045209.

(43) Knoll, W.; Advincula, R. C. *Functional Polymer Films, 2 Volume Set*; John Wiley & Sons, 2013.

(44) Lu, N.; Wang, X.; Suo, Z.; Vlassak, J. Metal Films on Polymer Substrates Stretched beyond 50%. *Appl. Phys. Lett.* **2007**, *91*, 8–11.

(45) Macionczyk, F.; Brückner, W. Tensile Testing of AlCu Thin Films on Polyimide Foils. *J. Appl. Phys.* **1999**, *86*, 4922–4929.

(46) Song, R.; Schrickx, H.; Balar, N.; Siddika, S.; Sheikh, N.; O'Connor, B. T.; O'connor, B. T. Unveiling the Stress-Strain Behavior of Conjugated Polymer Thin Films for Stretchable Device Applications. *Macromolecules* **2020**, *53*, 1988–1997.

(47) Rodriquez, D.; Kim, J.-H.; Root, S. E.; Fei, Z.; Boufflet, P.; Heeney, M.; Kim, T.-S.; Lipomi, D. J. Comparison of Methods for Determining the Mechanical Properties of Semiconducting Polymer Films for Stretchable Electronics. *ACS Appl. Mater. Interfaces* **2017**, *9*, 8855–8862.

(48) Root, S. E.; Savagatrup, S.; Printz, A. D.; Rodriquez, D.; Lipomi, D. J. Mechanical Properties of Organic Semiconductors for Stretchable, Highly Flexible, and Mechanically Robust Electronics. *Chem. Rev.* **2017**, *117*, 6467–6499.

(49) Stafford, C. M.; Harrison, C.; Beers, K. L.; Karim, A.; Amis, E. J.;

VanLandingham, M. R.; Kim, H.-C.; Volksen, W.; Miller, R. D.; Simonyi, E. E. A Buckling-Based Metrology for Measuring the Elastic Moduli of Polymeric Thin Films. *Nat. Mater.* **2004**, *3*, 545–550.

(50)   Miyake, K.; Satomi, N.; Sasaki, S. Elastic Modulus of Polystyrene Film from near Surface to Bulk Measured by Nanoindentation Using Atomic Force Microscopy. *Appl. Phys. Lett.* **2006**, *89*, 10–13.

(51)   Oliver, G. M.; Pharr, W. C. Measurement of Thin Film Mechanical Properties Using Nanoindentation. *MRS Bull.* **1992**, *17*, 28–33.

(52)   Oliver, W. C.; Pharr, G. M. An Improved Technique for Determining Hardness and Elastic Modulus Using Load and Displacement Sensing Indentation Experiments. *J. Mater. Res.* **1992**, *7*, 1564–1583.

(53)   Pharr, G. M. Measurement of Mechanical Properties by Ultra-Low Load Indentation. *Mater. Sci. Eng. A* **1998**, *253*, 151–159.

(54)   Pharr, G. M.; Bolshakov, A. Understanding Nanoindentation Unloading Curves. *J. Mater. Res.* **2002**, *17*, 2660–2671.

(55)   Miyake, K.; Fujisawa, S.; Korenaga, A.; Ishida, T.; Sasaki, S. The Effect of Pile-up and Contact Area on Hardness Test by Nanoindentation. *Japanese J. Appl. Physics, Part 1 Regul. Pap. Short Notes Rev. Pap.* **2004**, *43*, 4602–4605.

(56)   Zeng, K.; Chen, Z.-K.; Shen, L.; Liu, B. Study of Mechanical Properties of Light-Emitting Polymer Films by Nano-Indentation Technique. *Thin Solid Films* **2005**, *477*, 111–118.

(57)   Gasperini, A.; Jeanbourquin, X. A.; Rahmanudin, A.; Yu, X.; Sivula, K. Enhancing the Thermal Stability of Solution-Processed Small-Molecule

Semiconductor Thin Films Using a Flexible Linker Approach. *Adv. Mater.* **2015**, *27*, 5541–5546.

(58)   Venkatanarayanan, R. I.; Krishnan, S.; Sreeram, A.; Yuya, P. A.; Patel, N. G.; Tandia, A.; McLaughlin, J. B. Simulated Dilatometry and Static Deformation Prediction of Glass Transition and Mechanical Properties of Polyacetylene and Poly(Para -Phenylene Vinylene). *Macromol. Theory Simulations* **2016**, *25*, 238–253.

(59)   Ocheje, M. U.; Selivanova, M.; Zhang, S.; Van Nguyen, T. H.; Charron, B. P.; Chuang, C.-H.; Cheng, Y.-H.; Billet, B.; Noori, S.; Chiu, Y.-C.; Gu, X.; Rondeau-Gagné, S. Influence of Amide-Containing Side Chains on the Mechanical Properties of Diketopyrrolopyrrole-Based Polymers. *Polym. Chem.* **2018**, *9*, 5531–5542.

(60)   Tweedie, C. A.; Constantinides, G.; Lehman, K. E.; Brill, D. J.; Blackman, G. S.; Van Vliet, K. J. Enhanced Stiffness of Amorphous Polymer Surfaces under Confinement of Localized Contact Loads. *Adv. Mater.* **2007**, *19*, 2540–2546.

(61)   Stafford, C. M.; Guo, S.; Harrison, C.; Chiang, M. Y. M. Combinatorial and High-Throughput Measurements of the Modulus of Thin Polymer Films. *Rev. Sci. Instrum.* **2005**, *76*, 062207.

(62)   Chung, J. Y.; Nolte, A. J.; Stafford, C. M. Surface Wrinkling: A Versatile Platform for Measuring Thin-Film Properties. *Adv. Mater.* **2011**, *23*, 349–368.

(63)   Lee, J. H.; Chung, J. Y.; Stafford, C. M. Effect of Confinement on Stiffness and Fracture of Thin Amorphous Polymer Films. *ACS Macro Lett.* **2012**, *1*, 122–126.

(64)   Chung, J. Y.; Douglas, J. F.; Stafford, C. M. A Wrinkling-Based Method for

Investigating Glassy Polymer Film Relaxation as a Function of Film Thickness and Temperature. *J. Chem. Phys.* **2017**, *147*, 154902.

(65) Oh, J. Y.; Rondeau-Gagné, S.; Chiu, Y.-C.; Chortos, A.; Lissel, F.; Wang, G.-J. N.; Schroeder, B. C.; Kurosawa, T.; Lopez, J.; Katsumata, T.; et al. Intrinsically Stretchable and Healable Semiconducting Polymer for Organic Transistors. *Nature* **2016**, *539*, 411–415.

(66) Wang, G.-J. N.; Shaw, L.; Xu, J.; Kurosawa, T.; Schroeder, B. C.; Oh, J. Y.; Benight, S. J.; Bao, Z. Inducing Elasticity through Oligo-Siloxane Crosslinks for Intrinsically Stretchable Semiconducting Polymers. *Adv. Funct. Mater.* **2016**, *26*, 7254–7262.

(67) Savagatrup, S.; Makaram, A. S.; Burke, D. J.; Lipomi, D. J. Mechanical Properties of Conjugated Polymers and Polymer-Fullerene Composites as a Function of Molecular Structure. *Adv. Funct. Mater.* **2014**, *24*, 1169–1181.

(68) Roth, B.; Savagatrup, S.; V. de los Santos, N.; Hagemann, O.; Carlé, J. E.; Helgesen, M.; Livi, F.; Bundgaard, E.; Søndergaard, R. R.; Krebs, F. C.; Lipomi, D. J. Mechanical Properties of a Library of Low-Band-Gap Polymers. *Chem. Mater.* **2016**, *28*, 2363–2373.

(69) Awartani, O. M.; Zhao, B.; Currie, T.; Kline, R. J.; Zikry, M. A.; O'Connor, B. T. Anisotropic Elastic Modulus of Oriented Regioregular Poly(3-Hexylthiophene) Films. *Macromolecules* **2016**, *49*, 327–333.

(70) Sun, T.; Song, R.; Balar, N.; Sen, P.; Kline, R. J.; O'Connor, B. T. Impact of Substrate Characteristics on Stretchable Polymer Semiconductor Behavior. *ACS Appl. Mater. Interfaces* **2019**, *11*, 3280–3289.

(71) O'Connor, B.; Chan, E. P.; Chan, C.; Conrad, B. R.; Richter, L. J.; Kline, R. J.; Heeney, M.; McCulloch, I.; Soles, C. L.; DeLongchamp, D. M. Correlations between Mechanical and Electrical Properties of Polythiophenes. *ACS Nano* **2010**, *4*, 7538–7544.

(72) Song, R.; Schrickx, H.; Balar, N.; Siddika, S.; Sheikh, N.; O'Connor, B. T. Unveiling the Stress–Strain Behavior of Conjugated Polymer Thin Films for Stretchable Device Applications. *Macromolecules* **2020**, *53*, 1988–1997.

(73) Huang, J.; Juszkiewicz, M.; Jeu, W. H. de; Cerda, E.; Emrick, T.; Menon, N.; Russell, T. P. Capillary Wrinkling of Floating Thin Polymer Films. *Science (80-.).* **2007**, *317*, 277–313.

(74) Bay, R. K.; Shimomura, S.; Liu, Y.; Ilton, M.; Crosby, A. J. Confinement Effect on Strain Localizations in Glassy Polymer Films. *Macromolecules* **2018**, *51*, 3647–3653.

(75) Zhang, S.; Ocheje, M. U.; Luo, S.; Ehlenberg, D.; Appleby, B.; Weller, D.; Zhou, D.; Rondeau-Gagné, S.; Gu, X. Probing the Viscoelastic Property of Pseudo Free-Standing Conjugated Polymeric Thin Films. *Macromol. Rapid Commun.* **2018**, *39*, 1800092.

(76) Bay, R. K.; Crosby, A. J. Uniaxial Extension of Ultrathin Freestanding Polymer Films. *ACS Macro Lett.* **2019**, *8*, 1080–1085.

(77) Kim, J.-H.; Nizami, A.; Hwangbo, Y.; Jang, B.; Lee, H.-J.; Woo, C.-S.; Hyun, S.; Kim, T.-S. Tensile Testing of Ultra-Thin Films on Water Surface. *Nat. Commun.* **2013**, *4*, 2520.

(78) Bay, R. K.; Zarybnicka, K.; Jančář, J.; Crosby, A. J. Mechanical Properties of

Ultrathin Polymer Nanocomposites. *ACS Appl. Polym. Mater.* **2020**, *2*, 2220–2227.

(79) Choi, W. J.; Bay, R. K.; Crosby, A. J. Tensile Properties of Ultrathin Bisphenol-A

Polycarbonate Films. *Macromolecules* **2019**, *52*, 7489–7494.

(80) Liu, Y.; Chen, Y.-C.; Hutchens, S.; Lawrence, J.; Emrick, T.; Crosby, A. J.

Directly Measuring the Complete Stress–Strain Response of Ultrathin Polymer

Films. *Macromolecules* **2015**, *48*, 6534–6540.

(81) Kim, J.-S.; Kim, J.-H.; Lee, W.; Yu, H.; Kim, H. J.; Song, I.; Shin, M.; Oh, J. H.;

Jeong, U.; Kim, T.-S.; Kim, B. J. Tuning Mechanical and Optoelectrical Properties

of Poly(3-Hexylthiophene) through Systematic Regioregularity Control.

Macromolecules **2015**, *48*, 4339–4346.

(82) Qian, Z.; Galuska, L. A.; Ma, G.; McNutt, W. W.; Zhang, S.; Mei, J.; Gu, X.

Backbone Flexibility on Conjugated Polymer's Crystallization Behavior and Thin

Film Mechanical Stability. *J. Polym. Sci.* **2022**, *60*, 548–558.

(83) Galuska, L. A.; Ocheje, M. U.; Ahmad, Z. C.; Rondeau-Gagné, S.; Gu, X.

Elucidating the Role of Hydrogen Bonds for Improved Mechanical Properties in a

High-Performance Semiconducting Polymer. *Chem. Mater.* **2022**,

acs.chemmater.1c04055.

(84) Zhang, S.; Koizumi, M.; Cao, Z.; Mao, K. S.; Qian, Z.; Galuska, L. A.; Jin, L.; Gu,

X. Directly Probing the Fracture Behavior of Ultrathin Polymeric Films. *ACS*

Polym. Au **2021**, acspolymersau.1c00005.

(85) Zhang, S.; Cheng, Y.; Galuska, L.; Roy, A.; Lorenz, M.; Chen, B.; Luo, S.; Li, Y.;

Hung, C.; Qian, Z.; et al. Tacky Elastomers to Enable Tear-Resistant and

Autonomous Self-Healing Semiconductor Composites. *Adv. Funct. Mater.* **2020**,

30, 2000663.

(86) Galuska, L. A.; Muckley, E. S.; Cao, Z.; Ehlenberg, D. F.; Qian, Z.; Zhang, S.; Rondeau-Gagné, S.; Phan, M. D.; Ankner, J. F.; Ivanov, I. N.; Gu, X. SMART Transfer Method to Directly Compare the Mechanical Response of Water-Supported and Free-Standing Ultrathin Polymeric Films. *Nat. Commun.* **2021**, *12*, 2347.

(87) Galuska, L. A.; McNutt, W. W.; Qian, Z.; Zhang, S.; Weller, D. W.; Dhakal, S.; King, E. R.; Morgan, S. E.; Azoulay, J. D.; Mei, J.; Gu, X. Impact of Backbone Rigidity on the Thermomechanical Properties of Semiconducting Polymers with Conjugation Break Spacers. *Macromolecules* **2020**, *53*, 6032–6042.

(88) O'Connell, P. A. Rheological Measurements of the Thermoviscoelastic Response of Ultrathin Polymer Films. *Science (80-.).* **2005**, *307*, 1760–1763.

(89) O'Connell, P. A.; Hutcheson, S. A.; McKenna, G. B. Creep Behavior of Ultra-Thin Polymer Films. *J. Polym. Sci. Part B Polym. Phys.* **2008**, *46*, 1952–1965.

(90) Li, X.; McKenna, G. B. Ultrathin Polymer Films: Rubbery Stiffening, Fragility, and T g Reduction. *Macromolecules* **2015**, *48*, 6329–6336.

(91) Chapuis, P.; Montgomery, P. C.; Anstotz, F.; Leong-Hoï, A.; Gauthier, C.; Baschnagel, J.; Reiter, G.; McKenna, G. B.; Rubin, A. A Novel Interferometric Method for the Study of the Viscoelastic Properties of Ultra-Thin Polymer Films Determined from Nanobubble Inflation. *Rev. Sci. Instrum.* **2017**, *88*.

(92) O'Connell, P. A.; McKenna, G. B. Novel Nanobubble Inflation Method for Determining the Viscoelastic Properties of Ultrathin Polymer Films. *Rev. Sci. Instrum.* **2007**, *78*, 013901.

(93)   O'Connell, P. A.; Wang, J.; Ishola, T. A.; McKenna, G. B. Exceptional Property Changes in Ultrathin Films of Polycarbonate: Glass Temperature, Rubbery Stiffening, and Flow. *Macromolecules* **2012**, *45*, 2453–2459.

(94)   Wang, B.; Luo, D.; Li, Z.; Kwon, Y.; Wang, M.; Goo, M.; Jin, S.; Huang, M.; Shen, Y.; Shi, H.; Ding, F.; Ruoff, R. S. Camphor-Enabled Transfer and Mechanical Testing of Centimeter-Scale Ultrathin Films. *Adv. Mater.* **2018**, *30*, 1800888.

(95)   Zhang, H.; Fujiki, K.; Ido, K.; Kusayanagi, N.; Sakagami, D.; Li, J.; Okamura, Y. Tensile Testing of Freestanding Polymer Thin Films With Non-Standard Geometries. *Polym. Test.* **2020**, *91*, 106825.

(96)   Keddie, J. L.; Jones, R. A. L.; Cory, R. A. Size-Dependent Depression of the Glass Transition Temperature in Polymer Films. *Europhys. Lett.* **1994**, *27*, 59–64.

(97)   Keddie, J. L.; Jones, R. A. L.; Cory, R. A. Interface and Surface Effects on the Glass-Transition Temperature in Thin Polymer Films. *Faraday Discuss.* **1994**, *98*, 219.

(98)   Ellison, C. J.; Torkelson, J. M. The Distribution of Glass-Transition Temperatures in Nanoscopically Confined Glass Formers. *Nat. Mater.* **2003**, *2*, 695–700.

(99)   Roth, C. B.; Pound, A.; Kamp, S. W.; Murray, C. A.; Dutcher, J. R. Molecular-Weight Dependence of the Glass Transition Temperature of Freely-Standing Poly(Methyl Methacrylate) Films. *Eur. Phys. J. E* **2006**, *20*, 441–448.

(100) Kim, S.; Torkelson, J. M. Distribution of Glass Transition Temperatures in Free-Standing, Nanoconfined Polystyrene Films: A Test of de Gennes' Sliding Motion Mechanism. *Macromolecules* **2011**, *44*, 4546–4553.

(101) Zhang, C.; Guo, Y.; Priestley, R. D. Glass Transition Temperature of Polymer Nanoparticles under Soft and Hard Confinement. *Macromolecules* **2011**, *44*, 4001–4006.

(102) Pye, J. E.; Roth, C. B. Above, below, and in-between the Two Glass Transitions of Ultrathin Free-Standing Polystyrene Films: Thermal Expansion Coefficient and Physical Aging. *J. Polym. Sci. Part B Polym. Phys.* **2015**, *53*, 64–75.

(103) White, R. P.; Price, C. C.; Lipson, J. E. G. Effect of Interfaces on the Glass Transition of Supported and Freestanding Polymer Thin Films. *Macromolecules* **2015**, *48*, 4132–4141.

(104) Baglay, R. R.; Roth, C. B. Local Glass Transition Temperature T g (z) of Polystyrene next to Different Polymers: Hard vs. Soft Confinement. *J. Chem. Phys.* **2017**, *146*, 203307.

(105) Chai, Y.; Salez, T.; Forrest, J. A. Using Mw Dependence of Surface Dynamics of Glassy Polymers to Probe the Length Scale of Free-Surface Mobility. *Macromolecules* **2020**, *53*, 1084–1089.

(106) Roth, C. B.; Dutcher, J. R. Glass Transition and Chain Mobility in Thin Polymer Films. *J. Electroanal. Chem.* **2005**, *584*, 13–22.

(107) KIM, S.; ROTH, C. B.; TORKELSON1, J. M. Effect of Nanoscale Confinement on the Glass Transition Temperature of Free-Standing Polymer Films: Novel, Self-Referencing Fluorescence Method. **2008**, *46*, 2754–2764.

(108) Gagnon, Y. J.; Roth, C. B. Local Glass Transition Temperature T g (z) Within Polystyrene Is Strongly Impacted by the Modulus of the Neighboring PDMS Domain. *ACS Macro Lett.* **2020**, *9*, 1625–1631.

187

(109) García, N. A.; Barrat, J.-L. Entanglement Reduction Induced by Geometrical Confinement in Polymer Thin Films. *Macromolecules* **2018**, *51*, 9850–9860.

(110) Bernazzani, P.; Simon, S. L.; Plazek, D. J.; Ngai, K. L. Effects of Entanglement Concentration on Tg and Local Segmental Motions. *Eur. Phys. J. E* **2002**, *8*, 201–207.

(111) Forrest, J. A.; Dalnoki-Veress, K.; Stevens, J. R.; Dutcher, J. R. Effect of Free Surfaces on the Glass Transition Temperature of Thin Polymer Films. *Phys. Rev. Lett.* **1996**, *77*, 2002–2005.

(112) Mattsson, J.; Forrest, J. A.; Börjesson, L. Quantifying Glass Transition Behavior in Ultrathin Free-Standing Polymer Films. *Phys. Rev. E* **2000**, *62*, 5187–5200.

(113) Dalnoki-Veress, K.; Forrest, J. A.; Murray, C.; Gigault, C.; Dutcher, J. R. Molecular Weight Dependence of Reductions in the Glass Transition Temperature of Thin, Freely Standing Polymer Films. *Phys. Rev. E* **2001**, *63*, 031801.

(114) Pye, J. E.; Roth, C. B. Two Simultaneous Mechanisms Causing Glass Transition Temperature Reductions in High Molecular Weight Freestanding Polymer Films as Measured by Transmission Ellipsometry. *Phys. Rev. Lett.* **2011**, *107*, 235701.

(115) Velikov, V. The Glass Transition of Water, Based on Hyperquenching Experiments. *Science (80-.).* **2001**, *294*, 2335–2338.

(116) Stafford, C. M.; Vogt, B. D.; Harrison, C.; Julthongpiput, D.; Huang, R. Elastic Moduli of Ultrathin Amorphous Polymer Films. *Macromolecules* **2006**, *39*, 5095–5099.

(117) Torres, J. M.; Stafford, C. M.; Vogt, B. D. Impact of Molecular Mass on the Elastic Modulus of Thin Polystyrene Films. *Polymer (Guildf).* **2010**, *51*, 4211–

4217.

(118) Spinks, G. M.; Brown, H. R.; Liu, Z. Indentation Testing of Polystyrene through the Glass Transition. *Polym. Test.* **2006**, *25*, 868–872.

(119) Torres, J. M.; Stafford, C. M.; Vogt, B. D. Elastic Modulus of Amorphous Polymer Thin Films: Relationship to the Glass Transition Temperature. *ACS Nano* **2009**, *3*, 2677–2685.

(120) Savagatrup, S.; Zhao, X.; Chan, E.; Mei, J.; Lipomi, D. J. Effect of Broken Conjugation on the Stretchability of Semiconducting Polymers. *Macromol. Rapid Commun.* **2016**, *37*, 1623–1628.

(121) Society, A. C. Structure/Properties of Conjugated Conductive Polymers. 1. Neutral Poly(3-Alkylthiophene)S. *Macromolecules* **1992**, *25*, 6081–6089.

(122) Müller, C. On the Glass Transition of Polymer Semiconductors and Its Impact on Polymer Solar Cell Stability. *Chem. Mater.* **2015**, *27*, 2740–2754.

(123) Zhan, P.; Zhang, W.; Jacobs, I. E.; Nisson, D. M.; Xie, R.; Weissen, A. R.; Colby, R. H.; Moulé, A. J.; Milner, S. T.; Maranas, J. K.; Gomez, E. D. Side Chain Length Affects Backbone Dynamics in Poly(3-alkylthiophene)S. *J. Polym. Sci. Part B Polym. Phys.* **2018**, *56*, 1193–1202.

(124) Qian, Z.; Cao, Z.; Galuska, L.; Zhang, S.; Xu, J.; Gu, X. Glass Transition Phenomenon for Conjugated Polymers. *Macromol. Chem. Phys.* **2019**, *220*, 1900062.

(125) Cao, Z.; Galuska, L.; Qian, Z.; Zhang, S.; Huang, L.; Prine, N.; Li, T.; He, Y.; Hong, K.; Gu, X. The Effect of Side-Chain Branch Position on the Thermal Properties of Poly(3-Alkylthiophenes). *Polym. Chem.* **2020**, *11*, 517–526.

(126) Wellinghoff, S. T.; Baer, E. Microstructure and Its Relationship to Deformation
       Processes in Amorphous Polymer Glasses. *J. Appl. Polym. Sci.* **1978**, *22*, 2025–
       2045.

(127) Wu, S. Secondary Relaxation, Brittle–Ductile Transition Temperature, and Chain
       Structure. *J. Appl. Polym. Sci.* **1992**, *46*, 619–624.

(128) Onorato, J.; Pakhnyuk, V.; Luscombe, C. K. Structure and Design of Polymers for
       Durable, Stretchable Organic Electronics. *Polym. J.* **2017**, *49*, 41–60.

(129) Ashizawa, M.; Zheng, Y.; Tran, H.; Bao, Z. Intrinsically Stretchable Conjugated
       Polymer Semiconductors in Field Effect Transistors. *Prog. Polym. Sci.* **2020**, *100*,
       101181.

(130) Koch, F. P. V.; Rivnay, J.; Foster, S.; Müller, C.; Downing, J. M.; Buchaca-
       Domingo, E.; Westacott, P.; Yu, L.; Yuan, M.; Baklar, M.; et al. The Impact of
       Molecular Weight on Microstructure and Charge Transport in Semicrystalline
       Polymer Semiconductors–Poly(3-Hexylthiophene), a Model Study. *Prog. Polym.
       Sci.* **2013**, *38*, 1978–1989.

(131) Gu, K.; Onorato, J. W.; Luscombe, C. K.; Loo, Y. The Role of Tie Chains on the
       Mechano-Electrical Properties of Semiconducting Polymer Films. *Adv. Electron.
       Mater.* **2020**, *6*, 1901070.

(132) Balar, N.; Rech, J. J.; Henry, R.; Ye, L.; Ade, H.; You, W.; O'Connor, B. T. The
       Importance of Entanglements in Optimizing the Mechanical and Electrical
       Performance of All-Polymer Solar Cells. *Chem. Mater.* **2019**, *31*, 5124–5132.

(133) McCulloch, I.; Heeney, M.; Bailey, C.; Genevicius, K.; MacDonald, I.; Shkunov,
       M.; Sparrowe, D.; Tierney, S.; Wagner, R.; Zhang, W.; Chabinyc, M. L.; Kline, R.

190

J.; McGehee, M. D.; Toney, M. F. Liquid-Crystalline Semiconducting Polymers with High Charge-Carrier Mobility. *Nat. Mater.* **2006**, *5*, 328–333.

(134) Galuska, L. A.; Ocheje, M. U.; Ahmad, Z. C.; Rondeau-Gagné, S.; Gu, X. Elucidating the Role of Hydrogen Bonds for Improved Mechanical Properties in a High-Performance Semiconducting Polymer. *Chem. Mater.* **2022**, acs.chemmater.1c04055.

(135) Zhang, W.; Smith, J.; Watkins, S. E.; Gysel, R.; McGehee, M.; Salleo, A.; Kirkpatrick, J.; Ashraf, S.; Anthopoulos, T.; Heeney, M.; McCulloch, I. Indacenodithiophene Semiconducting Polymers for High-Performance, Air-Stable Transistors. *J. Am. Chem. Soc.* **2010**, *132*, 11437–11439.

(136) Noriega, R.; Rivnay, J.; Vandewal, K.; Koch, F. P. V.; Stingelin, N.; Smith, P.; Toney, M. F.; Salleo, A. A General Relationship between Disorder, Aggregation and Charge Transport in Conjugated Polymers. *Nat. Mater.* **2013**, *12*, 1038–1044.

(137) Zheng, Y.; Wang, G. N.; Kang, J.; Nikolka, M.; Wu, H.; Tran, H.; Zhang, S.; Yan, H.; Chen, H.; Yuen, P. Y.; Mun, J.; Dauskardt, R. H.; McCulloch, I.; Tok, J. B. H.; Gu, X.; Bao, Z. An Intrinsically Stretchable High-Performance Polymer Semiconductor with Low Crystallinity. *Adv. Funct. Mater.* **2019**, *29*, 1905340.

(138) Di Lorenzo, M. L.; Righetti, M. C. Crystallization-Induced Formation of Rigid Amorphous Fraction. *Polym. Cryst.* **2018**, *1*, e10023.

(139) Wunderlich, B. Reversible Crystallization and the Rigid–Amorphous Phase in Semicrystalline Macromolecules. *Prog. Polym. Sci.* **2003**, *28*, 383–450.

(140) Martín, J.; Stingelin, N.; Cangialosi, D. Direct Calorimetric Observation of the Rigid Amorphous Fraction in a Semiconducting Polymer. *J. Phys. Chem. Lett.*

2018, *9*, 990–995.

(141) Xu, J.; Wang, S.; Wang, G.-J. N.; Zhu, C.; Luo, S.; Jin, L.; Gu, X.; Chen, S.; Feig, V. R.; To, J. W. F.; et al. Highly Stretchable Polymer Semiconductor Films through the Nanoconfinement Effect. *Science (80-.)*. **2017**, *355*, 59–64.

(142) Zhang, S.; Ocheje, M. U.; Luo, S.; Ehlenberg, D.; Appleby, B.; Weller, D.; Zhou, D.; Rondeau-Gagné, S.; Gu, X. Probing the Viscoelastic Property of Pseudo Free-Standing Conjugated Polymeric Thin Films. *Macromol. Rapid Commun.* **2018**, *39*, 1800092.

(143) Inal, S.; Rivnay, J.; Suiu, A. O.; Malliaras, G. G.; McCulloch, I. Conjugated Polymers in Bioelectronics. *Acc. Chem. Res.* **2018**, *51*, 1368–1376.

(144) Himmelberger, S.; Salleo, A. Engineering Semiconducting Polymers for Efficient Charge Transport. *MRS Commun.* **2015**, *5*, 383–395.

(145) Müller, C. On the Glass Transition of Polymer Semiconductors and Its Impact on Polymer Solar Cell Stability. *Chem. Mater.* **2015**, *27*, 2740–2754.

(146) Aime, J. P.; Bargain, F.; Schott, M. Structural Study of Conducting Polymers in Solution. *Synth. Met.* **1989**, *28*, C407–C417.

(147) Yamamoto, T.; Komarudin, D.; Arai, M.; Lee, B.-L.; Suganuma, H.; Asakawa, N.; Inoue, Y.; Kubota, K.; Sasaki, S.; Fukuda, T.; Matsuda, H. Extensive Studies on π-Stacking of Poly(3-Alkylthiophene-2,5-Diyl)s and Poly(4-Alkylthiazole-2,5-Diyl)s by Optical Spectroscopy, NMR Analysis, Light Scattering Analysis, and X-Ray Crystallography. *J. Am. Chem. Soc.* **1998**, *120*, 2047–2058.

(148) McCulloch, B.; Ho, V.; Hoarfrost, M.; Stanley, C.; Do, C.; Heller, W. T.; Segalman, R. A. Polymer Chain Shape of Poly(3-Alkylthiophenes) in Solution

Using Small-Angle Neutron Scattering. *Macromolecules* **2013**, *46*, 1899–1907.

(149) Fytas, G.; Nothofer, H. G.; Scherf, U.; Vlassopoulos, D.; Meier, G. Structure and Dynamics of Nondilute Polyfluorene Solutions. *Macromolecules* **2002**, *35*, 481–488.

(150) Gettinger, C. L.; Heeger, A. J.; Drake, J. M.; Pine, D. J. A Photoluminescence Study of Poly(Phenylene Vinylene) Derivatives: The Effect of Intrinsic Persistence Length. *J. Chem. Phys.* **1994**, *101*, 1673–1678.

(151) Reid, D. R.; Jackson, N. E.; Bourque, A. J.; Snyder, C. R.; Jones, R. L.; de Pablo, J. J. Aggregation and Solubility of a Model Conjugated Donor–Acceptor Polymer. *J. Phys. Chem. Lett.* **2018**, *9*, 4802–4807.

(152) Kuei, B.; Gomez, E. D. Chain Conformations and Phase Behavior of Conjugated Polymers. *Soft Matter* **2017**, *13*, 49–67.

(153) Zhang, W.; Gomez, E. D.; Milner, S. T. Predicting Chain Dimensions of Semiflexible Polymers from Dihedral Potentials. *Macromolecules* **2014**, *47*, 6453–6461.

(154) Zhang, S.; Ocheje, M. U.; Huang, L.; Galuska, L.; Cao, Z.; Luo, S.; Cheng, Y.; Ehlenberg, D.; Goodman, R. B.; Zhou, D.; Liu, Y.; Chiu, Y.; Azoulay, J. D.; Rondeau-Gagné, S.; Gu, X. The Critical Role of Electron-Donating Thiophene Groups on the Mechanical and Thermal Properties of Donor–Acceptor Semiconducting Polymers. *Adv. Electron. Mater.* **2019**, *5*, 1800899.

(155) Gasperini, A.; Bivaud, S.; Sivula, K. Controlling Conjugated Polymer Morphology and Charge Carrier Transport with a Flexible-Linker Approach. *Chem. Sci.* **2014**, *5*, 4922–4927.

(156) Zhao, Y.; Zhao, X.; Zang, Y.; Di, C.; Diao, Y.; Mei, J. Conjugation-Break Spacers in Semiconducting Polymers: Impact on Polymer Processability and Charge Transport Properties. *Macromolecules* **2015**, *48*, 2048–2053.

(157) Zhao, X.; Zhao, Y.; Ge, Q.; Butrouna, K.; Diao, Y.; Graham, K. R.; Mei, J. Complementary Semiconducting Polymer Blends: The Influence of Conjugation-Break Spacer Length in Matrix Polymers. *Macromolecules* **2016**, *49*, 2601–2608.

(158) Schroeder, B. C.; Chiu, Y. C.; Gu, X.; Zhou, Y.; Xu, J.; Lopez, J.; Lu, C.; Toney, M. F.; Bao, Z. Non-Conjugated Flexible Linkers in Semiconducting Polymers: A Pathway to Improved Processability without Compromising Device Performance. *Adv. Electron. Mater.* **2016**, *2*.

(159) Zhao, Y.; Zhao, X.; Roders, M.; Gumyusenge, A.; Ayzner, A. L.; Mei, J. Melt-Processing of Complementary Semiconducting Polymer Blends for High Performance Organic Transistors. *Adv. Mater.* **2017**, *29*, 1–7.

(160) Wang, G. J. N.; Molina-Lopez, F.; Zhang, H.; Xu, J.; Wu, H. C.; Lopez, J.; Shaw, L.; Mun, J.; Zhang, Q.; Wang, S.; Ehrlich, A.; Bao, Z. Nonhalogenated Solvent Processable and Printable High-Performance Polymer Semiconductor Enabled by Isomeric Nonconjugated Flexible Linkers. *Macromolecules* **2018**, *51*, 4976–4985.

(161) Oh, J. Y.; Rondeau-Gagné, S.; Chiu, Y.-C.; Chortos, A.; Lissel, F.; Wang, G.-J. N.; Schroeder, B. C.; Kurosawa, T.; Lopez, J.; Katsumata, T.; et al. Intrinsically Stretchable and Healable Semiconducting Polymer for Organic Transistors. *Nature* **2016**, *539*, 411–415.

(162) Melenbrink, E. L.; Hilby, K. M.; Alkhadra, M. A.; Samal, S.; Lipomi, D. J.; Thompson, B. C. Influence of Systematic Incorporation of Conjugation-Break

Spacers into Semi-Random Polymers on Mechanical and Electronic Properties. *ACS Appl. Mater. Interfaces* **2018**, *10*, 32426–32434.

(163) Melenbrink, E. L.; Hilby, K. M.; Choudhary, K.; Samal, S.; Kazerouni, N.; McConn, J. L.; Lipomi, D. J.; Thompson, B. C. Influence of Acceptor Side-Chain Length and Conjugation-Break Spacer Content on the Mechanical and Electronic Properties of Semi-Random Polymers. *ACS Appl. Polym. Mater.* **2019**, *1*, 1107–1117.

(164) McNutt, W. W.; Gumyunsenge, A.; Galuska, L. A.; Qian, Z.; He, J.; Gu, X.; Mei, J. N-Type Complimentary Semiconducting Polymer Blends. *ACS Appl. Polym. Mater.* **2020**.

(165) Pedersen, J. S.; Schurtenberger, P. Scattering Functions of Semiflexible Polymers with and without Excluded Volume Effects. *Macromolecules* **1996**, *29*, 7602–7612.

(166) Zhang, S.; Ocheje, M. U.; Luo, S.; Ehlenberg, D.; Appleby, B.; Weller, D.; Zhou, D.; Rondeau-Gagné, S.; Gu, X. Probing the Viscoelastic Property of Pseudo Free-Standing Conjugated Polymeric Thin Films. *Macromol. Rapid Commun.* **2018**, *39*, 1800092.

(167) Oosterhout, S. D.; Savikhin, V.; Zhang, J.; Zhang, Y.; Burgers, M. A.; Marder, S. R.; Bazan, G. C.; Toney, M. F. Mixing Behavior in Small Molecule:Fullerene Organic Photovoltaics. *Chem. Mater.* **2017**, *29*, 3062–3069.

(168) Printz, A. D.; Savagatrup, S.; Burke, D. J.; Purdy, T. N.; Lipomi, D. J. Increased Elasticity of a Low-Bandgap Conjugated Copolymer by Random Segmentation for Mechanically Robust Solar Cells. *RSC Adv.* **2014**, *4*, 13635–13643.

(169) Kim, J. S.; Kim, J. H.; Lee, W.; Yu, H.; Kim, H. J.; Song, I.; Shin, M.; Oh, J. H.; Jeong, U.; Kim, T. S.; Kim, B. J. Tuning Mechanical and Optoelectrical Properties of Poly(3-Hexylthiophene) through Systematic Regioregularity Control. *Macromolecules* **2015**, *48*, 4339–4346.

(170) Son, S. Y.; Kim, Y.; Lee, J.; Lee, G. Y.; Park, W. T.; Noh, Y. Y.; Park, C. E.; Park, T. High-Field-Effect Mobility of Low-Crystallinity Conjugated Polymers with Localized Aggregates. *J. Am. Chem. Soc.* **2016**, *138*, 8096–8103.

(171) SasView. 2019.

(172) Bi, Z.; Naveed, H. B.; Mao, Y.; Yan, H.; Ma, W. Importance of Nucleation During Morphology Evolution of the Blade-Cast PffBT4T-2OD-Based Organic Solar Cells. *Macromolecules* **2018**, *51*, 6682–6691.

(173) Qian, Z.; Galuska, L.; McNutt, W. W.; Ocheje, M. U.; He, Y.; Cao, Z.; Zhang, S.; Xu, J.; Hong, K.; Goodman, R. B.; Rondeau-Gagné, S.; Mei, J.; Gu, X. Challenge and Solution of Characterizing Glass Transition Temperature for Conjugated Polymers by Differential Scanning Calorimetry. *J. Polym. Sci. Part B Polym. Phys.* **2019**, *57*, 1635–1644.

(174) Sharma, A.; Pan, X.; Campbell, J. A.; Andersson, M. R.; Lewis, D. A. Unravelling the Thermomechanical Properties of Bulk Heterojunction Blends in Polymer Solar Cells. *Macromolecules* **2017**, *50*, 3347–3354.

(175) Wang, G.-J. N.; Zheng, Y.; Zhang, S.; Kang, J.; Wu, H.-C.; Gasperini, A.; Zhang, H.; Gu, X.; Bao, Z. Tuning the Cross-Linker Crystallinity of a Stretchable Polymer Semiconductor. *Chem. Mater.* **2019**, *31*, 6465–6475.

(176) Ocheje, M. U.; Selivanova, M.; Zhang, S.; Van Nguyen, T. H.; Charron, B. P.;

Chuang, C.-H.; Cheng, Y.-H.; Billet, B.; Noori, S.; Chiu, Y.-C.; Gu, X.; Rondeau-Gagné, S. Influence of Amide-Containing Side Chains on the Mechanical Properties of Diketopyrrolopyrrole-Based Polymers. *Polym. Chem.* **2018**, *9*, 5531–5542.

(177) Lin, B.; Zhang, L.; Zhao, H.; Xu, X.; Zhou, K.; Zhang, S.; Gou, L.; Fan, B.; Zhang, L.; Yan, H.; Gu, X.; Ying, L.; Huang, F.; Cao, Y.; Ma, W. Molecular Packing Control Enables Excellent Performance and Mechanical Property of Blade-Cast All-Polymer Solar Cells. *Nano Energy* **2019**, *59*, 277–284.

(178) Tummala, N. R.; Risko, C.; Bruner, C.; Dauskardt, R. H.; Brédas, J.-L. Entanglements in P3HT and Their Influence on Thin-Film Mechanical Properties: Insights from Molecular Dynamics Simulations. *J. Polym. Sci. Part B Polym. Phys.* **2015**, *53*, 934–942.

(179) Koch, F. P. V.; Rivnay, J.; Foster, S.; Müller, C.; Downing, J. M.; Buchaca-Domingo, E.; Westacott, P.; Yu, L.; Yuan, M.; Baklar, M.; et al. The Impact of Molecular Weight on Microstructure and Charge Transport in Semicrystalline Polymer Semiconductors–Poly(3-Hexylthiophene), a Model Study. *Prog. Polym. Sci.* **2013**, *38*, 1978–1989.

(180) Balar, N.; Rech, J. J.; Henry, R.; Ye, L.; Ade, H.; You, W.; O'Connor, B. T. The Importance of Entanglements in Optimizing the Mechanical and Electrical Performance of All-Polymer Solar Cells. *Chem. Mater.* **2019**, *31*, 5124–5132.

(181) Xie, R.; Aplan, M. P.; Caggiano, N. J.; Weisen, A. R.; Su, T.; Müller, C.; Segad, M.; Colby, R. H.; Gomez, E. D. Local Chain Alignment via Nematic Ordering Reduces Chain Entanglement in Conjugated Polymers. *Macromolecules* **2018**, *51*,

10271–10284.

(182) Xie, R.; Lee, Y.; Aplan, M. P.; Caggiano, N. J.; Müller, C.; Colby, R. H.; Gomez, E. D. Glass Transition Temperature of Conjugated Polymers by Oscillatory Shear Rheometry. *Macromolecules* **2017**, *50*, 5146–5154.

(183) Xie, R.; Colby, R. H.; Gomez, E. D. Connecting the Mechanical and Conductive Properties of Conjugated Polymers. *Adv. Electron. Mater.* **2018**, *4*.

(184) Costanzo, S.; Pasquino, R.; Läuger, J.; Grizzuti, N. Milligram Size Rheology of Molten Polymers. *Fluids* **2019**, *4*, 28.

(185) van Gurp, M.; Palmen, J. Time-Temperature Superposition for Polymeric Blends. *J Rheol Bull* **1998**, *65*, 5–8.

(186) Trinkle, S. VanGurp-Palmen-Plot. *Rheol. Acta* **2001**, *40*, 322–328.

(187) Qian, Z.; Koh, Y. P.; Pallaka, M. R.; Chang, A. B.; Lin, T.-P.; Guzmán, P. E.; Grubbs, R. H.; Simon, S. L.; McKenna, G. B. Linear Rheology of a Series of Second-Generation Dendronized Wedge Polymers. *Macromolecules* **2019**, *52*, 2063–2074.

(188) Ferry, J. *Viscoelastic Properties of Polymers. 3rd Ed.*, 3rd ed.; John Wiley & Sons, Inc., 1980.

(189) Brinkmann, M.; Gonthier, E.; Bogen, S.; Tremel, K.; Ludwigs, S.; Hufnagel, M.; Sommer, M. Segregated versus Mixed Interchain Stacking in Highly Oriented Films of Naphthalene Diimide Bithiophene Copolymers. *ACS Nano* **2012**, *6*, 10319–10326.

(190) Takacs, C. J.; Treat, N. D.; Krämer, S.; Chen, Z.; Facchetti, A.; Chabinyc, M. L.; Heeger, A. J. Remarkable Order of a High-Performance Polymer. *Nano Lett.* **2013**,

13, 2522–2527.

(191) Walker, L. M.; Wagner, N. J. SANS Analysis of the Molecular Order in Poly(γ-

Benzyl. *Society* **1996**, No. 29, 2298–2301.

(192) O'Connor, B.; Kline, R. J.; Conrad, B. R.; Richter, L. J.; Gundlach, D.; Toney, M.

F.; DeLongchamp, D. M. Anisotropic Structure and Charge Transport in Highly

Strain-Aligned Regioregular Poly(3-Hexylthiophene). *Adv. Funct. Mater.* **2011**,

21, 3697–3705.

(193) Gurau, M. C.; Delongchamp, D. M.; Vogel, B. M.; Lin, E. K.; Fischer, D. A.;

Sambasivan, S.; Richter, L. J. Measuring Molecular Order in Poly(3-

Alkylthiophene) Thin Films with Polarizing Spectroscopies. *Langmuir* **2007**, *23*,

834–842.

(194) Root, S. E.; Savagatrup, S.; Printz, A. D.; Rodriquez, D.; Lipomi, D. J. Mechanical

Properties of Organic Semiconductors for Stretchable, Highly Flexible, and

Mechanically Robust Electronics. *Chem. Rev.* **2017**, *117*, 6467–6499.

(195) Oh, J. Y.; Son, D.; Katsumata, T.; Lee, Y.; Kim, Y.; Lopez, J.; Wu, H.-C.; Kang,

J.; Park, J.; Gu, X.; Mun, J.; Wang, N. G.-J.; Yin, Y.; Cai, W.; Yun, Y.; Tok, J. B.

H.; Bao, Z. Stretchable Self-Healable Semiconducting Polymer Film for Active-

Matrix Strain-Sensing Array. *Sci. Adv.* **2019**, *5*, eaav3097.

(196) Yang, Z.; Fujii, Y.; Lee, F. K.; Lam, C.; Tsui, O. K. C. Glass Transition Dynamics

and Surface Layer Mobility in Unentangled Polystyrene Films. *Science (80-.).*

2010, *328*, 1676–1679.

(197) Ediger, M. D.; Forrest, J. a. Dynamics near Free Surfaces and the Glass Transition

in Thin Polymer Films: A View to the Future. *Macromolecules* **2014**, *47*, 471–478.

(198) Forrest, J. A.; Dalnoki-Veress, K.; Dutcher, J. R. Interface and Chain Confinement Effects on the Glass Transition Temperature of Thin Polymer Films. *Phys. Rev. E* **1997**, *56*, 5705–5716.

(199) Torres, J. M.; Stafford, C. M.; Uhrig, D.; Vogt, B. D. Impact of Chain Architecture (Branching) on the Thermal and Mechanical Behavior of Polystyrene Thin Films. *J. Polym. Sci. Part B Polym. Phys.* **2012**, *50*, 370–377.

(200) VanLandingham, M. R. Nanoindentation of Polymers : An Overview. *Macromol. Symp.* **2001**, *167*, 15–43.

(201) Hasegawa, H.; Ohta, T.; Ito, K.; Yokoyama, H. Stress-Strain Measurement of Ultra-Thin Polystyrene Films: Film Thickness and Molecular Weight Dependence of Crazing Stress. *Polymer (Guildf).* **2017**, *123*, 179–183.

(202) Bijleveld, J. C.; Verstrijden, R. A. M.; Wienk, M. M.; Janssen, R. A. J. Copolymers of Diketopyrrolopyrrole and Thienothiophene for Photovoltaic Cells. *J. Mater. Chem.* **2011**, *21*, 9224.

(203) Muckley, E. S.; Collins, L.; Srijanto, B. R.; Ivanov, I. N. Machine Learning-Enabled Correlation and Modeling of Multimodal Response of Thin Film to Environment on Macro and Nanoscale Using "Lab-on-a-Crystal." *Adv. Funct. Mater.* **2020**, *30*, 1908010.

(204) Yoon, S. M.; Cho, N. J.; Kanazawa, K. Analyzing Spur-Distorted Impedance Spectra for the QCM. *J. Sensors* **2009**, *2009*, 1–8.

(205) Ankner, J. F.; Tao, X.; Halbert, C. E.; Browning, J. F.; Michael Kilbey, S.; Swader, O. A.; Dadmun, M. S.; Kharlampieva, E.; Sukhishvili, S. A. The SNS Liquids Reflectometer. *Neutron News* **2008**, *19*, 14–16.

(206) Doucet, M.; Ferraz Leal, R. M.; Hobson, T. C. Web Interface for Reflectivity Fitting. *SoftwareX* **2018**, *7*, 287–293.

(207) Forrest, J. A.; Dalnoki-Veress, K. The Glass Transition in Thin Polymer Films. *Adv. Colloid Interface Sci.* **2001**, *94*, 167–195.

(208) Napolitano, S.; Glynos, E.; Tito, N. B. Glass Transition of Polymers in Bulk, Confined Geometries, and near Interfaces. *Reports Prog. Phys.* **2017**, *80*.

(209) Askar, S.; Evans, C. M.; Torkelson, J. M. Residual Stress Relaxation and Stiffness in Spin-Coated Polymer Films: Characterization by Ellipsometry and Fluorescence. *Polymer (Guildf).* **2015**, *76*, 113–122.

(210) Tobolsky, A. V. Some Viewpoints on Polymer Physics. *J. Polym. Sci. Part C Polym. Symp.* **1965**, *9*, 157–191.

(211) Forrest, J. A.; Dalnoki-Veress, K.; Dutcher, J. R. Brillouin Light Scattering Studies of the Mechanical Properties of Thin Freely Standing Polystyrene Films. *Phys. Rev. E* **1998**, *58*, 6109–6114.

(212) Roth, C. B.; Dutcher, J. R. Hole Growth in Freely Standing Polystyrene Films Probed Using a Differential Pressure Experiment. *Phys. Rev. E* **2005**, *72*, 021803.

(213) Roth, C. B.; Dutcher, J. R. Hole Growth as a Microrheological Probe to Measure the Viscosity of Polymers Confined to Thin Films. *J. Polym. Sci. Part B Polym. Phys.* **2006**, *44*, 3011–3021.

(214) Paeng, K.; Swallen, S. F.; Ediger, M. D. Direct Measurement of Molecular Motion in Freestanding Polystyrene Thin Films. *J. Am. Chem. Soc.* **2011**, *133*, 8444–8447.

(215) Gao, S.; Koh, Y. P.; Simon, S. L. Calorimetric Glass Transition of Single Polystyrene Ultrathin Films. *Macromolecules* **2013**, *46*, 562–570.

(216) Awartani, O.; Lemanski, B. I.; Ro, H. W.; Richter, L. J.; DeLongchamp, D. M.; O'Connor, B. T. Correlating Stiffness, Ductility, and Morphology of Polymer:Fullerene Films for Solar Cell Applications. *Adv. Energy Mater.* **2013**, *3*, 399–406.

(217) Yimer, Y. Y.; Yang, B.; Bhatta, R. S.; Tsige, M. Interfacial and Wetting Properties of Poly(3-Hexylthiophene)–Water Systems. *Chem. Phys. Lett.* **2015**, *635*, 139–145.

(218) Muckley, E. S.; Lynch, J.; Kumar, R.; Sumpter, B.; Ivanov, I. N. PEDOT:PSS/QCM-Based Multimodal Humidity and Pressure Sensor. *Sensors Actuators B Chem.* **2016**, *236*, 91–98.

(219) Horinouchi, A.; Yamada, N. L.; Tanaka, K. Aggregation States of Polystyrene at Nonsolvent Interfaces. *Langmuir* **2014**, *30*, 6565–6570.

(220) Rim, Y. S.; Bae, S. H.; Chen, H.; De Marco, N.; Yang, Y. Recent Progress in Materials and Devices toward Printable and Flexible Sensors. *Adv. Mater.* **2016**, *28*, 4415–4440.

(221) Shih, C. C.; Lee, W. Y.; Lu, C.; Wu, H. C.; Chen, W. C. Enhancing the Mechanical Durability of an Organic Field Effect Transistor through a Fluoroelastomer Substrate with a Crosslinking-Induced Self-Wrinkled Structure. *Adv. Electron. Mater.* **2017**, *3*, 1–8.

(222) Dang, W.; Vinciguerra, V.; Lorenzelli, L.; Ocheje, M. U.; Charron, B. P.; Nyayachavadi, A.; Rondeau-Gagné, S. Flexible and Printed Electronics Stretchable Electronics: Recent Progress in the Preparation of Stretchable and Self-Healing Semiconducting Conjugated Polymers Related Content Multiscale

Assembly of Solution-Processed Organic Electronics: The Critical Rol. *Flex.*
Print. Electron **2017**, *2*, 43002.

(223) Galant, O.; Bae, S.; Silberstein, M. N.; Diesendruck, C. E. Highly Stretchable
Polymers: Mechanical Properties Improvement by Balancing Intra- and
Intermolecular Interactions. *Adv. Funct. Mater.* **2020**, *30*, 1–8.

(224) Hammock, M. L.; Chortos, A.; Tee, B. C. K.; Tok, J. B. H.; Bao, Z. 25th
Anniversary Article: The Evolution of Electronic Skin (E-Skin): A Brief History,
Design Considerations, and Recent Progress. *Adv. Mater.* **2013**, *25*, 5997–6038.

(225) Takamatsu, T.; Chen, Y.; Yoshimasu, T.; Nishizawa, M.; Miyake, T.
Bioelectronics: Highly Efficient, Flexible Wireless-Powered Circuit Printed on a
Moist, Soft Contact Lens (Adv. Mater. Technol. 5/2019). *Adv. Mater. Technol.*

(226) Rivnay, J.; Owens, R. M.; Malliaras, G. G. The Rise of Organic Bioelectronics.
Chem. Mater. **2014**, *26*, 679–685.

(227) Gubbi, J.; Buyya, R.; Marusic, S.; Palaniswami, M. Internet of Things (IoT): A
Vision, Architectural Elements, and Future Directions. *Futur. Gener. Comput.*
Syst. **2013**, *29*, 1645–1660.

(228) Zhan, Y.; Mei, Y.; Zheng, L. Materials Capability and Device Performance in
Flexible Electronics for the Internet of Things. *J. Mater. Chem. C* **2014**, *2*, 1220–
1232.

(229) Wu, H.-C.; Benight, S. J.; Chortos, A.; Lee, W.-Y.; Mei, J.; To, J. W. F.; Lu, C.;
He, M.; Tok, J. B. H.; Chen, W.-C.; Bao, Z. A Rapid and Facile Soft Contact
Lamination Method: Evaluation of Polymer Semiconductors for Stretchable
Transistors. *Chem. Mater.* **2014**, *26*, 4544–4551.

(230) Li, Y.; Tatum, W. K.; Onorato, J. W.; Barajas, S. D.; Yang, Y. Y.; Luscombe, C. K. An Indacenodithiophene-Based Semiconducting Polymer with High Ductility for Stretchable Organic Electronics. *Polym. Chem.* **2017**, *8*, 5185–5193.

(231) Savagatrup, S.; Makaram, A. S.; Burke, D. J.; Lipomi, D. J. Mechanical Properties of Conjugated Polymers and Polymer-Fullerene Composites as a Function of Molecular Structure. *Adv. Funct. Mater.* **2014**, *24*, 1169–1181.

(232) Choi, D.; Kim, H.; Persson, N.; Chu, P. H.; Chang, M.; Kang, J. H.; Graham, S.; Reichmanis, E. Elastomer-Polymer Semiconductor Blends for High-Performance Stretchable Charge Transport Networks. *Chem. Mater.* **2016**, *28*, 1196–1204.

(233) Selivanova, M.; Chuang, C.-H.; Billet, B.; Malik, A.; Xiang, P.; Landry, E.; Chiu, Y.-C.; Rondeau-Gagné, S. Morphology and Electronic Properties of Semiconducting Polymer and Branched Polyethylene Blends. *ACS Appl. Mater. Interfaces* **2019**.

(234) Xu, J.; Wu, H.-C.; Zhu, C.; Ehrlich, A.; Shaw, L.; Nikolka, M.; Wang, S.; Molina-Lopez, F.; Gu, X.; Luo, S.; et al. Multi-Scale Ordering in Highly Stretchable Polymer Semiconducting Films. *Nat. Mater.* **2019**, *18*, 594–601.

(235) Savagatrup, S.; Zhao, X.; Chan, E.; Mei, J.; Lipomi, D. J. Effect of Broken Conjugation on the Stretchability of Semiconducting Polymers. *Macromol. Rapid Commun.* **2016**, *37*, 1623–1628.

(236) Bronstein, H.; Nielsen, C. B.; Schroeder, B. C.; McCulloch, I. The Role of Chemical Design in the Performance of Organic Semiconductors. *Nat. Rev. Chem.* **2020**, *4*, 66–77.

(237) Savagatrup, S.; Printz, A. D.; O'Connor, T. F.; Zaretski, A. V.; Lipomi, D. J.

Molecularly Stretchable Electronics. *Chem. Mater.* **2014**, *26*, 3028–3041.

(238) Yu, Z.; Niu, X.; Liu, Z.; Pei, Q. Intrinsically Stretchable Polymer Light-Emitting Devices Using Carbon Nanotube-Polymer Composite Electrodes. *Adv. Mater.* **2011**, *23*, 3989–3994.

(239) Gasperini, A.; Wang, G. J. N.; Molina-Lopez, F.; Wu, H. C.; Lopez, J.; Xu, J.; Luo, S.; Zhou, D.; Xue, G.; Tok, J. B. H.; Bao, Z. Characterization of Hydrogen Bonding Formation and Breaking in Semiconducting Polymers under Mechanical Strain. *Macromolecules* **2019**, *52*, 2476–2486.

(240) Yao, J.; Yu, C.; Liu, Z.; Luo, H.; Yang, Y.; Zhang, G.; Zhang, D. Significant Improvement of Semiconducting Performance of the Diketopyrrolopyrrole–Quaterthiophene Conjugated Polymer through Side-Chain Engineering via Hydrogen-Bonding. *J. Am. Chem. Soc.* **2016**, *138*, 173–185.

(241) Ocheje, M. U.; Goodman, R. B.; Lu, K.; Wang, Y.; Galuska, L. A.; Soullard, L.; Cao, Z.; Zhang, S.; Yadiki, M.; Gu, X.; Chiu, Y.; Rondeau-Gagné, S. Precise Control of Noncovalent Interactions in Semiconducting Polymers for High-Performance Organic Field-Effect Transistors. *Chem. Mater.* **2021**, *33*, 8267–8277.

(242) Ocheje, M. U.; Charron, B. P.; Cheng, Y.-H.; Chuang, C.-H.; Soldera, A.; Chiu, Y.-C.; Rondeau-Gagné, S. Amide-Containing Alkyl Chains in Conjugated Polymers: Effect on Self-Assembly and Electronic Properties. *Macromolecules* **2018**, *51*, 1336–1344.

(243) McGahan, W. A.; Johs, B.; Woollam, J. A. Techniques for Ellipsometric Measurement of the Thickness and Optical Constants of Thin Absorbing Films.

Thin Solid Films **1993**, *234*, 443–446.

(244) Baker, J. L.; Jimison, L. H.; Mannsfeld, S.; Volkman, S.; Yin, S.; Subramanian, V.; Salleo, A.; Alivisatos, A. P.; Toney, M. F. Quantification of Thin Film Crystallographic Orientation Using X-Ray Diffraction with an Area Detector. *Langmuir* **2010**, *26*, 9146–9151.

(245) Rivnay, J.; Mannsfeld, S. C. B.; Miller, C. E.; Salleo, A.; Toney, M. F. Quantitative Determination of Organic Semiconductor Microstructure from the Molecular to Device Scale. *Chem. Rev.* **2012**, *112*, 5488–5519.

(246) Zhang, S.; Galuska, L. A.; Gu, X. Water-assisted Mechanical Testing of Polymeric Thin-films. *J. Polym. Sci.* **2021**, No. May, pol.20210281.

(247) Son, S. Y.; Kim, Y.; Lee, J.; Lee, G.-Y.; Park, W.-T.; Noh, Y.-Y.; Park, C. E.; Park, T. High-Field-Effect Mobility of Low-Crystallinity Conjugated Polymers with Localized Aggregates. *J. Am. Chem. Soc.* **2016**, *138*, 8096–8103.

(248) Printz, A. D.; Savagatrup, S.; Burke, D. J.; Purdy, T. N.; Lipomi, D. J. Increased Elasticity of a Low-Bandgap Conjugated Copolymer by Random Segmentation for Mechanically Robust Solar Cells. *RSC Adv.* **2014**, *4*, 13635–13643.

(249) Yılgör, E. Hydrogen Bonding: A Critical Parameter in Designing Silicone Copolymers. *Polymer (Guildf).* **2001**, *42*, 7953–7959.

(250) Lee, C.; Stahlberg, E. A.; Fitzgerald, G. Chemical Structure of Urea in Water. *J. Phys. Chem.* **1995**, *99*, 17737–17741.

(251) Venkateshvaran, D.; Nikolka, M.; Sadhanala, A.; Lemaur, V.; Zelazny, M.; Kepa, M.; Hurhangee, M.; Kronemeijer, A. J.; Pecunia, V.; Nasrallah, I.; Romanov, I.; Broch, K.; McCulloch, I.; Emin, D.; Olivier, Y.; Cornil, J.; Beljonne, D.;

Sirringhaus, H. Approaching Disorder-Free Transport in High-Mobility Conjugated Polymers. *Nature* **2014**, *515*, 384–388.

(252) Peng, Z.; Ye, L.; Ade, H. Understanding, Quantifying, and Controlling the Molecular Ordering of Semiconducting Polymers: From Novices to Experts and Amorphous to Perfect Crystals. *Mater. Horizons* **2022**, *9*, 577–606.

(253) Mollinger, S. A.; Krajina, B. A.; Noriega, R.; Salleo, A.; Spakowitz, A. J. Percolation, Tie-Molecules, and the Microstructural Determinants of Charge Transport in Semicrystalline Conjugated Polymers. *ACS Macro Lett.* **2015**, *4*, 708–712.

(254) Menczel, J.; Wunderlich, B. Heat Capacity Hysteresis of Semicrystalline Macromolecular Glasses. *J. Polym. Sci. Polym. Lett. Ed.* **1981**, *19*, 261–264.

(255) Menczel, J. D.; Jaffe, M. How Did We Find the Rigid Amorphous Phase? *J. Therm. Anal. Calorim.* **2007**, *89*, 357–362.

(256) Androsch, R.; Wunderlich, B. The Link between Rigid Amorphous Fraction and Crystal Perfection in Cold-Crystallized Poly(Ethylene Terephthalate). *Polymer (Guildf).* **2005**, *46*, 12556–12566.

(257) Di Lorenzo, M. L.; Righetti, M. C. Effect of Thermal History on the Evolution of Crystal and Amorphous Fractions of Poly[(R)-3-Hydroxybutyrate] upon Storage at Ambient Temperature. *Eur. Polym. J.* **2013**, *49*, 510–517.

(258) Beckingham, B. S.; Ho, V.; Segalman, R. A. Formation of a Rigid Amorphous Fraction in Poly(3-(2′-Ethyl)Hexylthiophene). *ACS Macro Lett.* **2014**, *3*, 684–688.

(259) Remy, R.; Wei, S.; Campos, L. M.; Mackay, M. E. Three-Phase Morphology of Semicrystalline Polymer Semiconductors: A Quantitative Analysis. *ACS Macro*

Lett. **2015**, *4*, 1051–1055.

(260) Siddika, S.; Balar, N.; Booth, R. E.; O'Connor, B. T. Dynamic Mechanical
Analysis of Polymer Thin Films Using a Kirigami-Inspired Support. *ACS Macro
Lett.* **2021**, *10*, 1107–1112.

(261) Chew, A. R.; Ghosh, R.; Shang, Z.; Spano, F. C.; Salleo, A. Sequential Doping
Reveals the Importance of Amorphous Chain Rigidity in Charge Transport of
Semi-Crystalline Polymers. *J. Phys. Chem. Lett.* **2017**, *8*, 4974–4980.

(262) Joshi, S.; Pingel, P.; Grigorian, S.; Panzner, T.; Pietsch, U.; Neher, D.; Forster, M.;
Scherf, U. Bimodal Temperature Behavior of Structure and Mobility in High
Molecular Weight P3HT Thin Films. *Macromolecules* **2009**, *42*, 4651–4660.

(263) Tran, D. T.; Gumyusenge, A.; Luo, X.; Roders, M.; Yi, Z.; Ayzner, A. L.; Mei, J.
Effects of Side Chain on High Temperature Operation Stability of Conjugated
Polymers. *ACS Appl. Polym. Mater.* **2020**, *2*, 91–97.

(264) Jiang, Y.; Ning, L.; Liu, C.; Sun, Y.; Li, J.; Liu, Z.; Yi, Y.; Qiu, D.; He, C.; Guo,
Y.; Hu, W.; Liu, Y. Alignment of Linear Polymeric Grains for Highly Stable N-
Type Thin-Film Transistors. *Chem* **2021**, *7*, 1258–1270.

(265) Gumyusenge, A.; Tran, D. T.; Luo, X.; Pitch, G. M.; Zhao, Y.; Jenkins, K. A.;
Dunn, T. J.; Ayzner, A. L.; Savoie, B. M.; Mei, J. Semiconducting Polymer Blends
That Exhibit Stable Charge Transport at High Temperatures. *Science (80-.).* **2018**,
362, 1131–1134.

(266) Kim, J.-H.; Gadisa, A.; Schaefer, C.; Yao, H.; Gautam, B. R.; Balar, N.; Ghasemi,
M.; Constantinou, I.; So, F.; O'Connor, B. T.; Gundogdu, K.; Hou, J.; Ade, H.
Strong Polymer Molecular Weight-Dependent Material Interactions: Impact on the

Formation of the Polymer/Fullerene Bulk Heterojunction Morphology. *J. Mater. Chem. A* **2017**, *5*, 13176–13188.

(267) Li, Y.; Singh, S. P.; Sonar, P. A High Mobility P-Type DPP-Thieno[3,2-b]Thiophene Copolymer for Organic Thin-Film Transistors. *Adv. Mater.* **2010**, *22*, 4862–4866.

(268) Zhao, X.; Zhao, Y.; Ge, Q.; Butrouna, K.; Diao, Y.; Graham, K. R.; Mei, J. Complementary Semiconducting Polymer Blends: The Influence of Conjugation-Break Spacer Length in Matrix Polymers. *Macromolecules* **2016**, *49*, 2601–2608.

(269) McNutt, W. W.; Gumyusenge, A.; Galuska, L. A.; Qian, Z.; He, J.; Gu, X.; Mei, J. N-Type Complementary Semiconducting Polymer Blends. *ACS Appl. Polym. Mater.* **2020**, *2*, 2644–2650.

(270) Huang, L.; Eedugurala, N.; Benasco, A.; Zhang, S.; Mayer, K. S.; Adams, D. J.; Fowler, B.; Lockart, M. M.; Saghayezhian, M.; Tahir, H.; King, E. R.; Morgan, S.; Bowman, M. K.; Gu, X.; Azoulay, J. D. Open-Shell Donor–Acceptor Conjugated Polymers with High Electrical Conductivity. *Adv. Funct. Mater.* **2020**, *30*, 1909805.

(271) Bittle, E. G.; Basham, J. I.; Jackson, T. N.; Jurchescu, O. D.; Gundlach, D. J. Mobility Overestimation Due to Gated Contacts in Organic Field-Effect Transistors. *Nat. Commun.* **2016**, *7*, 10908.

(272) Horowitz, G. Organic Field-Effect Transistors. *Adv. Mater.* **1998**, *10*, 365–377.

(273) Bässler, H.; Köhler, A. Charge Transport in Organic Semiconductors. In *Topics in Current Chemistry*; 2011; Vol. 312, pp 1–65.

(274) Sirringhaus, H.; Brown, P. J.; Friend, R. H.; Nielsen, M. M.; Bechgaard, K.;

Langeveld-Voss, B. M. W.; Spiering, A. J. H.; Janssen, R. A. J.; Meijer, E. W.; Herwig, P.; de Leeuw, D. M. Two-Dimensional Charge Transport in Self-Organized, High-Mobility Conjugated Polymers. *Nature* **1999**, *401*, 685–688.

(275) Monnier, X.; Cavallo, D.; Righetti, M. C.; Di Lorenzo, M. L.; Marina, S.; Martin, J.; Cangialosi, D. Physical Aging and Glass Transition of the Rigid Amorphous Fraction in Poly(l -Lactic Acid). *Macromolecules* **2020**, *53*, 8741–8750.

(276) Marcus, M.; Tozer, O. R.; Barford, W. Theory of Optical Transitions in Conjugated Polymers. II. Real Systems. *J. Chem. Phys.* **2014**, *141*.

(277) Vezie, M. S.; Few, S.; Meager, I.; Pieridou, G.; Dörling, B.; Ashraf, R. S.; Goñi, A. R.; Bronstein, H.; McCulloch, I.; Hayes, S. C.; Campoy-Quiles, M.; Nelson, J. Exploring the Origin of High Optical Absorption in Conjugated Polymers. *Nat. Mater.* **2016**, *15*, 746–753.

(278) Wood, S.; Wade, J.; Shahid, M.; Collado-Fregoso, E.; Bradley, D. D. C.; Durrant, J. R.; Heeney, M.; Kim, J.-S. Natures of Optical Absorption Transitions and Excitation Energy Dependent Photostability of Diketopyrrolopyrrole (DPP)-Based Photovoltaic Copolymers. *Energy Environ. Sci.* **2015**, *8*, 3222–3232.

(279) Scharber, M. C.; Sariciftci, N. S. Low Band Gap Conjugated Semiconducting Polymers. *Adv. Mater. Technol.* **2021**, *6*, 2000857.

(280) Zhang, X.; Richter, L. J.; DeLongchamp, D. M.; Kline, R. J.; Hammond, M. R.; McCulloch, I.; Heeney, M.; Ashraf, R. S.; Smith, J. N.; Anthopoulos, T. D.; Schroeder, B.; Geerts, Y. H.; Fischer, D. A.; Toney, M. F. Molecular Packing of High-Mobility Diketo Pyrrolo-Pyrrole Polymer Semiconductors with Branched Alkyl Side Chains. *J. Am. Chem. Soc.* **2011**, *133*, 15073–15084.

(281) Cao, Z.; Ma, G.; Leng, M.; Zhang, S.; Chen, J.; Do, C.; Hong, K.; Fang, L.; Gu, X. Variable-Temperature Scattering and Spectroscopy Characterizations for Temperature-Dependent Solution Assembly of PffBT4T-Based Conjugated Polymers. *ACS Appl. Polym. Mater.* **2022**, acsapm.1c01511.

(282) Mun, J.; Wang, G.-J. N.; Oh, J. Y.; Katsumata, T.; Lee, F. L.; Kang, J.; Wu, H.-C.; Lissel, F.; Rondeau-Gagné, S.; Tok, J. B.-H.; Bao, Z. Effect of Nonconjugated Spacers on Mechanical Properties of Semiconducting Polymers for Stretchable Transistors. *Adv. Funct. Mater.* **2018**, *28*, 1804222.

(283) Wang, G.-J. N.; Molina-Lopez, F.; Zhang, H.; Xu, J.; Wu, H.-C.; Lopez, J.; Shaw, L.; Mun, J.; Zhang, Q.; Wang, S.; Ehrlich, A.; Bao, Z. Nonhalogenated Solvent Processable and Printable High-Performance Polymer Semiconductor Enabled by Isomeric Nonconjugated Flexible Linkers. *Macromolecules* **2018**, *51*, 4976–4985.

(284) Cao, K.; Feng, S.; Han, Y.; Gao, L.; Hue Ly, T.; Xu, Z.; Lu, Y. Elastic Straining of Free-Standing Monolayer Graphene. *Nat. Commun.* **2020**, *11*, 284.

(285) Zhang, P.; Ma, L.; Fan, F.; Zeng, Z.; Peng, C.; Loya, P. E.; Liu, Z.; Gong, Y.; Zhang, J.; Zhang, X.; Ajayan, P. M.; Zhu, T.; Lou, J. Fracture Toughness of Graphene. *Nat. Commun.* **2014**, *5*, 3782.

(286) Akinwande, D.; Brennan, C. J.; Bunch, J. S.; Egberts, P.; Felts, J. R.; Gao, H.; Huang, R.; Kim, J.-S.; Li, T.; Li, Y.; et al. A Review on Mechanics and Mechanical Properties of 2D Materials—Graphene and Beyond. *Extrem. Mech. Lett.* **2017**, *13*, 42–77.

(287) Lee, C.; Wei, X.; Kysar, J. W.; Hone, J. Measurement of the Elastic Properties and Intrinsic Strength of Monolayer Graphene. *Science (80-.).* **2008**, *321*, 385–388.

(288) Cooper, R. C.; Lee, C.; Marianetti, C. A.; Wei, X.; Hone, J.; Kysar, J. W. Nonlinear Elastic Behavior of Two-Dimensional Molybdenum Disulfide. *Phys. Rev. B* **2013**, *87*, 035423.

(289) Evans, C. M.; Deng, H.; Jager, W. F.; Torkelson, J. M. Fragility Is a Key Parameter in Determining the Magnitude of T g -Confinement Effects in Polymer Films. *Macromolecules* **2013**, *46*, 6091–6103.

(290) Napolitano, S.; Wübbenhorst, M. Structural Relaxation and Dynamic Fragility of Freely Standing Polymer Films. *Polymer (Guildf).* **2010**, *51*, 5309–5312.

(291) Rivnay, J.; Inal, S.; Salleo, A.; Owens, R. M.; Berggren, M.; Malliaras, G. G. Organic Electrochemical Transistors. *Nat. Rev. Mater.* **2018**, *3*, 17086.

(292) Rivnay, J.; Inal, S.; Salleo, A.; Owens, R. M.; Berggren, M.; Malliaras, G. G. Organic Electrochemical Transistors. *Nat. Rev. Mater.* **2018**, *3*, 17086.

(293) Moser, M.; Savagian, L. R.; Savva, A.; Matta, M.; Ponder, J. F.; Hidalgo, T. C.; Ohayon, D.; Hallani, R.; Reisjalali, M.; Troisi, A.; Wadsworth, A.; Reynolds, J. R.; Inal, S.; McCulloch, I. Ethylene Glycol-Based Side Chain Length Engineering in Polythiophenes and Its Impact on Organic Electrochemical Transistor Performance. *Chem. Mater.* **2020**, *32*, 6618–6628.

(294) Duong, D. T.; Tuchman, Y.; Chakthranont, P.; Cavassin, P.; Colucci, R.; Jaramillo, T. F.; Salleo, A.; Faria, G. C. A Universal Platform for Fabricating Organic Electrochemical Devices. *Adv. Electron. Mater.* **2018**, *4*, 1800090.

(295) Giovannitti, A.; Sbircea, D.-T.; Inal, S.; Nielsen, C. B.; Bandiello, E.; Hanifi, D. A.; Sessolo, M.; Malliaras, G. G.; McCulloch, I.; Rivnay, J. Controlling the Mode of Operation of Organic Transistors through Side-Chain Engineering. *Proc. Natl.*

Acad. Sci. **2016**, *113*, 12017–12022.

(296) Khodagholy, D.; Rivnay, J.; Sessolo, M.; Gurfinkel, M.; Leleux, P.; Jimison, L. H.; Stavrinidou, E.; Herve, T.; Sanaur, S.; Owens, R. M.; Malliaras, G. G. High Transconductance Organic Electrochemical Transistors. *Nat. Commun.* **2013**, *4*, 2133.